THE UNIVERSITY
OF BIRMINGHAM

CFD STUDIES OF COMPLEX FLUID FLOWS IN PIPES

By

MUHAMMAD EESA

A thesis submitted to

The University of Birmingham

For the degree of

DOCTOR OF PHILOSOPHY

Department of Chemical Engineering
College of Engineering and Physical Sciences
The University of Birmingham

March 2009

ABSTRACT

The flow of rheologically complex fluids in industrial equipment poses a number of challenges, not least from a modelling point of view. Research is needed to further understand and be able to predict the flow behaviour of such materials and to investigate ways of improving their processing. This work investigates the numerical modelling of complex fluids in three areas: flow and heat transfer under an externally imposed mechanical vibration, and steady-state solid-liquid flows as a first step in extending the vibration studies to these multiphase systems. Validated CFD simulations were used to study the effects of rotational and transversal mechanical vibrations on the pipe flow of viscous non-Newtonian fluids of the power-law, Bingham plastic, and Herschel-Bulkley types. Vibration frequencies in the sonic range of 0-300 Hz and linear amplitudes of 0-4 mm were used. The results showed that rotational and transversal vibrations give rise to substantial enhancements in flow for shear thinning and viscoplastic fluids, while shear thickening fluids experienced flow retardation. The flow enhancement was found to depend on vibration frequency and amplitude, fluid rheological properties, and pressure gradient. These vibrations can be effective at enhancing the flow of low to moderately viscous fluids in industries such as the confectionery industry. For extremely viscous fluids (consistency index ~10 kPa s^n and yield stress ~200 kPa), ultrasonic frequencies (> 16 kHz) were found to produce orders of magnitude enhancements in flow. These results suggest that vibration can increase the fluidity of highly viscous fluids in industrial applications such as polymer extrusion.

Results are also reported for the effects of transversal vibration on heat transfer and temperature uniformity in Newtonian and non-Newtonian shear thinning fluids. Vibration was found to generate sufficient chaotic fluid motion that led to considerable radial mixing which translated into a large enhancement in wall heat transfer as well as a near-uniform radial temperature field. Vibration also caused the temperature profile to develop very rapidly in the axial direction, thus, reducing the thermal entrance length by a large factor, so that much shorter pipes can be used to achieve a desired exit temperature. These effects increased with both vibration frequency and amplitude but were more sensitive to the amplitude. Higher fluid viscosities required larger amplitudes and/or frequencies to achieve substantial

temperature uniformity. These results have significant implications for processes where a wide temperature distribution over the pipe cross-section is undesirable as it leads to an uneven distribution of fluid heat treatment, such as in the thermal sterilisation of food products.

A numerical study was also conducted of the laminar pipe transport of coarse spherical particles (d = 2-9 mm) in non-Newtonian carrier fluids of the power law type using an Eulerian-Eulerian CFD model. The predicted flow fields were validated by PEPT experimental measurements of particle velocity profiles and passage times, whilst solid-liquid pressure drop was validated using relevant correlations gleaned from the literature. The study was concerned with nearly-neutrally buoyant particles (density ~1020 kg m^{-3}) flowing in a horizontal or vertical pipe at concentrations up to 40% v/v. The effects of various parameters on the flow properties of such mixtures were investigated over a wide range of conditions. Whilst the effects of varying the power law parameters and the mixture flow rate for shear thinning fluids were relatively small over the range of values considered, particle size and concentration had a significant bearing on the flow regime, the uniformity of the normalised particle radial distribution, the normalised velocity profiles of both phases, and the magnitude of the solid-liquid pressure drop. The maximum particle velocity was always significantly less than twice the mean flow velocity for shear thinning fluids, but it can exceed this value in shear thickening fluids. In vertical down-flow, particles were uniformly distributed over the pipe cross-section, and particle diameter and concentration had little effect on the normalised velocity and concentration profiles. Pressure drop, however, was greatly influenced by particle concentration. These results can help in understanding and predicting the flow behaviour of such solid-liquid mixtures in industrial applications, such as the conveying of particulate food suspensions.

AKNOLEDGEMENTS

I am most grateful to my supervisor Professor Mostafa Barigou for his excellent support and guidance throughout my PhD. I have been very fortunate to work under his supervision, and I thank him sincerely for his advice, encouragement and patience.

I would like to thank Dr Waldemar Bujalski, Department of Chemical Engineering, for his continuous help with the software and hardware used in this work. I would also like to thank the on-line technical support team at ANSYS UK, Ltd., for their effective help with software issues and for providing valuable modelling advice. In particular, I wish to thank Dr Justin Penrose, Dr Phil Stopford, Mark Turrell, Jon Lewin, and Chris Staples.

I would also like to express my appreciation to the Department of Chemical Engineering, University of Birmingham, for the significant contribution in funding this work.

Last but not least, I am most indebted to my parents, without whose support and encouragement I could not have achieved so much.

TABLE OF CONTENTS

LIST OF FIGURES

CHAPTER 4

CHAPTER 5

LIST OF TABLES

CHAPTER 1

INTRODUCTION

1. INTRODUCTION

A vast range of fluids of complex structures are now used in manufacturing an increasing number of products in a wide spectrum of industries including food, polymer, pharmaceutical, and chemical industries, in addition to applications in the oil, mining, construction, water treatment and power generation industries. Examples of such fluids include industrial oils, polymeric solutions, foams, organic suspensions such as paints, inorganic suspensions, and foodstuffs such as yogurt, mayonnaise, juice and fruit and vegetable purées.

Most of these complex fluids exhibit a non-Newtonian rheology making Newtonian behaviour the exception rather than the rule. The rheology of such fluids often gives rise to complex flow behaviours in industrial equipment. Even Newtonian fluids may sometimes exhibit complex flow behaviour under unsteady flow conditions or in flows involving mass or heat transfer. It is therefore imperative for the sound design and operation of processes in which such fluids are involved that a good understanding of their flow behaviour is available.

Non-Newtonian fluids have received significant attention from researchers over the past decades due to their increasing importance in industry. This is reflected in the growing volume of research dealing with the structure, properties and flow behaviour of such fluids. Nonetheless, this area of research is vast and growing, and further studies into the behaviour of non-Newtonian fluids in complex flow situations are still needed.

A number of experimental techniques have been used in studying non-Newtonian flows, such as Laser Doppler Velocimetry (LDV) and Particle Imaging Velocimetry (PIV). However, most of these techniques require the fluid to be transparent to the wavelength of the illuminating laser. This is a severe constraint and precludes the use of such techniques in studying most non-Newtonian fluids which are usually opaque. Nuclear Magnetic Resonance Imaging has been widely used due to its ability to probe optically opaque systems. However, the spatial constraints imposed by the requirement of generating high magnetic fields in the sample in addition to the

expense of an NMR spectrometer impose some limitations on its use. The Positron Emission Particle Tracking (PEPT) technique can also be used with opaque fluids, but its application in this area has so far been limited.

Computational Fluid Dynamics (CFD) is a useful tool for studying non-Newtonian flows. The impressive improvements in computer performance, matched by developments in numerical methods, have resulted in a growing confidence in the ability of CFD to model complex fluid flows. CFD techniques have been applied on a broad scale in the process industry to gain insight into various flow phenomena, examine different equipment designs or compare performance under different operating conditions. There are currently, however, limitations to the application of CFD, particularly in turbulent and multiphase flows.

The use of viscous non-Newtonian fluids in industry poses a number of challenges. Highly viscous fluids require much energy to flow in pipelines and processing equipment. However, for a non-Newtonian fluid with shear thinning characteristics, generating additional shear in the fluid can lead to significant reductions in its viscosity, thus facilitating its flow. This additional shear can be generated by means of mechanical shaking. Indeed, mechanical oscillation in the direction of flow has been shown to give rise to a significant enhancement in the flow of viscous non-Newtonian fluids. This phenomenon has been exploited for many years, for example, in the building and confectionery industries but mainly on an empirical basis. Considering the significance of this phenomenon, the data available in the literature on the flow enhancing effects of vibration are very limited. The available studies in this area have been limited to narrow ranges of vibration conditions and rheological behaviours. No data have been reported in the literature relating to vibration modes other than longitudinal (in the direction of flow) and transversal (normal to the direction of flow).

Mechanical vibration has another promising potential. In the continuous thermal processing of viscous fluids, where the fluid is heated through the pipe wall, the velocity distribution across the pipe results in a wide temperature distribution. This in

turn results in significant local variations in the thermal treatment received by the product, which may have adverse effects on the product quality. To avoid or minimise such effects, it is essential to ensure that all parts of the fluid receive an equal heat treatment by inducing some degree of fluid mixing. This is especially important in the food and pharmaceutical industries, where significant variations in the thermal treatment received by the fluid may affect its sterility or quality. Fluid mixing can be achieved using turbulent flow, but the high viscosity of the fluids involved makes this an impractical option. In-line static mixers can also be used to induce radial mixing, but their intricate geometries make them difficult to clean, and where hygiene is of the essence as in food and pharmaceutical production, the risk of contamination prohibits the use of such devices. In such cases, mechanical vibration seems a more suitable method. The benefits of vibration in this context do not appear to have been studied before. The study of these flows is complicated by the unsteady nature of the flow and the temperature-dependent rheological properties of the fluids involved.

The problem is even further complicated when coarse solid particles are added to the fluid. The large size of the solid particles means that the simplifying assumption of a homogeneous mixture used for fine particle suspensions is clearly inapplicable, and thus the mixture cannot be modelled as a single-phase. Solid-liquid mixtures have been widely studied in the literature, but most of the studies relate to water-based slurries of usually fine solid particles. A review of the literature reveals a severe lack of data on the flow of coarse solids in non-Newtonian flows; in particular, measurements of the solid phase velocity profile in such flows are very limited.

The research reported in this thesis aims to investigate the flow behaviour of rheologically complex fluids in three areas: flow and heat transfer under an imposed mechanical vibration, and two-phase solid-liquid flow. The work is conducted using numerical CFD models supported by validation studies. The objectives of the study are:

i. To investigate the effects of mechanical vibration on the flow of non-Newtonian fluids using different modes of oscillation.

ii. To investigate the potential of enhancing heat transfer and radial temperature uniformity in Newtonian and non-Newtonian fluids with temperature-dependent viscosities flowing in a heated pipe, by means of mechanical vibration.

iii. To assess the capability of CFD to simulate the flow of coarse solid particles in non-Newtonian fluids.

iv. To investigate the effects of various process parameters on the flow of coarse nearly-neutrally buoyant solid particles in non-Newtonian carrier fluids, especially the effects on solid phase velocity and concentration profiles.

By using CFD to study complex fluid flows, the thesis demonstrates the capabilities of CFD in modelling such flows and the potentials it offers in this area of research, while also highlighting some of its current limitations. It also highlights the need for further research in areas where information is lacking.

The thesis is divided into self-contained chapters, as follows.

Chapter 2 provides a general background to CFD including its applications, advantages, CFD analysis procedure, and methodology, and outlines the numerical techniques used in this work.

Chapter 3 reports an investigation of the effects of sinusoidal vibrations on the laminar flow of non-Newtonian fluids over a wide range of rheological behaviours and vibration conditions. The fluids used are of the power-law, Bingham plastic, and Herschel-Bulkley types. Two modes of vibration are studied: rotational and transversal. For very highly viscous fluids, vibrations in the ultrasonic range of frequency are applied. The effects of vibration frequency and amplitude, rheological

parameters, and pressure gradient on the flow enhancement due to vibration are investigated.

Chapter 4 is a study of the effects of transversal pipe vibration on the heat transfer and radial temperature uniformity in viscous Newtonian and non-Newtonian flows. It reports promising results that may lay the ground for the potential utilisation of mechanical vibration in processes such as food sterilisation.

In **Chapter 5**, an Eulerian CFD model is used to simulate the flow of coarse nearly-neutrally buoyant particles in non-Newtonian fluids. The CFD model is assessed using experimental data and empirical and semi-empirical correlations from the literature. The model is then used to conduct a parametric study of the effects of particle size and concentration, fluid rheology, and flow velocity on the solid and fluid phase velocity profile, particle concentration profile and pressure drop. This study prepares the ground for extending the vibration studies reported earlier to such multiphase systems.

Chapter 6 summarises the main conclusions of this work and makes recommendations for further work.

This research has thus far led to the following journal publications:

- Eesa, M. & Barigou, M. 2009. CFD investigation of the pipe transport of coarse solids in laminar power law fluids. *Chemical Engineering Science*, 64, 322-333.

- Eesa, M. & Barigou, M. 2008. Horizontal laminar flow of coarse nearly-neutrally buoyant particles in non-Newtonian conveying fluids: CFD and PEPT experiments compared. *Int. J. Multiphase Flow,* 34, 997-1007.

- Eesa, M. & Barigou, M. 2008. CFD analysis of viscous non-Newtonian flow under the influence of a superimposed rotational vibration. *Computers & Fluids,* 37 (1), 24-34.

CHAPTER 2

GENERAL BACKGROUND TO CFD AND NUMERICAL TECHNIQUES

Summary

In this chapter, an introduction to Computational Fluid Dynamics (CFD) is given including applications, advantages and methodology. The steps of the CFD analysis procedure are explained, and the three discretisation methods, namely finite difference, finite element, and finite volume methods are outlined. The discretisation technique used by the CFD code adopted in this work to discretise each of the terms in the governing equations is explained, and the strategy used to solve the resulting numerical equations is described including the coupled solver and the Algebraic Multigrid method. The main tools used for results analysis are also given.

2.1. DEFINITION AND HISTORY

Computational Fluid Dynamics (CFD) is the use of computer-based simulation to analyse systems involving fluid flow, heat transfer and associated phenomena such as chemical reaction (Versteeg and Malalasekera, 1996). A numerical model is first constructed using a set of mathematical equations that describe the flow. These equations are then solved using a computer programme in order to obtain the flow variables throughout the flow domain.

Since the advent of the digital computer, CFD has received extensive attention and has been widely used to study various aspects of fluid dynamics. The development and application of CFD have undergone considerable growth, and as a result it has become a powerful tool in the design and analysis of engineering and other processes. In the early 1980s, computers became sufficiently powerful for general-purpose CFD software to become available.

2.2. APPLICATIONS OF CFD

The earliest adopters of CFD were the aerospace, automotive and nuclear industries (Bakker *et al.*, 2001). Further growth and development in CFD and its ability to model complex phenomena along with the rapid increase in computer power have constantly widened the range of application of CFD. CFD is applied in a wide range of industries including mechanical, process, petroleum, power, metallurgical, biomedical, pharmaceutical and food industries.

CFD techniques have been applied on a broad scale in the process industry to gain insight into various flow phenomena, examine different equipment designs or compare performance under different operating conditions. Examples of CFD applications in the chemical process industry include drying, combustion, separation, heat exchange, mass transfer, pipeline flow, reaction, mixing, multiphase systems and material processing. CFD has also been applied to a number of food processing operations such as drying, refrigeration, sterilisation, mixing and heat exchangers (Xia and Sun, 2002). For example, CFD has been used to predict the air flow and velocity

during drying, optimise food mixing processing to minimise energy input and shorten the processing time, and model heat and mass transfer in food refrigeration.

CFD has also been successfully used in modelling various multiphase flow systems, particularly gas-solid mixtures, although some limitations still exist. Multiphase CFD models can help understand the complex interactions between the different phases and provide detailed 3-D transient information that experimental approaches may not be able to provide.

These applications, amongst others, demonstrate the potential of CFD to simulate complex flows and therefore the possibility of utilising it to investigate a wider range of processes. For instance, the application of CFD in food sterilisation has been limited to liquid foods in steady flow, and hence there is a clear need to extend this application to the more complex solid-liquid food systems or to complex unsteady flows.

2.3. VALIDATION OF CFD MODELS

Validation of CFD models is often required to assess the accuracy of the computational model. This assessment can assist in the development of reliable CFD models. Validation is achieved by comparing CFD results with available experimental, theoretical, or analytical data. Validated models become established as reliable, while those which fail the validation test need to be modified and re-validated. Different CFD models have been validated in a wide range of areas, such as food processing and mixing in stirred tanks, and this contributes to the growing application of CFD in industry and research. However, validation using experimental or theoretical data is not always possible, since such data are sometimes unavailable. A review of the literature in CFD validation can be found in Oberkampf and Trucano (2002).

2.4. ADVANTAGES OF CFD

Although the use of CFD may have a number of pitfalls, which can mostly be reduced to the user's inexperience and are therefore not fundamental, these pitfalls are far overweighed by its benefits (Bakker *et al*., 2001). There are situations, however, where complete fundamental knowledge of all the underlying physics may not exist, thus leading to inherent assumptions in the mathematical model adopted which give rise to possible inaccuracy. Nonetheless, CFD enjoys a number of advantages which contribute to the growing application of general-purpose CFD codes, including the following:

i. Ability to study systems where controlled experiments are not feasible.

ii. While the range of data that experiments can provide may sometimes be limited due to equipment or technique limitations, CFD can provide a wide range of comprehensive data as no such limitations are usually present.

iii. The complex physical interactions which occur in a flow situation can be modelled simultaneously since no limiting assumptions are usually needed.

iv. CFD can provide comprehensive flow visualisation. In fact, in many industrial applications CFD is more commonly applied as a flow visualisation tool than a source of absolute quantitative data (Gaylard, 2001).

2.5. CFD ANALYSIS PROCEDURE

A successful CFD analysis requires the following information:

i. *a grid of points* at which to store the variables calculated by CFD;
ii. *boundary conditions* required for defining the conditions at the boundaries of the flow domain and which enable the boundary values of all variables to be calculated;
iii. *fluid properties* such as viscosity and thermal conductivity;

iv. *flow models* which define the various aspects of the flow, such as turbulence, mass and heat transfer, and multiphase models;
v. *initial conditions* used to provide an initial guess of the solution variables in a steady state simulation or the initial state of the flow for a transient simulation; and
vi. *solver control parameters* required to control the behaviour of the numerical solution process.

The complete CFD analysis procedure can be divided into the following six stages.

2.5.1. Initial thinking

It is very important to understand as much as possible about the problem being simulated in order to accurately define it. This stage involves collecting all the necessary data required for the simulation including geometry details, fluid properties, flow specifications, and boundary and initial conditions.

2.5.2. Geometry creation

The geometry of the flow domain is created using specialised drawing software. Usually, 2-D sketches are first drawn and 3-D tools are then used to generate the full geometry.

2.5.3. Mesh generation

In this stage the continuous space of the flow domain is divided into sufficiently small discrete cells, the distribution of which determines the positions where the flow variables are to be calculated and stored. Variable gradients are generally more accurately calculated on a fine mesh than on a coarse one. A fine mesh is therefore particularly important in regions where large variations in the flow variables are expected. A fine mesh, however, requires more computational power and time. The mesh size is optimised by conducting a mesh-independence test whereby, starting with a coarse mesh, the mesh size is refined until the simulation results are no longer affected by any further refinement.

2.5.4. Flow specification

Flow specification involves defining the fluid physical properties, flow models, boundary conditions, and initial flow conditions, as determined in the initial thinking stage.

2.5.5. Calculation of the numerical solution

When all the information required for the simulation has been specified, the CFD software performs iterative calculations to arrive at a solution to the numerical equations representing the flow. The user needs also to provide the information that will control the numerical solution process such as the advection scheme (see Section 2.9.3 for details) and convergence criteria (see Section 2.10).

2.5.6. Results analysis

Having obtained the solution, the user can then analyse the results in order to check that the solution is satisfactory and to determine the required flow data. If the results obtained are unsatisfactory, the possible source of error needs to be identified, which can be an incorrect flow specification, a poor mesh quality, or a conceptual mistake in the formulation of the problem (Shaw, 1992).

Figure 2.1 shows a flowchart of the CFD analysis process (Shaw, 1992).

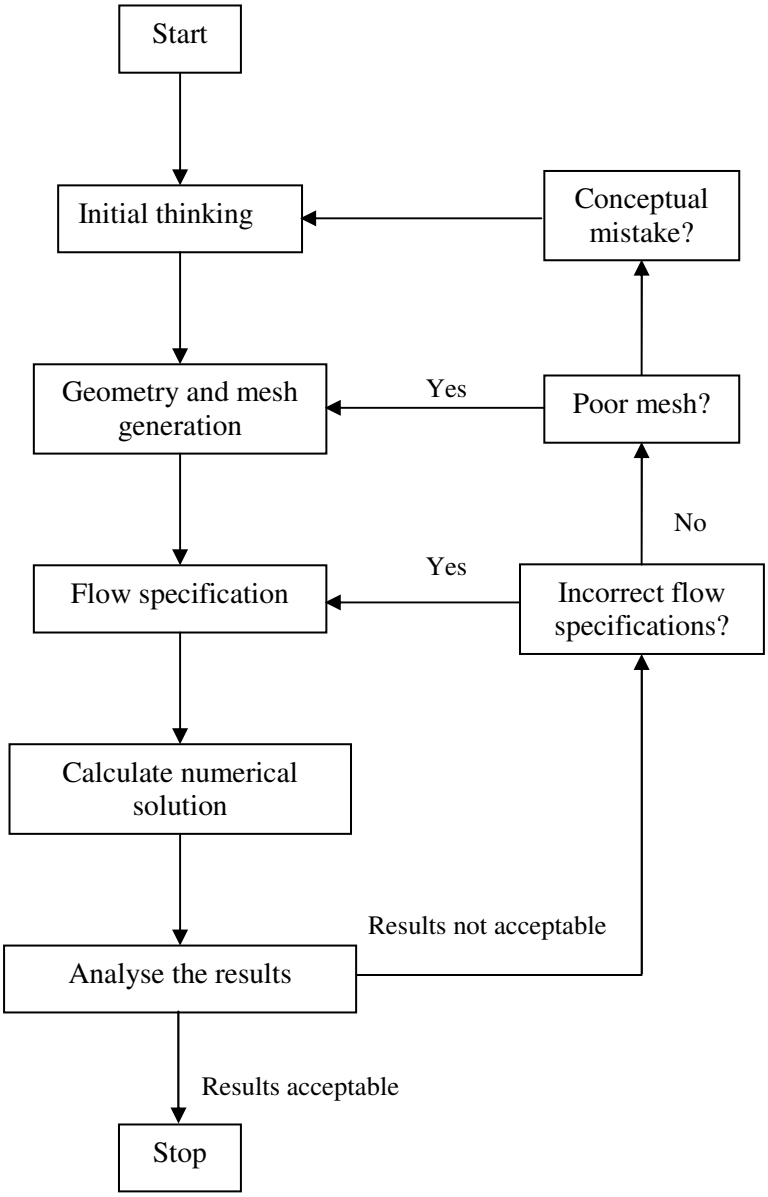

Figure 2.1: A flowchart of the CFD analysis process.

2.6. CFD METHODOLOGY

The mathematical modelling of a flow problem is achieved through three steps:

1. developing the governing equations which describe the flow;
2. discretisation of the governing equations; and
3. solving the resulting numerical equations.

2.6.1. Equations describing fluids in motion

The mathematical equations used to describe the flow of fluids are the continuity and momentum equations, which describe the conservation of mass and momentum, respectively. The momentum equations are also known as the Navier-Stokes equations. For flows involving heat transfer, another set of equations is required to describe the conservation of energy.

The continuity equation is derived by applying the principle of mass conservation to a small patch of fluid. In Cartesian coordinates, three equations of the following form are obtained (Abbott and Basco, 1989)

$$\frac{\partial \rho}{\partial t} + \frac{\partial}{\partial x_i}\left(\rho u_i\right) = 0 \tag{2.1}$$

where ρ is fluid density, t is time, u is velocity, and x is the coordinate. The subscript i indicates the Cartesian coordinates and the respective velocity components.

The momentum equations are derived by applying Newton's second law of motion to a small patch of fluid. According to Newton's second law, the rate of change of momentum for a patch of fluid is equal to the sum of all external forces acting on this patch of fluid. The resulting momentum equations in Cartesian coordinates take the general form (Abbott and Basco, 1989)

$$\frac{\partial}{\partial t}\left(\rho u_i\right) + \frac{\partial}{\partial x_j}\left(\rho u_j u_i\right) = -\frac{\partial P}{\partial x_i} + \frac{\partial}{\partial x_j}\left[\mu\left(\frac{\partial u_i}{\partial x_j} + \frac{\partial u_j}{\partial x_i}\right)\right] \tag{2.2}$$

where P is pressure and μ is fluid viscosity. Note that for a Newtonian fluid, the viscosity is constant, while for a non-Newtonian fluid, the shear rate-dependence of viscosity is taken into account using a constitutive equation for viscosity. The first term on the left hand side of the above equation represents the temporal variation of momentum, while the second term is the fluid acceleration. The forces on the right hand side represent the normal stresses (i.e. the pressure gradient force) and the

tangential shear stresses (i.e. the viscous force). Other forces, such as gravity, can be added to the equations as required using a source term.

2.6.2. Discretisation

The governing equations shown above are partial differential equations (PDEs). Since digital computers can only recognise and manipulate numerical data, these equations cannot be solved directly. Therefore, the PDEs must be transformed into numerical equations containing only numbers and no derivates. This process of producing a numerical analogue to the PDEs is called 'numerical discretisation'. The discretisation process involves an error since the numerical terms are only approximations to the original partial differential terms. This error, however, can be minimised to very low, and therefore acceptable, levels.

The major techniques used for discretisation are the finite difference method, the finite element method, and the finite volume method.

2.6.2.1. Finite-difference method

This method is based on the use of the Taylor series to transform the partial differential equations into a library of numerical equations that describe the derivatives of a variable as the differences between values of the variable at various points in space and time (Shaw, 1992).

Consider, for example, velocity, u, as a function of the independent variable, the distance x. According to the finite difference method, if the velocity value is known at one point p, then the Taylor series expansion can be used to determine the values of u at two points a small distance h away from p, thus

$$u^{p+h} = u^p + h\frac{du}{dx} + \frac{1}{2}h^2\frac{d^2u}{dx^2} + \frac{1}{6}h^3\frac{d^3u}{dx^3} + \ldots \tag{2.3}$$

$$u^{p-h} = u^p - h\frac{du}{dx} + \frac{1}{2}h^2\frac{d^2u}{dx^2} - \frac{1}{6}h^3\frac{d^3u}{dx^3} + \ldots \tag{2.4}$$

The first and second derivatives can be obtained by subtracting or adding the above two equations, respectively, to yield:

$$\frac{du}{dx} = \frac{1}{2h}\left(u^{p+h} - u^{p-h}\right) + O(h^2) \tag{2.5}$$

$$\frac{d^2u}{dx^2} = \frac{1}{h^2}\left(u^{p+h} - 2u^{p} + u^{p-h}\right) + O(h^2) \tag{2.6}$$

Derivatives can also be obtained by rearranging Equations (2.3) and (2.4). For example, the first derivative can be formed from Equation (2.3) as:

$$\frac{du}{dx} = \frac{1}{h}\left(u^{p+h} - u^{p}\right) + O(h) \tag{2.7}$$

or, from Equation (2.4) as:

$$\frac{du}{dx} = \frac{1}{h}\left(u^{p} - u^{p-h}\right) + O(h) \tag{2.8}$$

The term $O(h^n)$, known as the truncated term, represents the sum of n- and higher-order terms and is a function of the mesh spacing, represented by the distance h. For small h values, $O(h^n)$ terms are very small and can therefore be ignored. The order-accuracy of any discrete approximation is determined by the exponent of h in the largest term of the truncated term. Increasing the order-accuracy of an approximation implies that errors are reduced more rapidly with decreasing mesh size. This increase in accuracy, however, comes at a price. In addition to increasing the computational load, high-order accurate approximations are generally less robust than their low-order accurate counterparts as they may result in what is known as the wiggle phenomenon (for details see Abbott and Basco, 1989).

Equations (2.5) and (2.6) are called central difference formulae due to the geometrical relationship of the points used in the calculations, and are second-order accurate since the neglected terms are of order h^2 or higher. Equally, Equation (2.7) is a forward

difference formula and Equation (2.8) is a backward difference formula, both of which are first-order accurate since the neglected terms are of order *h* or higher.

2.6.2.2. Finite-element method

In this method, the domain is divided into a finite number of small sub-domains or elements. A simple variation of the dependent variables is assumed over each element, and these variations are then used to generate a description of how the variables vary over the whole domain. The variation of a variable within each element is calculated based on the values of the variable at the end-points of the element, known as the nodes of the element. The equations obtained for each element are then assembled in global matrices, and boundary conditions are imposed on the matrices so that the equations can be solved.

While the finite difference method produces the numerical equations at a given point based on the values at neighbouring points, as shown above, the finite element method produces equations for each element independently of all the other elements (Shaw, 1992). The interaction between elements is taken into account only when the element equations are assembled into matrices.

2.6.2.3. Finite volume method

The finite volume method is probably the most popular method used for numerical discretisation in CFD. This method is similar in some ways to the finite different method but some of its implementations draw on features taken from the finite element method.

This approach involves the discretisation of the spatial domain into finite control volumes. A control volume overlaps with many mesh elements and can therefore be divided into sectors each of which belongs to a different mesh element, as shown in Figure 2.2.

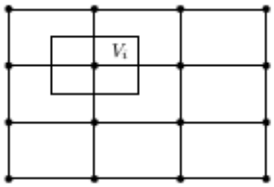

Figure 2.2: A control volume (V_i) surrounded by mesh elements.

The governing equations in their differential form are integrated over each control volume. The resulting integral conservation laws are exactly satisfied for each control volume and for the entire domain, which is a distinct advantage of the finite volume method. Each integral term is then converted into a discrete form, thus yielding discretised equations at the centroids, or nodal points, of the control volumes.

Similar to the finite difference method, the numerical equations at a given point are based on the values at neighbouring points. The basic mathematical formulation of the finite volume method is dealt with in Section 2.9, while a more elaborate description can be found in Versteeg and Malalasekera (1996).

2.6.3. Producing a solution

Once the discrete numerical equations have been obtained, they are solved by specialised computer software to obtain a set of numerical values for the variables at a set of discrete locations determined by the mesh. These equations are solved as a set of simultaneous equations, and owing to the usually very large number of equations in any such set of simultaneous equations, an iterative method is required to solve them. In an iterative method, an initial guess is taken for the values of the solution variables and then a more accurate approximation to the numerical equations is produced based on the error in the equations produced by the initial guess. This new updated solution is then used as the new starting solution to produce an even more accurate approximation, and the process is repeated until the error in the equations, known as the residual error, is reduced to sufficiently small values; the solution is then said to converge since the values of the variables at all points in the domain tend to move

towards some fixed values. If the error gets ever larger, the solution is said to be diverging and the final solution will be wrong.

The residual error is measured as the difference between the left-hand side and the right-hand side of the numerical equation being solved. This residual error does not exactly reach zero, but the solution process can be terminated when the maximum residual error to be tolerated is reached.

If the problem being solved is unsteady, i.e. time-dependent, the real time of the flow is divided into smaller time intervals, called time steps, and an approximate solution to the flow at each time step must be reached before moving to the next time step. This adds another loop of iteration to the solution process.

2.7. COMMERCIAL CFD SOFTWARE

The rapid growth in CFD, its applications, and computation power have made possible the development of several commercial CFD codes such as CFX, FLUENT, PHOENICS, and STAR-CD. These general-purpose codes can now cope with high levels of complexity in many application areas.

Typically, a CFD software package consists of three main groups of software:

- A pre-processor
- A solver
- A post-processor

2.7.1. Pre-processing

Pre-processing includes geometry and mesh generation, flow specification, and setting solver control parameters. Once the geometry has been generated and meshed, the fluid properties, flow models and solver control parameters are specified and boundary and initial conditions applied. These steps are usually carried out through a graphical interface.

2.7.2. Solving the equations

All the data defined in the pre-processing step are fed into the solver programme in the form of a data file. The solver is a specialised programme that solves the numerical equations based on the data specified in the data file. The results obtained by the solver are written to a results file for examination using the post-processor software.

2.7.3. Post-processing

In this software, the data obtained by the solver can be visualised and displayed using a variety of graphical methods such as contour, plane, vector and line plots. Calculations can also be made to obtain the values of scalar and vector variables, such as pressure and velocity, at different locations. Further details on post-processing are given in Section 2.11.

2.8. ANSYS CFX

The software packages used in the current work are ICEM CFD 4.CFX (for geometry and mesh generation), CFX 5.7, and ANSYS Workbench 10.0, all of which developed by ANSYS Inc. The software package ANSYS Workbench 10.0 consists of the following specialised components:

- *DesignModeler* for building geometries
- *CFX Mesh* for mesh generation
- *CFX-Pre* for flow specification
- *CFX-Solver* for solving the numerical equations
- *CFX-Post* for examining the results

CFX 5.7, which consists of the same last three components, was initially used in conjunction with ICEM CFD 4.CFX, which was used for geometry and mesh generation. ANSYS Workbench 10.0 contains an updated version of the code CFX. The CFX solver is based on the finite-volume discretisation method. Details of the discretisation and solution methods used in CFX are given below.

2.9. DISCRETISATION METHODS

The governing equations of flow possess the following general convection-diffusion form

$$\underbrace{\frac{\partial}{\partial t}(\rho\phi)}_{\substack{\text{Transient}\\ \text{term}}} + \underbrace{\frac{\partial}{\partial x_i}(\rho u_i \phi)}_{\substack{\text{Convection}\\ \text{term}}} - \underbrace{\frac{\partial}{\partial x_i}\left(\Gamma_\phi \frac{\partial \phi}{\partial x_i}\right)}_{\substack{\text{Diffusion}\\ \text{term}}} = \underbrace{S_\phi}_{\substack{\text{Source}\\ \text{term}}} \tag{2.9}$$

where ϕ is a dependent variable, Γ_ϕ is a diffusion coefficient for ϕ, and S_ϕ a source term. Equation (2.9) describes the processes by which a dependent variable ϕ is transported through the fluid, and is therefore called the transport equation. For the continuity equation (Equation (2.1)), $\phi = 1$, while both Γ_ϕ and S_ϕ are equal to zero. For the momentum equation (Equation (2.2)), the variable transported is velocity u_i, Γ_ϕ is viscosity, and S_ϕ is the sum of the forces acting on a patch of fluid.

The convection term in Equation (2.9) represents the flux of the variable ϕ convected by the flow. The diffusion term represents the random motion of molecules due to gradients in the density or number of molecules. The source term describes the production or destruction of ϕ and can also be used to model any term that cannot be represented by either of the advection or diffusion terms. Owing to the non-linearity of the advection term, being a product of dependent variables, the governing equations must be solved using an iterative method.

In the finite volume method used in this work, the partial differential equations of flow, represented by the above general equation, are integrated over each control volume. Consider the control volume shown at the centre of Figure 2.3 with its centre at P. The centres of the surrounding control volumes, where variable values are stored, are denoted by W (West), E (East), N (North), and S (South), while the respective faces of the control volume are denoted by lower case letters, as shown in the figure.

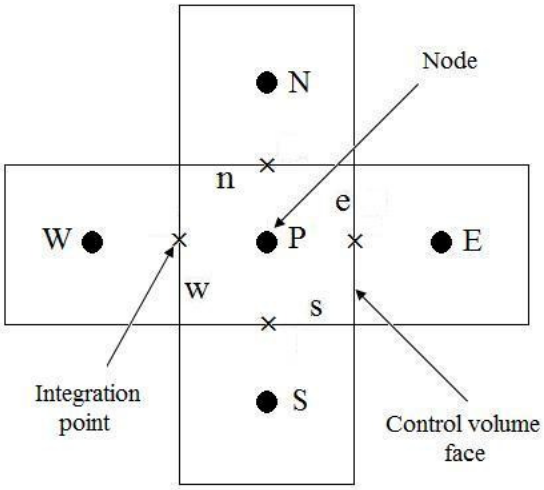

Figure 2.3: Control volumes in the finite volume method.

Integration of the transport equation (Equation (2.9)) over a control volume V gives:

$$\int_V \frac{\partial}{\partial t}(\rho\phi)dV + \int_V \frac{\partial}{\partial x_i}(\rho u_i \phi)dV - \int_V \frac{\partial}{\partial x_i}\left(\Gamma_\phi \frac{\partial \phi}{\partial x_i}\right)dV = \int_V S_\phi dV \tag{2.10}$$

The diffusion and advection volume integrals can be converted into surface integrals over the surface S of the control volume using the Gauss Divergence Theorem, thus

$$\int_V \frac{\partial}{\partial t}(\rho\phi)dV + \int_S \rho u_i \phi n_i dS - \int_S \Gamma_\phi \frac{\partial \phi}{\partial x_i} n_i dS = \int_V S_\phi dV \tag{2.11}$$

where n_i is the Cartesian component of the outward normal surface vector. This equation contains four terms which need to be discretised: a transient term, a diffusion term, a convection term, and a source term. The momentum equation (Equation (2.2)) also contains a pressure term which does not satisfy a transport equation. In the following, a description of the discretisation of these five terms in 2-D is given, which can be extended to 3-D by analogy.

2.9.1. Transient term

The transient (temporal) term in the transport equation in its integral form (Equation (2.11)) at time level *n* is given by the following approximation for incompressible flow (Abbott and Basco, 1989)

$$\int_v \frac{\partial}{\partial t}\rho\phi dV \approx V\rho\frac{\phi^{n+\frac{1}{2}}-\phi^{n-\frac{1}{2}}}{\Delta t} \tag{2.12}$$

in which the variable values at the start and end of the current timestep *n* are assigned the superscripts $n-\frac{1}{2}$ and $n+\frac{1}{2}$, respectively, and where Δt is the size of the time step. These values can be obtained using the First Order Backward Euler scheme or the Second Order Backward Euler scheme. In the first order scheme, these values are approximated using the current and old time level solution values, i.e. ϕ^n and ϕ^{n-1} respectively, thus

$$\int_v \frac{\partial}{\partial t}\rho\phi dV = V\rho\frac{\phi^{n}-\phi^{n-1}}{\Delta t} \tag{2.13}$$

The more accurate, but computationally more expensive, Second Order Backward Euler scheme approximates the values at the start and end of timestep *n* using the previous two time level solution values, i.e. ϕ^{n-1} and ϕ^{n-2}, thus

$$\phi^{n-\frac{1}{2}} = \phi^{n-1} + \frac{1}{2}\left(\phi^{n-1}-\phi^{n-2}\right) \tag{2.14}$$

$$\phi^{n+\frac{1}{2}} = \phi^{n} + \frac{1}{2}\left(\phi^{n}-\phi^{n-1}\right) \tag{2.15}$$

More memory is required in this scheme compared to the First Order Backward Euler scheme as the variable needs to be stored at an extra time step.

2.9.2. Diffusion term

Diffusion terms are usually discretised using central differencing (see Section 2.6.2.1), as follows

$$\int_S \Gamma_\phi \frac{\partial \phi}{\partial x_i} n_i dS = \frac{\Gamma_\phi A_e}{(\delta x)_e}(\phi_E - \phi_P) - \frac{\Gamma_\phi A_w}{(\delta x)_w}(\phi_P - \phi_W) + \frac{\Gamma_\phi A_n}{(\delta x)_n}(\phi_N - \phi_P) - \frac{\Gamma_\phi A_s}{(\delta x)_s}(\phi_P - \phi_S)$$
$$= D_e(\phi_E - \phi_P) - D_w(\phi_P - \phi_W) + D_n(\phi_N - \phi_P) - D_s(\phi_P - \phi_S) \quad (2.16)$$

in which $D_e = \frac{\Gamma_\phi A_e}{(\delta x)_e}$, $D_w = \frac{\Gamma_\phi A_w}{(\delta x)_w}$, etc. and where δx is the distance between the respective node centre and P, and A is the surface area of the respective cell face.

2.9.3. Convection term

The convection term in Equation (2.11) is integrated as the sum of fluxes over the four faces surrounding the control volume, thus

$$\int_S \rho u_i \phi n_i dS = \rho u_e A_e \phi_e - \rho u_w A_w \phi_w + \rho u_n A_n \phi_n - \rho u_s A_s \phi_s \quad (2.17)$$

As can be seen, the integration yields values of ϕ at the faces of the control volume. However, solution variables are stored at grid nodes (i.e. control volume centres P, E, etc.). It is therefore necessary to express the face values of ϕ in Equation (2.17) in terms of adjacent nodal values. The method of specifying face values in terms of adjacent nodal values is called an 'advection scheme'. The face value of a variable is calculated at an integration point, ϕ_{ip}, from the variable value at the upwind node, ϕ_{up}, and the variable gradient, $\nabla\phi$, thus

$$\phi_{ip} = \phi_{up} + \beta \nabla \phi . \Delta \vec{r} \quad (2.18)$$

where β is a blend factor and $\Delta\vec{r}$ is the vector from the upwind node to the integration point. Particular choices of β and $\nabla\phi$ yield different advection schemes as follows (CFX manual, ANSYS, Inc.):

(i) First order Upwind Differencing Scheme

This scheme is obtained when $\beta = 0$. The variable value at an integration point is therefore equal to its value at the upwind node. This scheme is first-order accurate and introduces discretisation error due to numerical diffusion, but it is very robust as it does not result in non-physical values.

(ii) Numerical Advection Correction Scheme (Specify Blend)

In this scheme, a value for β between 0 and 1 is chosen and the gradient $\nabla\phi$ is calculated as the average of the adjacent nodal gradients. This scheme reduces the errors associated with the Upwind Differencing Scheme. The choice $\beta = 0$ results in a first-order accurate scheme, while $\beta = 1$ is formally second-order accurate. With $\beta = 1$, the scheme is not bounded as it may produce non-physical oscillations in regions of rapid solution variation.

(iii) High Resolution Scheme

This scheme is intended to satisfy both accuracy and boundedness requirements by computing β locally to be as close to 1 as possible without resulting in non-physical values, while the gradient $\nabla\phi$ is set equal to the control volume gradient at the upwind node. The recipe for β adopted in CFX is based on the boundedness principles used by Barth and Jesperson (1989).

2.9.4. Source term

The source term is discretised as follows (Patankar, 1980)

$$\int_V S_\phi dV = \overline{S_\phi} V \tag{2.19}$$

where $\overline{S_\phi}$ is the average value of the source S_ϕ throughout the control volume. When S_ϕ is a function of ϕ, $\overline{S_\phi}$ is decomposed into a solution-independent part, b_P, and a solution-dependent part, thus

$$\overline{S_\phi} = b_P + S_P \phi_P \quad , \qquad S_P \leq 0 \tag{2.20}$$

2.9.5. Pressure-velocity coupling

Pressure is given indirectly by the continuity equation in that when the correct pressure is substituted into the momentum equation, the resulting velocity field must satisfy continuity. The calculations of pressure and velocity are therefore coupled.

The pressure term is discretised by central differencing, where the pressure difference between the west and east faces of the control volume, for example, is calculated as

$$P_w - P_e = \frac{P_W + P_P}{2} - \frac{P_E + P_P}{2} = \frac{P_W - P_E}{2} \tag{2.21}$$

This means that the pressure term is calculated using alternate nodal pressure values rather than adjacent ones (see Figure 2.3). This means that an oscillatory pressure field, in which, for example, the pressure at consecutive grid nodes follows the sequence 1, 10, 1, 10, 1, etc., would be treated as a uniform pressure field since alternate grid points have the same value. This can also result in pressure-velocity decoupling. To overcome this problem, CFX employs the Rhie Chow algorithm (for details, see Rhie and Chow, 1983).

2.10. SOLUTION STRATEGY

2.10.1. Solving the numerical equations

Application of the finite volume method to all elements in the domain results in a linear set of equations. These equations are solved in CFX using a coupled solver, whereby the hydrodynamic equations for velocity and pressure are solved as a single

system. Consider a simple case where a set of simultaneous equations consists of three equations each of which contains three variables, ϕ_1, ϕ_2, and ϕ_3. The discretised numerical equations can be written in the form:

$$\left.\begin{aligned} a_{11}\phi_1 + a_{12}\phi_2 + a_{13}\phi_3 &= b_1 \\ a_{21}\phi_1 + a_{22}\phi_2 + a_{23}\phi_3 &= b_2 \\ a_{31}\phi_1 + a_{32}\phi_2 + a_{33}\phi_3 &= b_3 \end{aligned}\right\} \tag{2.22}$$

where a_{ij} are coefficients of the variable ϕ_j, and b_i are known values in the equations. This linearised system of discrete equations can be written in the general matrix form (Shaw, 1992)

$$[A][\phi] = [B] \tag{2.23}$$

where $[A]$ is the coefficient matrix, $[\phi]$ is the solution vector (i.e. vector of variables), and $[B]$ is the right-hand side matrix. This equation is solved iteratively by starting with a guessed initial solution, ϕ^n, and substituting it in Equation (2.23) to obtain a residual, r^n, thus

$$r^n = B - A\phi^n \tag{2.24}$$

This residual is used to calculate a correction, ϕ', which in turn is used to produce an improved solution ϕ^{n+1}, thus

$$\phi^{n+1} = \phi^n + \phi' \tag{2.25}$$

where the correction ϕ' is obtained by solving the equation

$$A\phi' = r^n \tag{2.26}$$

This algorithm is repeated until the residual of the equations solved reaches a pre-defined level.

To enhance the performance of the solver, CFX uses an Algebraic Multigrid method. In this method, early iterations are carried out on the original mesh, while later iterations are carried out on progressively coarser virtual ones. Whilst a fine mesh reduces local errors in the solution, coarse grids allow the solver to reduce global errors by imposing conservation requirements over larger volumes. By using coarse grids, this method also accelerates the solution.

2.10.2. Controlling the iterative process

The iterative solution process must be controlled in order to help the solution converge. For any steady state simulation, the maximum number of iterations to be performed must be specified along with the convergence target, i.e. the normalised residual error in the final iteration. The solution process will terminate when either the residual target is met or the maximum number of iterations is reached.

Two methods are commonly used to control the iterative procedure in a steady state problem: under-relaxation or the use of a time-dependent scheme (Shaw, 1992).

The use of an under-relaxation parameter smooths the iterative process and can prevent divergence. In this method, the solution calculated during an iteration is scaled so that the solution used in the next iteration is not too different from the solution at the start of the current iteration. The value of a solution variable calculated at the end of the current iteration, ϕ_{cal}, and the value at the start of the current iteration, ϕ_s, are used to calculate the value of the variable at the start of the next iteration, ϕ_{new}, using an under-relaxation factor, ω, thus

$$\phi_{new} = \omega\phi_{cal} + (1-\omega)\phi_s \tag{2.27}$$

The new value of the variable is between ϕ_s and ϕ_{cal}. The under-relaxation factor ω varies from 0 to 1. When ω = 1, the current solution calculated at the end of the iteration is used at the start of the new iteration, i.e. no under-relaxation is applied.

The second method of controlling the solution process is to use a time-dependent scheme even if the flow is steady. The modelling of time variation smooths out the way in which the solution proceeds from one iteration to the next.

For time-dependent flows, the flow is solved over a time period which is chosen so as to represent the time scale of the flow phenomenon investigated (e.g. fluid residence time in a pipe). This time period is divided into a number of smaller time steps, i.e. is discretised. The solution must converge at each time step before moving to the next time step. A number of iterations are therefore required at each time step to lead the solution to convergence. The size of the time step has to be sufficiently small to capture the temporal changes in the flow variables accurately. Small time steps also help the solution converge and require fewer iterations per time step. On the other hand, a small time step size means that a large number of time steps are required, thus prolonging the simulation. The choice of the time step size should also take account of the requirement that the final solution must be independent of the time step.

2.11. RESULTS ANALYSIS

The ability of CFD to display results effectively is an invaluable tool. The variation of flow variables throughout the domain can be visualised graphically in CFX, as in other CFD software, using different types of plots. Data can also be exported from CFX to be processed in other types of software such as Excel and SigmaPlot.

2.11.1. X-Y charts

X-Y charts are a very useful way to present numerical data, and are widely used for profiles of flow variables, particularly velocity. For example, the development of flow can be visualised by plotting several successive velocity profiles starting at the flow inlet.

2.11.2. Contour plots

These are 2-D colour maps intended to show the variation of a variable on a surface within the domain. Colour is an excellent medium to convey information and present data.

2.11.3. Streamlines

A Streamline is a curve that is instantaneously tangential to the velocity vector of the flow. It represents the path that a particle of zero mass would take through the fluid domain at a given instant. Streamlines are useful in showing flow patterns, especially in complex flows, but should be interpreted carefully when the flow is unsteady, i.e. time-dependent, as they represent the path of particles only at a given instant.

2.11.4. Particle tracks

This tool is used to reveal the actual trajectory of fluid or solid particles in the flow. This can be particularly useful to show the presence or extent of mixing in single- or multi-phase flows. Unlike streamlines, particle tracks can show the actual path of particles in unsteady flow.

2.11.5. Animation

Advanced CFD software allows the user to create animations of different types to reveal the space or time variation of a variable. For example, particles can be visualised as they travel along their trajectories, and the time evolution of a variable on a contour plot can be shown.

NOMENCLATURE

A	surface area of cell face
h	distance between two points in the finite difference method
$O(h)$	truncated term
P	pressure
r^n	residual error
S	surface of control volume
S_ϕ	source term
t	time
Δt	timestep
u	velocity
V	volume of control volume
x	Cartesian coordinate
δx	distance between adjacent cell nodes in the finite volume method

Greek letters

β	blend factor
Γ_ϕ	diffusion coefficient for ϕ
μ	fluid viscosity
ρ	fluid density
ϕ	dependent variable
ω	under-relaxation factor

REFERENCES

Abbott, M.B. & Basco, D.R. (1989). Computational fluid dynamics: an introduction for engineers. Longman Group UK Limited.

Bakker, A., Haidari, A.H. & Oshinowo, L.M. 2001. Realize greater benefits from CFD. *Fluid/Solids Handling, AIChE's CEP magazine*, March 2001, 45-53.

Barth, T.J. & Jesperson, D.C. 1989. The design and application of upwind schemes on unstructured meshes. *AIAA*, Paper 89-0366.

CFX 5.7 User Manual. 2005. ANSYS, Inc.

Gaylard, A. 2001. In: Computational fluid dynamics in practice. Rhodes, N. (Editor). Proffesional Engineering Publishing.

Norton, T. & Sun, D-W. 2006. Computational fluid dynamics (CFD) – an effective and efficient design and analysis tool for the food industry: a review. *Trends in Food Science & Technology*, 17, 600-620.

Oberkampf, W.L. & Trucano, T.G. 2002. Verification and validation in computational fluid dynamics. *Progress in Aerospace Sciences*, 38, 209–272.

Patankar, S.V. 1980. Numerical heat transfer and fluid flow. Taylor & Francis.

Shaw, C.T. (1992). Using computational fluid dynamics. Prentice Hall International (UK) Ltd.

Versteeg, H.K. & Malalasekera, W. 1996. Introduction to computational fluid dynamics: the finite volume method. Addison-Wesley.

Xia, B. & Sun, D-W. 2002. Applications of computational fluid dynamics (CFD) in the food industry: a review. *Computers and electronics in agriculture*, 34, 5-24.

CHAPTER 3

NON-NEWTONIAN LAMINAR FLOW UNDER THE EFFECT OF FORCED VIBRATION

Summary

The effects of a superimposed sinusoidal rotational vibration on the flow of non-Newtonian fluids in a 4 mm diameter tube are studied numerically using a CFD model. The model was validated using experimental data from the literature. Inelastic time-independent fluids of the power law, Bingham plastic, Herschel-Bulkley, and Newtonian types are investigated. Results show that Newtonian flow is unchanged by any superimposed oscillations, but the flow of non-Newtonian fluids is greatly affected. The flow of shear thinning fluids and viscoplastic fluids is enhanced, whilst the flow of shear thickening fluids is retarded. The effects of the various rheological as well as vibration parameters are studied in detail. Flow enhancement is affected by both vibration frequency and amplitude, but different amplitude-frequency combinations which correspond to the same peak acceleration result in the same enhancement. Mechanical vibration in the sonic range of frequency generates substantial flow enhancements in low to moderately viscous fluids, but has limited scope for highly viscous fluids. Mechanical vibration in the ultrasound range, however, has a very good potential for the processing of highly viscous materials, being able to generate orders of magnitude enhancement in flow. The extent of flow enhancement achieved is also dependent on the nature of the superimposed vibration: a rotational oscillation produces more flow enhancement than a transversal oscillation, but less than a longitudinal oscillation. Flow visualisation shows an angular secondary fluid motion that increases near the vibrating wall.

3.1. LITERATURE REVIEW

3.1.1. INTRODUCTION

A wide range of industrial processes involve the flow of rheologically complex fluids that are characterised by diverse and often significant deviations from simple Newtonian behaviour. Indeed, in the process industries Newtonian fluids are nowadays often the exception rather than the rule. Non-Newtonian fluids are encountered in a vast range of industrial applications, including most multi-phase mixtures (e.g. emulsions, suspensions, foams/froths, dispersions), high molecular weight systems and their solutions (e.g. polymers, proteins, gums), foods, pharmaceuticals, personal care products, agricultural chemicals, synthetic propellants, and slurry fuels.

Typical non-Newtonian characteristics include shear thinning, viscoplasticity, viscoelasticity and time dependence; though certain pastes and suspensions can also display a shear thickening behaviour. Shear thinning or pseudoplasticity, however, is by far the most common of all non-Newtonian characteristics wherein the apparent viscosity of a substance decreases with increasing shear rate. Most industrial fluids, however, tend to exhibit a combination of shear thinning and viscoplasticity or viscoelasticity.

Non-Newtonian flows are usually complex requiring much pumping energy to drive the fluid through pipelines and processing equipment, so that various ways of facilitating their flow and processing have been sought over the years. Barnes *et al*. (1971) observed that the time-averaged volumetric flow rate could be increased when a polymer solution is subjected to a pulsating pressure gradient in the axial direction. The observed increase in flow rate seemed to require less energy to maintain than the corresponding steady state flow, thus making the process economically advantageous. Their theoretical investigation, based on an Oldroyd rheological model for the fluid and a perturbation scheme in terms of the amplitude and the superimposed sinusoidal pressure gradient, concluded that: (i) the fluid must be shear thinning in order to

exhibit any flow enhancement; and (ii) the enhancement in flow diminishes with increasing pulsation frequency. Later, Sundstrom and Kaufman (1977), through numerical work using an Ellis rheological model, found that the extra power required in pulsating the flow was always positive and thus there was no economic advantage in pulsating the flow, a conclusion subsequently confirmed by Phan-Thien and Dudek (1982) using a power law rheological model.

The fluidity of non-Newtonian fluids can also be enhanced by subjecting the flow to vibrational motion caused by mechanical shaking. This phenomenon is well known in the building and confectionery industries and has been exploited for many years, but mainly on an empirical basis. For example, during the process of moulding of chocolate bars and shells and the coating of confectionery, the chocolate liquid is vibrated to spread it evenly in the mould, to disengage air bubbles enclosed in the liquid, and to provide a thin and uniform layer of chocolate on the centres, thus ensuring savings and a better product (Barigou *et al.*, 1998). Vibration technologies have also been applied during polymer processing in order to control the flow pattern or the internal structure of the polymer (Wu *et al.*, 2003). Ultrasonic vibration has been shown to lead to a significant reduction in the viscosity of polymer melts and thus an increase in flow rate (Wu *et al.*, 2003; and Piau and Piau, 2002).

Vibrational motion can result in a range of complex effects on the flow of non-Newtonian and even Newtonian fluids. The effects of vibration depend generally on the type of vibration imposed on the flow and the rheological properties of the fluid in motion.

3.1.2. EFFECTS OF VIBRATION ON NEWTONIAN FLUIDS

A number of studies have shown that the flow structure of Newtonian fluids can be influenced by mechanical vibration. Elkholy (1997) carried out a numerical study to investigate the possibility of inducing flow in a stagnant Newtonian fluid in a horizontal pipeline by means of sinusoidal oscillation. The pipe, which was 50 mm in diameter, was subjected to small-amplitude axial oscillations at one end while the

other end of the pipe was held stationary. Oscillation frequencies of 10, 20, and 30 Hz, and amplitudes of $\pi/20$, $\pi/40$ and $\pi/60$ were used. The results showed that a reasonable flow velocity of the stagnant fluid can be induced when the ratio of oscillation frequency to fluid viscosity exceeds a certain value. By calculating the velocity profile over the pipe cross-section, it was shown that fluid movement occurs mainly at the layer adjacent to the wall due to viscous effects. The author concluded that part of the energy expended on vibrating the pipe was absorbed by the fluid as pressure and kinetic energy, thus causing the fluid to flow, while the remaining part was absorbed as strain energy in the pipe wall.

Benhamou *et al*. (2001) carried out a numerical study on the laminar flow of a Newtonian fluid within a horizontal pipe subjected to sinusoidal oscillations around the vertical diameter at the pipe entrance. The governing equations were solved numerically using a control volume method and the advection terms were discretised using an upwind difference scheme. The steady-state solution, which served as the initial condition for the vibrated flow simulation, and the vibrated flow solution were validated using analytical and experimental results from the literature. The numerical results, obtained for a pipe Reynolds number $Re = 1000$, showed the time evolution of a secondary flow that occurred in the transversal direction. This flow was characterised by a pair of counter-rotating vortices, the intensity of which varied with time and axial distance, and which influenced the axial flow. The velocity profile in the axial direction was obtained at different time intervals during the first oscillation cycle and was found to be distorted in comparison to the steady-state velocity profile, with one half of the profile showing increased velocities while the velocities in the other half decreased by the same magnitude, thus resulting in an overall unaltered mean flow velocity.

In a later study, the authors conducted an experimental investigation of the same type of oscillation in a 3.78 cm diameter pipe (Benhamou *et al*. 2004). The study investigated the effects of both flow and oscillation Reynolds numbers on the transition from laminar to turbulent flow using flow visualisation achieved by injecting a fluorescent dye and illuminating the pipe. The maximum angular

displacement of the pipe relative to its position when stationary was 8.4°, a value dictated by space limitations. Under test conditions, the pipe Reynolds number ranged from 210 to 2313 and the oscillation Reynolds number ranged from 242 to 2788. Oscillation was found to induce an earlier transition to turbulence compared to stationary pipe flow. For example, under steady-state conditions, transition to turbulence was observed within the range $2313 < Re < 2498$, while under oscillation, with an oscillation Reynolds number of 1013, transition was observed at $Re \sim 1850$. As the oscillation Reynolds number increased, the flow Reynolds number at which transition occurred decreased until it reached a point beyond which no further reduction was obtained. This early transition to turbulence was attributed to the Coriolis force which induces a transversal flow that causes a strong momentum transfer which, in turn, extracts energy from the main axial flow thus destabilising the flow and causing an early transition to turbulence.

3.1.3. EFFECTS OF VIBRATION ON NON-NEWTONIAN FLUIDS

Several studies have been reported on the effects of vibration on the flow of non-Newtonian fluids. Kasakia and Rivlin (1978 and 1979) carried out a theoretical study to investigate the pressure flow of non-Newtonian viscoelastic fluids between two infinite parallel plates both subjected to simultaneous and synchronous transversal vibration. The authors obtained explicit expressions for the change in flow rate due to the non-Newtonian behaviour of the fluids.

The flow of viscoelastic fluids through vibrated pipes was examined by Mena *et al*. (1979). In their work, a longitudinal oscillation was superimposed on Newtonian and non-Newtonian flows driven by a constant pressure gradient in circular pipes of 26 and 52 mm diameters. Vibration frequencies of 0 to 75 rad s^{-1} and amplitudes of 0.65, 1 and 1.3 cm were used. Non-Newtonian solutions of polyacrylamide in addition to water, glycerol and water-glycerol solutions (Newtonian) were used. An increase in the time-averaged flow rate of the non-Newtonian fluids was obtained, and the effects of oscillation frequency and amplitude on the flow enhancement were investigated. Maximum enhancement was obtained at the maximum frequency and amplitude used.

The authors expected that flow enhancement should reach a value beyond which it would cease to increase, but due to experimental limitations this point was not attained. By means of flow visualisation, achieved using a dye of the same density as the test fluid, the effect of oscillation on the velocity profile was analysed. For a purely viscous glycerol solution, the velocity profile was not affected by oscillation. For viscoelastic fluids, however, the velocity profile was drastically elongated as a result of oscillation. This effect was more pronounced as the oscillation amplitude was increased. By separating the elastic from viscous effects, the authors concluded that the dominating factor in the oscillating flow of viscoelastic liquids in tubes was the shear-dependent viscosity. The elastic effects of the fluids, although of secondary importance, were not negligible.

Isayev *et al*. (1990) carried out an experimental and theoretical investigation into the effects of orthogonal oscillation in the sonic range of frequency on the flow of polymer melts through an annular die. It was observed that the die pressure decreased at a constant flow rate as a result of oscillation. Increasing the oscillation frequency or amplitude led to a continuous reduction in the die pressure as well as an increase in the melt temperature. A model was developed to describe the reduction in die pressure. At high oscillation frequencies, the pressure reduction was attributed to a decrease in viscosity induced by the temperature rise and viscoelastic effects. At low frequencies, however, the pressure reduction was attributed to viscoelastic effects only.

Deshpande and Barigou (2001) studied, experimentally and numerically, the effects of longitudinal oscillation on the time-averaged flow rate of Newtonian and non-Newtonian fluids in laminar flow through pipes of 4 and 6 mm diameters. The non-Newtonian fluids used were of the power law, Herschel-Bulkley and Bingham plastic types. Vibration frequencies up to 40 Hz and amplitudes up to 1.6 mm were used. The CFD numerical model was constructed using the commercial software CFX 4.3. The CFD results agreed very well with experimental evidence. The study concluded that: (i) vibration of Newtonian fluids does not produce any flow enhancement; (ii) shear thinning fluids exhibit flow enhancement under vibration; (iii) shear thickening

fluids exhibit flow retardation; and (iv) flow enhancement is most sensitive to the flow behaviour index or shear thinning/shear thickening index. From conclusions (ii) and (iii) it was also inferred that the superimposed shear at the tube wall affects the fluid apparent viscosity, which, in turn, affects the time-averaged flow rate. The study showed that orders of magnitude enhancements in flow were potentially possible, depending on the fluid rheological properties and vibration frequency and amplitude used. The results also showed that flow enhancement increases with vibration amplitude and frequency, but different combinations of amplitude and frequency corresponding to the same peak acceleration generated identical enhancements.

Piau and Piau (2002) carried out a theoretical study to investigate the effects of longitudinal wall motion on the flow of viscoplastic fluids through circular tubes. In order to validate the theoretical model, experiments were performed using extrusion flows with high-power ultrasound oscillations at a frequency of 20 kHz applied to a circular die using a specially designed ultrasonic apparatus. The study showed that, while vibration had no effect on the flow rate of Newtonian fluids, a strong influence on the flow properties of viscoplastic fluids was obtained resulting in an increase in flow rate. A viscoplastic fluid that exhibits shear-thinning behaviour was found to exhibit large increases in flow rate. The enhancement in this case was considered as a combination of the effects of shear-thinning and yield stress (i.e. yield stress/shear thinning coupling). The experimental results showed significant reductions in pressure drop (50-60%) at a given flow rate and large increases in flow rate (up to ~500%) at a given pressure drop. Thermal effects were present in the experimental study but were not considered in the theoretical study. Flow rate or pressure drop variations between flows at the same temperature with and without vibration were compared in order to separate the roles played by thermal and mechanical effects. It was found that lower pressure drops and higher flow rates could be achieved by applying vibration at a given temperature than by increasing the temperature in the absence of vibration.

The authors also reported a European patent application by the Goodrich Company in 1988 relating to the shear processing of thermoplastics in the presence of ultrasonic

vibration. The vibrations were applied at an angle of less than 45° to the direction of flow resulting in a reduction in the extrusion pressure by 10-23% (Lee and Cranston, 1988).

Along the same lines, Wu *et al.* (2003) showed experimentally that longitudinal oscillations of the ultrasonic type have a great influence on the behaviour of metallocene-catalysed linear low-density polyethylene (mLLDPE) flowing through extrusion dies. They used a frequency of 20 kHz and an ultrasonic power of up to 250 W. Measurements of die pressure were performed at temperatures of 180, 190 and 200°C. The effect of the oscillations was a remarkable reduction in die pressure; this reduction increased linearly with increasing ultrasonic power. Reductions in die pressure of up to ~70% were obtained, depending on the die material and oscillation power. At a constant die pressure it was shown that ultrasonic oscillation reduced the polymer viscosity and hence gave rise to higher flow rates. This reduction in viscosity and increase in flow rate increased with oscillation power. Enhancements in flow rate of up to ~100% were obtained, depending on the die material and oscillation power. It was concluded that such ultrasonic oscillations could greatly increase the productivity of the mLLDPE melt process and could therefore be used to improve the processability of mLLDPE.

Shin *et al.* (2003) experimentally investigated the effect of transversal acoustic vibration on the flow resistance of both Newtonian fluids and human blood in a capillary tube. The vibration was generated using a loud speaker positioned at right angles to the direction of flow. While experimental results showed that transversal vibration had no effect on Newtonian fluids, a reduction in the flow resistance of blood was observed which was attributed to the breakdown of aggregated red blood cells. The extent of reduction was strongly dependent on both the frequency and amplitude of vibration, but more detailed work, numerical as well as experimental, was deemed necessary to explain the effects.

More recently, Piau and Piau (2005) presented a theoretical study in which the effects of ultrasound longitudinal and transversal vibrations on the flow of a Bingham fluid in

plane Couette flow were demonstrated for low vibrational Reynolds numbers. The effects of longitudinal and transversal vibrations were compared. The superimposition of vibration gave rise to significant reductions in the average stress of a Bingham fluid. Average stress reductions of about 100% could be achieved. However, this reduction in stress came at a cost in terms of power dissipation, which was higher for transversal vibration than for longitudinal vibration. For a Newtonian fluid, no such reductions were predicted. It was concluded that (i) vibrations of moderate to high velocity applied to the wall can enhance plane Couette flow rates for viscoplastic materials; and (ii) at moderate amplitudes, longitudinal vibration may be 1.5-2 times more efficient than transversal vibration.

The yield stress/shear thinning coupling effect referred to by Piau and Piau (2002) was further discussed and analyzed by the authors in a later work (Piau and Piau, 2007). The individual and coupled effects of yield stress and shear thinning on stress reduction and flow enhancement induced by longitudinal and transversal ultrasonic vibrations were analyzed in Poiseuille pipe and Couette plane flows. Theoretical results were compared with experimental results obtained for pipe extrusion of viscoplastic Herschel-Bulkley rubber compounds and those obtained in the authors' earlier study (Piau and Piau, 2002) for a Bingham fluid. The study was concerned with the flow regime induced by oscillation at low vibrational Reynolds numbers. Both yield stress and shear thinning gave rise to flow enhancement and pressure drop reduction. Their coupling was found to give rise to an even higher flow enhancement. Experiments confirmed that a Herschel-Bulkley fluid exhibits much higher flow enhancements under longitudinal vibration compared to a Bingham fluid within the same range of Bingham number. Results of the theoretical analysis showed that reducing the flow behaviour index of a Herschel-Bulkley fluid results in substantial increases in flow enhancement. In the case of Poiseuille pipe flow, transversal vibration was found to yield much smaller effects than those produced by longitudinal vibration.

An important conclusion can be drawn from the studies reviewed above which confirms that mechanical vibration has significant effects on the flow of non-

Newtonian fluids. However, such studies have been limited to the longitudinal and transversal modes of vibration and to narrow ranges of vibration amplitude and frequency and fluid rheological behaviours. Therefore, more research is needed in this area to investigate other modes of vibration and provide more comprehensive results for a wider range of vibration conditions and rheological behaviours.

Owing to the difficulty of conducting experiments of vibrational flow using a wide range of frequencies and amplitudes (especially high values) and for a variety of rheologically complex behaviours, CFD offers an easier and more convenient approach for investigating such flows. Although limited, existing experimental data (Deshpande and Barigou, 2001) in this area can be used to validate any CFD model constructed for this purpose.

In this chapter, a CFD model is used to investigate the effects of rotational oscillation on the laminar flow of four types of fluid: Newtonian, power law, Bingham plastic and Herschel-Bulkley fluids, in a 4 mm diameter pipe. All four types of fluid are assumed to be inelastic and time-independent, and the flow is driven by a constant pressure gradient along the pipe. The accuracy of the vibrational flow model is assessed using the experimental results of Deshpande and Barigou (2001) relating to longitudinal vibration of non-Newtonian fluids. The effects of oscillation frequency and amplitude, fluid rheology, and pressure gradient on flow enhancement are studied both in the sonic (0-300 Hz) and ultrasonic (16-28 kHz) ranges of vibration frequency. The ultrasonic frequencies were used for very highly viscous fluids. Pipe oscillation in the transversal direction was also investigated. A brief comparison is then made between the extent of the flow enhancement obtained with rotational, longitudinal and transversal oscillations.

3.2. THEORY

3.2.1. NON-NEWTONIAN FLUIDS

3.2.1.1. Definition and classification

The rheology of a fluid is characterised by its flow curve, which represents the relationship between shear stress and shear rate. The ratio of shear stress to shear rate is the fluid apparent viscosity. A Newtonian fluid is characterised by a linear flow curve which passes through the origin, as shown in Figure 3.1. The viscosity of such a fluid is therefore constant and independent of shear rate. Examples of Newtonian behaviour include water, milk, and sugar solutions (Holdsworth, 1993). A non-Newtonian fluid, on the other hand, is one whose flow curve is non-linear or/and does not pass through the origin. The apparent viscosity of such a fluid depends on the shear rate, which, in turn, is variable in shear flow. More complex non-Newtonian fluids have an apparent viscosity which depends, in addition, on the duration of shearing and the kinematic history of the fluid, and are therefore described as time-dependent. The behaviour of a non-Newtonian fluid can be related to the behaviour of a hypothetical Newtonian fluid using the concept of effective viscosity, which is the viscosity of a hypothetical Newtonian fluid which would give the same flow rate-pressure drop relationship as the non-Newtonian fluid.

Time-independent non-Newtonian fluids can be described by the following relationship:

$$\tau = \mu\dot{\gamma} \tag{3.1}$$

where τ is shear stress, $\dot{\gamma}$ is shear rate, and μ is the apparent viscosity function, thus

$$\mu = \mu(\dot{\gamma}) \tag{3.2}$$

Different forms of the function in Equation (3.2) yield different types of non-Newtonian fluids:

1. Shear thinning
2. Shear thickening
3. Viscoplastic (Bingham plastic and Herschel-Bulkley fluids)

Qualitative flow curves for these types of fluid rheological behaviour, along with a Newtonian flow curve, are depicted in Figure 3.1.

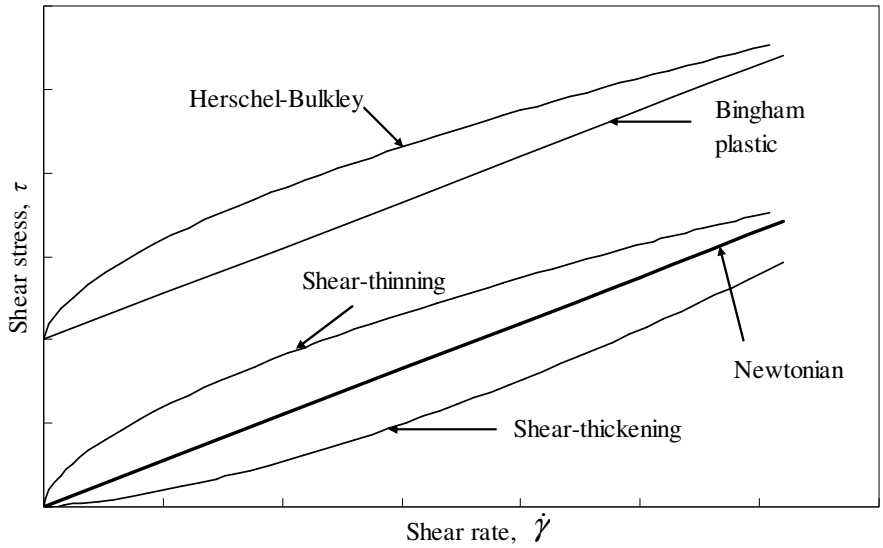

Figure 3.1: Flow curves for Newtonian and non-Newtonian fluids.

3.2.1.2. Shear thinning fluids

Shear thinning fluids, also known as pseudoplastic fluids, are characterised by an apparent viscosity which decreases with increasing shear rate. This behaviour is typical of polymer melts and solutions (e.g. aqueous polyacrylamide solutions), protein concentrates, and cream (Chhabra and Richardson, 1999; Holdsworth, 1993). Most shear thinning fluids, however, exhibit a Newtonian behaviour at very low and very high shear rates, resulting in two limiting values of the apparent viscosity, a zero shear viscosity, μ_0, and an infinite shear viscosity, μ_∞, respectively. Figure 3.2 shows a qualitative logarithmic plot of apparent viscosity as a function of shear rate for a shear thinning fluid based on the Carreau model described below. Both at very low and very high shear rates the apparent viscosity is constant, thus, indicating

Newtonian behaviour in this region, with a non-Newtonian regime in between where viscosity decreases with increasing shear rate. The rate of this decrease and the shear rate values marking the upper and lower limits of this non-Newtonian regime vary from one material to another.

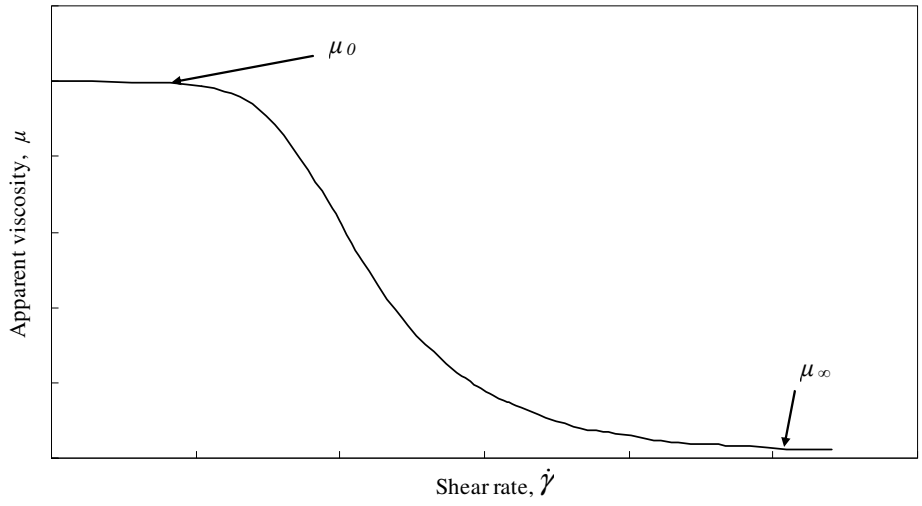

Figure 3.2: The relationship between apparent viscosity and shear rate for a shear thinning fluid of the Carreau model.

Shear thinning behaviour can be represented using different mathematical models, as described below.

(i) Power-law or Ostwald de Waele model

This model describes the relationship between shear stress and shear rate using a power-law expression of the form

$$\tau = k\dot{\gamma}^n \tag{3.3}$$

where the constants k and n are known as the flow consistency index and flow behaviour index, respectively. These two parameters are determined empirically by curve-fitting. The practical range of values the flow behaviour index, n, may take is (0-1) for shear thinning fluids. The smaller the value of n, the greater the degree of

shear thinning and, thus, the more pronounced the non-Newtonian behaviour of the fluid. For $n = 1$, the fluid reduces to a Newtonian one with a constant viscosity equal to k.

The apparent viscosity expression of a shear thinning fluid can be derived from Equations (3.1) and (3.3), to give

$$\mu = k\dot{\gamma}^{n-1} \tag{3.4}$$

One of the shortcomings of this model is that it can only be used to describe the shear thinning regime of the flow curve, and therefore does not predict the zero and infinite shear viscosities at low and high shear rates, respectively. Furthermore, the empirically determined values of k and n depend on the range of shear rate considered (Chhabra and Richardson, 1999). Nevertheless, the power law model offers the simplest representation of shear thinning fluids, and due to its simplicity it is perhaps the most widely used model.

(ii) Carreau model

When the fluid experiences very low and very high shear rates, deviations from the power law model can be significant. The model proposed by Carreau (1972) takes account of the limiting values of viscosity at such extremes of shear rate, and is given by:

$$\frac{\mu - \mu_\infty}{\mu_0 - \mu_\infty} = \left[1 + (\lambda\dot{\gamma})^2\right]^{(n-1)/2} \tag{3.5}$$

where λ is a curve-fitting parameter, given in time units.

(iii) Ellis model

This model takes account of the zero shear viscosity only and is therefore appropriate when the deviations from the power law model are significant only at low shear rates.

Unlike the power law and Carreau models, the Ellis model expresses apparent viscosity in terms of shear stress rather than shear rate, thus

$$\mu = \frac{\mu_0}{1+\left(\frac{\tau}{\tau_{1/2}}\right)^{\alpha-1}} \tag{3.6}$$

where $\tau_{1/2}$ is the shear stress at which the apparent viscosity has dropped to $\mu_0/2$, and α is a measure of the extent of shear thinning.

Details of other shear thinning models can be found in the literature (see, for example, Holdsworth, 1993).

3.2.1.3. Shear thickening fluids

In contrast with shear thinning fluids, shear thickening fluids, also known as dilatant fluids, have an apparent viscosity which increases with increasing shear rate. This type of fluid is most widely observed in concentrated solid-liquid suspensions, such as china clay and corn flour in water (Chhabra and Richardson, 1999). However, shear thickening fluids are much less widespread in the chemical and processing industries than shear thinning fluids. The mathematical representation of the shear thickening behaviour is described by the power law equations (Equations (3.3) and (3.4)) with $n > 1$.

3.2.1.4. Viscoplastic fluids

Viscoplastic fluids are those which do not flow or deform until the shear stress exceeds a certain value, known as the yield stress, τ_0. Hence, the flow curve for such materials does not pass through the origin (Figure 3.1). When the shear stress is below the yield stress value of the material, the material will deform elastically, i.e. like a rigid body. Once the applied shear stress has exceeded the yield stress, the material begins to flow. This rheological behaviour can be explained by postulating that, when at rest, the viscoplastic material has a rigid three dimensional structure

which resists external stresses below τ_0, but which breaks down when the stress exceeds τ_0 (Chhabra and Richardson, 1999; Holdsworth, 1993).

At very low shear rates, the apparent viscosity is effectively infinite before the viscoplastic material yields and begins to flow. This is somewhat similar to the behaviour of shear thinning fluids whose viscosity decreases with increasing shear. It is therefore possible to regard viscoplastic materials as possessing some kind of shear thinning instead of a true yield stress. Nonetheless, the concept of a yield stress has proved to be a convenient approximation of the flow behaviour of some materials.

At shear stress values greater than the yield stress, the flow curve may be linear or non-linear. The Bingham plastic and Herschel-Bulkley models are two popular models used to describe such flow behaviours.

(i) Bingham plastic model

This model is used to describe the behaviour of viscoplastic materials whose flow curve is linear (see Figure 3.1), and is given by

$$\begin{aligned} &\tau = \tau_0 + \mu_B \dot{\gamma} \ , \quad \text{for} \quad \tau > \tau_o \\ &\dot{\gamma} = 0 \ , \qquad\quad \text{for} \quad \tau \le \tau_o \end{aligned} \tag{3.7}$$

where μ_B is the so-called plastic viscosity. The apparent viscosity of a Bingham plastic fluid is then given by

$$\begin{aligned} &\mu = \mu_B + \frac{\tau_o}{\dot{\gamma}}, \quad \text{for} \quad \tau \ge \tau_o \\ &\mu \to \infty \ , \qquad\quad \text{for} \quad \tau \le \tau_o \end{aligned} \tag{3.8}$$

(ii) Herschel-Bulkley model

This model describes viscoplastic fluids with a non-linear flow curve (Figure 3.1). The non-linearity is represented by a power law term, thus

$$\begin{aligned} &\tau = \tau_0 + k\dot{\gamma}^n \text{ , for } \quad \tau > \tau_o \\ &\dot{\gamma} = 0 \text{ , } \qquad \text{for } \quad \tau \le \tau_o \end{aligned} \tag{3.9}$$

The apparent viscosity is given by

$$\begin{aligned} &\mu = k\dot{\gamma}^{n-1} + \frac{\tau_o}{\dot{\gamma}}, \text{ for } \quad \tau \ge \tau_o; \text{ and} \\ &\mu \to \infty \text{ , } \qquad \text{for } \quad \tau \le \tau_o \end{aligned} \tag{3.10}$$

3.2.1.5. Flow rate and velocity profile for non-Newtonian fluids

For a non-Newtonian fluid flowing in a pipe in laminar flow, the flow rate and velocity profile can both be obtained theoretically.

The steady volumetric flow rate, Q, of a Herschel-Bulkley fluid in laminar flow driven by a constant pressure gradient, $\Delta p/L$, can be calculated from the following exact expression (Borghesani, 1988):

$$Q = \frac{\pi R^3 n}{{\tau_w}^3}\left(\frac{\tau_w - \tau_0}{k}\right)^{1/n}(\tau_w - \tau_0)\left[\frac{(\tau_w - \tau_0)^2}{3n+1} + \frac{2\tau_0(\tau_w - \tau_0)}{2n+1} + \frac{\tau_0^2}{n+1}\right] \tag{3.11}$$

where R is the pipe radius, and τ_w is the wall shear stress, given by

$$\tau_w = \frac{R\Delta p}{2L} \tag{3.12}$$

For flow driven purely by gravity, the pressure gradient $\Delta p/L$ is equal to gL, where g is gravitational acceleration.

For a power law fluid with $\tau_0 = 0$, Equation (3.11) reduces to the following expression

$$Q = \frac{\pi R^3 n}{(3n+1)}\left(\frac{R}{2k}\frac{\Delta p}{L}\right)^{\frac{1}{n}} \tag{3.13}$$

It reduces to the Buckingham-Reiner equation for a Bingham plastic fluid with $k = \mu_B$ and $n = 1$, thus:

$$Q = \frac{\pi R^3}{\tau_w{}^3}\left(\frac{\tau_w - \tau_0}{\mu_B}\right)^{1/n}(\tau_w - \tau_0)\left[\frac{(\tau_w - \tau_0)^2}{4} + \frac{2\tau_0(\tau_w - \tau_0)}{3} + \frac{\tau_0^2}{2}\right] \tag{3.14}$$

And it reduces to the Poiseuille equation for a Newtonian fluid with $\tau_o = 0$, $k = \mu$, and $n = 1$, thus:

$$Q = \frac{\pi R^4}{8\mu}\frac{\Delta p}{L} \tag{3.15}$$

It can be shown that the velocity distribution of a power law fluid is given as a function of radial position, r, by the expression (Chhabra and Richardson, 1999)

$$u(r) = \left(\frac{\Delta p}{2kL}\right)^{1/n}\left(\frac{n}{n+1}\right)\left[R^{(n+1)/n} - r^{(n+1)/n}\right] \tag{3.16}$$

For a Bingham plastic fluid, the velocity profile outside the plug region is given by

$$u(r) = \left(\frac{\Delta p}{L}\right)\frac{\left(R^2 - r^2\right)}{4\mu_B} - \frac{\tau_0}{\mu_B}(R - r)\ , \qquad \text{for } r \geq R_p \tag{3.17}$$

where R_p is the radius of the plug region and can be calculated from

$$R_p = \frac{2L\tau_0}{\Delta p} \tag{3.18}$$

The velocity of the plug region is given by

$$u(r)=\left(\frac{\Delta p}{L}\right)\frac{R^2}{4\mu_B}\left(1-\frac{R_p}{R}\right)^2 \tag{3.19}$$

And for a Herschel-Bulkley fluid, the velocity profile is given by

$$u(r)=\frac{nR}{n+1}\left(\frac{\tau_w}{k}\right)^{1/n}\left[(1-\phi)^{(n+1)/n}-\left(\frac{r}{R}-\phi\right)^{(n+1)/n}\right] \tag{3.20}$$

where ϕ is the ratio of yield stress to wall shear stress, i.e. τ_0/τ_w.

The Reynolds number of a Newtonian fluid is given in terms of the effective viscosity of the fluid, μ_{eff}, thus

$$\mathrm{Re}=\frac{\rho\bar{u}D}{\mu_{eff}} \tag{3.21}$$

where $\bar{u}$ is the mean flow velocity, and D is the pipe diameter. For a non-Newtonian fluid, the effective viscosity is given by (Chhabra and Richardson, 1999)

$$\mu_{eff}=m'\left(\frac{8\bar{u}}{D}\right)^{n'-1} \tag{3.22}$$

For a power law fluid,

$$m'=k\left(\frac{3n+1}{4n}\right)^n \qquad \text{and} \quad n'=n \tag{3.23}$$

For a Bingham plastic fluid,

$$n' = \frac{1 - \frac{4}{3}\phi + \frac{\phi^4}{3}}{1 - \phi^4} \tag{3.24}$$

and

$$m' = \tau_w \left[\frac{\mu_B}{\tau_w \left(1 - \frac{4}{3}\phi + \frac{\phi^4}{3} \right)} \right]^{n'} \tag{3.25}$$

3.2.2. FORMULATION OF CFD MODEL

The aim of the numerical model implemented in this study is to simulate the flow of laminar non-Newtonian fluids in a straight pipe subjected to sinusoidal oscillations of sonic and ultrasonic frequencies. The flow geometry consists of a straight pipe 4 mm in diameter and 6 mm in length, as shown in Figure 3.3. Rotational and transversal vibrations are separately imposed on the pipe wall and the effects on flow rate and velocity profile are predicted. For the purpose of validating the model using available experimental data pertaining to longitudinal vibration (Deshpande and Barigou, 2001), longitudinal vibration was also modelled. The three modes of vibration used are shown in Figure 3.3.

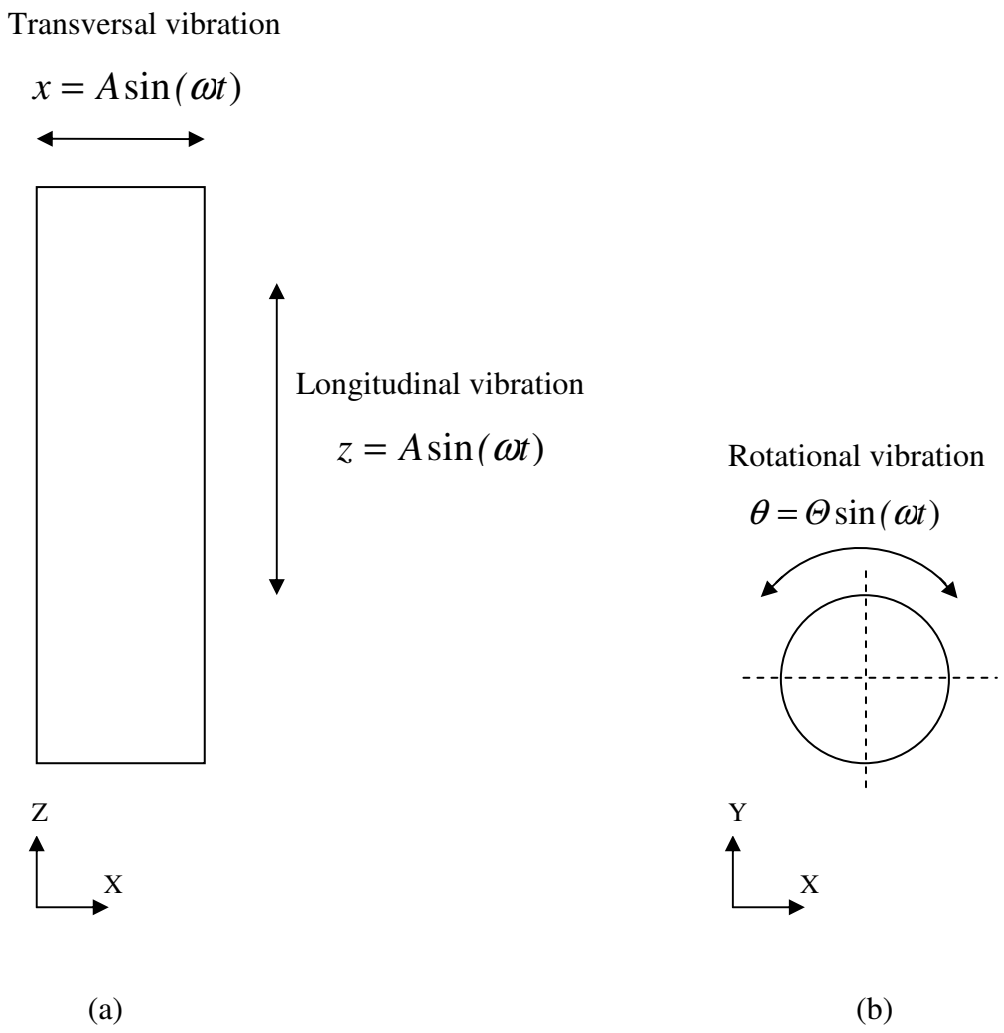

Figure 3.3: Geometry of vibrated pipe: (a) general view; (b) pipe cross-section.

The model considered assumes that flow through the pipe is laminar, incompressible, isothermal and fully developed. The fact that the flow was laminar was confirmed by the pipe Reynolds number, $Re < 100$, for all cases of steady and vibrated flows in the sonic range of frequency; and $Re < 400$ in the ultrasonic range. In vibrational flow, the following vibrational Reynolds number is defined:

$$\mathrm{Re}_v = \frac{A\omega D}{\upsilon} \tag{3.26}$$

where A is the linear amplitude of vibration, ω is the angular frequency, and υ is the fluid kinematic viscosity. Values of Re_v were also in the laminar regime (< 30) for all the cases investigated.

3.2.2.1. Hydrodynamic entrance length

For a fluid entering a pipe, for example from a reservoir, the initial velocity profile at the pipe inlet will be flat and will then progressively change until fully developed flow is established. The distance required for the centreline velocity to reach 98% of its value for fully developed flow is called the hydrodynamic entrance length L_h. The pressure gradient in the entrance region, which is defined by the entrance length, is different from that for a fully developed flow. Therefore, the pipe length L is usually selected to be much greater than the hydrodynamic entrance length L_h. For a Newtonian fluid, the entrance length can be estimated from the following equation (Shook and Roco, 1991):

$$\frac{L_h}{D} = 0.062\,\mathrm{Re} \tag{3.27}$$

For a shear-thinning non-Newtonian fluid, the fully developed velocity distribution is flatter than for a Newtonian fluid. The constant in Equation (3.27) decreases for more shear thinning fluids (Rohsenow *et al*., 1998). The entrance length for a shear thinning fluid is therefore lower than that estimated using Equation (3.27). Correlations for estimating the entrance length for different fluid rheological models can be found in Steffe (1992).

Since the entrance length is proportional to the flow Reynolds number, a substantial pipe length may be required as the Reynolds number increases. As a result, the pipe length must be chosen so as to satisfy the entrance length condition for the case with the highest Reynolds number. A large pipe length, however, would make the CFD simulations computationally expensive.

The use of a pressure boundary condition at the pipe inlet allows the CFD software to calculate the fully developed velocity profile based on the static pressure value prescribed at the pipe inlet, thus allowing the use of a small pipe length to keep the computational cost low. Hence, even at the highest Reynolds numbers, the flow was fully developed throughout the pipe, and the pipe length of 6 mm was sufficient for the purpose of this study.

3.2.2.2. Governing equations

The equations governing the flow are the continuity equation, which can be written in the form

$$\nabla u = 0 \tag{3.28}$$

where u is the fluid velocity; and the momentum equation (Deshpande and Barigou, 2001)

$$\rho \frac{Du}{Dt} = -\nabla p - [\nabla \tau] + \rho g \tag{3.29}$$

where ρ is fluid density and t is time. This can also be rewritten as

$$\rho \frac{Du}{Dt} = -\nabla p + [\nabla \mu \dot{\gamma}] + \rho g \tag{3.30}$$

The term on the left hand side of the equation represents the mass per unit volume multiplied by acceleration; the first term on the right hand side is the pressure force per unit volume, the second is the viscous force per unit volume, and the third is the gravitational force per unit volume.

In addition to the Newtonian rheology wherein the fluid viscosity is constant, non-Newtonian fluids of the power law, Bingham plastic and Herschel-Bulkley models

were considered in this study, with the apparent viscosity function as given by Equations (3.4), (3.8) and (3.10), respectively.

3.2.2.3. Forced vibration

The sinusoidal vibrational movement of the pipe wall is modelled using a velocity function as the boundary condition at the wall. This vibrational movement can be described mathematically as follows:

(i) Rotational vibration

For a pipe rotating sinusoidally around its axis (Figure 3.3), the angle of rotation, θ, is given by the function

$$\theta = \Theta \sin(\omega t) \tag{3.31}$$

with the angular frequency

$$\omega = 2\pi f \tag{3.32}$$

where Θ is the vibration angular amplitude and f is the vibration frequency. The angular velocity, v_θ, can then be obtained by differentiating Equation (3.31) with respect to time, thus

$$v_\theta = \frac{d\theta}{dt} = \Theta\omega\cos(\omega t) \tag{3.33}$$

(ii) Transversal vibration

For vibration in a direction perpendicular to the direction of flow (Figure 3.3), the linear sinusoidal displacement of the pipe wall along the X axis is given by

$$x = A\sin(\omega t) \tag{3.34}$$

The linear velocity, v_x, of the wall is then given by

$$v_x = \frac{dx}{dt} = A\omega\cos(\omega t) \tag{3.35}$$

(iii) Longitudinal vibration

The sinusoidal displacement of the pipe wall due to vibration in the longitudinal direction Z, i.e. along the pipe axis as shown in Figure 3.3, is given by

$$z = A\sin(\omega t) \tag{3.36}$$

The vibrational velocity of the pipe wall in the flow direction, v_z, is thus obtained

$$v_z = \frac{dz}{dt} = A\omega\cos(\omega t) \tag{3.37}$$

The effect of vibration on flow rate at constant pressure drop can be expressed as an enhancement ratio, defined as

$$E = \frac{Q_v}{Q} \tag{3.38}$$

where Q_v is the time-averaged volumetric flow rate in the unsteady (vibrated) state, and is calculated from the solution of the governing equations obtained by the CFD code. The steady state flow rate, Q, is calculated for the fluids considered here from the relevant expression amongst Equations (3.11), (3.13), (3.14) and (3.15).

The effect of vibration can also be expressed as a reduction in pressure drop at constant flow rate. The percentage reduction in pressure drop is calculated as $\frac{\Delta p - \Delta p_v}{\Delta p} \times 100$ where Δp is the steady state pressure drop, and Δp_v is the pressure drop for flow under vibration that would be required to maintain the flow rate at its steady state value.

3.3. CFD SIMULATIONS

3.3.1. SCOPE OF SIMULATIONS

Numerical simulations were conducted of the steady and vibrational flows of Newtonian, Bingham plastic, power-law, and Herschel-Bulkley fluids. Simulations of rotational vibration were performed in the sonic and ultrasound ranges of frequency. The range of parameter values considered are summarised in Table 3.1. In the sonic range of frequency, the rheological parameters were chosen partly to coincide with those used in the work of Deshpande and Barigou (2001) pertaining to longitudinal vibration, for the purpose of comparing the effects of longitudinal and rotational vibrations. Vibration frequency and amplitude were varied over a wide range of values in order to show any limiting behaviour. For the less extensive study in the ultrasonic range of frequency, smaller ranges of parameters were used to generally demonstrate the potential for enhancing the flow of very highly viscous fluids using ultrasonic frequencies of vibration, while the values of density and rheological parameters were those of rubber compounds used by Piau and Piau (2002).

Three-dimensional simulations were set up and executed using the commercial software CFX 5.7 and ICEM CFD 4.CFX both developed by ANSYS, Inc. The software ICEM CFD 4.CFX was used to build the domain geometry and create the mesh, while flow specification, solving and post-processing were all performed using CFX 5.7, with its three specialised components: CFX-Pre, CFX-Solve, and CFX-Post.

3.3.2. GEOMETRY

The geometry of the flow domain was created in Cartesian (X, Y, Z) coordinates, with the pipe axial centreline along the Z axis. The geometry consisted of a straight pipe 4 mm in diameter and 6 mm in length with three surface boundaries: inlet (for inflow), outlet (for outflow), and wall. This pipe length was sufficient to ensure a fully developed flow throughout the whole domain under the boundary conditions used in the study, even at the highest Reynolds numbers used, as discussed earlier (Section

3.2.2). Computational tests indeed confirmed that much longer pipes did not affect the results although they made computational time much longer.

Table 3.1: Range of vibration parameters and fluid rheological properties used in rotational flow simulations.

Parameter	Rotational vibration		Transversal vibration
	Sonic range	Ultrasonic range	
Vibration frequency, f (Hz)	0-300	$(16\text{-}28) \times 10^3$	0-160
Angular amplitude, Θ (rad)	0-π/4	0- π/45	-
Linear amplitude*, A (mm)	0-1.57	0-0.14	0-5
Flow behaviour index, n (-)	0.57-1.40	0.33	0.57-1.40
Yield stress, τ_0 (Pa)	0-6	$(180\text{-}220) \times 10^3$	0-6
Consistency index, k (Pa s^n)	0.5-15	1×10^4	0.3-5.0
Density, ρ (kg m^{-3})	1000	1350	1000
Pressure gradient, $\Delta p/L$ (kPa m^{-1})	3-100	267×10^3	3-100

*The linear amplitude in rotational vibration is equal to $R\Theta$.

Although a pipe where the hydrostatic pressure gradient was the only driving force, i.e. equivalent to a vertical tube with purely gravity driven flow, was used in most of the simulations, the influence of an external pressure gradient was also studied and the results are therefore independent of the orientation of the pipe.

3.3.3. MESH

The geometry was meshed with tetrahedral cells of defined global size, as shown in Figure 3.4. To optimise the mesh size it was necessary to carry out a mesh-independence study; this was done by performing a number of simulations with different mesh sizes, starting from a coarse mesh and refining it until results were no more dependent on the mesh size. In this way, the global mesh size was determined giving a maximum cell size of approximately 170 μm in the core region of the tube. To account for the high variable gradients which usually exist near the pipe wall due to the no-slip condition of the wall, inflation layers were created near the wall (Figure 3.4). This results in a more accurate prediction of the flow variables in this region. Twenty inflation layers covering around 30% of the tube radius were thus created.

3.3.4. FLOW SPECIFICATION

The problem of flow through a vibrated pipe was solved in two steps: steady state flow simulation and vibrated flow simulation.

3.3.4.1. Steady state flow simulation

The mesh generated in ICEM CFD 4.CFX was imported into CFX-Pre for pre-processing. The rheological models describing the non-Newtonian fluids simulated in the current work are not available in CFX. New fluids were therefore created and their properties defined. Viscosity was defined as a function of shear rate using the relevant equation from amongst Equations (3.4), (3.8), and (3.10), for power-law, Bingham plastic, and Herschel-Bulkley fluids, respectively. Since the flow considered is isothermal and laminar, no turbulence or heat transfer models were applied.

The flow was simulated under a constant pressure drop so as to allow the simulation to predict any changes in the flow rate due to vibration. Pressure-specified boundaries at the pipe inlet and outlet were used. The use of a pressure boundary condition at the inlet also allowed the CFD software to impose the fully developed velocity profile at the inlet, thus ensuring a fully developed flow throughout the pipe and avoiding the

need for a long pipe. At the inlet, a static pressure equal to the total pressure drop along the pipe was specified; the boundary condition at the outlet was then a zero static pressure. These pressure values were relative to the reference pressure, which was set at 100 kPa. For gravity driven flow, the pressure drop along the pipe was chosen such that $\Delta p/L = \rho g$, which gave a relative pressure at the inlet of 58.86 Pa.

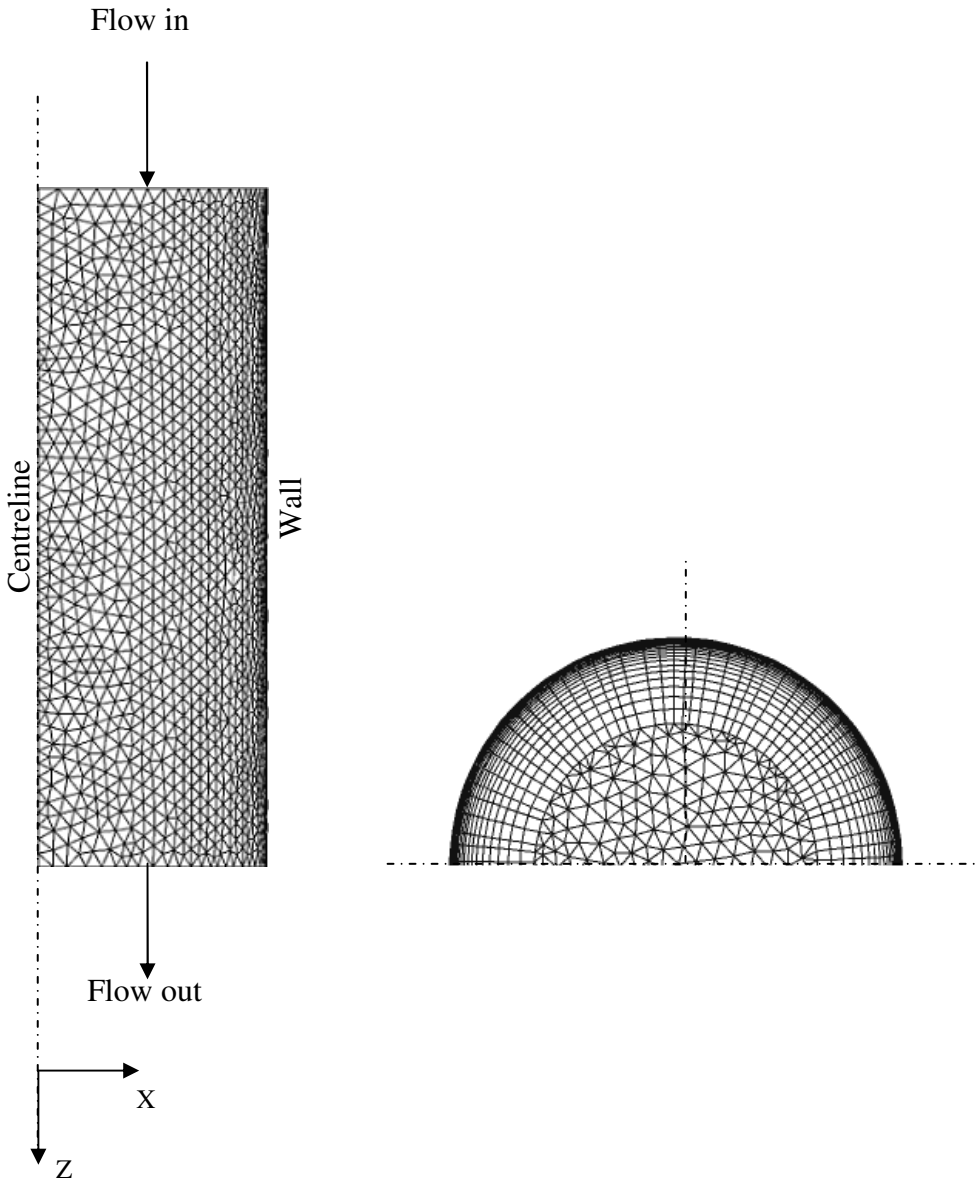

Figure 3.4: Meshed geometry of vibrated pipe

A no-slip wall boundary condition was applied at the pipe wall. This allows the fluid layer adjacent to the wall to have a velocity equal to that of the wall. For steady state flow, this velocity is equal to zero, thus

$$u = 0 \quad at \quad r = R \tag{3.39}$$

The CFX code is based on the finite-volume method of discretisation. The advection scheme used to discretise the convection terms in the momentum equations was the Numerical Advection Correction Scheme (see Chapter 2, Section 2.9.3) with β = 1 (Equation (2.18)), which is second order accurate.

The solution was assumed to have converged when the root mean square (RMS) of the normalised residual error reached 10^{-5} for all of the equations. To reach this level of convergence, around 200 iteration loops were typically required.

3.3.4.2. Vibrational flow simulation

In the second step of solving the problem, the converged steady-state solution was used as an initial solution for the simulation of the vibrational flow. The same pressure boundary conditions used in the steady-state flow simulation were used in the vibrational flow simulation at the inlet and outlet.

For rotational vibration, sinusoidal rotation was imposed on the flow by using a rotating wall with an angular velocity function given by Equation (3.33) and the pipe centreline as the axis of rotation (Figure 3.3). For transversal vibration, where the direction of vibration is perpendicular to the direction of flow, a moving wall was used with a linear vibration velocity as given by Equation (3.35). For the longitudinal vibration cases simulated here for the purpose of validation, Equation (3.37) was used to describe the wall velocity imposed in the direction of flow.

Since the flow is unsteady, the simulation was run in the transient mode. The problem was solved over a maximum of 10 oscillation periods corresponding to a total

simulation time $t_f = \frac{40\pi}{2\omega}$, divided into a number of equal time steps. Solving over more than 10 periods did not affect the results but increased the simulation runtime in proportion. The number of time steps was a critical issue, and its optimisation required a considerable amount of computational experimentation. Also, for the solution to converge at each time step, the number of iterations per time step had to be sufficient. Whilst a large number of time steps gives better accuracy and requires a smaller number of iterations per time step to achieve convergence, it does, however, prolong the simulation considerably. The optimum number of time steps which gave an acceptable level of accuracy whilst keeping simulation time reasonable was 240, with 8-20 iterations required to achieve convergence per time step depending mainly on the fluid rheological properties, in particular a fluid with a yield stress term usually required more iterations. Convergence was assumed when the root mean square (RMS) of mass and momentum residuals reached 10^{-4} at each time step. Such a level of convergence is high, and typically required a total of ~2000 iterations.

The High Resolution Advection Scheme was used to discretise the convection terms in most of the simulations. In this scheme, the blend factor, β, is not constant but is calculated locally to be as close to 1 as possible, i.e. as close to second order accurate as possible (see Chapter 2, Section 2.9.3). In cases involving a yield stress term, for example, where convergence to target could not be attained under the High Resolution Advection Scheme, the Upwind Differencing Scheme was used and convergence was then achieved. This scheme is first-order accurate, β being equal to 0, but it is very robust and does not result in non-physical values. Therefore, solutions under this scheme are easy to obtain as they converge readily (Shaw, 1992).

The Second Order Backward Euler Scheme was used as the transient scheme because it can accelerate convergence within the time step; it initialises the solution within each time step by extrapolating the solutions from the previous two time steps to the new time step (see Chapter 2, Section 2.9.1 for details).

3.3.4.3. Particle tracking simulation

To compute the trajectories of fluid particles flowing in the pipe under the influence of rotational vibration, the particle tracking model within CFX 5.7 was used. A simulation was set up with two fluid phases, the primary fluid under investigation and a secondary fluid created for the purpose of tracking the flow of the primary fluid. The properties of the secondary fluid were identical to those of the primary fluid so that the former exactly mimics the flow of the latter. A small number of particles were sufficient to obtain the trajectories of fluid particles at various positions, and, consequently, a very small volumetric concentration of the secondary fluid was used in order to minimise the computational cost of the simulations. The same boundary conditions, advection and transient schemes, and convergence controls as used in the single-phase vibrational flow simulation were applied here. Since the secondary fluid had identical properties to the primary fluid and was introduced in a very small concentration, the addition of this phase did not affect the convergence behaviour of the simulation.

3.4. VALIDATION OF CFD MODEL

3.4.1. VALIDATION OF STEADY STATE FLOW SIMULATIONS

The accuracy of the steady state solution is particularly important since this solution constitutes the initial condition for the unsteady (vibrated) flow simulation. Validation of the steady state solution was carried out by comparing CFD predictions of the velocity field and the total volumetric flow rate through the pipe with the exact analytical solutions obtained by theory. As will be shown below, CFD is generally capable of yielding very accurate predictions of the steady laminar flow of Newtonian and non-Newtonian fluids in pipes.

3.4.1.1. Flow rate

The steady state flow rate computed by CFD was compared with the exact value given by the relevant relationship amongst Equations (3.11), (3.13) (3.14) and (3.15), and the results are shown in Table 3.2. The percentage error shown in the table is calculated as $\frac{Q_{(CFD)} - Q_{(Theory)}}{Q_{(Theory)}} \times 100$.

The agreement between CFD predictions and the exact solution was very good, with the percentage error being generally within 1% of the exact value for all of the fluids investigated except for the Herschel-Bulkley fluids where the error was slightly higher but still small at around 2-3%. The larger error in this case is probably due to the first order accurate scheme used as the advection scheme. A higher-order accurate scheme was not used in this case because under such a scheme full convergence to target could not be achieved owing to the complex rheology of Herschel-Bulkley fluids involving both yield stress and shear thinning.

Table 3.2: Comparison between CFD and theoretical predictions of flow rate for a range of fluids.

Fluid model	N (-)	k (Pa s^n)	τ_0 (Pa)	$Q \times 10^8$ (CFD) ($m^3\ s^{-1}$)	$Q \times 10^8$ (Theory) ($m^3\ s^{-1}$)	Error (%)
Newtonian	1.00	1.40	0.0	4.39	4.40	-0.48
	1.00	1.00	0.0	6.13	6.16	-0.32
	1.00	0.50	0.0	12.30	12.30	0.00
Power-law	0.57	1.47	0.0	14.75	14.82	-0.47
	0.65	1.47	0.0	10.20	10.30	-0.97
	0.75	1.47	0.0	7.26	7.28	-0.27
	0.85	1.47	0.0	5.59	5.61	-0.36
	0.95	1.47	0.0	4.55	4.57	-0.44
Bingham plastic	1.00	1.00	1.0	5.29	5.32	-0.64
	1.00	1.00	3.0	3.36	3.67	-1.01
	1.00	1.00	5.0	2.16	2.11	+2.17
Herschel-Bulkley	0.57	1.47	1.0	11.30	11.60	-2.31
	0.57	1.47	3.0	6.20	6.38	-2.78
	0.57	1.47	5.0	2.66	2.74	-2.90

3.4.1.2. Velocity profile

The velocity profile obtained by CFD was compared with the theoretical velocity profile for three fluids of each of the Newtonian (Equation (3.16) with n = 1 and $k = \mu$), power-law (Equation (3.16)), Bingham plastic (Equations (3.17) and (3.19)), and Herschel-Bulkley (Equation (3.20)) models, as shown in Figures 3.5, 3.6, 3.7 and 3.8, respectively. The predicted velocity field did not show any axial variation and accurately matched the fully developed theoretical profile. The CFD prediction of velocity profile was particularly accurate for the shear-thinning power-law fluids. For the more complex fluids of the Herschel-Bulkley model, CFD seems to underestimate the velocity of the plug region slightly, thus resulting in a slight underestimation of the flow rate as discussed above, but the agreement is nonetheless very good.

Furthermore, the radial velocity, u_r, was practically zero (i.e. $u_r < 10^{-7}$ m s^{-1}) confirming the unidimensionality of flow.

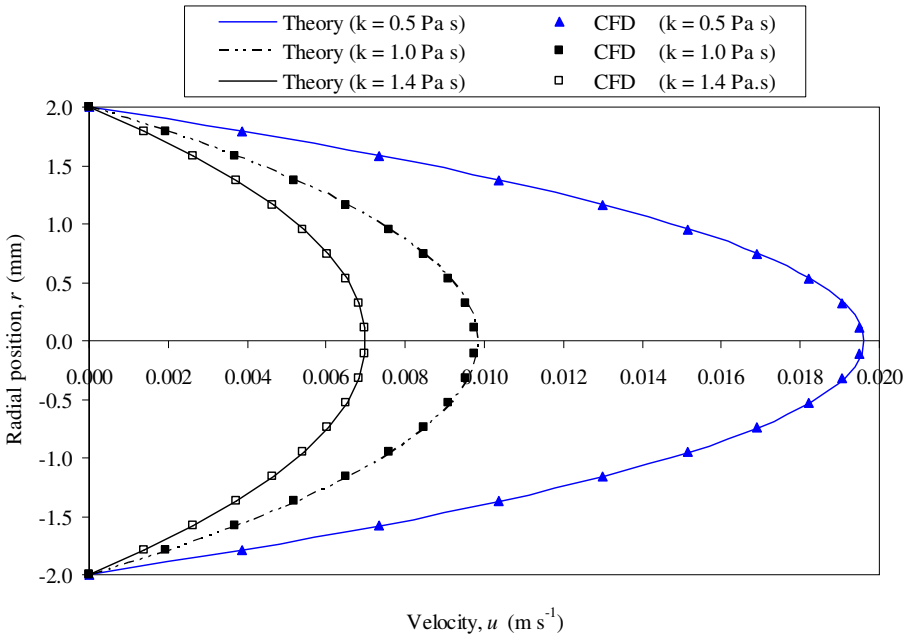

Figure 3.5: Comparison of CFD-predicted and theoretical velocity profiles for three Newtonian fluids: ρ = 1000 kg m^{-3}; $\Delta p/L$ = 9.81 kPa m^{-1}.

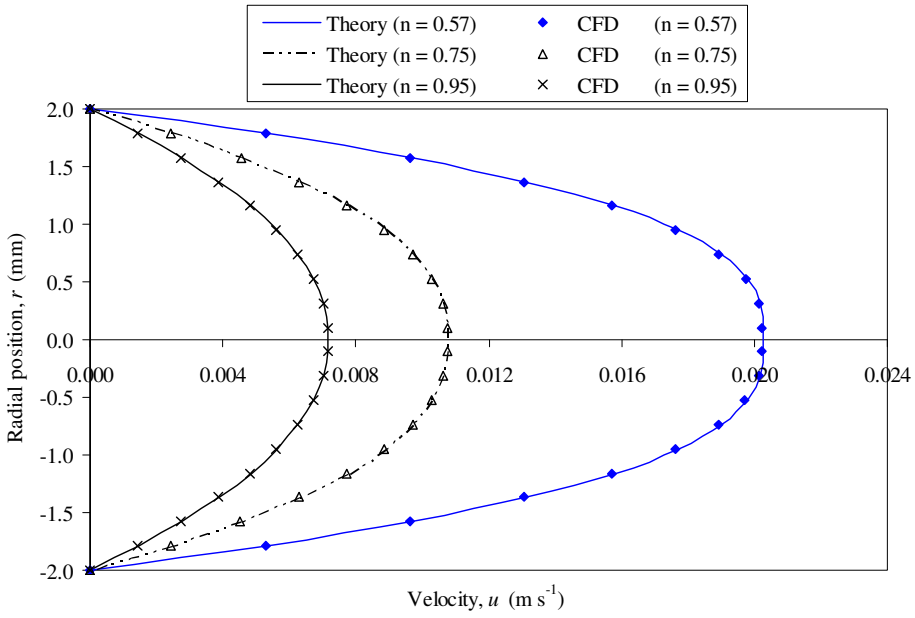

Figure 3.6: Comparison of CFD-predicted and theoretical velocity profiles for three shear-thinning power-law fluids with n = 0.57, n = 0.75, and n = 0.95: k = 1.47 Pa s^n; ρ = 1000 kg m^{-3}; $\Delta p/L$ = 9.81 kPa m^{-1}.

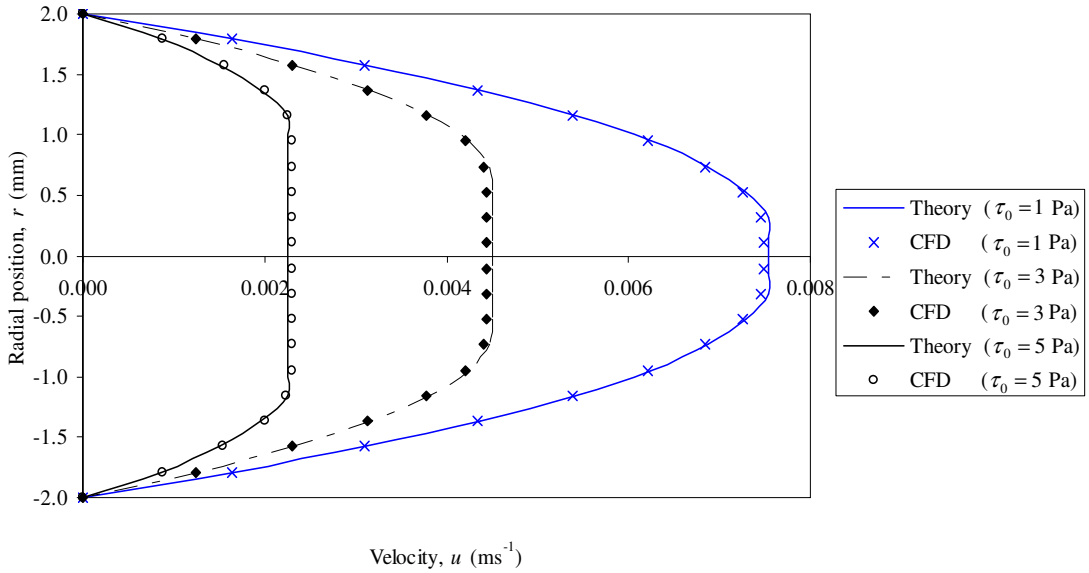

Figure 3.7: Comparison of CFD-predicted and theoretical velocity profiles for three Bingham plastic fluids with $\tau_0 = 1$ Pa, $\tau_0 = 3$ Pa, and $\tau_0 = 5$ Pa: $\mu_B = 1.0$ Pa s; $\rho = 1000$ kg m^{-3}; $\Delta p/L = 9.81$ kPa m^{-1}.

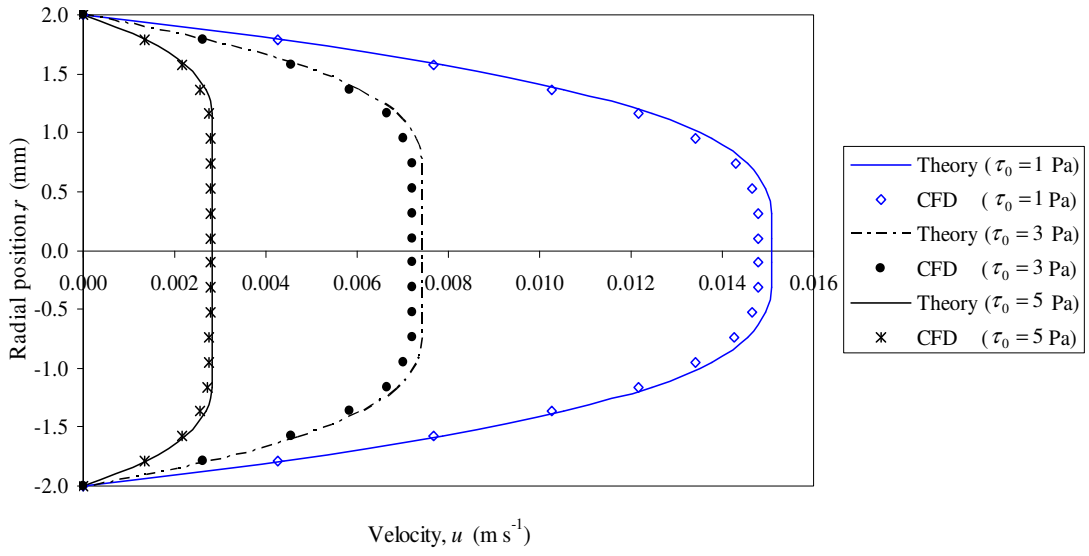

Figure 3.8: Comparison of CFD-predicted and theoretical velocity profiles for three Herschel-Bulkley fluids with $\tau_0 = 1$ Pa, $\tau_0 = 3$ Pa, and $\tau_0 = 5$ Pa: $k = 1.47$ Pa s^n; $n = 0.57$; $\rho = 1000$ kg m^{-3}; $\Delta p/L = 9.81$ kPa m^{-1}.

3.4.2. VALIDATION OF VIBRATIONAL FLOW SIMULATIONS

The solution of the vibrational flow simulation was validated using available experimental results relating to longitudinal vibration. The experimental results were obtained by Deshpande and Barigou (2001) who investigated the effects of longitudinal vibration on the flow rate of non-Newtonian fluids of different types. A brief description of the experimental procedure is provided here.

The experimental setup used is depicted in Figure 3.9. The available system was only capable of generating linear sinusoidal oscillations and, consequently, results could only be obtained for oscillations in the longitudinal mode along the direction of flow. In this case, a flow tube, 4 mm in diameter and 500 mm in length, was attached to a mechanical vibrator connected to a digital sine-wave controller and a power amplifier. The tube was connected to a fluid reservoir using a short flexible tube and a stop-valve. The reservoir was filled to a fixed level and the flow tube was vibrated longitudinally. The flow rate through the tube was determined by measuring the weight of liquid collected at the tube exit over a given period of time. In an experiment, the level in the reservoir remained practically constant since the cross section area of the reservoir was more than 1000 times that of the flow tube.

In the current work, simulations were conducted to obtain CFD predictions of the flow enhancement ratio (Equation (3.38)) under vibration conditions for which the experimental results were obtained. A power-law fluid was used with k = 1.47 Pa s^{-1} and n = 0.57; vibration amplitude of 1.6 mm and frequencies in the range 10-40 Hz were used. A very good agreement was found between CFD and experiment, as shown in Figure 3.10. Deshpande and Barigou (2001) also carried out numerical simulations using the commercial software CFX 4.3, an older version of the software used in the current study. Their CFD results also showed a very good agreement with their experimental results, similar to the CFD results obtained here.

It can be seen in Figure 3.10 that the agreement between CFD and experiment deteriorates slightly at the highest frequency used (40 Hz). Deshpande and Barigou (2001) argued that under such experimental conditions the vibration was quite severe

and, because the tube was fairly long, some slight lateral oscillations were unavoidable. As a result, the experimental enhancement ratio was somewhat smaller than predicted by CFD.

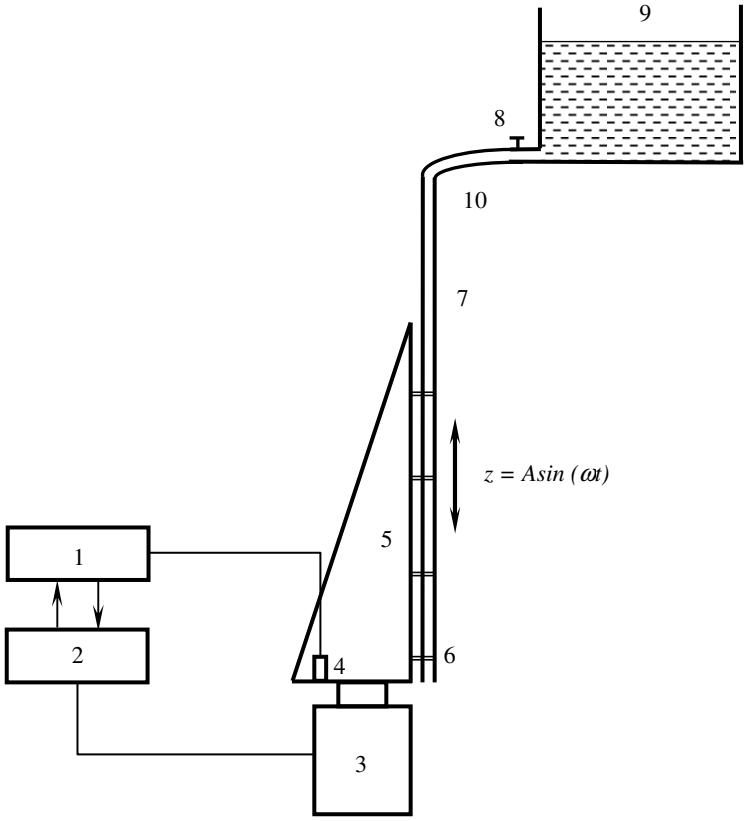

Figure 3.9: Experimental rig: 1. sine-wave controller; 2. power amplifier; 3. mechanical vibrator; 4. accelerometer probe; 5. support frame; 6. tube fasteners; 7. flow tube; 8. stop valve; 9. liquid reservoir; 10. flexible tube.

Also, simulations of the vibrational flow of a Newtonian fluid confirmed that vibration does not affect the flow rate or velocity field of Newtonian fluids, in agreement with the experimental observations.

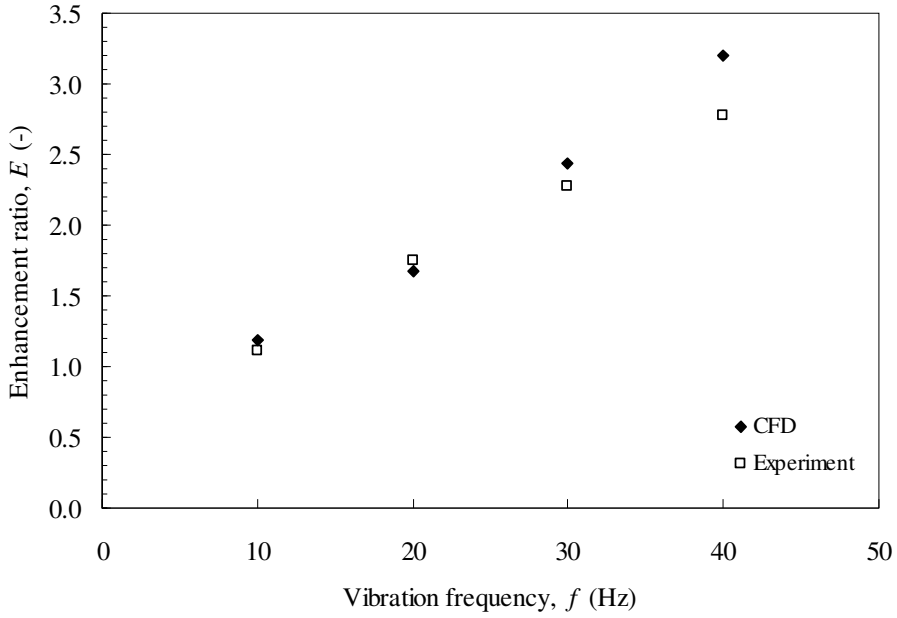

Figure 3.10: CFD results compared with experimental results for a power law fluid subjected to longitudinal vibration:
k = 1.47 Pa s^n; n = 0.57; ρ = 1000 kg m^{-3}; A = 1.60 mm; $\Delta p/L$ = 9.81 kPa m^{-1}.

This comparison with the experimental results of longitudinal vibration serves as a good validation for the rotational and transversal vibration simulations, as the simulation set-up was similar in all three simulations, the only difference being the direction in which the wall velocity function (Equations (3.33), (3.35) or (3.37)) was applied.

3.5. RESULTS AND DISCUSSION

3.5.1. NEWTONIAN FLUIDS

Results showed that rotational vibration does not affect the flow rate of a Newtonian fluid, the flow enhancement ratio E being equal to 1 irrespective of viscosity, vibration amplitude and frequency. This was experimentally demonstrated for longitudinal vibration by Deshpande and Barigou (2001), and is consistent with other reports by Mena *et al*. (1979), Shin *et al.* (2003), and Piau and Piau (2002 and 2005).

For a Newtonian fluid the viscosity is independent of shear rate. Consequently, it will not be affected by the superimposition of an external rotational shear and the flow rate will remain unchanged. The Newtonian case here also served as a useful initial validation check for the CFD model.

3.5.2. POWER LAW FLUIDS

The flow of power law fluids (Equation (3.4)) was substantially affected by the superimposed oscillatory rotation of the tube. Results showed that vibrating the tube gives rise to an enhanced flow, i.e. $E > 1$, for shear thinning fluids with $n < 1$. The extent of flow enhancement was dependent on the fluid behaviour index, n, consistency index, k, oscillation frequency, f, and amplitude, Θ, and pressure gradient, $\Delta p/L$. The effect of each of these factors was independently investigated through a parametric study in which each factor was varied over a wide range, as shown in Table 3.1.

The effect of oscillation on the shear-dependent apparent viscosity leads to a significant change in the fluid velocity profile. The velocity profile is considerably stretched or elongated in the axial direction with a mean axial velocity much greater than the steady flow value, and hence the observed flow enhancement.

Figure 3.11 shows an example of transient results of flow rate, shear rate and apparent viscosity obtained from CFD. The rotational vibration is superimposed on the axial steady state flow at time $t = 0$. The effect of such a vibration is fully felt after two oscillation cycles for the case shown. The shear rate shown is the resultant shear rate in the tube averaged over the tube cross-section; similarly, the viscosity is the cross-sectional area-averaged viscosity. The additional shear introduced by the oscillations, as shown in Figure 3.11, causes enhanced shear thinning of the fluid which is reflected into a reduced apparent viscosity below the steady state value. Thus, the superimposition of a rotational vibration at the wall leads to an increase in the time-averaged flow rate above the steady state value. The oscillations observed in the transients are due to the rotational oscillations superimposed at the wall. The transient results are consistent with the physical interpretation of the phenomenon, in that the viscosity is minimum and the flow rate is maximum when the shear rate is maximum and vice versa.

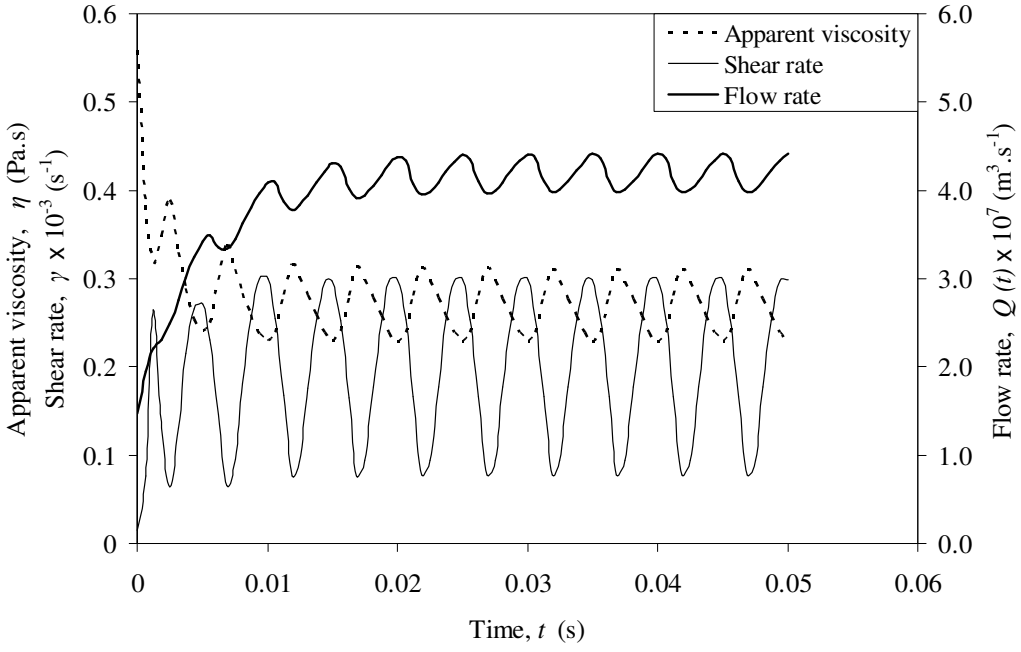

Figure 3.11: Transients of shear rate, apparent viscosity, and flow rate for a shear-thinning power law fluid:

$k = 1.47$ Pa s^n; $n = 0.65$; $f = 100$ Hz; $\Theta = \pi/10$ rad; $\Delta p/L = 9.81$ kPa m^{-1}.

For the flow of a shear thinning fluid under a given flow rate, calculations show that vibration can result in significant reductions in the pressure drop required to maintain the same flow rate compared to the steady state. Such results show that vibration can lower the power requirement necessary to generate and maintain the flow. This saving in power, however, must be weighed against the cost of generating vibrations of the required amplitude and frequency in order to determine the viability of vibration as a means of reducing power requirements. For a shear thickening fluid, however, it was found that vibration increases the pressure drop required to maintain the flow rate at its steady state value.

3.5.2.1. Effect of vibration frequency, f

The frequency of oscillation was varied within the range f = 0-300 Hz, while all other parameters were kept constant, i.e. $\Theta = \pi/10$ rad, k = 1.47 Pa s^n, and n = 0.57. Figure 3.12 shows the variations of the flow enhancement ratio as a function of f. Overall, a positive increase in the time-averaged flow rate with the oscillation frequency is obtained. For pseudoplastic fluids, the observed flow enhancement is due to the mechanism of shear thinning of the fluid. The rotational vibration at the wall introduces additional shear which reduces the local apparent viscosity and, hence, the observed increase in flow rate. The curve in Figure 3.12 shows a sharp increase in E starting at $f \sim 20$ Hz. At frequencies above 150 Hz, the rate of enhancement starts to slow down, levelling off at about 300 Hz. Higher frequencies do not produce any significant extra enhancement.

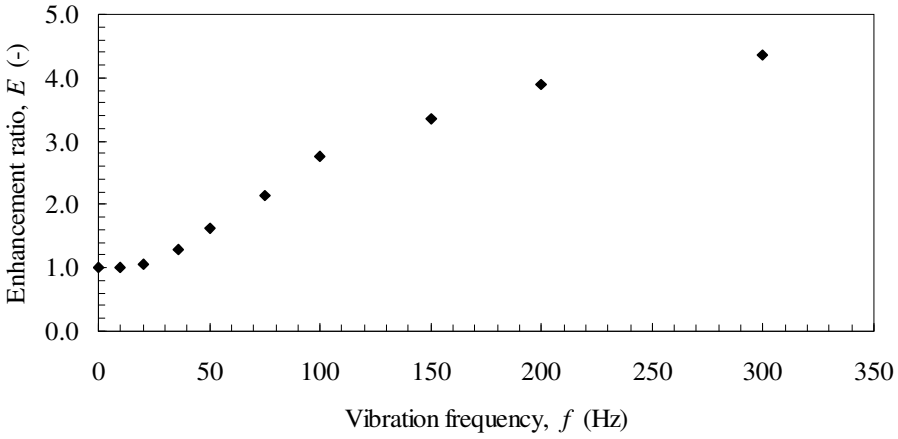

Figure 3.12: Effect of vibration frequency on flow enhancement in a power law fluid: k = 1.47 Pa s^n; n = 0.57; $\Theta = \pi/10$ rad; $\Delta p/L$ = 9.81 kPa m^{-1}.

The reason for this behaviour becomes apparent when the fluid apparent viscosity is monitored. Figure 3.13 shows the effect of vibration frequency on the area-averaged apparent viscosity of the fluid calculated over a pipe cross-section, for the cases plotted in Figure 3.12. As expected, vibration reduces viscosity substantially, thus increasing the flow rate. At high frequencies, however, the viscosity tends to a limiting value beyond which no further reduction is attainable. It is interesting to note that in the work of Mena *et al.* (1979), the increase of flow rate in a viscoelastic fluid due to longitudinal vibration was expected to level off at high frequencies when the other parameters are kept constant, but this was not proved due to experimental limitations. Deshpande and Barigou (2001), however, demonstrated a similar trend for longitudinal vibration of inelastic fluids.

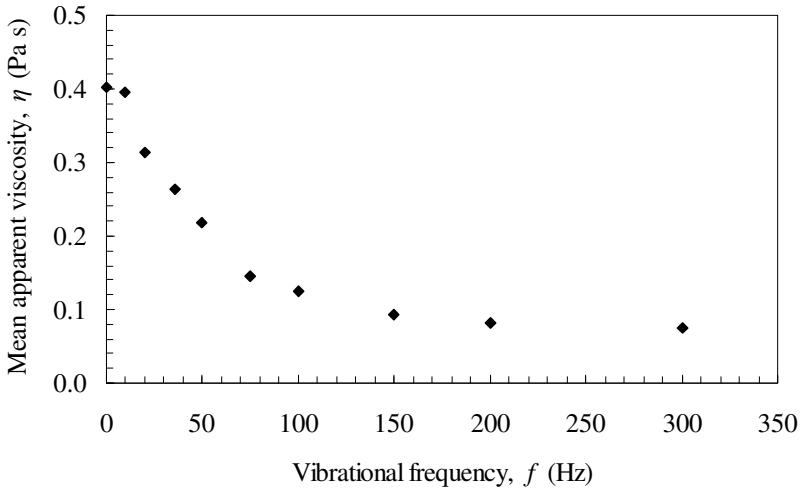

Figure 3.13: Effect of vibration frequency on area-weighted mean apparent viscosity of a power law fluid (see Figure 3.12):
k = 1.47 Pa s^n; n = 0.57; $\Theta = \pi/10$ rad; $\Delta p/L$ = 9.81 kPa m^{-1}.

The superimposition of an external shear on the flow alters the shear distribution over the pipe cross section, thus, producing an altered velocity profile. Results confirmed that the velocity profile is greatly affected by the superimposition of rotational vibration, and that this effect is largely dependent on frequency. Figure 3.14 compares the steady state velocity profile with the velocity profile under vibration for three vibration frequencies, 20, 50 and 150 Hz. It can be seen that vibration causes elongation of the velocity profile in the flow direction, and that this effect becomes more pronounced with increasing vibration frequency.

Not only does vibration increase the mean flow velocity and stretch the velocity profile, it may also alter the shape of the normalised velocity profile. The normalised velocity, u_n, at any radial position is calculated from the point value of velocity at that position, u, and the mean flow velocity, $\bar{u}$, thus

$$u_n = \frac{u}{\bar{u}} \tag{3.40}$$

The normalised velocity profile thus obtained is plotted for two different vibration frequencies, 50 and 150 Hz, in Figure 3.15, which shows that with increasing vibration frequency the normalised velocity profile becomes more flattened compared with the normalised velocity profile under steady state. This increased flattening can be measured by calculating the reduction in the maximum normalised velocity, which occurs at the pipe centre, under vibration relative to its value under steady state conditions. Even at the high vibration frequency of 150 Hz this reduction amounts to only 11% under the vibration conditions for which the data in Figure 3.15 are obtained, suggesting that this effect is somewhat weak. It is interesting to note that this effect is qualitatively similar to the effect of reducing the flow behaviour index n.

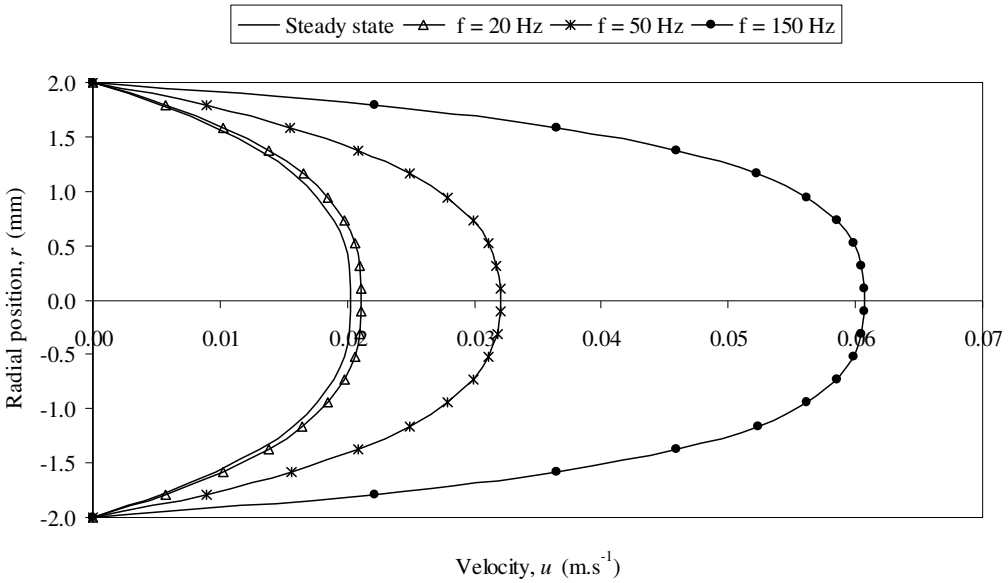

Figure 3.14: Effect of vibration frequency on velocity profile for a power law fluid: k = 1.47 Pa s^n; n = 0.57; $\Theta = \pi/10$ rad; $\Delta p/L$ = 9.81 kPa m^{-1}.

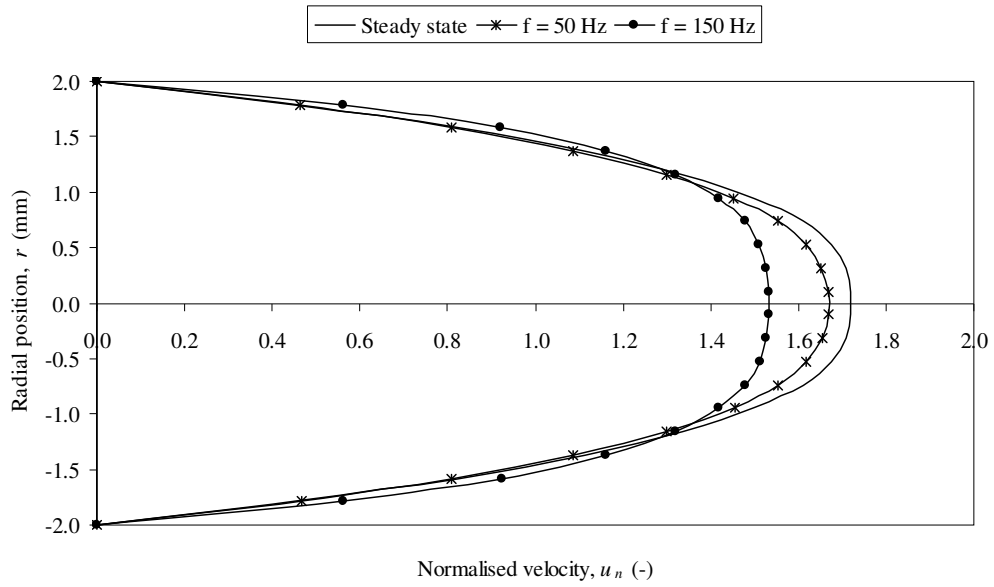

Figure 3.15: Effect of vibration frequency on normalised velocity profile for a power law fluid: k = 1.47 Pa s^n; n = 0.57; $\Theta = \pi/10$ rad; $\Delta p/L$ = 9.81 kPa m^{-1}.

3.5.2.2. Effect of vibration amplitude, Θ

The effect of vibration amplitude was studied for values up to $\Theta = \pi/4$ rad corresponding to a linear amplitude of 1.57 mm. All other parameters were fixed at their basic values throughout the simulations, i.e. f = 100 Hz, k = 1.47 Pa s^n, and n = 0.57, so that the resulting effect was attributed solely to the variation of Θ. Figure 3.16 shows that increasing Θ increases E over the range of values studied. Even with small amplitudes, substantial increases in flow rate are achieved. The rate at which E increases with Θ, however, seems to decline at high amplitudes.

The effect of vibration amplitude on the velocity profile was studied, and results are shown in Figure 3.17. The higher the vibration amplitude, the greater the elongation of the velocity profile compared to the steady state velocity profile. This is in qualitative agreement with the results of Mena *et al.* (1979) who found that the superimposition of longitudinal vibration on a viscoelastic fluid flowing in a pipe results in drastic elongation of its velocity profile, and that this effect increases with vibration amplitude.

The effect of vibration amplitude on the normalised velocity profile was weak within the range of amplitudes studied, as shown in Figure 3.18.

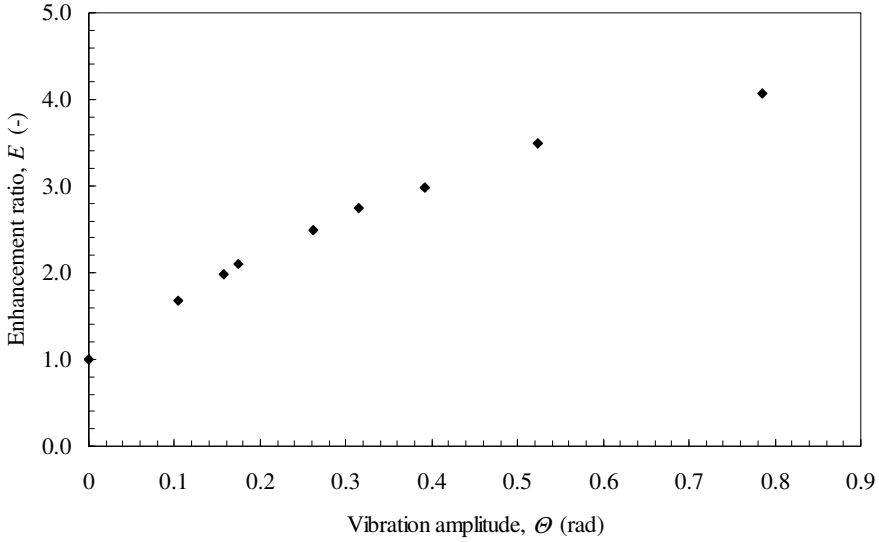

Figure 3.16: Effect of vibration amplitude on flow enhancement in a power law fluid: k = 1.47 Pa s^n; n = 0.57; f = 100 Hz; $\Delta p/L$ = 9.81 kPa m^{-1}.

Note that 0.1 rad = 5.73°.

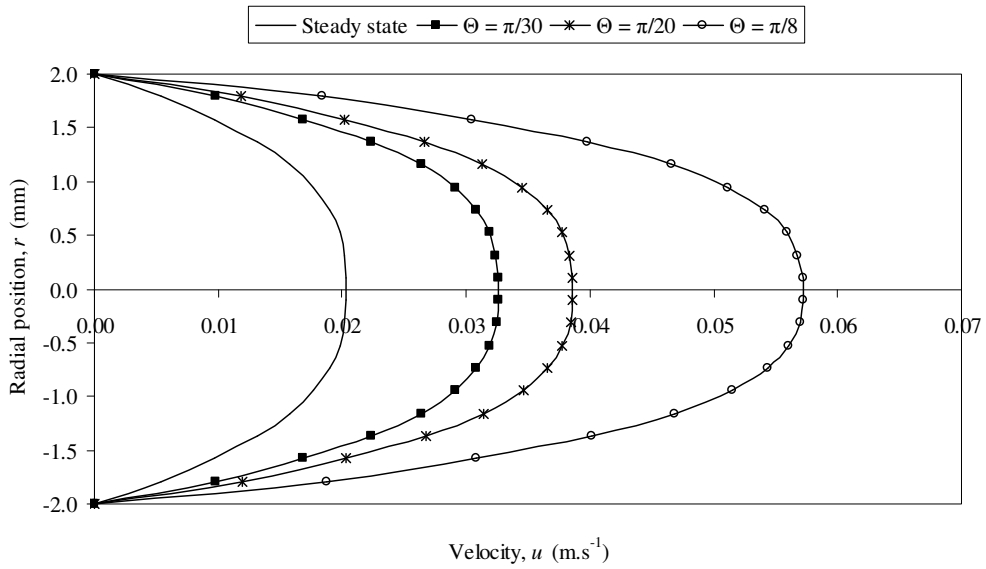

Figure 3.17: Effect of vibration amplitude on velocity profile for a power-law fluid: k = 1.47 Pa s^n; n = 0.57; f = 100 Hz; $\Delta p/L$ = 9.81 kPa m^{-1}.

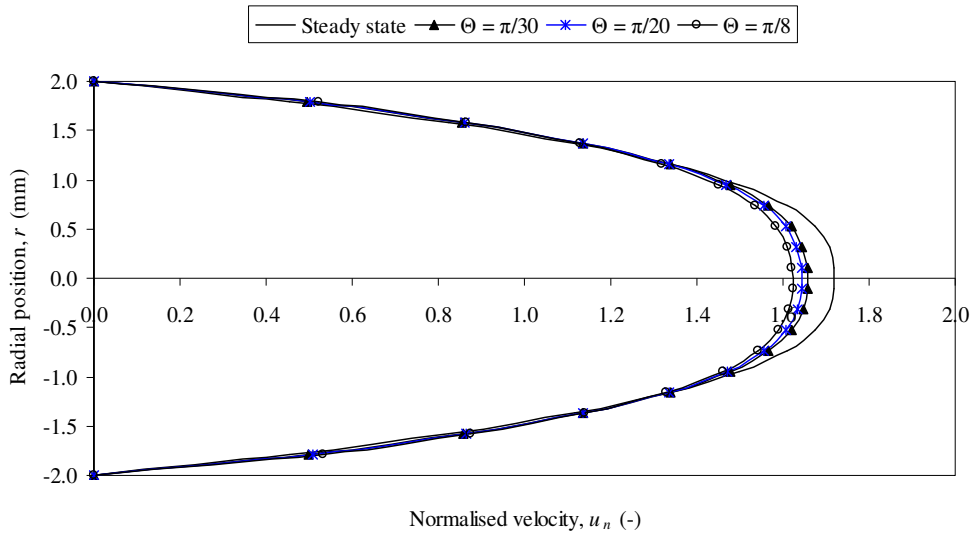

Figure 3.18: Effect of vibration amplitude on normalised velocity profile for a power law fluid:

k = 1.47 Pa s^n; n = 0.57; f = 100 Hz; $\Delta p/L$ = 9.81 kPa m^{-1}.

Results also showed that different combinations of vibration frequency and amplitude giving the same maximum peak acceleration yield the same flow enhancement, within computational error; an example is shown in Table 3.3 for a fixed maximum peak acceleration of 248.1 m s^{-2}. Similar results were obtained by Deshpande and Barigou (2001) for a Herschel-Bulkley fluid flowing under the influence of longitudinal vibration. In practice, the choice of vibration amplitude and frequency will be dictated by what is practically feasible, but the flow enhancement will be governed by the maximum acceleration of the oscillations used.

Table 3.3: Flow enhancement at constant maximum acceleration for a power law fluid.

f (Hz)	Θ (rad)	$R\Theta\omega^2$ (m s^{-2})	E (-)
100	0.31	248.1	2.8
90	0.39	248.1	2.9
80	0.49	248.1	2.9
70	0.56	248.1	2.9

3.5.2.3. Effect of flow behaviour index, n

For a shear-thinning power law fluid, where $n < 1$, the apparent viscosity decreases as the rate of shear increases. The smaller the value of n, the greater the degree of shear thinning. For a shear thickening fluid, where $n > 1$, the apparent viscosity increases with shear rate; the greater the value of n, the more pronounced the shear thickening behaviour. When $n = 1$ the fluid is Newtonian.

Figure 3.19 shows the effect of varying n over a wide range on the flow enhancement ratio. In the shear thinning region, flow enhancement decreases as n is increased, i.e. as the shear thinning behaviour becomes less pronounced, reaching unity at $n = 1$, which corresponds to a Newtonian fluid with no enhancement, $E = 1$. In the shear thickening region, as n is increased above 1, E continues to decrease below unity, thus, indicating that the superimposed angular vibration at the tube wall causes flow retardation, i.e. the vibrational flow rate is lower than the steady state flow rate. The increased shear in this case results in an increase in the apparent viscosity of the fluid, hence the observed flow retardation. The more shear thickening the fluid is, the more flow retardation it will experience due to the added shear generated by vibration. These results confirm that for fluids with a shear-dependent viscosity, it is the extra shear thinning (or thickening) induced by the oscillations which is responsible for the changes, whether enhancement or retardation, in the flow. Therefore, the more pronounced the non-Newtonian behaviour of the fluid, the greater the effect of vibration on the flow. Figure 3.19 also suggests that the relationship between n and E is nearly exponential.

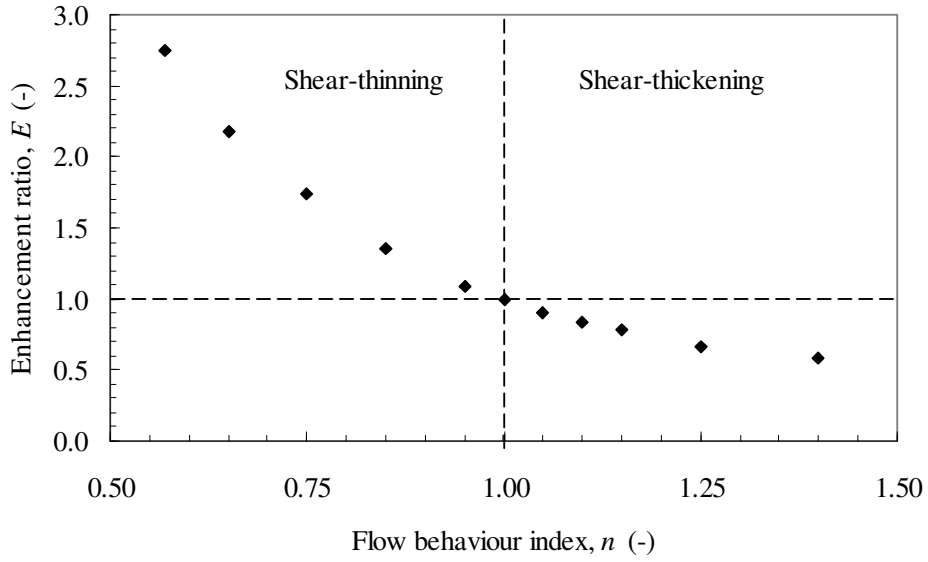

Figure 3.19: Effect of flow behaviour index on flow enhancement in a power law fluid:
k = 1.47 Pa s^n; f = 100 Hz; $\Theta = \pi/10$ rad; $\Delta p/L$ = 9.81 kPa m^{-1}.

The effect of vibration on the velocity profile is shown in Figures 3.20, 3.21, 3.22, and 3.23 for n values of 0.65, 0.75, 0.85, and 1.25, respectively. As discussed above, vibration results in velocity profile elongation in the flow direction. From the figures it can be seen that the more shear thinning the fluid, i.e. the lower the value of n, the more elongated the velocity profile under vibration. Vibration of a shear thickening fluid gives rise to a more flattened velocity profile (Figure 3.23), hence the observed flow retardation.

The effect of vibration on the normalised velocity profile was again small at all n values investigated. Figures 3.24 and 3.25 show sample results of the normalised velocity profile for a shear thinning (n = 0.75) and a shear thickening (n = 1.25) fluid, respectively. For the shear thinning fluid, there is a small reduction in the maximum normalised velocity compared to the steady state value, while the normalised velocity profile of the shear thickening fluid showed an even smaller deviation from the steady state profile. It can therefore be said that the characteristics of the flow remain almost unchanged under vibration.

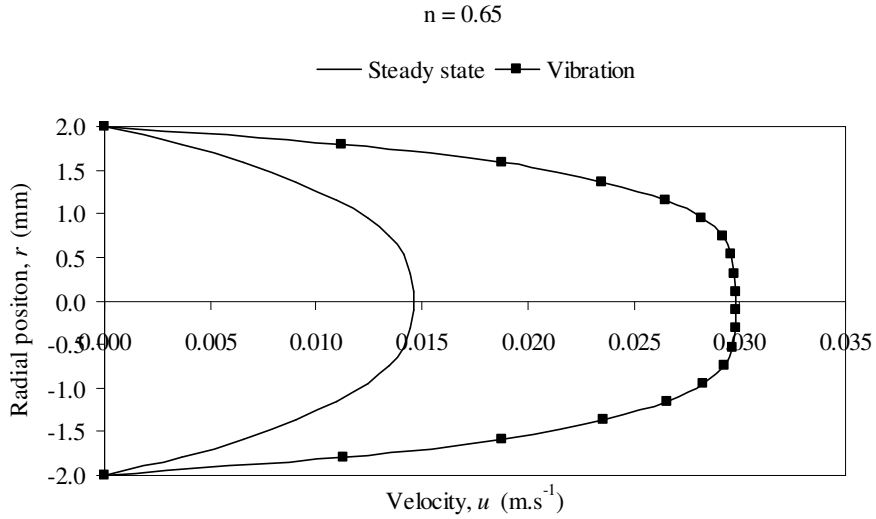

Figure 3.20: Effect of vibration on velocity profile for a shear-thinning power law fluid:

k = 1.47 Pa s^n; n = 0.65; f = 100 Hz; $\Theta = \pi/10$ rad; $\Delta p/L$ = 9.81 kPa m^{-1}.

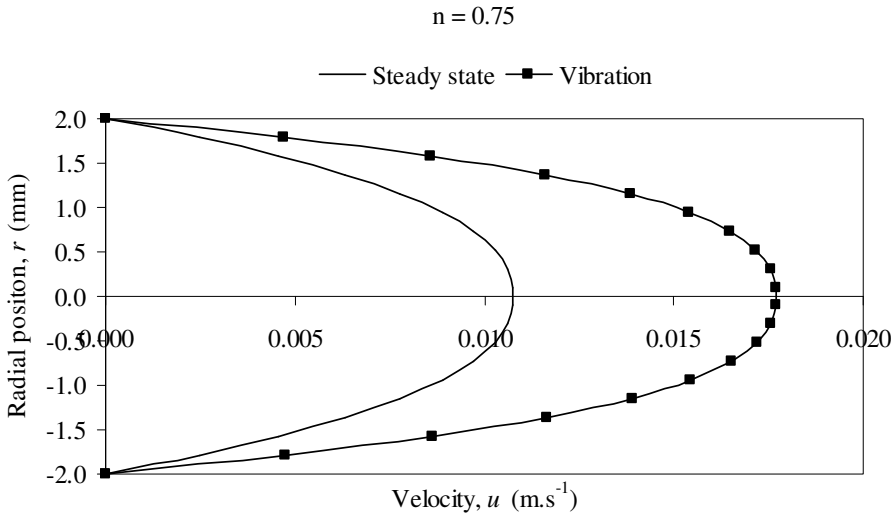

Figure 3.21: Effect of vibration on velocity profile for a shear-thinning power law fluid:

k = 1.47 Pa s^n; n = 0.75; f = 100 Hz; $\Theta = \pi/10$ rad; $\Delta p/L$ = 9.81 kPa m^{-1}.

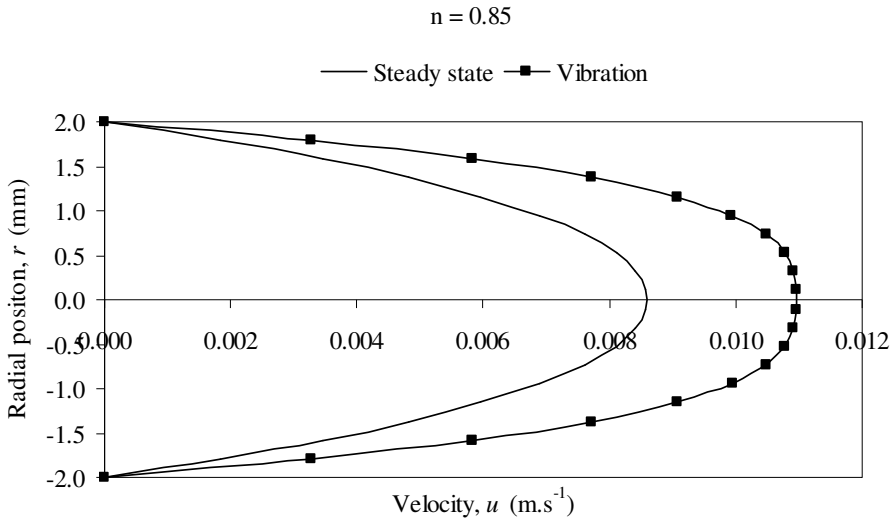

Figure 3.22: Effect of vibration on velocity profile for a shear-thinning power law fluid:

k = 1.47 Pa s^n; n = 0.85; f = 100 Hz; $\Theta = \pi/10$ rad; $\Delta p/L$ = 9.81 kPa m^{-1}.

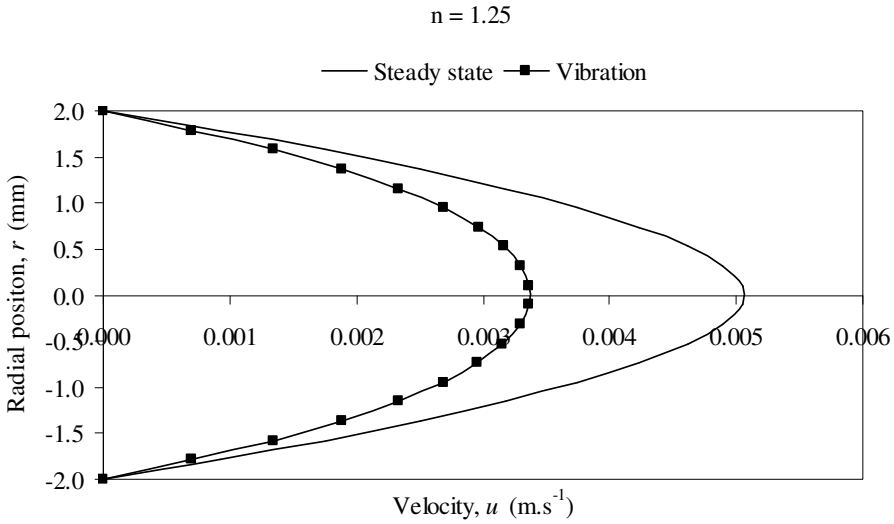

Figure 3.23: Effect of vibration on velocity profile for a shear-thickening power law fluid:

k = 1.47 Pa s^n; n = 1.25; f = 100 Hz; $\Theta = \pi/10$ rad; $\Delta p/L$ = 9.81 kPa m^{-1}.

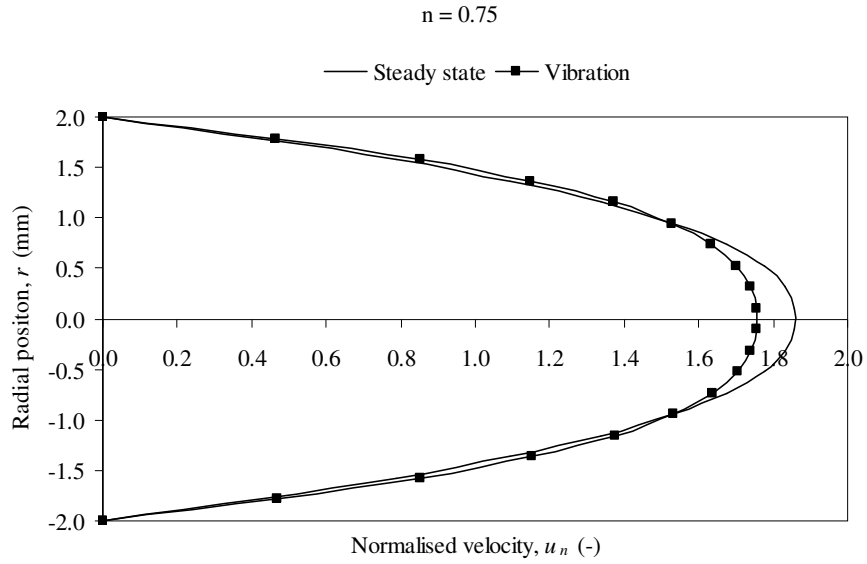

Figure 3.24: Effect of vibration on normalised velocity profile for a shear-thinning power law fluid:

k = 1.47 Pa s^n; n = 0.75; f = 100 Hz; $\Theta = \pi/10$ rad; $\Delta p/L$ = 9.81 kPa m^{-1}.

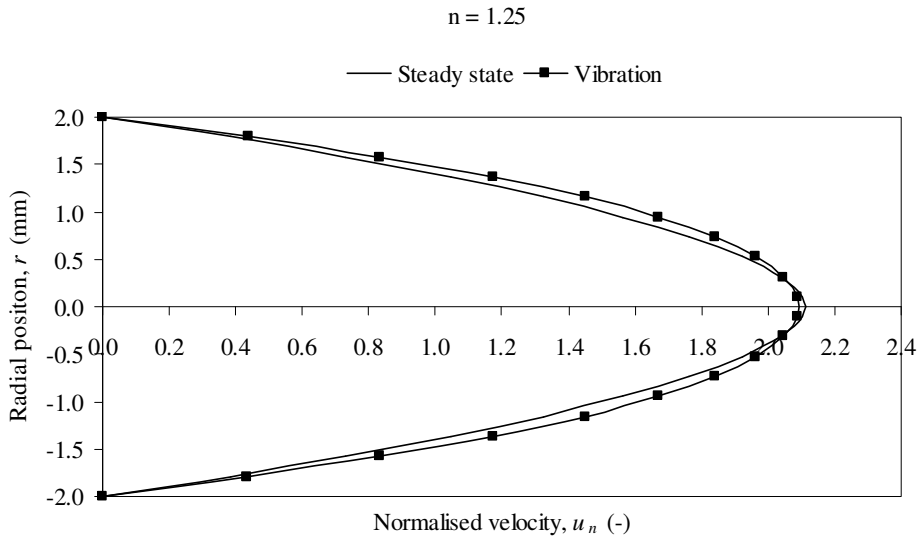

Figure 3.25: Effect of vibration on velocity profile for a shear-thickening power law fluid:

k = 1.47 Pa s^n; n = 1.25; f = 100 Hz; $\Theta = \pi/10$ rad; $\Delta p/L$ = 9.81 kPa m^{-1}.

3.5.2.4. Effect of fluid consistency index, k

The index k is a measure of the consistency of the fluid; the greater the value of k, the more viscous the fluid. The effect of k on the enhancement ratio is shown in Figure 3.26, with E increasing as a function of k, indicating that the effectiveness of rotational vibration increases for more viscous fluids, but only to a limit. For the fluids considered here, the increase in enhancement ratio seems to level off at about k = 15 Pa s^n. A similar trend was observed by Deshpande and Barigou (2001) for a Herschel-Bulkley fluid under longitudinal vibration. This trend shows that for relatively high values of k, i.e. relatively thick fluids, the flow enhancement that can be achieved at a given vibration frequency and amplitude is limited. This result suggests that highly thick fluids require high vibration frequencies and amplitudes in order to obtain very large E values.

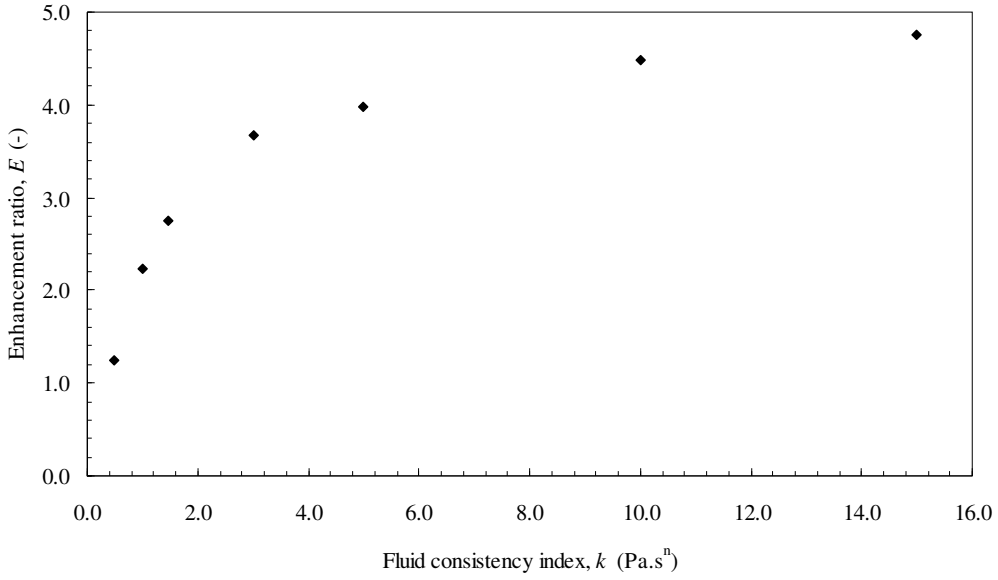

Figure 3.26: Effect of fluid consistency index on flow enhancement in a power law fluid:

n = 0.57; f = 100 Hz; $\Theta = \pi/10$ rad; $\Delta p/L$ = 9.81 kPa m^{-1}.

The velocity profiles show that the more viscous the fluid, i.e. the higher the value of k, the more elongated the velocity profile under vibration compared to the steady state profile, as shown in Figures 3.27, 3.28 and 3.29 for k = 1.0, 3.0, and 10.0 Pa s^n

respectively. For the case with k = 10 Pa s^n, the maximum velocity is increased by over 300% as a result of vibration. The normalised velocity profile, on the other hand, is only slightly flattened for all k values, as shown in Figures 3.30, 3.31, and 3.32.

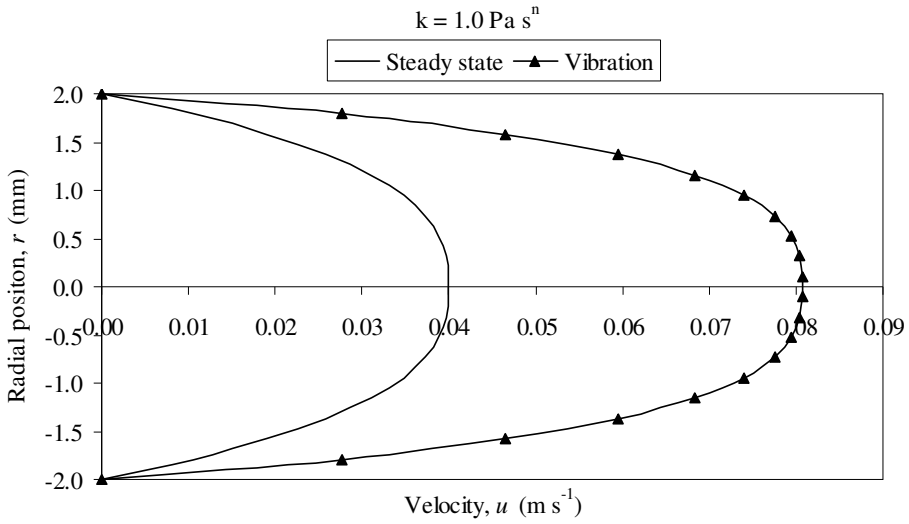

Figure 3.27: Effect of fluid consistency index on velocity profile for power law fluid: k = 1.0 Pa s^n; n = 0.57; f = 100 Hz; Θ = π/10 rad; $\Delta p/L$ = 9.81 kPa m^{-1}.

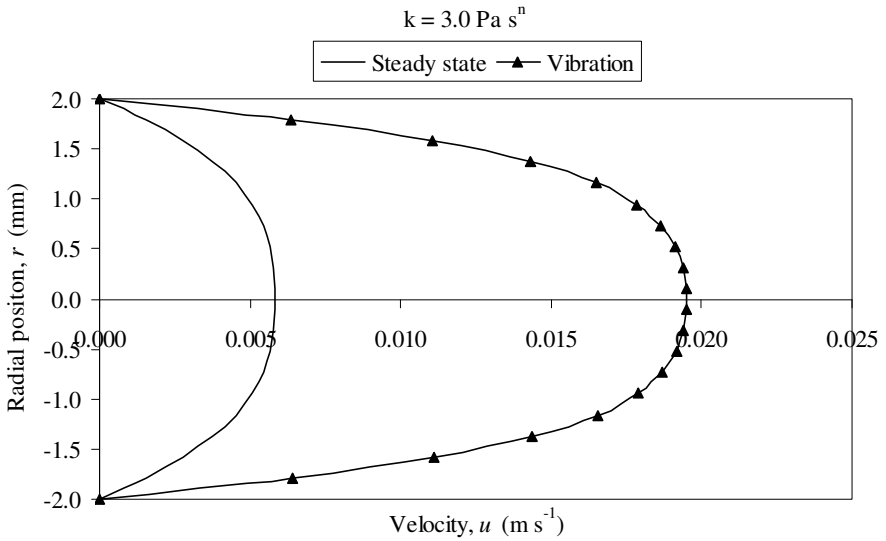

Figure 3.28: Effect of fluid consistency index on flow enhancement in a power law fluid:

k = 3.0 Pa s^n; n = 0.57; f = 100 Hz; Θ = π/10 rad; $\Delta p/L$ = 9.81 kPa m^{-1}.

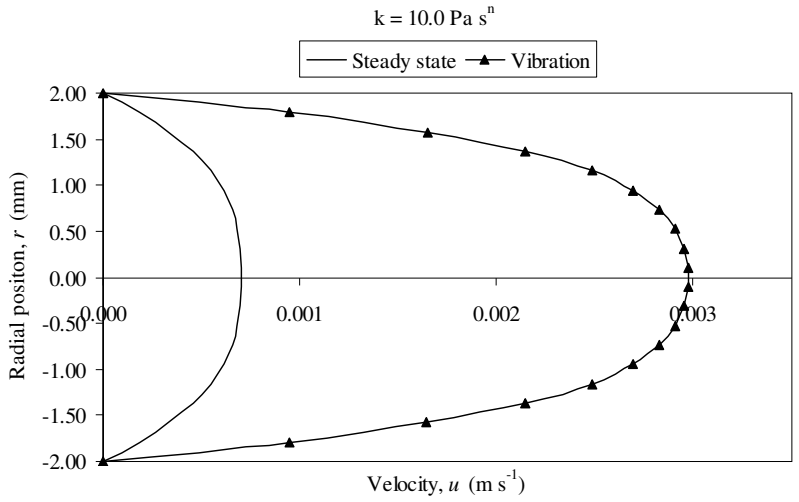

Figure 3.29: Effect of fluid consistency index on flow enhancement in a power law fluid:

k = 10.0 Pa s^n; n = 0.57; f = 100 Hz; Θ = π/10 rad; $\Delta p/L$ = 9.81 kPa m^{-1}.

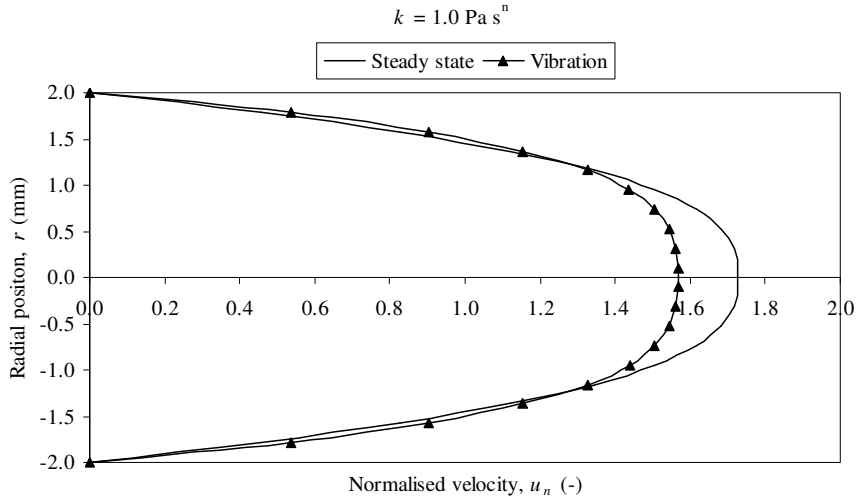

Figure 3.30: Effect of fluid consistency index on normalised velocity profile for power law fluid:

k = 1.0 Pa s^n; n = 0.57; f = 100 Hz; Θ = π/10 rad; $\Delta p/L$ = 9.81 kPa m^{-1}.

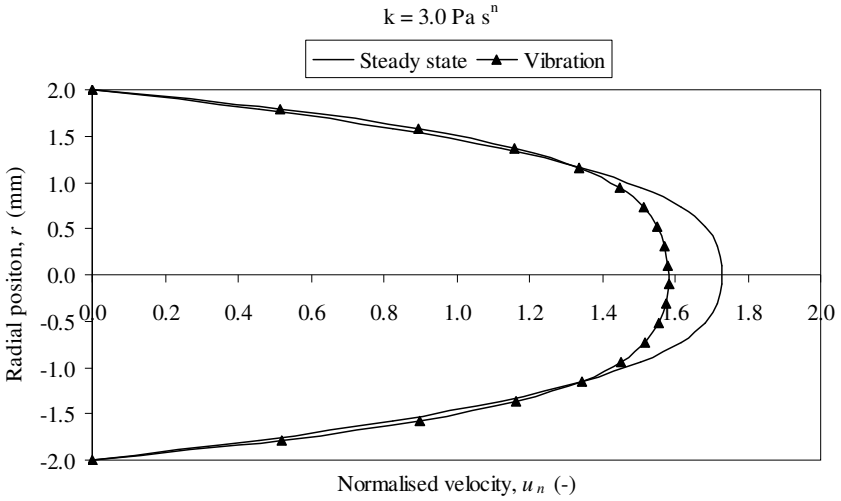

Figure 3.31: Effect of fluid consistency index on normalised velocity profile for power law fluid:

k = 3.0 Pa s^n; n = 0.57; f = 100 Hz; Θ = π/10 rad; $\Delta p/L$ = 9.81 kPa m^{-1}.

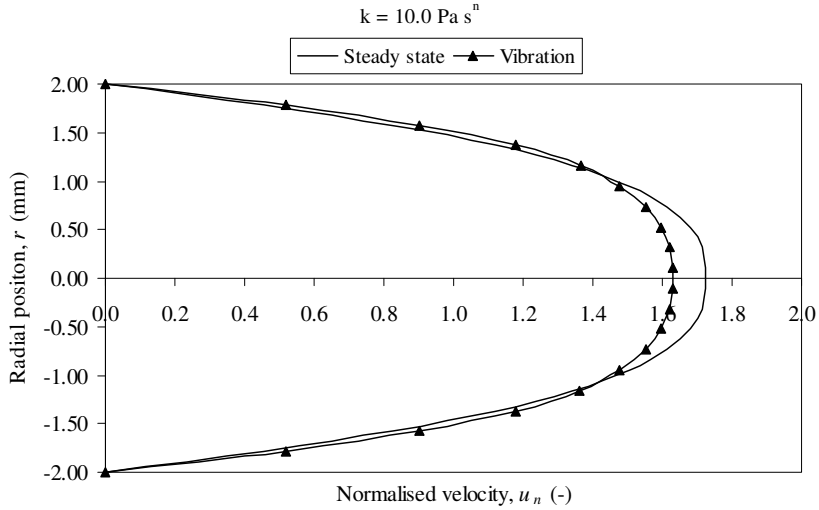

Figure 3.32: Effect of fluid consistency index on normalised velocity profile for power law fluid:

k = 10.0 Pa s^n; n = 0.57; f = 100 Hz; Θ = π/10 rad; $\Delta p/L$ = 9.81 kPa m^{-1}.

3.5.2.5. Effect of pressure gradient, Δp/L

Numerical simulations were conducted for a range of $\Delta p/L$ values, as shown in Figure 3.33. The results are therefore independent of the orientation of the pipe. At low pressure gradients, the flow enhancement ratio is high but decreases sharply as $\Delta p/L$ increases, gradually approaching unity. A similar trend was reported for longitudinal vibration by Deshpande and Barigou (2001). For the particular case considered here, the superimposed vibration has no significant effect on the flow beyond ~ 60 kPa m^{-1}. Note that a pressure drop of 9.81 kPa m^{-1} corresponds to a vertical gravity-driven flow. Under greater pressure gradients, the steady state flow is high (i.e. the shear viscosity is low as most of the fluid structure has been broken down under high shear in such a shear thinning fluid) and the extra flow generated by vibrating the tube becomes comparatively insignificant.

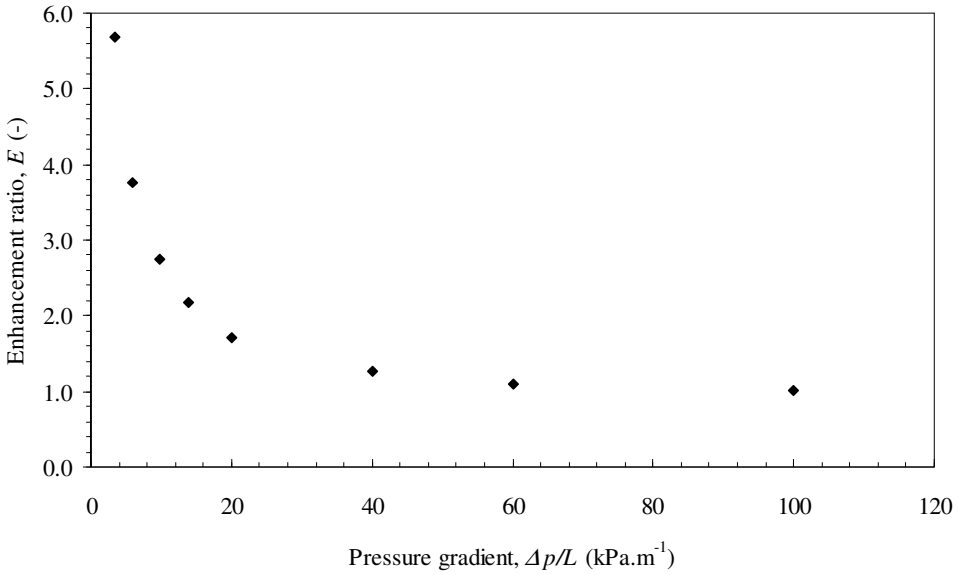

Figure 3.33: Effect of pressure gradient on flow enhancement in a power law fluid: k = 1.47 Pa s^n; n = 0.57; f = 100 Hz; $\Theta = \pi/10$ rad.

3.5.3. VISCOPLASTIC FLUIDS

3.5.3.1. Bingham plastic fluids

In viscoplastic fluids, a new parameter is introduced which is the apparent yield stress (Equation (3.7)). The effect of increasing the yield stress on the flow enhancement of a Bingham plastic fluid was studied in the range 0-6 Pa, with a constant plastic viscosity μ_B = 1 Pa s. As shown in Figure 3.34, there is an exponential rise in flow enhancement as the yield stress increases. Note that E = 1 for the Newtonian case where τ_0 = 0 Pa. It is interesting to note that a Bingham plastic fluid exhibits an apparent viscosity that decreases non-linearly with increasing shear rate (Equation (3.8)). At very low shear rates, the apparent viscosity is effectively infinite just before yielding occurs and flow commences. It is thus possible to regard these materials as possessing a particular type of shear thinning behaviour, as discussed earlier (Section 3.2.1.4), which explains the enhancement in flow obtained with a superimposed oscillation. In fact, there is an interesting similarity between the effect of increasing τ_0 and that of decreasing n, i.e. increasing shear thinning (Section 3.5.2.3).

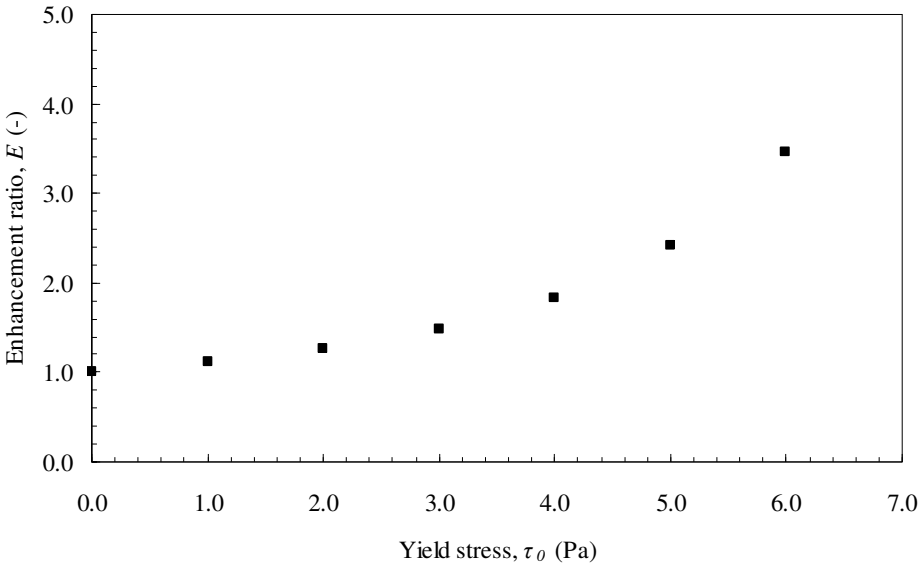

Figure 3.34: Effect of apparent yield stress on flow enhancement in a Bingham plastic fluid:
μ_B = 1 Pa s; f = 100 Hz; $\Theta = \pi/10$ rad; $\Delta p/L$ = 9.81 kPa m^{-1}.

3.5.3.2. Generalised power law or Herschel-Bulkley fluids

A generalised power law or Herschel-Bulkley fluid (Equation (3.9)) is simply a power law fluid with an apparent yield stress. It is worth noting that the shear thinning effect in a Herschel-Bulkley fluid results from the power law term as well as the yield stress term in a similar way to a Bingham plastic fluid. The roles of the parameters *k* and *n* in determining the extent of flow enhancement achieved by angular oscillations are similar to those observed for simple power law fluids, as discussed above. However, the added shear thinning effect due to the yield stress term warrants a more detailed investigation.

Numerical simulations were executed for values of the yield stress, τ_0, less than the wall shear stress (Equation (3.12)) to enable some flow to occur under steady state conditions. Note that no flow occurs for $\tau_0 > \tau_w$, as the shear stress is below the yield stress throughout the fluid. The effect of varying τ_0 for a Herschel-Bulkley fluid is similar in trend to that obtained for a Bingham plastic fluid, as shown in Figure 3.35. Much larger enhancement ratios are, however, achievable as the shear thinning is a combination of both the power law term as well as the yield stress term. These results are in line with the theoretical and experimental results of Piau and Piau (2007) who studied the effects of coupling yield stress and shear thinning on the flow enhancement and pressure drop reduction in viscoplastic fluids. It was observed that a Herschel-Bulkley fluid exhibits much higher flow enhancements under longitudinal vibration compared to a Bingham fluid within the same range of Bingham number.

For a fixed pressure gradient, $\Delta p/L$, increasing τ_0 widens the central plug (uniform velocity) flow region in the tube; in the limit when $\tau_0 = \tau_w$ the plug fills the whole tube cross-section. The plug velocity (i.e. maximum flow velocity) which is proportional to $\left(1-\tau_0/\tau_w\right)$ then decreases and so does the steady state flow rate, Q (Equation (3.11)), as shown in Figure 3.36. Therefore, the additional flow produced by the oscillations due to shear thinning of the fluid near the wall becomes relatively more significant; hence the observed increase in the value of E (Figure 3.35). Note that when $\tau_0 = \tau_w = 9.81$ Pa, no flow occurs in the pipe, i.e. $Q = 0$.

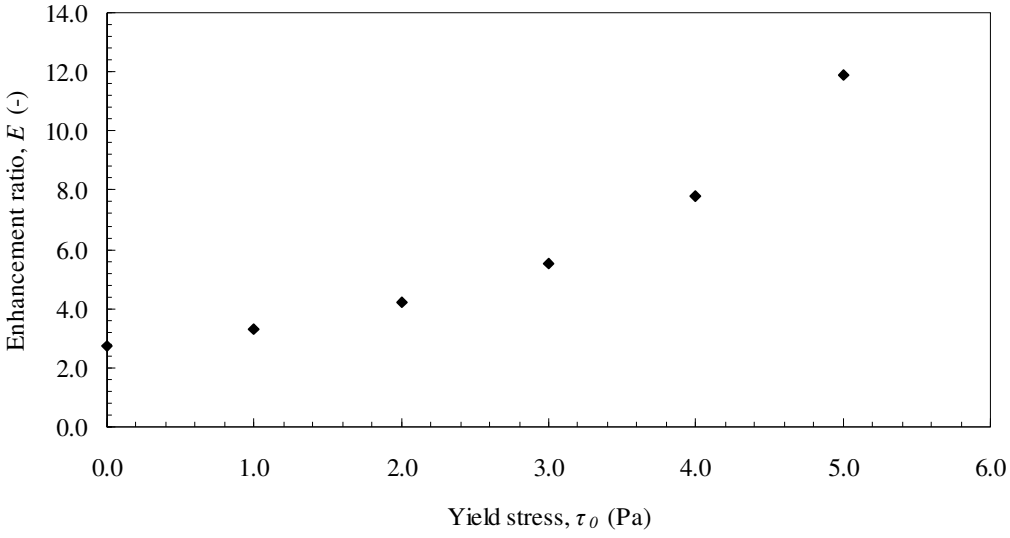

Figure 3.35: Effect of apparent yield stress on flow enhancement in a Herschel-Bulkley fluid:

k = 1.47 Pa s^n; n = 0.57; f = 100 Hz; $\Theta = \pi/10$ rad; $\Delta p/L$ = 9.81 kPa m^{-1}.

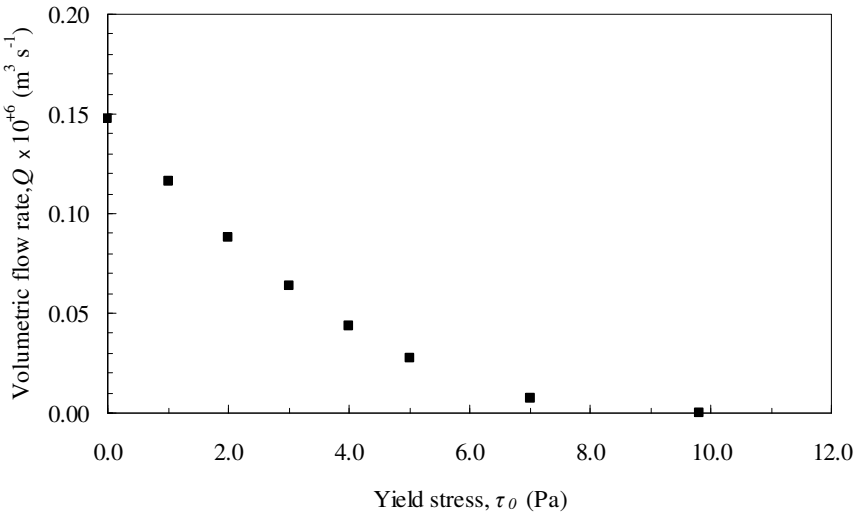

Figure 3.36: Effect of yield stress on steady state flow rate for a Herschel-Bulkley fluid:

k = 1.47 Pa s^n; n = 0.57; $\Delta p/L$ = 9.81 kPa m^{-1}.

3.5.4. ULTRASONIC VIBRATION

The above numerical experiments showed that, in general, significant flow enhancements can be achieved with non-Newtonian fluids using angular oscillations with frequencies on the Hz scale. It was shown, however, that the effects of increasing f and Θ are limited. In addition, the scope for enhancing the flow when the fluid is highly viscous or the pressure gradient is high is also limited. Many industrial non-Newtonian fluids, such as polymer melts, are extremely viscous. Producing substantial enhancement in the flow of such fluids requires vibrations on the ultrasonic scale of frequency, i.e. $f \geq 16$ kHz. The works by Piau and Piau (2002) and Wu *et al.* (2003) suggest that longitudinal ultrasonic vibration offers an interesting possibility. The effects of rotational oscillation in the ultrasonic range of frequency are investigated here.

A range of numerical simulations were conducted using a highly viscous Herschel-Bulkley fluid to mimic a polymer melt (k = 10 kPa s^n; n = 0.33; τ_0 = 200 kPa). A pressure gradient of 267 MPa m^{-1} was used, giving a laminar flow with Re < 20 in the steady state and Re < 400 in the vibrated state. The effects of varying the vibration frequency and amplitude, and the yield stress were studied, as shown in Table 3.1.

Figures 3.37 and 3.38 show that, within the range of values studied, the flow enhancement ratio increases steadily as a function of vibration frequency, f, and amplitude, Θ, reaching very large values corresponding to 2 orders of magnitude. The yield stress again has an exponential influence on the enhancement ratio, as shown in Figure 3.39, showing an increasingly high potential for flow enhancement as τ_0 increases. These effects demonstrate the great potential of ultrasonic vibration in the processing of highly viscous materials throughout the spectrum of industries concerned, such as in polymer processing. Provided that the increase in flow rate outweighs the cost of generating the required oscillation, the results suggest that ultrasonic vibration is an effective way of increasing the flow rate of such materials.

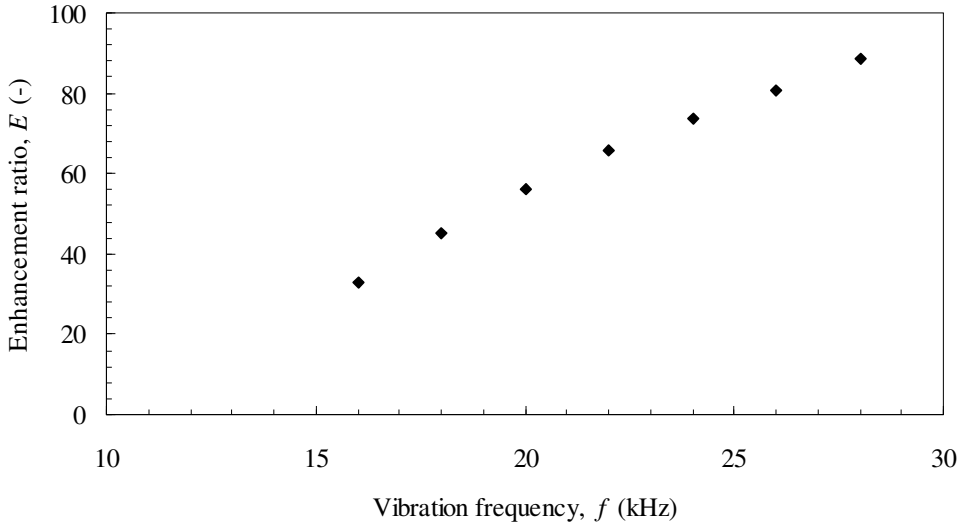

Figure 3.37: Effect of ultrasonic vibration frequency on flow enhancement in a highly viscous Herschel-Bulkley fluid:
k = 10 kPa s^n; n = 0.33; τ_0 = 200 kPa; ρ = 1350 kg m^{-3}; Θ = π/90 rad;
$\Delta p/L$ = 267 MPa m^{-1}.

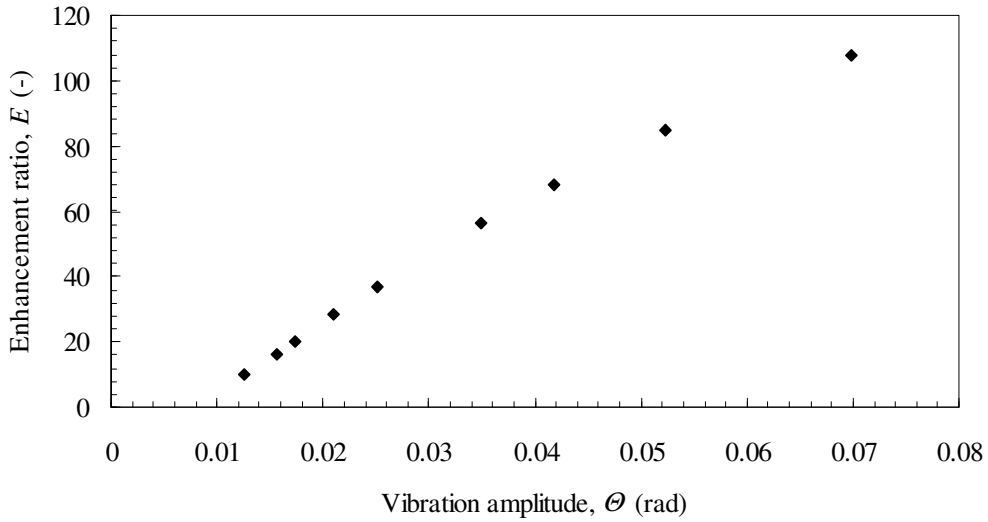

Figure 3.38: Effect of ultrasonic vibration amplitude on flow enhancement in a highly viscous Herschel-Bulkley fluid:
k = 10 kPa s^n; n = 0.33; τ_0 = 200 kPa; ρ = 1350 kg m^{-3}; f = 20 kHz;
$\Delta p/L$ = 267 MPa m^{-1}.

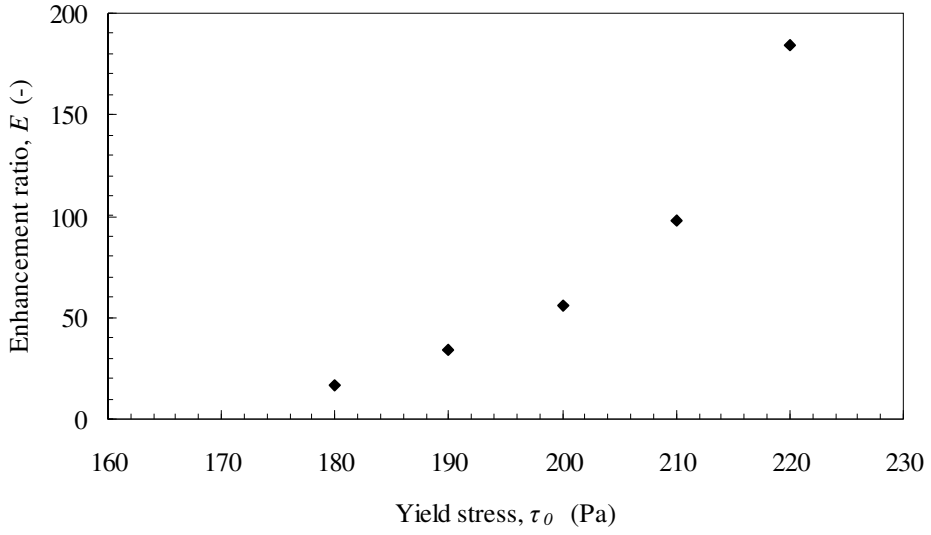

Figure 3.39: Effect of apparent yield stress on flow enhancement in a highly viscous Herschel-Bulkley fluid subjected to ultrasonic vibration:
k = 10 kPa s^n; n = 0.33; ρ = 1350 kg m^{-3}; f = 20 kHz; $\Theta = \pi/90$ rad;
$\Delta p/L$ = 267 MPa m^{-1}.

3.5.5. TRANSVERSAL VIBRATION

The results reported so far were obtained using rotational vibration. Simulations were also conducted of the unsteady flow under transversal vibration for the range of parameters given in Table 3.1. The results showed that this mode of vibration can also give rise to significant flow enhancement. However, the flow enhancement under transversal vibration was generally lower than that obtained under longitudinal and rotational vibrations. The effects of vibration parameters and fluid rheological properties, however, were qualitatively similar.

As with the longitudinal and rotational vibration modes, simulation results showed that transversal vibration does not affect the flow rate of Newtonian fluids, with E = 1. The flow rate and velocity field of shear thinning, shear thickening and viscoplastic fluids, however, were affected by the superimposition of transversal vibration. The extent of flow enhancement in shear thinning fluids was found to vary with vibration

frequency and amplitude, flow behaviour index, flow consistency index and pressure gradient. For viscoplastic fluids, the extent of flow enhancement varied with the yield stress.

3.5.5.1. Effect of vibration frequency

The flow enhancement ratio for a shear-thinning power law fluid was computed for a range of vibration frequencies, f, up to 160 Hz. The other parameters were kept constant: A = 1.6 mm, n = 0.57 and k = 1.47 Pa s^n. These values were chosen to coincide with those used by Deshpande and Barigou (2001) so that a comparison of the effects of transversal and longitudinal vibrations can be made.

CFD results showed a positive increase in the flow rate of shear thinning fluids, with the flow enhancement ratio increasing with vibration frequency, as shown in Figure 3.40. Significant increases in flow rate can be obtained at frequencies higher than ~ 40 Hz under the conditions used here. The increase in the flow enhancement ratio with frequency, however, levels off at fairly high frequencies (f > ~ 140 Hz), suggesting that the scope of enhancing the flow rate of a shear thinning fluid by increasing the frequency is limited. This effect has also been observed for rotational vibration (see Section 3.5.2.1).

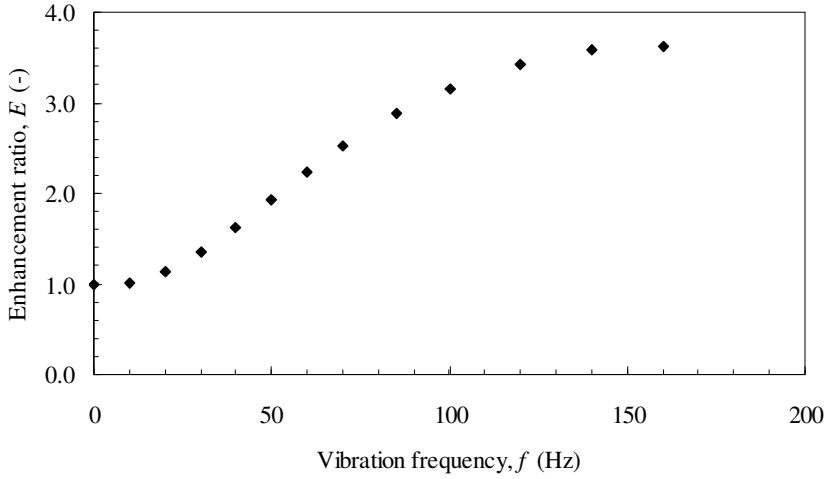

Figure 3.40: Effect of transversal vibration frequency on flow enhancement in a power law fluid:
k = 1.47 Pa s^n; n = 0.57; A = 1.6 mm; $\Delta p/L$ = 9.81 kPa m^{-1}.

3.5.5.2. Effect of vibration amplitude, A

The effect of A on the enhancement ratio is depicted in Figure 3.41 for f = 100 Hz. As expected, E increases with A over the range of values studied. At lower vibration frequencies, however, this increase in E with A becomes significantly less pronounced, as shown in Figure 3.42 where the effect of vibration amplitude on the value of E is plotted for f = 20 Hz.

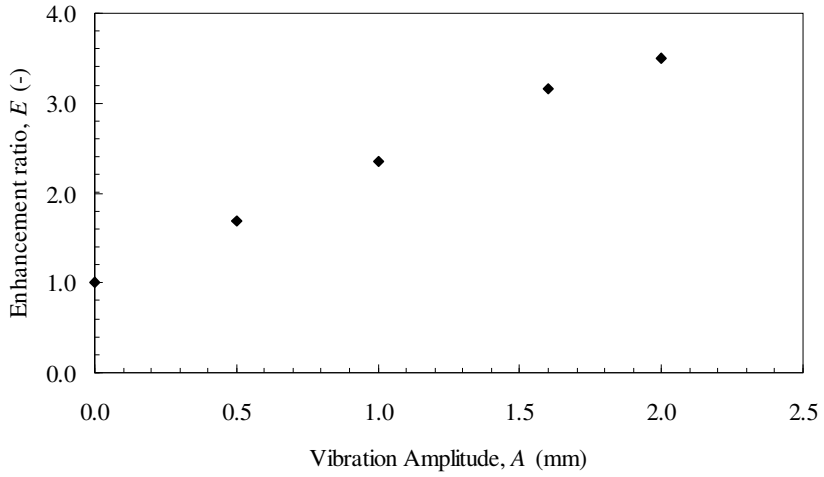

Figure 3.41: Effect of transversal vibration amplitude on flow enhancement in a power law fluid:
k = 1.47 Pa s^n; n = 0.57; f = 100 Hz; $\Delta p/L$ = 9.81 kPa m^{-1}.

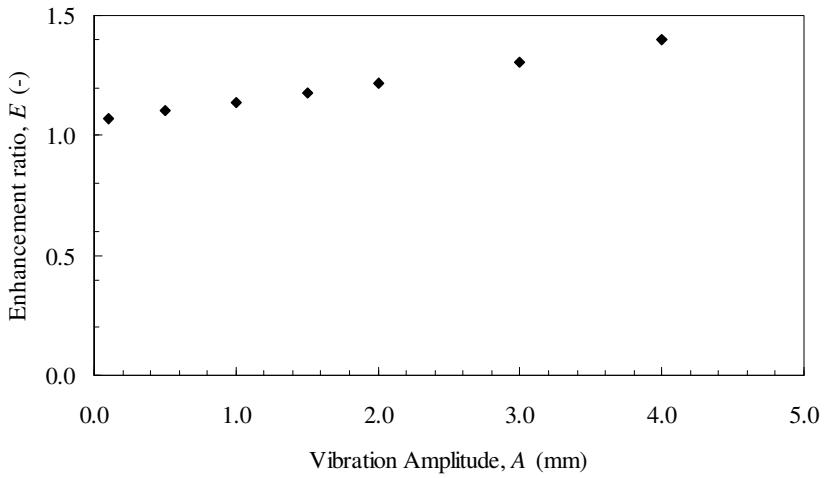

Figure 3.42: Effect of transversal vibration amplitude on flow enhancement in a power law fluid:
k = 1.47 Pa s^n; n = 0.57; f = 20 Hz; $\Delta p/L$ = 9.81 kPa m^{-1}.

It was also found that different frequency-amplitude combinations corresponding to the same peak acceleration $A\omega^2$ yield the same flow enhancement.

3.5.5.3. Effect of flow behaviour index, n

Figure 3.43 shows the effect of varying n on the flow enhancement ratio. For shear thinning fluids, the effect of transversal vibration diminishes as the shear thinning behaviour becomes less pronounced, with E decreasing as n is increased, reaching unity at n = 1, which corresponds to a Newtonian fluid with E = 1. For shear thickening fluids, E continues to decrease below 1 as n is increased above 1, thus, indicating that the superimposed transversal vibration leads to flow retardation.

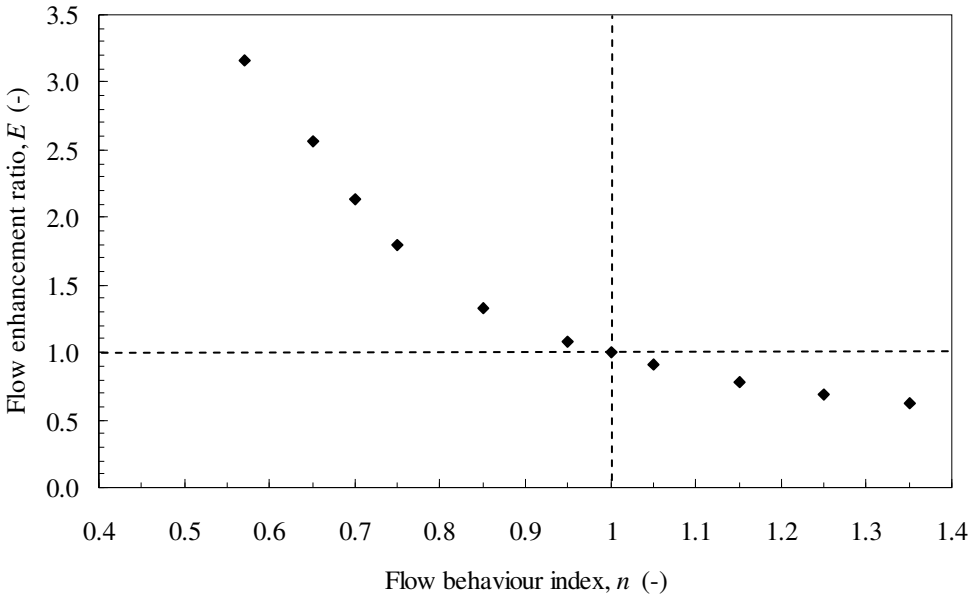

Figure 3.43: Effect of flow behaviour index on flow enhancement in a power law fluid:

k = 1.47 Pa s^n; f = 100 Hz; A = 1.6 mm; $\Delta p/L$ = 9.81 kPa m^{-1}.

3.5.5.4. Effect of fluid consistency index, k

Increasing the value of k led to an increase in E, as shown in Figure 3.44, indicating that vibration is more effective at enhancing the flow for more viscous fluids, but only up to a limit beyond which the curve levels off. This suggests that highly viscous

fluids require high vibration frequencies and amplitudes in order to obtain very large E values.

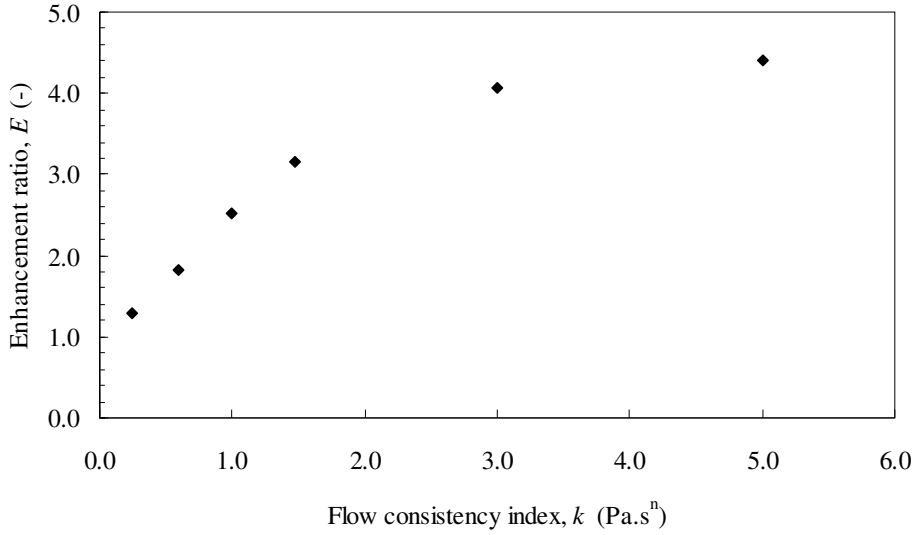

Figure 3.44: Effect of consistency index on flow enhancement in a power law fluid: $n = 0.57$; $f = 100$ Hz; $A = 1.6$ mm; $\Delta p/L = 9.81$ kPa m^{-1}.

3.5.5.5. Effect of pressure gradient, $\Delta p/L$

Figure 3.45 shows that E decreases with increasing pressure gradient. The potential for enhancing the flow is high when the pressure gradient, and hence the steady state flow rate, is low. Under high pressure gradients, the steady state flow is high, and the extra flow generated by vibrating the tube becomes comparatively insignificant.

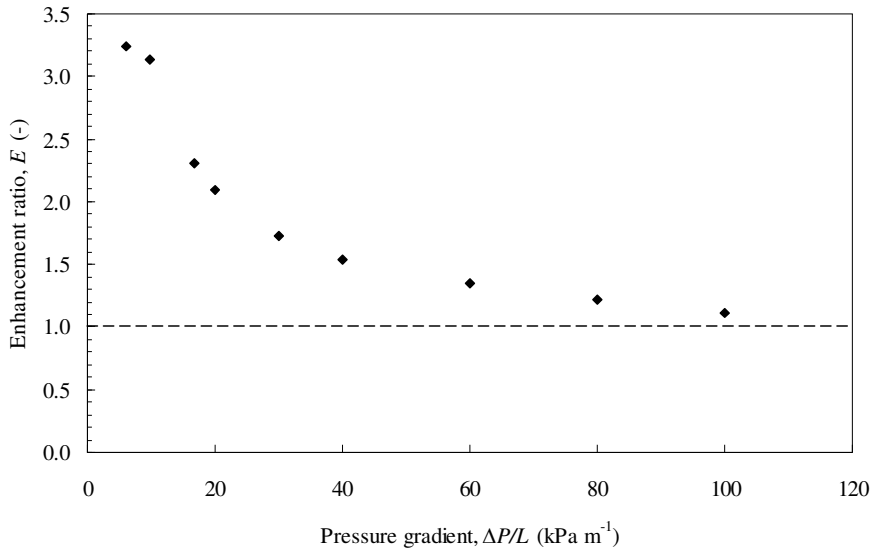

Figure 3.45: Effect of pressure gradient on flow enhancement in a power law fluid: k = 1.47 Pa s^n; n = 0.57; f = 100 Hz; A = 1.6 mm.

3.5.5.6. Effect of yield stress

The effect of increasing the yield stress on the flow enhancement of a Bingham plastic fluid was studied in the range 0-6 Pa, as shown in Figure 3.46. The flow enhancement ratio rises exponentially with the yield stress. As discussed in Section 3.5.3.1, it is possible to regard a Bingham plastic material as possessing a particular type of shear thinning which explains the enhancement in flow obtained.

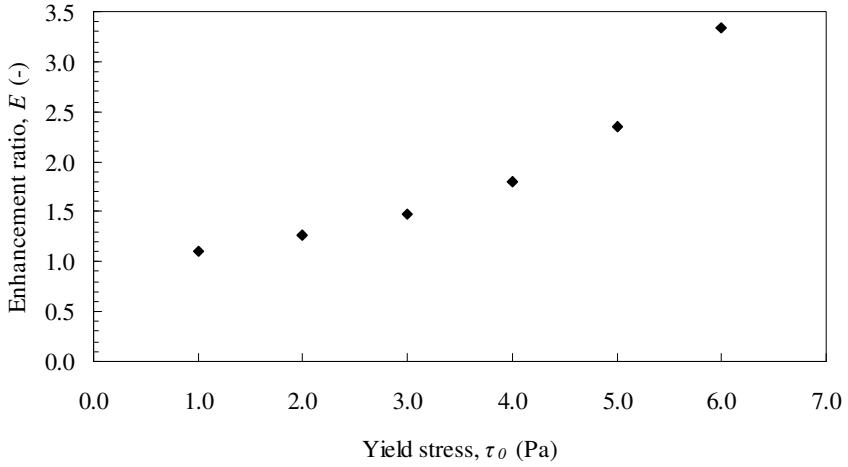

Figure 3.46: Effect of yield stress on flow enhancement in a Bingham plastic fluid: k = 1.0 Pa s^n; n = 0.57; f = 100 Hz; A = 1.6 mm; $\Delta p/L$ = 9.81 kPa m^{-1}.

3.5.6. COMPARISON OF DIFFERENT VIBRATION MODES

The flow enhancements obtained by superimposing a rotational, longitudinal, or transversal vibration were compared for a power law fluid with k = 1.47 Pa s^n and n = 0.57, and at a linear amplitude of 1.6 mm, frequency of 20 Hz, and pressure gradient $\Delta p/L$ = 9.81 kPa m^{-1}. The longitudinal vibration value of E under these conditions was obtained in the validation process (see Section 3.4.2). The enhancement obtained using longitudinal vibration was 1.68 compared to 1.22 for rotational vibration and 1.14 for transversal vibration. Although limited, these results suggest that longitudinal vibration is the most effective mode of vibration while transversal vibration is the least effective. Piau and Piau (2005) also found that longitudinal vibration can be more efficient than transversal vibration at enhancing the flow of viscoplastic materials in plane Couette flow.

Despite these differences in the extent of flow enhancement, it is clear from the results of this study and those of Deshpande and Barigou (2001) that all of the three modes of vibration produce substantial increases in flow rate. The choice of vibration mode for a given process is, therefore, largely a matter of convenience.

3.5.7. SECONDARY FLUID MOTION

In steady-state flow, the x- and y- components of velocity are effectively zero and flow occurs only in the axial direction. However, in addition to enhancing the flow of shear thinning fluids in the axial direction, rotational oscillation was found to induce a secondary fluid motion in the x direction (see Figure 3.47). The x-component of velocity was computed by CFD along the Y axis at a position near the pipe outlet and was found to vary significantly with time due to the periodic movement of the pipe wall. This secondary velocity profile was plotted at regular time intervals during one period of oscillation for a power law fluid with n = 0.57, k = 1.47 Pa s^n, f = 100 Hz, $A = \pi/10$, and $\Delta p/L$ = 9.81 kPa m^{-1}, in Figures 3.48-3.51.

The development of the x-velocity profile can be studied by dividing the oscillation period into four phases as the wall oscillates between three positions: C (Centre), R (Right), and L (Left), as shown in Figure 3.47. Starting from the central position C at the beginning of a new oscillation cycle, four phases can be identified:

(i) the pipe wall decelerates from a maximum velocity at C to reach zero velocity at R;
(ii) acceleration towards a maximum velocity at C;
(iii) deceleration towards zero velocity at position L; and
(iv) acceleration back to position C.

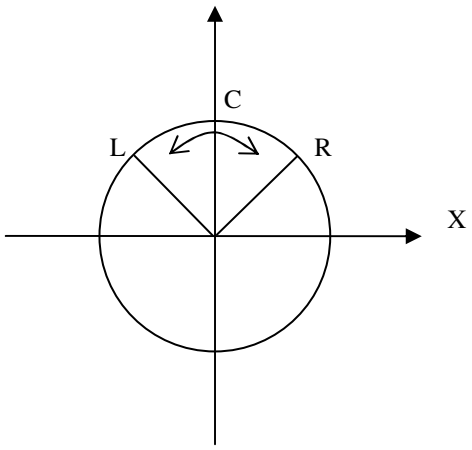

Figure 3.47: Pipe cross-section showing the angular positions of the wall during an oscillation period.

Phase (i):

In this phase, the clockwise motion of the wall decelerates from C to R. Figure 3.48 shows the development of the x-velocity profile during this phase. At position C, the wall velocity is at a maximum value attained at the end of the previous oscillation cycle (see Figure 3.51(d)), resulting in the fluid layer at the wall having a maximum x-velocity in the direction of the instantaneous wall movement. The magnitude of the x-velocity decreases from the wall towards the pipe centre reaching a region of zero velocity where no secondary movement is observed. As the pipe wall decelerates from C towards R, the x-velocity of the fluid at the wall decreases, but the velocity of the fluid in the core region increases in the direction of oscillation as the fluid in this

region is being sheared radially due to momentum transfer from the layers adjacent to the wall to this region. A time lag is therefore observed between the instantaneous motion of the wall and the secondary motion of the fluid near the pipe centre. As a result, a maximum velocity is reached at the boundary between the fluid layer adjacent to the wall ($r/R \sim 0.7$) and the bulk of the fluid when the wall comes to rest at position R, at which point the x-velocity of the fluid layer adjacent to the wall, having been decelerating, ultimately reaches zero, (Figure 3.48(d)).

Phase (ii):

The pipe wall begins to accelerate from rest at position R as it moves anti-clockwise towards C. The anti-clockwise velocity at the wall increases as the wall accelerates, while the clockwise velocity of the fluid in the core region, attained during phase (i), starts to decrease (Figure 3.49), being counteracted by the anti-clockwise momentum transferred from the pipe wall, and ultimately reaching zero when the wall velocity reaches its maximum value at C (Figure 3.49(d)).

Phase (iii)

The wall then starts to decelerate from its peak velocity at C as it continues its anti-clockwise movement towards position L. This deceleration leads to a reduction in the x-velocity of the fluid layer at the wall. The fluid in the core region, having reached a zero x-velocity at the end of phase (ii), reverses its direction of motion in the x direction and begins to follow the anti-clockwise motion of the pipe wall, as shown in Figure 3.50. At the end of this deceleration phase, the fluid layer at the wall comes to rest, while a velocity peak is observed at $r/R \sim 0.7$ (Figure 3.50(d)).

Phase (iv)

The wall starts a new acceleration phase moving clockwise from L towards C with increasing fluid velocity at the wall. The anti-clockwise x-velocity of the fluid in the core region, attained in phase (iii), then decreases, and is ultimately offset by the clockwise momentum transferred from the wall. The full phase is shown in Figure 3.51.

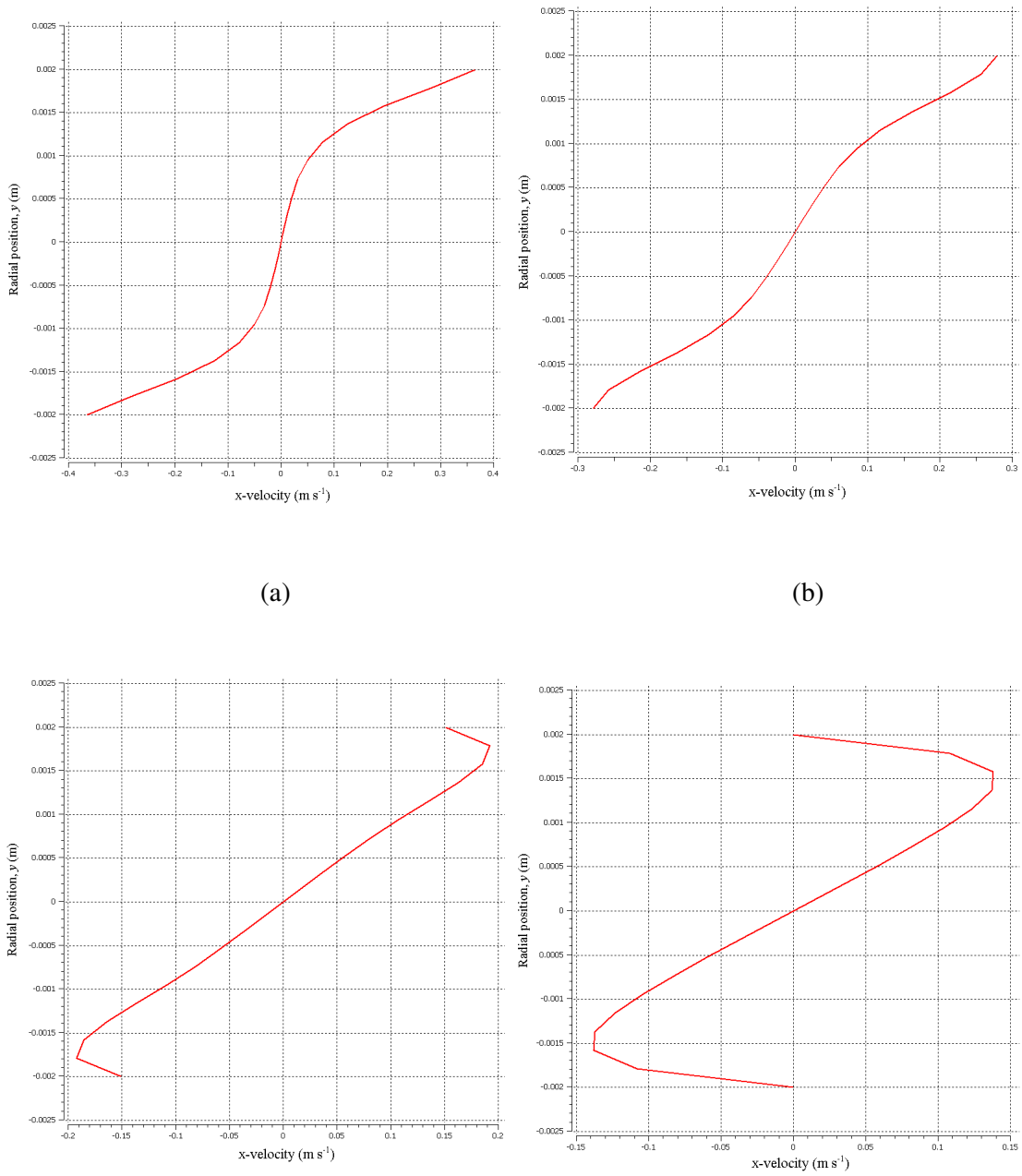

Figure 3.48: Development of x-velocity profile during phase (i) of the oscillation cycle at four equal time intervals.

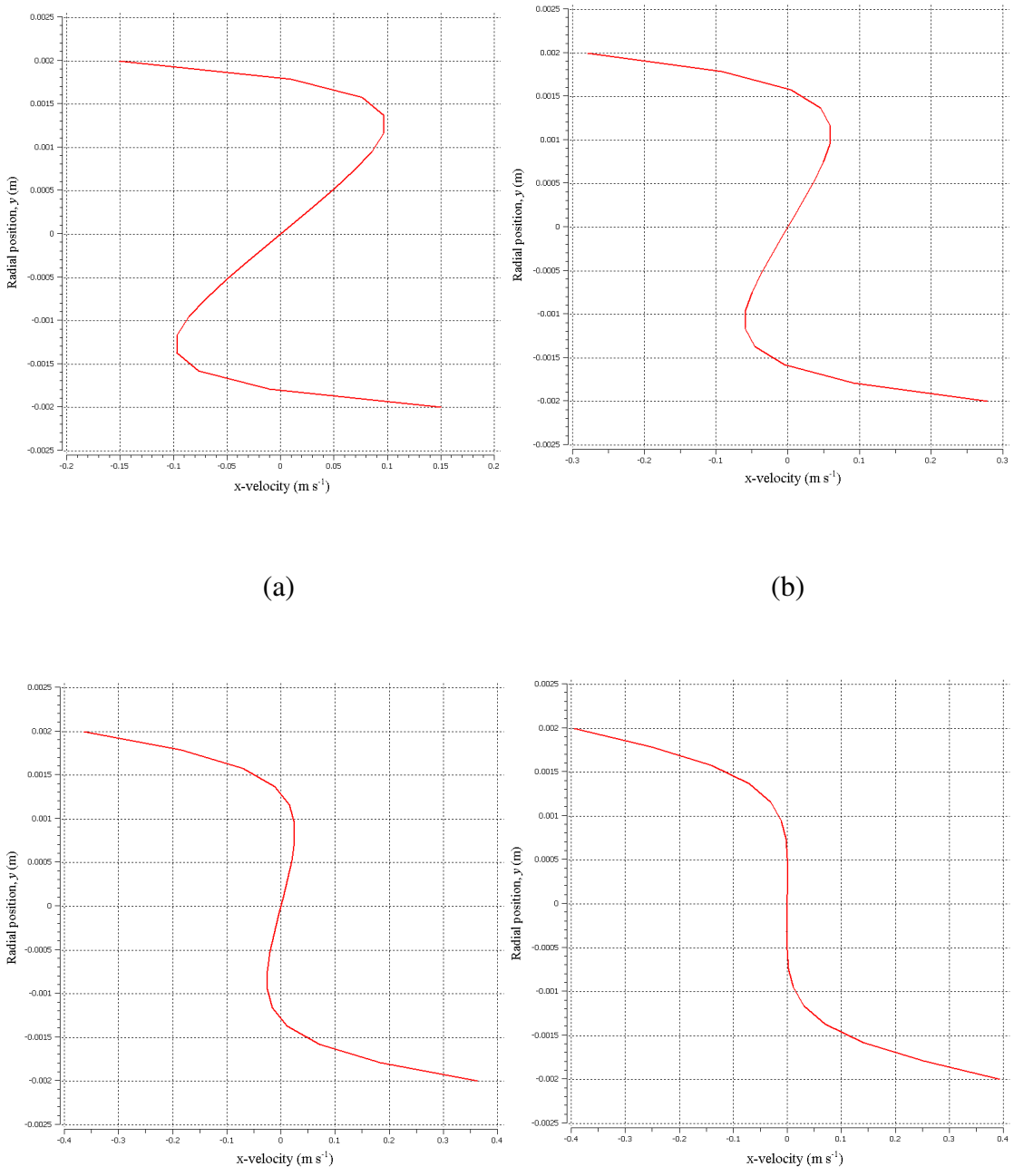

Figure 3.49: Development of x-velocity profile during phase (ii) of the oscillation cycle at four equal time intervals.

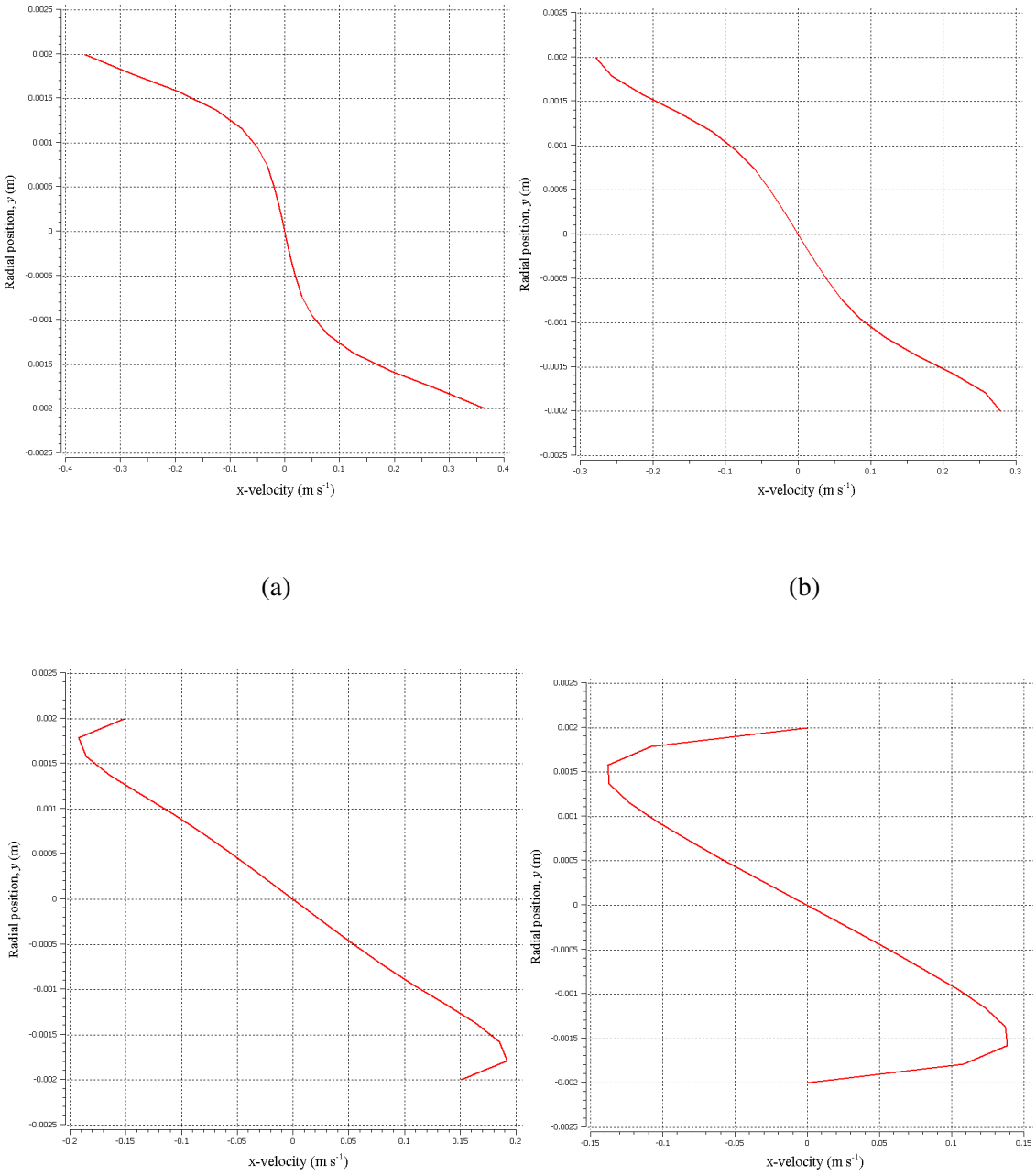

Figure 3.50: Development of x-velocity profile during phase (iii) of the oscillation cycle at four equal time intervals.

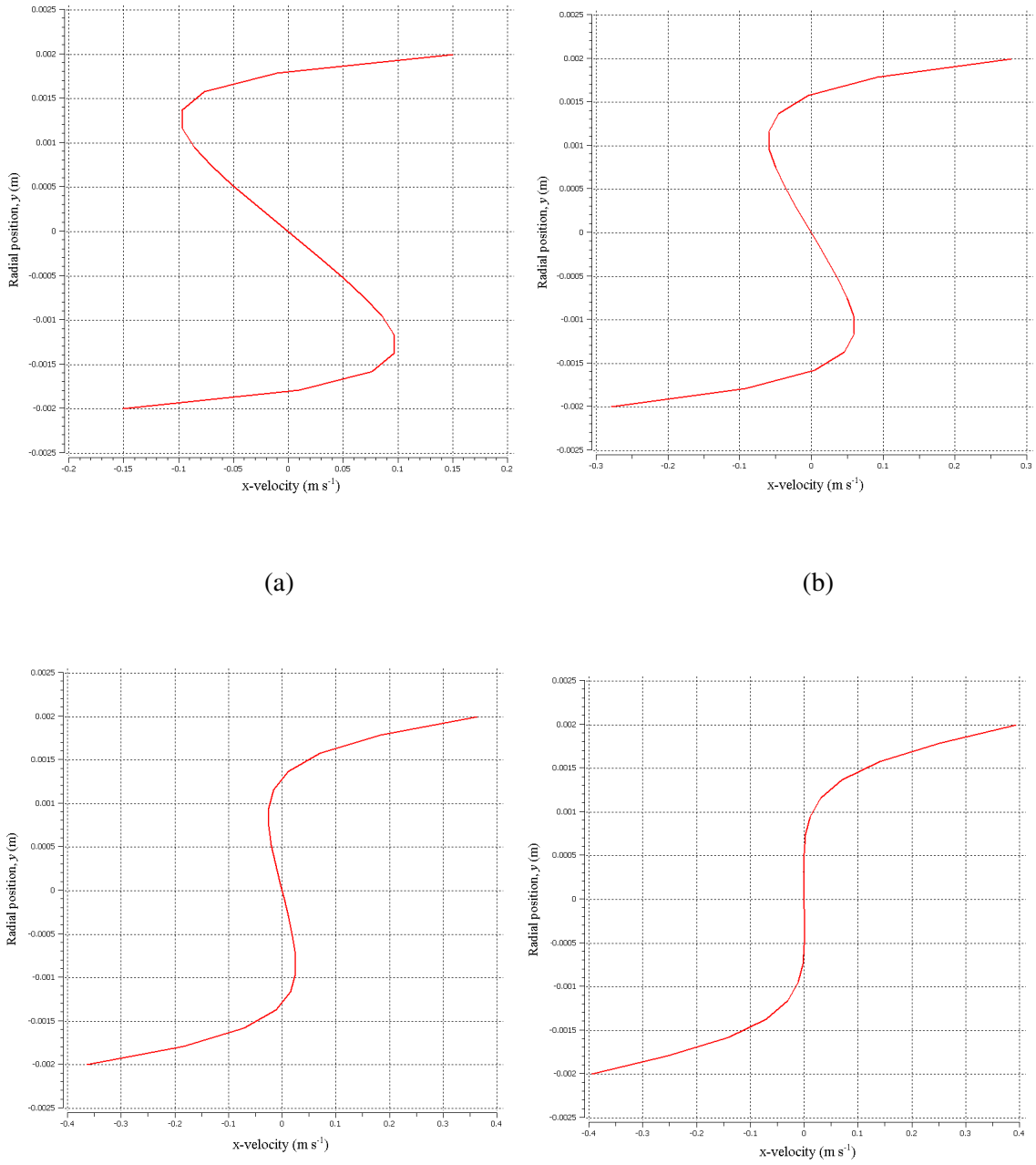

Figure 3.51: Development of x-velocity profile during phase (iv) of the oscillation cycle at four equal time intervals.

3.5.8. PARTICLE TRACKING

Particle tracking is a useful tool in CFX which allows the trajectories of fluid particles to be visualised. A simulation was executed wherein fluid particles were injected in the pipe and tracked in 3-D. The properties of the particles were identical to those of primary fluid so as to mimic its behaviour (see Section 3.3.4.3). Results, obtained using a power law fluid with n = 0.57, k = 1.47 Pa s^n, f = 100 Hz, $A = \pi/10$, and $\Delta p/L$ = 9.81 kPa m^{-1}, are presented here for two particles flowing at two different radial positions: near the pipe centre ($r/R \sim 0$) and away from the pipe centre ($r/R \sim 0.5$). The particle trajectories obtained are presented here as viewed from three different perspectives: X-Z and Y-Z plane views, and an isometric view along the pipe axis. The X-Z and Y-Z plane views show the variation of particle position along the X and Y axes, respectively.

3.5.8.1. Fluid motion near the pipe centre

The full isometric view of the trajectory of a fluid particle flowing near the pipe centre ($r/R \sim 0$) is shown in Figure 3.52(a). It can be clearly seen that the effect of wall oscillation is felt near the pipe centreline, resulting in the fluid particle oscillating angularly.

The X-Z plane view, presented in Figure 3.52(b), shows that the x-position of the particle oscillates periodically under the influence of rotation as the particle flows along the pipe. This clearly demonstrates that, although flow is laminar and the pipe Reynolds number is very small (< 1), rotational vibration induces a considerable degree of angular movement in the x direction. On the other hand, little movement was observed in the y direction, as shown in the Y-Z plane view presented in Figure 3.52(c).

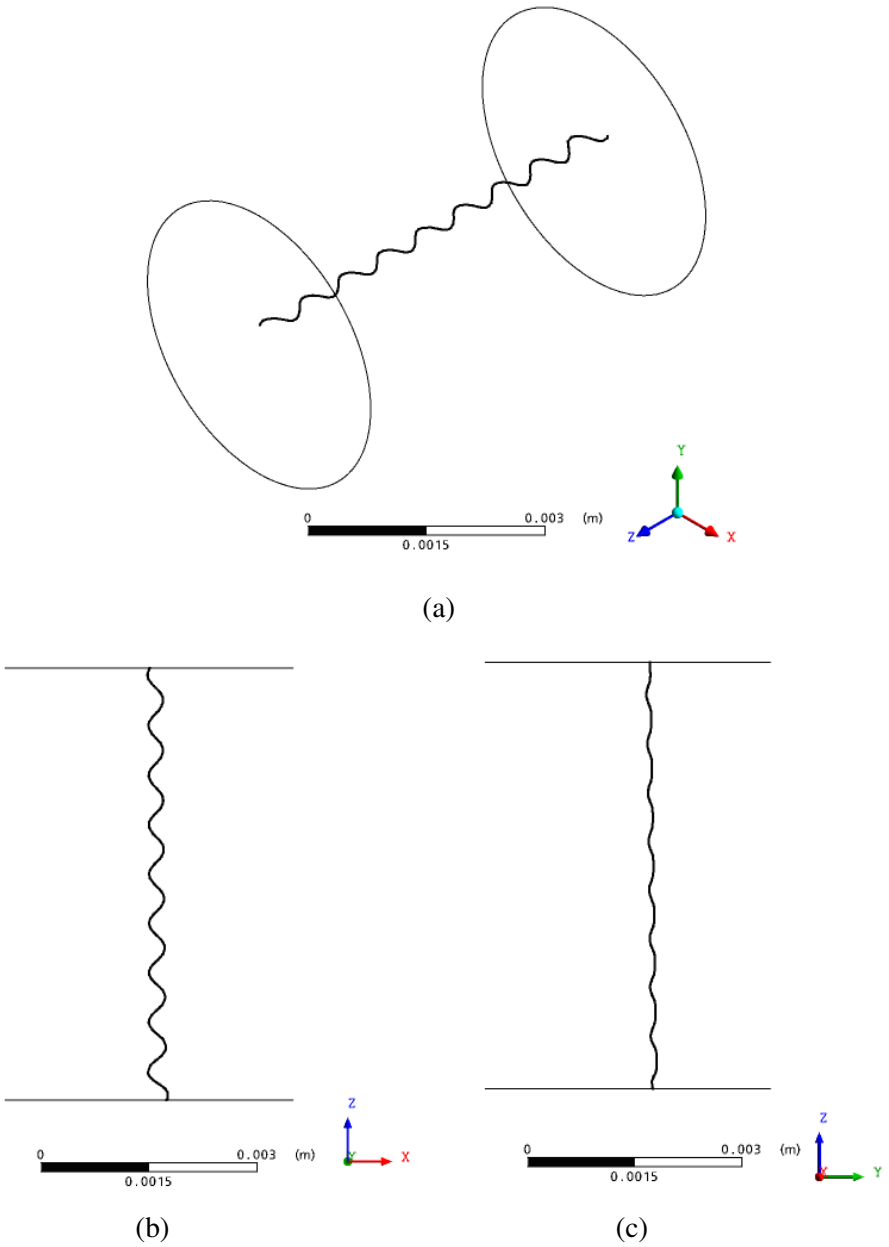

Figure 3.52: Views of the particle trajectory of a fluid particle travelling near the pipe centre under a superimposed rotational vibration: (a) isometric view; (b) X-Z plane view; (c) Y-Z plane view.

3.5.8.2. Away from the pipe centre

Figure 3.53(a) shows the full trajectory of a particle flowing at about half a radius from the wall. The effect of wall oscillation is evidently more pronounced here than for particles flowing close to the pipe centreline.

The X-Z plane view, depicted in Figure 3.53(b), shows that the fluid particle oscillates periodically along the X axis. This oscillation is accompanied by a slow shift in the axial motion of the particle towards the pipe wall. The angular movement is more evident in the Y-Z plane, as shown in Figure 3.53(c).

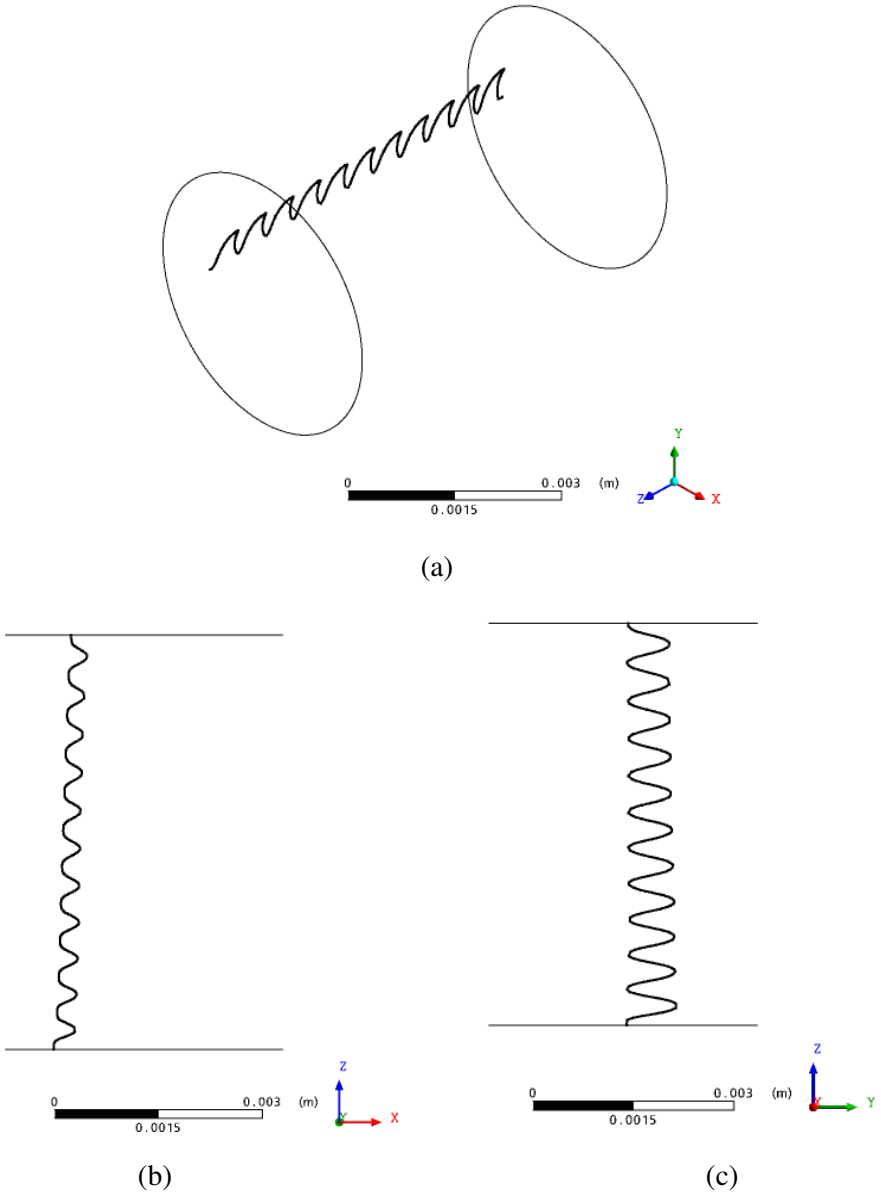

Figure 3.53: Views of the particle trajectory of a fluid particle travelling at *r/R* ~ 0.5 under a superimposed rotational vibration: (a) isometric view; (b) X-Z plane view; (c) Y-Z plane view.

Examining particle trajectories at various other radial positions confirmed that

(i) the amplitude of angular oscillation increases for particles flowing closer to the wall (i.e. as *r/R* increases); and

(ii) there is a general shift in the particle trajectories towards the pipe wall, this shift being most evident for particles flowing close to the wall (i.e. at high *r/R* values).

These observations are consistent with the results of the x-velocity profiles discussed above (Section 3.5.7), where it was shown that particles flowing near the pipe wall experience a greater variation in their x-velocity than those flowing closer to the pipe centreline.

3.6. CONCLUSIONS

A validated CFD model was used to investigate the effects of sinusoidal mechanical vibrations on the flow of non-Newtonian fluids in pipes. The results have shown that, while Newtonian fluids are not affected by the superimposition of vibration, non-Newtonian fluids undergo substantial changes. The superimposition of rotational oscillation was shown to have a large effect on the velocity profile, and hence flow rate, of shear thinning, shear thickening, and viscoplastic fluids. The changes in velocity profile and flow rate were attributed to changes in the apparent viscosity imparted by the additional applied shear. Vibration caused the velocity profiles of shear thinning and viscoplastic fluids to stretch in the flow direction, thus, increasing the total flow rate. The velocity profile of shear thickening fluids, on the other hand, was flattened under vibration due to the increase in viscosity caused by the added shear, thus, leading to flow retardation.

The extent of such effects was found to depend on vibration parameters, fluid rheological properties and pressure gradient. The enhancement ratio for a shear thinning fluid increased with vibration frequency and amplitude, but different combinations of frequency and amplitude corresponding to the same maximum acceleration gave the same enhancement. Increasing vibration frequency or amplitude resulted in elongated velocity profiles; however, the normalised velocity profile was only slightly affected, thus, indicating that vibration does not alter the flow characteristics significantly under the vibration and flow conditions used. Although flow enhancement ratios as high as 5 for power law fluids and 12 for Herschel-Bulkley fluids were achieved using sonic frequencies, it was found that the increase in enhancement ratio with vibration frequency reaches a limit beyond which no further enhancement is achieved. The effect of increasing vibration frequency, therefore, decreases at high frequencies.

The enhancement ratio was also sensitive to the flow behaviour index, consistency index, and yield stress. The more pronounced the non-Newtonian behaviour of the fluid, the stronger the effect of vibration on its flow. For shear thinning fluids, the

flow enhancement ratio increased as the flow behaviour index was reduced, i.e. as the shear thinning increased, due to the increased dependence of the viscosity on shear. The velocity profile underwent considerable elongation under vibration compared with the steady-state velocity profile for all flow behaviour index values considered (0.57-1.40). The normalised velocity profile was slightly flattened compared with the normalised profile under steady state. For shear thickening fluids, the flow enhancement ratio decreased below unity as the flow behaviour index was increased, due to the increased shear thickening. Increases in the flow consistency index for a shear thinning fluid gave rise to elongated velocity profiles which translated into significant flow enhancement ratios. For viscoplastic fluids, the flow enhancement ratio increased exponentially with the yield stress. This enhancement was most pronounced when shear thinning and yield stress effects were coupled (i.e. for Herschel-Bulkley fluids).

Increases in pressure gradient, and hence steady-state flow rate, led to reduced flow enhancements. The potential for flow enhancement, it can be concluded, diminishes with increasing steady-state flow rate.

Mechanical vibration with frequencies on the sonic scale produced substantial enhancements in the flow of low to moderately viscous fluids, but had limited scope for enhancing the flow of highly viscous fluids. Ultrasonic vibration, however, was very effective at enhancing the flow of extremely viscous materials, leading sometimes to two orders of magnitude increases in flow rate for extremely viscous Herschel-Bulkley fluids, thus, offering a great potential for the processing of such complex materials.

Different vibration modes resulted in different degrees of flow enhancement. Under identical conditions, sinusoidal pipe oscillations in the direction of flow produced flow enhancements which were greater than those generated by rotational oscillations, which, in turn, were greater than those produced by transversal oscillations in a direction normal to the flow. Nonetheless, the three modes of oscillation yielded substantial enhancements in flow.

In addition to enhancing the axial flow of shear thinning fluids, rotational oscillation was found to induce a degree of angular secondary motion in the fluid. Instantaneous profiles of the x-component of velocity showed considerable changes in x-velocity, especially near the pipe wall, during a full oscillation period. Particle trajectories showed that fluid particles flowing close to the oscillating wall experience angular oscillations, the amplitude of which increases as the distance from the wall decreases. Moreover, a slight net radial motion towards the pipe wall was observed in the trajectories, particularly for particles flowing close to the wall.

The results presented suggest that the fluidity of many industrial fluids, the rheological behaviour of which is usually non-Newtonian, can be enhanced and their flow rate increased by means of mechanical oscillation applied to the pipe wall. Alternatively, under a given flow rate, the pressure drop required to maintain the flow can be reduced substantially.

The effects of vibration on flow rate have thus been demonstrated. Further research is still required to investigate other potential benefits of mechanical vibration, such as enhancement of heat or mass transfer. In Chapter 4, the effects of transversal vibration on the heat transfer and temperature uniformity in Newtonian and non-Newtonian fluids are investigated.

NOMENCLATURE

A	linear amplitude, m
D	tube diameter, m
E	enhancement ratio, dimensionless
f	vibration frequency, Hz
g	gravitational acceleration, m s^{-2}
k	fluid consistency index, Pa s^n
L	tube length, m
L_h	hydrodynamic entrance length, m
n	flow behaviour index, dimensionless
p	fluid pressure, Pa
Δp	pressure drop, Pa
Q	steady-state volumetric flowrate, m^3 s^{-1}
Q_v	volumetric flowrate under vibration, m^3 s^{-1}
$Q(t)$	instantaneous volumetric flowrate, m^3 s^{-1}
r	radialposition, m
R	tube radius, m
Re	Reynolds number, dimensionless
Re_v	vibrational Reynolds number, dimensionless
t	time, s
t_f	simulation end time, s
u	fluid velocity, m s^{-1}
$\bar{u}$	mean fluid velocity, m s^{-1}
v_θ	angular velocity, rad s^{-1}
x	displacement along the X axis
z	displacement along the Z axis (direction of flow)

Subscripts

r	component in r direction
x	component in x direction
z	component in z direction
v	vibrational

Greek letters

$\dot{\gamma}$	shear rate, s^{-1}
μ	viscosity, Pa s
μ_B	plastic viscosity, Pa s
μ_{eff}	effective viscosity, Pa s
μ_0	zero shear viscosity, Pa s
μ_∞	infinite shear viscosity, Pa s
ρ	fluid density, kg m^{-3}
τ	shear stress, Pa
τ_w	wall shear stress, Pa

τ_0 yield stress, Pa
θ angle of rotation, rad
Θ vibration amplitude, rad
υ kinematic viscosity, $m^2\ s^{-1}$
ϕ ratio of yield stress to wall shear stress, dimensionless
ω angular frequency, s^{-1}

REFERENCES

Barigou, M., Morey, M.D. & Beckett, S.T. 1998. Chocolate: the shaking truth, *International Food Ingredients*, 4, 16-18.

Barnes, H.A., Townsend, P. & Walters, K. 1971. On pulsatile flow of non-Newtonian liquids. *Rheologica Acta*, 10, 517-527.

Benhamou, B., Laneville, A. & Galanis, N. 2004. Transition to turbulence: The case of a pipe in radial oscillation. *International Journal of Thermal Sciences,* 43, 1141-1151.

Benhamou, B., Galanis, N. & Laneville, A. 2001. Transient effects of orthogonal pipe oscillations on laminar developing incompressible flow. *International Journal for Numerical Methods in Fluids*, 34, 561-584.

Borghesani, A. F. 1988. Non-Newtonian flow behaviour of coal-fuel oil suspensions. In: N. P. Cheremisinoff (Ed.), Encyclopedia of Fluid Mechanics, Rheology and Non-Newtonian Flows, Vol. 7, 89 – 134. Houston, Gulf publishing company.

Carreau, P.J. 1972. Rheological equations from molecular network theories. *Trans. Soc. Rheol.*, 16, 99-127.

Chhabra, R.P. & Richardson, J.F. 1999. Non-Newtonian flow in the process industries: Fundamentals and engineering applications. Butterworth Heinemann.

Deshpande, N.S. & Barigou, M. 2001. Vibrational flow of non-Newtonian fluids, *Chemical Engineering Science*, 56, 3845-3853.

Elkholy, A.H. 1997. Sinusoidal excitation of viscous fluids in pipes. *Int. J. Pres. Ves. & Piping*, 70, 161-165.

Holdsworth, S.D. 1993. Rheological models used for the prediction of the flow properties of food products: a literature review. *Trans IChemE*, 71, Part C, 139-179.

Isayev, A.I. Wong, C.M. & Zeng, X. 1990. Flow of thermoplastics in an annular die under orthogonal oscillations. *Journal of Non-Newtonian Fluid Mechanics*, 34, 375-397.

Kasakia, V.Y. & Rivlin, R.S. 1979. The influence of vibration on Poiseuille flow of a non-Newtonian fluid II. *Rheol. Acta*, 18, 244.

Kasakia, V.Y. & Rivlin, R.S. 1978. The influence of vibration on Poiseuille flow of a non-Newtonian fluid I. *Rheol. Acta,* 17, 210.

Lee, B.-L. & Cranston, C. 1988. Shear processing thermoplastics in the presence of ultrasonic vibration. European patent 0 303 998 A1.

Mena, B., Manero, O. & Binding, D.M. 1979. Complex flow of viscoelastic fluids through oscillating pipes – Interesting effects and applications. *Journal of Non-Newtonian Fluid Mechanics*, 5, 427-448.

Phan-Thien, N. & Dudek, J. 1982. Pulsating flow revisited. *Journal of Non-Newtonian Fluid Mechanics*, 11, 147-161.

Piau, M. & Piau, J.M. 2007. Wall vibrations and yield stress–shear thinning coupling (small vibrational inertia). *Journal of Non-Newtonian Fluid Mechanics*, 144, 59-72.

Piau, M. & Piau, J.M. 2005. Plane Couette flow of viscoplastic materials along a slippery vibrating wall. *Journal of Non-Newtonian Fluid Mechanics*, 125, 71–85.

Piau, J.M. & Piau, M. 2002. Easier flow of viscoplastic materials with ultrasonic longitudinal wall motion. *Journal of Non-Newtonian Fluid Mechanics*, 104, 185-226.

Rohsenow, W.M., Hartnett, J.P. & Cho, Y.I. 1998. Handbook of heat transfer. McGraw-Hill Professional.

Shaw, C.T. 1992. Using computational fluid dynamics. Prentice Hall International (UK) Ltd.

Shin, S., Ku, Y., Suh, J.S., Moon, S.Y. & Jang, J.Y. 2003. Characteristics of blood flow resistance under transverse vibration: red blood cell suspension in Dextran-40, *Ann. Biomed. Eng.*, 31 (9), 1077-83.

Shook, C.A. & Roco, M.C. 1991. Slurry flow: principles and practice. Butterworth-Heimemann.

Steffe, J.F. 1992. Rheological methods in food process engineering. Freeman Press, Michigan.

Sundstrom, D.W. & Kaufman, A. 1977. Pulsating flow of polymer solutions. *Industrial Engineering Chemistry Process Design and Development*, 16, 320-325.

Wu, H., Guo, S.Y., Chen, G.S., Lin, J., Chen, W. & Wang, H.T. 2003. Ultrasonic Oscillations effect on rheological and processing properties of mettallocene-catalyzed linear low density polyethylene. *Journal of Applied Polymer Science*, 90 (7), 1873-1878.

CHAPTER 4

EFFECTS OF FORCED VIBRATION ON HEAT TRANSFER IN LAMINAR FLOW

Summary

Radial heat transfer in laminar pipe flow is limited to slow thermal conduction which results in a wide temperature distribution over the pipe cross-section. This is undesirable in many industrial processes as it leads to an uneven distribution of fluid heat treatment. Often the fluids involved are relatively viscous and processing them under turbulent conditions is impractical and uneconomical. On the other hand, the use of static in-line mixers to promote radial mixing may be prohibited in hygienic processes because they are difficult to keep clean. A validated CFD model is used in this study to show that the imposition of a transversal vibration motion on a steady laminar flow generates sufficient chaotic fluid motion which leads to considerable radial mixing. This results in a large enhancement in wall heat transfer as well as a near-uniform radial temperature field. Vibration also causes the temperature profile to develop very rapidly in the axial direction reducing the thermal entrance length by a large factor, so that much shorter pipes can be used to achieve a desired temperature at the outlet. These effects are quantitatively demonstrated for Newtonian and non-Newtonian pseudoplastic fluids at different vibration amplitudes and frequencies.

4.1. LITERATURE REVIEW

Laminar flow conditions of Newtonian and non-Newtonian fluids with heat transfer prevail in a number of industrial operations such as the processing of polymer melts, pharmaceutical formulations, and foodstuffs where the fluids to be heated (or cooled) are often viscous and temperature dependent. Such conditions can give rise to a largely uneven thermal treatment of the product reflected in a wide temperature distribution which may lead to undesirable effects on the product quality.

4.1.1. HEAT TRANSFER IN THERMAL STERILISATION

Sterilisation is a complex and important operation in the food processing industry. Its purpose is to destroy any viable microorganisms capable of causing food poisoning or deterioration. A number of methods can be used to achieve product sterility including thermal heating, irradiation, exposure to ultrasonic waves, and exposure to chemical agents. Among these methods, thermal sterilisation is the most widely adopted technique due to its economy and reliability (Lin, 1976).

Thermal sterilisation is achieved in three stages (Jung and Fryer, 1999):

(i) heating the product to a temperature sufficiently high to achieve microbial inactivation,
(ii) holding the product at this temperature for a time sufficient to ensure that the required level of sterility has been achieved, and
(iii) cooling the product.

The choice of temperature/time combination is crucial. For the adequate destruction of the spores of pathogenic microorganisms, temperatures of 110-130°C are normally required for times which depend on the nature of the food product (Holdsworth, 2004). Increasing the process temperature reduces the time required to achieve sterility. One of the most heat resistant pathogenic microorganisms is *Clostridium botulinum*, and its destruction is therefore the general requirement of thermal

sterilisation of food products (Lin, 1976). Any less resistant microorganism will thereby be inactivated. *Clostridium botulinum* can be inactivated by holding the product at a temperature of 121°C for 3 minutes (Holdsworth, 2004); lowering the temperature increases the time needed.

Thermal sterilisation can be carried out in batch or continuous mode. Although conventional batch processing yields a safe product, it can also result in quality losses since the time required for heat to reach the centre of the product is usually long, thus causing parts of the product to be overheated. Product quality losses include nutrient denaturisation, flavour changes, and structure and texture changes (Holdsworth, 2004). Lin (1976) showed that at temperatures higher than 115°C, bacterial inactivation of *Clostridium botulinum* is more rapid than the rate of denaturisation of vitamin B_1. This fact accounts for the wide application of high-temperature-short-time (HTST) continuous processing, which achieves the required level of sterility in a short time, thus reducing quality losses. This is achieved by means of flow and high sterilisation temperatures. Continuous processing is carried out in devices such as plate heat exchangers or pipes.

In HTST continuous sterilisation, the laminar pipe flow of liquid foods of relatively high viscosities results in a wide distribution of velocity over the pipe cross-section, thus leading to a wide residence time distribution. The fluid near the pipe centre travels at velocities significantly higher than the mean flow velocity, while the fluid flowing near the pipe wall moves at much lower velocities. This, in turn, translates into a significant radial temperature distribution, which results in a wide variation of product sterility and nutritional quality across the pipe. The optimisation of such thermal processes poses a challenging manufacturing problem. The overriding importance of safety often results in the food being exposed to a more severe process than is desirable from a quality aspect, resulting in poor sensory and nutritional attributes, especially with sensitive products. To ensure product safety, the velocity distribution must be taken into account when choosing the length of the holding tube so that all of the fluid is subjected to the required temperature for a sufficient length of time. It is common practice in the food processing industry to assume laminar

Newtonian flow and design the length of the holding tube based on twice the mean velocity (Lareo *et al.*, 1997). Although this ensures sterility of the whole product, it causes overexposure of the slow-moving parts resulting in a significant deterioration in product quality. However, without confidence in the design data, processes will always be overdesigned for safety.

This issue has been addressed in a limited number of studies (e.g. Jung and Fryer, 1999; Liao *et al.*, 2000). Jung and Fryer (1999) used a finite-element Computational Fluid Dynamics (CFD) model to simulate the HTST processing of Newtonian and non-Newtonian power-law food fluids in circular pipes with a uniform wall temperature. Pipe diameters of 3 and 4 cm were used with a maximum pipe length of 12 m for each of the heating, holding, and cooling pipes. The CFD-computed velocity and temperature profiles were validated using available analytical solutions. Simulation results together with conventional food processing sterility and quality kinetics were used to study the efficiency of HTST sterilisation processes. In particular, the study aimed to investigate the validity of the Newtonian flow assumption. The model adopted in the study accounted for the temperature dependence of viscosity since temperature has a significant effect on the viscosity of most liquid foods. Sterility and quality were quantified using defined functions.

It was observed that, under some conditions, the temperature gradients within the flow system were such that the fluid in near-wall regions was over-processed. Designing the holding tube based on twice the average flow velocity led to a safe product but at the expense of a significant degradation in product quality. For the Newtonian fluid used and at a wall temperature of 140°C, the mean fluid temperature at the exit of the heating section reached 106°C, with the temperature of the wall region at 131°C while that at the pipe centre did not exceed 83°C. In the holding section, however, the temperature at the centre reached 105°C. These wide variations of temperature within the fluid demonstrate the problem of processing viscous fluids. Using the mean values of velocity and temperature in estimating the sterility and quality values was shown to lead to overestimation. Accurate calculation of temperature profiles is therefore essential in predicting the output conditions.

For the temperature-dependent power-law fluid, the high temperatures near the pipe wall caused a reduction in viscosity which, in turn, resulted in an increase in the fluid velocity in this region, thus reducing the residence time. Since losses in quality are more significant near the wall, the increase in fluid velocity in this region will lead to a better quality compared to a fluid with a temperature-independent viscosity.

The authors also investigated the relationship between the heater wall temperature and the holding tube length. For each heater wall temperature, the holding tube length required to achieve a certain level of sterility was calculated. At low wall temperatures, the holding tube length was large and the fluid residence time was correspondingly long. Increasing the heater wall temperature resulted in a reduction in the tube length required, thus reducing the residence time of the fluid and achieving the high-temperature-short-time condition. However, increasing the wall temperature may lead to product overcooking in the wall region. Shortening the holding tube in this case does not solve the problem since most of the damage to the product takes place in the heating tube. In short, the holding tube length is determined by the requirement of achieving sterility at the pipe centre, but this will result in excessive processing in the wall region.

Liao *et al*. (2000) used a CFD model to investigate the thermo-rheological behaviour of a starch dispersion in a continuous sterilisation process at a constant wall temperature. Simulations were conducted for pipe diameters of 1.8 and 2.4 cm, wall temperatures of 139 and 145°C, and flow rates of 1.0 and 1.5 L/min. A power-law equation combined with the Arrhenius equation for the temperature dependence of viscosity was used to describe the rheology of the gelatinised starch dispersion. Velocity and temperature profiles, as well as bacterial lethality and nutrient retention in the axial direction were obtained. Results showed that nutrient retention increased by reducing the pipe diameter and was almost unaffected by reductions of wall temperature or flow rate. Increasing the flow rate, however, required a longer pipe to achieve sterility.

These studies demonstrated that validated CFD models are useful tools for investigating such systems. Both studies confirmed the wide radial variation in temperature. However, whilst such studies have served to highlight the importance of the problem posed by a non-uniform temperature profile in viscous flow, effective technological solutions to this problem are still missing.

4.1.2. ENHANCEMENT OF TEMPERATURE DISTRIBUTION AND HEAT TRANSFER

It is evident from the above discussion that in order to minimise the loss in product quality caused by the presence of a wide temperature distribution, it is necessary to enhance the transfer of heat to the inner parts of the fluid so that all parts of the fluid are treated under substantially uniform conditions. In addition, since the rheological properties of most liquids are dependent on temperature, the radial temperature gradients in the pipe may lead to significant variations in the rheological properties of the fluid leading to a distorted velocity profile, which in turn alters the temperature distribution. A more uniform temperature profile, however, would reduce such variations in the rheological properties, thus making the flow behaviour of the fluid more predictable. Therefore, methods of increasing radial mixing must be sought in order to improve the temperature uniformity in such flows.

Radial mixing can be achieved by turbulent flow conditions. However, the fluids in question are usually of such high viscosities that processing them under turbulent conditions is impractical and may not be very economical (Simpson and Williams, 1974). Alternatively, radial mixing can be achieved by inserting static mixers but their intricate geometries make them difficult to clean, and where hygiene is of the essence as in food and pharmaceutical production, the risk of contamination precludes the use of such devices.

In Chapter 3, it has been shown that mechanical vibration has a significant effect on the flow of non-Newtonian fluids. The application of mechanical vibration as a means of enhancing heat transfer has also been investigated in a limited number of

studies (Sastry *et al*., 1989; Klaczak, 1997; Lee and Chang, 2003). Lee and Chang (2003) conducted an experimental investigation of the effects of transverse tube vibration on critical heat flux (CHF). Vibration was imposed on a heated tube 8 mm in diameter. Frequencies of 0-70 Hz and amplitudes of 0.1-1.0 mm were used, and heat flux was measured under different vibration conditions and mass flow rates. It was found that vibration gives rise to enhanced critical heat flux. This enhancement was calculated as the ratio of the heat flux under vibration to that measured in the absence of vibration. The authors attributed this enhancement to turbulent mixing induced by vibration. Results showed that heat flux increases with vibration Reynolds number, which represents the combined effect of vibration frequency and amplitude. Moreover, CHF enhancement was found to be more dependent on vibration amplitude than on frequency.

While highlighting the general effects of vibration on heat transfer, such studies, however, made no attempt to investigate the effects of vibration on the radial temperature distribution in viscous liquids undergoing thermal processing in pipes. Moreover, results in this area are not always consistent, probably due to the narrow ranges of vibration conditions used or the different geometries studied. There is evidently a severe lack of information on the effects of vibration on the radial temperature distribution in such systems.

In the current study, a CFD model is used to investigate the use of forced mechanical vibration as a means of enhancing the heat transfer characteristics and, in particular, the radial temperature distribution in the laminar flow of Newtonian and inelastic non-Newtonian fluids in a pipe with a constant wall temperature. The effects are demonstrated for a range of vibration conditions and rheological properties. Account is taken of the temperature-dependence of the viscosity of all the fluids used.

4.2. THEORY

4.2.1. FLUID RHEOLOGY AND VELOCITY PROFILES

The fluids considered in this study were Newtonian or inelastic non-Newtonian pseudoplastic (or shear thinning) of the power law type. A Newtonian fluid is characterised by a constant shear-independent viscosity. The fully developed laminar velocity profile of a Newtonian fluid in a circular pipe of radius *R*, is given by the parabolic function

$$u(r) = 2\overline{u}\left[1-\left(\frac{r}{R}\right)^2\right] \tag{4.1}$$

where *r* is radial position and $\overline{u}$ is the mean velocity of flow.

For a non-Newtonian power law fluid, the constitutive equation is

$$\tau = k\dot{\gamma}^n \tag{4.2}$$

where τ is shear stress, *k* is the fluid consistency index, $\dot{\gamma}$ is shear rate, and *n* is the flow behaviour index. The apparent viscosity function, η, is then given by

$$\eta = k\dot{\gamma}^{n-1} \tag{4.3}$$

The fully developed laminar velocity profile for a power law fluid is given by the expression (Chhabra and Richardson, 1999)

$$u(r) = \overline{u}\left(\frac{3n+1}{n+1}\right)\left[1-\left(\frac{r}{R}\right)^{\frac{n+1}{n}}\right] \tag{4.4}$$

4.2.2. INFLUENCE OF TEMPERATURE ON VISCOSITY

Heat transfer characteristics can be influenced by the variation of the fluid physical properties with temperature. For liquids, only the temperature-dependence of viscosity is of major importance (Kreith and Bohn, 1986). The influence of temperature on the viscosity, μ, of a Newtonian fluid is usually expressed by an Arrhenius type equation (Steffe, 1996), thus

$$\mu = k_0 \exp\left(\frac{E_a}{R_G T}\right) \tag{4.5}$$

where T is temperature, E_a is the activation energy for viscosity, R_G is the gas constant, and k_0 is a pre-exponential factor. The constants k_0 and E_a are determined experimentally and their values for various fluids can be found in the literature (e.g. Steffe, 1996). The higher the value of E_a, the more rapid the change in viscosity with temperature.

For a non-Newtonian fluid of the power law type subjected to temperature and shear gradients, Christiansen and Craig (1962) combined the Arrhenius model (Equation (4.5)) with the power law rheological model (Equation (4.2)) to obtain the following equation, which is widely used to describe the variation with temperature of the consistency index, k:

$$k = k_0 \exp\left(\frac{E_a}{R_G T}\right)^n \tag{4.6}$$

The variation of the flow behaviour index, n, with temperature is usually small and can therefore be neglected (Steffe, 1996). It is noteworthy that the variation of the consistency index, k, with temperature at a constant shear rate is given by the Newtonian form, i.e. Equation (4.5) (Rao *et al*., 2005).

Kwant *et al*. (1973(a)) developed another exponential relationship that describes the temperature variation of the consistency index, k, of power law fluids, thus

$$k = k' \exp\left[-b\left(T - T'\right)\right] \tag{4.7}$$

where k' is the consistency index at a reference temperature T', and b is a viscosity variation parameter. The deviation from isoviscous (i.e. temperature-independent viscosity) behaviour is given by the quantity Q, defined as

$$Q \equiv b\left(T_w - T_{in}\right) \tag{4.8}$$

where T_w and T_{in} are the wall and inlet temperatures, respectively. This model was found to give predictions which were in close agreement with those yielded by Equation (4.6) (Kwant *et al*., 1973(a)).

4.2.3. TEMPERATURE PROFILE

Consider the case of steady-state laminar flow in a circular pipe with heat transfer. There are no closed form solutions to this problem that take account of the temperature dependence of the fluid properties including viscosity. In the following, the fluid properties including viscosity are all assumed to be independent of temperature. At the inlet to the pipe, the fluid temperature T_{in} is both constant and uniform. The pipe wall is subjected to a constant and uniform temperature T_w, and the temperature at any radial position r within the pipe is T. Neglecting viscous dissipation, i.e. shear heating effects, and thermal conduction in the axial direction z, heat transfer is governed by the equation

$$u(r)\frac{\partial \theta}{\partial z} = \frac{\lambda}{\rho C_p}\left(\frac{\partial^2 \theta}{\partial r^2} + \frac{1}{r}\frac{\partial \theta}{\partial r}\right) \tag{4.9}$$

where λ is thermal conductivity, ρ is density, C_p is specific heat capacity, and the z origin is taken at the pipe inlet (Tanner, 1985). The dimensionless temperature θ is defined as

$$\theta = \frac{T - T_w}{T_{in} - T_w} \tag{4.10}$$

Equation (4.9) assumes that the velocity profile is fully developed but it holds in the thermal entrance region where the temperature profile is not fully developed. This equation must be solved subject to the following boundary conditions:

at the pipe wall, $r = R,\ \theta = 0$ for $z > 0$ (4.11)

at the pipe centre, $r = 0,\ \frac{\partial \theta}{\partial r} = 0$ for $z \geq 0$ (4.12)

at the pipe inlet, $z = 0,\ \theta = 1$ for $r \leq R$ (4.13)

The solution depends on the velocity profile *u(r)*. Closed form solutions only exist for plug flow or fully developed flow of a Newtonian or power law fluid. Note that both plug flow and Newtonian flow are simply limits of pseudoplastic power-law behaviour, i.e. plug flow represents the limiting condition of 'infinite pseudo-plasticity' when $n = 0$, and Newtonian flow represents the condition of 'zero pseudo-plasticity' when $n = 1$.

For a Newtonian fluid, substituting the fully developed parabolic velocity profile from Equation (4.1) into Equation (4.9) gives

$$2\overline{u}\left[1 - \left(\frac{r}{R}\right)^2\right]\frac{\partial \theta}{\partial z} = \frac{\lambda}{\rho C_p}\left(\frac{\partial^2 \theta}{\partial r^2} + \frac{1}{r}\frac{\partial \theta}{\partial r}\right) \tag{4.14}$$

For a power law fluid, substituting the fully developed velocity profile from Equation (4.4) into Equation (4.9) gives

$$\overline{u}\left(\frac{3n+1}{n+1}\right)\left[1-\left(\frac{r}{R}\right)^{\frac{n+1}{n}}\right]\frac{\partial\theta}{\partial z}=\frac{\lambda}{\rho C_p}\left(\frac{\partial^2\theta}{\partial r^2}+\frac{1}{r}\frac{\partial\theta}{\partial r}\right) \tag{4.15}$$

Note that putting $n = 1$ in Equation (4.15) leads to the Newtonian case, i.e. Equation (4.14). Lyche and Bird (1956) derived the complete solutions and tabulated the results for the cases $n = 1$, 1/2, 1/3, 0 and small values of the Graetz number. These results have been presented in graphical form in many references (see for example Chhabra and Richardson, 1999).

An approximate solution has also been developed which leads to the following expression of the Nusselt number, *Nu*, assuming a temperature-independent viscosity (Chhabra and Richardson, 1999)

$$Nu=\frac{hD}{\lambda}=1.75\left(\frac{3n+1}{4n}\right)^{1/3}Gz^{1/3} \tag{4.16}$$

in terms of the Graetz number, *Gz*, defined as

$$Gz=\frac{\dot{m}C_p}{\lambda L} \tag{4.17}$$

where h is the wall heat transfer coefficient, D is the pipe diameter, and $\dot{m}$ is the fluid mass flow rate. When $n = 1$, Equation (4.16) reduces to its Newtonian form

$$Nu=1.75Gz^{1/3} \tag{4.18}$$

4.2.4. FORMULATION OF CFD MODEL

4.2.4.1. Governing equations

The equations that form the basis of the description of flow and heat transfer for a generalised Newtonian fluid in a pipe are the three transport equations written in their general form (Bird *et al*., 1987), thus

Continuity $$\nabla \cdot U = 0 \tag{4.19}$$

where U is the velocity vector;

Momentum $$\rho \frac{DU}{Dt} = -\nabla p + [\nabla \cdot \eta\dot{\gamma}] + \rho g \tag{4.20}$$

where t is time and g is the gravitational acceleration. The term on the left hand side represents mass per unit volume times acceleration, while the forces on the right hand side are, successively, the pressure force, viscous force, and gravity or external force per unit volume. The gravity term was ignored here for a horizontal pipe.

Energy $$\rho C_p \frac{DT}{Dt} = (\nabla \cdot \lambda \nabla T) + \frac{1}{2}\eta(\dot{\gamma} : \dot{\gamma}) \tag{4.21}$$

The term on the left hand side represents the rate of increase of internal energy per unit volume, and the terms on the right hand side are, successively, the rate of addition of energy by heat conduction per unit volume, and the rate of conversion of mechanical to thermal energy per unit volume. The last term representing viscous energy dissipation is insignificant at low flow velocities and was therefore neglected in this study.

In addition to the simultaneous solution of the above equations, the temperature dependence of the fluid physical properties needs to be taken into account. In this study, account was taken of the temperature dependence of the viscosity only, while other properties (density, thermal conductivity, heat capacity) were assumed constant.

The CFD model used here, constructed in Cartesian coordinates (X, Y, Z), assumes that flow through the pipe is laminar and incompressible. The fluid is heated through the pipe wall which is held at a constant and uniform temperature. The pipe length for most of the cases studied was 400 mm. This length was amply sufficient to allow the velocity profile to fully develop and allow the fluid to receive an adequate amount of heat so as to enable a demonstration of the effect of vibration on the temperature profile. Using much longer pipes on the metre scale, as usually used in real industrial processes such as food sterilisation, would hugely prolong the runtime of the vibrational flow simulations, e.g. a 3 m pipe would typically increase the runtime from a few days to a month. A few simulations, however, were conducted using 800 and 1200 mm long pipes to investigate the effect of pipe length.

4.2.4.2. Hydrodynamic and thermal entrance length

For all of the cases investigated, the pipe Reynolds number was sufficiently small (Re < 50) for flow to achieve a fully developed velocity profile. This was confirmed by the fact that the hydrodynamic entrance length, L_h, was much shorter than the pipe length (i.e. $L_h \ll 400$ mm). L_h can be estimated from the following approximate expression (Shook and Roco, 1991)

$$\frac{L_h}{D} = 0.062\,\mathrm{Re} \tag{4.22}$$

where the flow Reynolds number, Re, is expressed as

$$\mathrm{Re} = \frac{\rho \bar{u} D}{\mu_e} \tag{4.23}$$

and μ_e is the effective viscosity for a non-Newtonian fluid. For a Newtonian fluid, $\mu_e = \mu$. Note that slightly different values of the constant in Equation (4.22) have been reported (e.g. Shook and Roco, 1991; Rohsenow *et al*., 1998; Çengel, 2003). For shear thinning power-law fluids, Rohsenow *et al*. (1998) reported values of 0.0575, 0.048, and 0.034 for n = 1, 0.75, and 0.5, respectively.

The temperature profile is said to be thermally fully developed when (Çengel, 2003)

$$\frac{\partial}{\partial z}\left(\frac{T_w - T(r,z)}{T_w - T_m(z)}\right) = 0 \tag{4.24}$$

where T_m is the area-averaged fluid temperature. In other words, the dimensionless temperature profile denoted by

$$\Psi = \frac{T_w - T(r,z)}{T_w - T_m(z)} \neq f(z) \tag{4.25}$$

remains unchanged in the axial direction. Note that whilst the temperature profile in the thermally fully developed region may vary with z in the flow direction, and it usually does, the dimensionless temperature profile defined above remains unchanged when the temperature at the wall is constant and uniform. Similarly, the local heat transfer coefficient, h, remains unchanged in the thermally fully developed region. The thermal entrance length, L_{th}, can be estimated from (Çengel, 2003)

$$\frac{L_{th}}{D} \approx L_h.\mathrm{Pr} \tag{4.26}$$

where the Prandtl number, Pr, is given by

$$\mathrm{Pr} = \frac{C_p \mu_e}{\lambda} \tag{4.27}$$

Pr is a ratio of momentum diffusivity to thermal diffusivity, i.e. a measure of the relative growth of the velocity and thermal boundary layers. In practice, for most viscous fluids, Pr is greater than 50, which makes the thermal entrance length much larger compared to the hydrodynamic entrance length (Tanner, 1985). For the cases investigated here, the values of Pr were such that a fully developed temperature profile was never achieved in steady flow.

4.2.4.3. Forced vibration

A transversal sinusoidal vibrational movement was imposed at the pipe wall in the x direction normal to the flow, as shown in Figure 4.1. In this case, the linear sinusoidal displacement of the pipe wall along the x axis is given by

$$x = A\sin(\omega t) \tag{4.28}$$

where A is the amplitude of vibration, and $\omega = 2\pi f$ where f is the frequency of vibration. The linear velocity, $\dot{x}$, of the wall is obtained by differentiating Equation (4.28) with respect to time, thus

$$\dot{x} = \frac{dx}{dt} = A\omega\cos(\omega t) \tag{4.29}$$

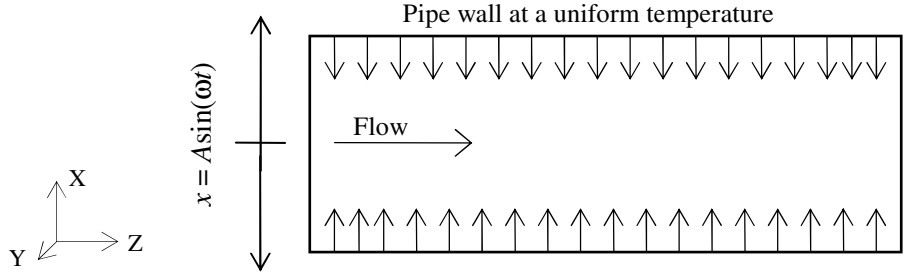

Figure 4.1: Vibrated pipe at a uniform wall temperature.

4.3. CFD SIMULATIONS

CFD simulations were conducted of the non-isothermal steady-state and vibrational flow of Newtonian and inelastic shear-thinning power law fluids. The viscosity of the Newtonian fluid was described using the Arrhenius model, given by Equation (4.5), and the shear-dependent viscosity of the power law fluid was described using Equation (4.3) with the temperature dependence of the consistency index as given by Equation (4.6). The values of the activation energy E_a, pre-exponential factor k_0, specific heat capacity C_p, and thermal conductivity λ used here are typical of a range of food fluids (Jung and Fryer, 1999; Barigou *et al*., 1998; Steffe, 1996). The flow and vibration parameters, in addition to the rheological and thermal properties of the fluids used are given in Table 4.1.

Three-dimensional simulations were set up and executed using the software package ANSYS Workbench 10.0. The flow geometry was created using the software DesignModeler and meshed using CFX-Mesh, while flow specification, solving and post-processing were all performed using CFX 10.0.

4.3.1. GEOMETRY

The geometry consisted of a straight pipe 20 mm in diameter. This value of the pipe diameter was chosen to be consistent with those normally used in studying thermal sterilisation (e.g. Liao *et al*., 2000; Jung and Fryer, 1999; Lin, 1976). A pipe length of 400 mm was used with three surface boundaries: inlet, outlet, and wall. Longer pipes of 800 mm and 1200 mm lengths were also used to investigate the effect of pipe length. The shortest pipe length used (i.e. L = 400 mm) was greater than the maximum hydrodynamic entrance length L_h, as discussed above (Section 4.2.4.2), and was therefore sufficient to obtain a fully developed velocity profile.

Table 4.1. Range of simulation parameters.

Fluid	D (mm)	f (Hz)	A (mm)	L (mm)	k_0 (Pa s^n)	E_a (kJ mol^{-1})	n (-)	$\bar{u}$ (m s^{-1})	ρ (kg m^{-3})	C_p (J kg^{-1} K^{-1})	λ (W m^{-1} K^{-1})
Newtonian	20	0-100	0-10	400, 800, 1200	5×10^{-7}-5×10^{-5}	35.0	1.0	0.090	1000	4180	0.668
Power-law	20	25	2.0	400	5×10^{-5}	35.0	0.65-1.0	0.090	1000	4180	0.668

4.3.2. MESH

An unstructured mesh with tetrahedral cells was generated using CFX-Mesh. To optimise the mesh size it was necessary to carry out a mesh-independence study; this was done by performing a number of simulations with different mesh sizes, starting from a coarse mesh and refining it until results were no longer dependent on the mesh size. The 3-D mesh obtained thus contained approximately 3,000 tetrahedral cells per centimetre of pipe length. Seven inflation layers covering around 20% of the tube radius were created near the wall to enhance mesh resolution in this region where high velocity and temperature gradients exist; the first layer has a thickness of 0.15 mm expanding by a factor of 1.2 in successive layers, as shown in Figure 4.2.

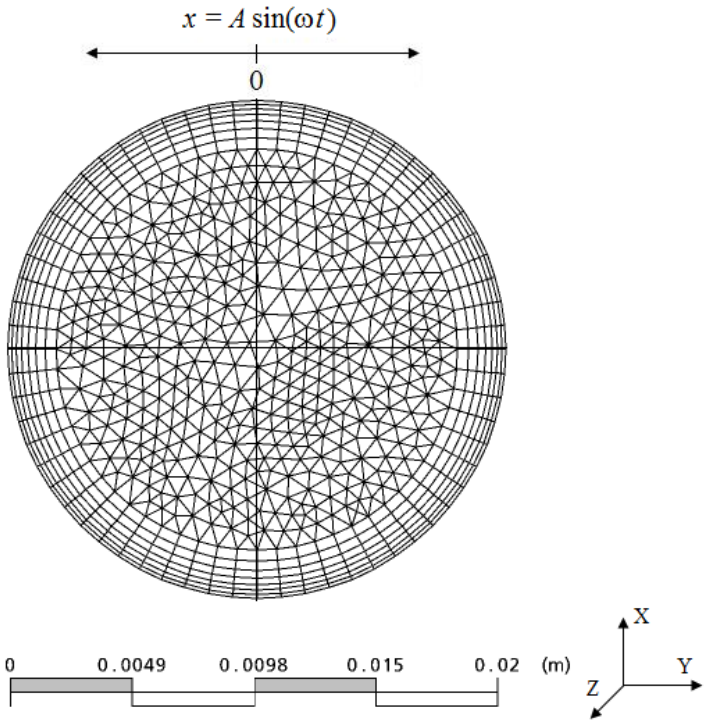

Figure 4.2. Meshed geometry of vibrated pipe.

4.3.3. FLOW SPECIFICATION

Flow specification was performed using the software component CFX-Pre. The problem was solved in three steps:

(i) steady state flow with uniform inlet velocity and temperature;
(ii) steady state flow with inlet boundary conditions of velocity and temperature profiles obtained from step (i); and
(iii) unsteady state flow with vibrational motion imposed using the solution from step (ii) as an initial solution.

The purpose of solving the steady state flow in two steps ((i) and (ii)) was twofold: (a) to enable the temperature profile to develop further, albeit not fully, so that vibration effects can be clearly demonstrated in step (iii); and (b) to allow the flow field in step (ii), which was used to initialise the vibrational flow simulation in step (iii), to be fully developed throughout the entire pipe. This was a computationally efficient procedure which enabled a clear demonstration of the vibrational effects in step (iii) without the need to use a long pipe.

4.3.3.1. Step (i) simulation

In step (i) of the numerical solution, a uniform temperature T_{in} = 60°C and a mass flow rate of $\dot{m} = 0.0282\,\text{kg s}^{-1}$ were specified at the pipe inlet, while a zero gauge pressure was set at the pipe outlet. The mass flow rate was chosen to give a mean flow velocity of $\bar{u}$ = 9.0 cm s^{-1}, which is typical of the values used in the food industry (Jung and Fryer, 1999; Steffe, 1996; Lin, 1976). A uniform wall temperature T_w = 180°C and a no-slip condition were assigned at the wall. The inlet and wall temperatures were selected to yield a fluid temperature at the outlet of at least 100°C, consistent with usual sterilisation conditions. In food processing, wall temperatures lower than 180°C are usually used in practice, but such temperatures would require a long pipe to achieve the required outlet temperature, thus making the simulations computationally expensive.

Heat transfer was modelled using the 'Thermal Energy' model within CFX. This model describes the transport of enthalpy through the domain while ignoring the effects of flow kinetic energy, and is therefore appropriate for flows with subsonic velocities.

The High Resolution Advection Scheme was implemented here to discretise the advection terms in the governing equations. In this scheme, the value of the blend factor β in Equation (2.18) is calculated locally to be as close to 1 as possible without resulting in non-physical variable values (see Chapter 2, Section 2.9.3).

Convergence was assumed when the root mean square (RMS) of mass, momentum and energy residuals reached 10^{-5}. This typically required ~100 iterations.

Given the small hydrodynamic entrance length, the first simulation in step (i) always yielded a fully developed velocity profile at the exit, but the temperature profile was not sufficiently developed.

4.3.3.2. Step (ii) simulation

The exit profiles of temperature and velocity obtained in step (i) were used as the inlet boundary conditions in step (ii), keeping the rest of the simulation set-up unchanged.

4.3.3.3. Step (iii) simulation

The full solution along the pipe resulting from step (ii) simulation was used to initialise the simulation of vibrational flow in step (iii). The inlet, outlet, and wall boundary conditions were the same as those used in step (ii). In addition, vibration was imposed on the pipe by applying a sinusoidal velocity function defined by Equation (4.29) at the wall. For a transversally moving boundary, the mesh deformation option in CFX was used which allows the specification of the motion of nodes on boundary regions of the mesh. The motion of all remaining nodes is determined by the so-called displacement diffusion model which is designed to preserve the relative mesh distribution of the initial mesh. The mesh displacement was specified using Equation (4.28).

The vibrational flow simulation was conducted in the transient mode due to the unsteady nature of the flow. The transient scheme used for the solution to march in time was the Second Order Backward Euler Scheme wherein the solution is initialised within each time step by extrapolating the solutions from the previous two time steps to the new time step (see Chapter 2, Section 2.9.1). The simulation was solved over the entire mean residence time of the fluid which is determined by the pipe length and mean flow velocity. For example, for a pipe length of 400 mm and flow velocity of 0.09 m s^{-1}, the fluid residence time in the pipe is 4.4 s. This time duration was divided into equal time steps, the size of which was determined by dividing the vibration cycle period, which in turn depended on vibration frequency, into an optimised number of 12 equal time steps. Using a larger number of time steps per vibration cycle did not affect the simulation results but prolonged the simulations considerably. A typical size of the time step thus obtained was 1.67 ms.

Convergence was assumed when the root mean square (RMS) of mass, momentum and energy residuals reached 10^{-3} at each time step. Achieving this level of convergence typically required 5-10 iterations per time step. Most of the equations generally, however, reached RMS residual values well below the specified target. Using a residual target of less than 10^{-3} in this case did not affect the results significantly but prolonged the simulations considerably.

Transient simulations typically required 1-5 days of runtime using a 3.2 GHz Intel Xeon processor with 4.00 GB of RAM.

4.4. VALIDATION OF CFD MODEL

The computational model used was validated either by comparing results with theoretical solutions or experimental data from the literature where possible. The intention here was to try and validate the CFD model as much as possible so as to establish confidence in the numerical results. The various stages of the validation process are described below.

4.4.1. STEADY-STATE FLOW

CFD simulation of the isothermal steady flow of inelastic non-Newtonian fluids has been validated in Chapter 3 for a variety of rheological behaviours, namely power law, Herschel-Bulkley and Bingham plastic, showing excellent agreement on the order of 1% with exact analytical solutions.

The steady-state flow model with heat transfer was first validated for the simple case of temperature-independent viscosity. The numerical solution of Equation (4.9) relating to this case was first obtained and tabulated by Lyche and Bird (1956) for Newtonian and power law fluids at a Graetz number of 5.24 (see also Chhabra and Richardson (1999) for a graphical representation of the data). Comparison of this solution in Figure 4.3 with the CFD-predicted temperature profile for a Newtonian fluid and a considerably shear thinning fluid shows a very good agreement.

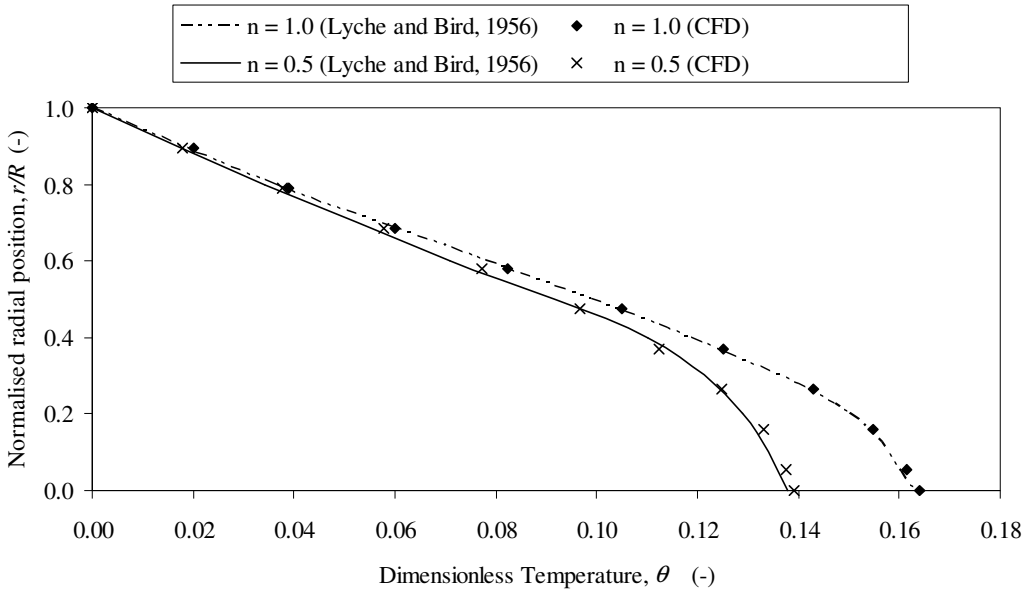

Figure 4.3: Comparison of CFD-predicted and theoretical (Equation (4.9)) temperature profiles for isoviscous Newtonian and shear-thinning power law fluids in steady-state flow: (n = 1; μ = 1.0 Pa s); (n = 0.5; k = 1.0 Pa s^n); T_{in} = 27°C; T_w = 127°C; $\overline{u}$ = 0.01 m s^{-1}.

The heat transfer coefficient, h, was also computed from the CFD results using an energy balance, as follows

$$\dot{m}C_p\left(T_{out}-T_{in}\right)=ha\Delta T_m \tag{4.30}$$

$$\Delta T_m=\frac{\left(T_w-T_{out}\right)-\left(T_w-T_{in}\right)}{\ln\left[\left(T_w-T_{out}\right)/\left(T_w-T_{in}\right)\right]} \tag{4.31}$$

where a is the wall surface area and T_{out} is the area-averaged temperature at the pipe outlet. Comparison in Table 4.2 of the value of h thus obtained from CFD with the theoretical value predicted by Equation (4.16) shows an excellent agreement for Newtonian and non-Newtonian fluids with different values of n.

Table 4.2: Comparison of h values predicted by Equation (4.16) and CFD for an isoviscous fluid in steady-state flow.

n (-)	h (W m^{-2} K^{-1})		Deviation (%)
	Theory	CFD	
0.65	585	580	-0.8
0.80	572	573	+0.2
0.90	566	564	-0.4
1.00	561	555	-1.1

Since the variation of viscosity with temperature alters the flow field of the fluid, it was also necessary to validate the velocity profile computed by CFD under these conditions (i.e. non-isoviscous conditions). Kwant *et al*. (1973(b)) measured the laminar velocity profile of a temperature-dependent Newtonian fluid at a constant wall temperature using an optical arrangement for flow visualisation. The CFD predictions of the fully developed steady-state velocity profile was compared with their experimental measurements for Q = 1.49 (Equations (4.7) and (4.8)) in Figure 4.4. The figure shows a very good agreement between CFD and experiment. Furthermore, it shows that the temperature-dependence of the viscosity gives rise to a flattened velocity profile compared to that obtained under isothermal conditions (Equation (4.1)).

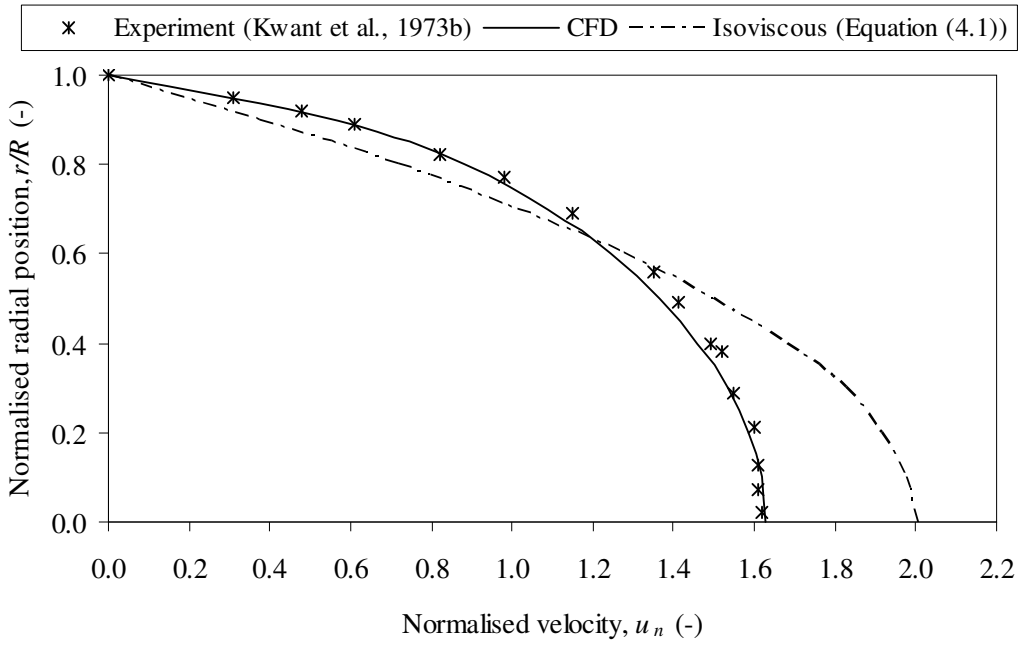

Figure 4.4: Comparison of CFD and experimental velocity profiles for a Newtonian fluid in steady-state flow:
T_{in} = 37°C; T_w = 127°C; $\bar{u}$ = 0.09 m s^{-1}; L = 1900 mm; n = 1; Q = 1.49, and k' = 1.3 Pa s^n at T' = 25°C (Equations (4.7) and (4.8)).

4.4.2. VIBRATIONAL FLOW

In Chapter 3, the CFD model of isothermal non-Newtonian flow under forced vibration was validated using the experimental results of Deshpande and Barigou (2001) (see Section 3.4). Comparison with experiment showed that CFD is able to predict such flows within ~10% under a wide range of vibration conditions and for a variety of rheological behaviours, namely power law, Herschel-Bulkley and Bingham plastic. There are, however, no experimental temperature profile data available relating to the flow of non-isothermal fluids when subjected to vibration. Nonetheless, the excellent agreement between CFD and theory or experimental results achieved in all the above stages of the validation process indicate that the present CFD model is robust and sufficiently reliable for the purposes of demonstrating the effects of vibration on the heat transfer characteristics of the flows considered here, especially that high accuracy in this case is not mandatory.

4.5. RESULTS AND DISCUSSION

CFD simulations were conducted for the range of variables shown in Table 4.1. The CFD results showed that transversal vibration can have a substantial effect on the radial temperature distribution of the fluid. There was also a large impact on the wall heat transfer coefficient. The extent of these effects was found to depend on the vibration amplitude and frequency, fluid rheology, and pipe length, as shown below. On the other hand, simulations of longitudinal and rotational vibrations showed no significant effects on the radial temperature distribution.

4.5.1. EFFECT OF VIBRATION AMPLITUDE

Simulations were conducted at a vibration frequency f = 50 Hz for vibration amplitudes of 1.0, 1.5, and 2.0 mm, while keeping all the other parameters constant. The temperature contour maps obtained at the pipe exit are compared in Figure 4.5, where the large effect of vibration on the radial temperature distribution is clearly demonstrated.

In steady laminar flow, heat is transferred by conduction in the radial direction and, as a result, in this relatively short pipe (L = 400 mm) only the fluid flowing near the wall is significantly heated, while the temperature of most of the fluid remains virtually at its inlet value. Transversal vibration, however, induces a substantial amount of radial mixing in the fluid. In steady-state flow the streamlines are straight lines along the pipe, as shown in Figure 4.6. Vibration, on the other hand, creates a swirling or spiralling motion in the fluid, as clearly represented by the complex streamlines and fluid trajectories depicted in Figure 4.7. Such a flow pattern is characterised by significant vortical structures in the flow which cause considerable radial mixing, thus, leading to a more uniform temperature distribution. This effect is sensitive to the amplitude of vibration, as shown in Figure 4.5.

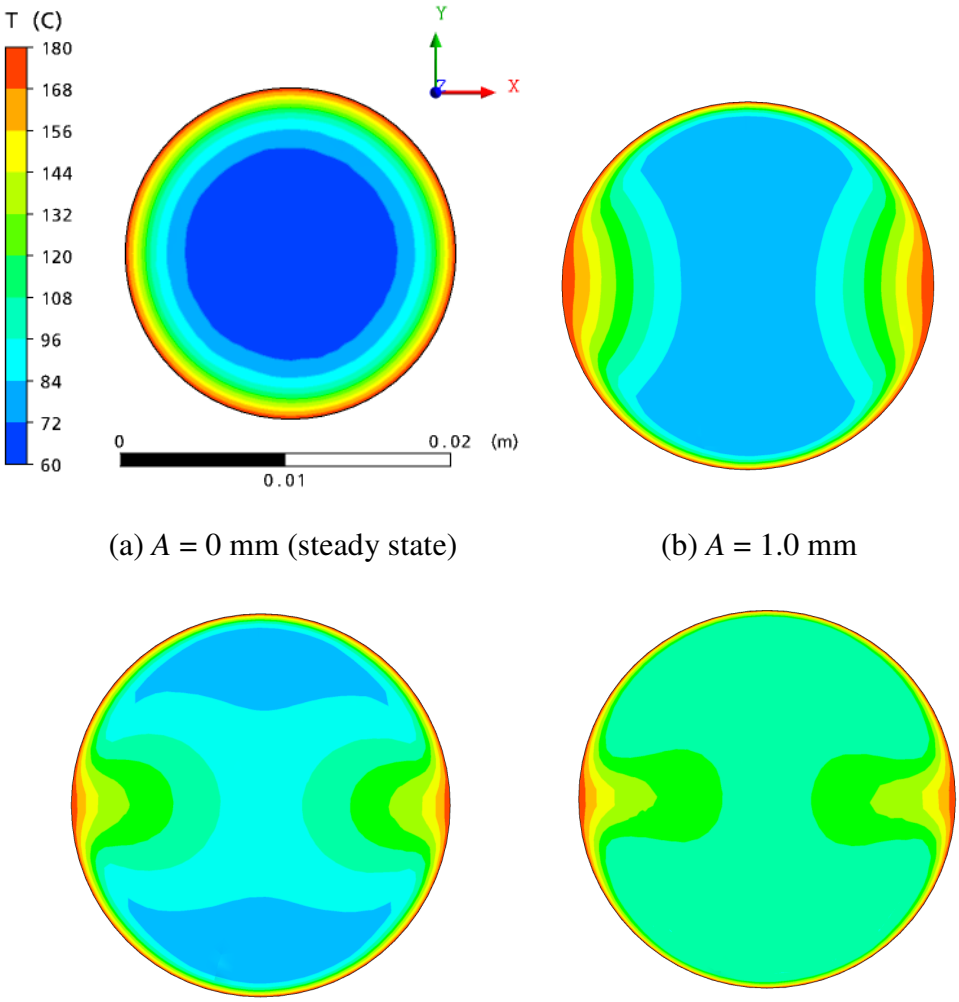

(a) A = 0 mm (steady state)

(b) A = 1.0 mm

(c) A = 1.5 mm

(d) A = 2.0 mm

Figure 4.5: Effect of vibration amplitude on temperature distribution at the pipe exit:
n = 1; $k_0 = 5\times10^{-7}$ Pa s^n; T_w = 180° C; T_{in} = 85° C; $\bar{u}$ = 0.09 m s^{-1}; f = 50 Hz; L = 400 mm.

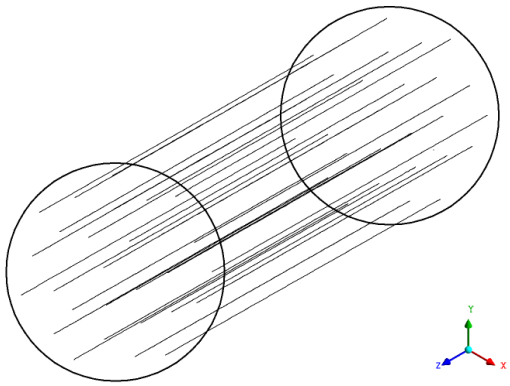

Figure 4.6: Fluid streamlines in steady flow.

The vortical structures induced by vibration can be quantified by calculating vorticity in the X-Y plane from the following equation:

$$\zeta = \frac{\partial u_y}{\partial x} - \frac{\partial u_x}{\partial y} \tag{4.32}$$

where u_y and u_x are the x- and y- components of velocity, respectively. Figure 4.8 shows vorticity contour maps obtained at the pipe exit for the three amplitudes used. The figure shows that the maximum vorticity increases fourfold as the amplitude is doubled. Note that the shaded area near the wall is a region of very high vorticity which exceeds the scale shown by 2 orders of magnitude and was therefore not shown. Since the strength of vortical fluid motion is directly responsible for the observed radial mixing, this explains the strong dependence of radial mixing, and hence temperature uniformity, on A (Figure 4.5).

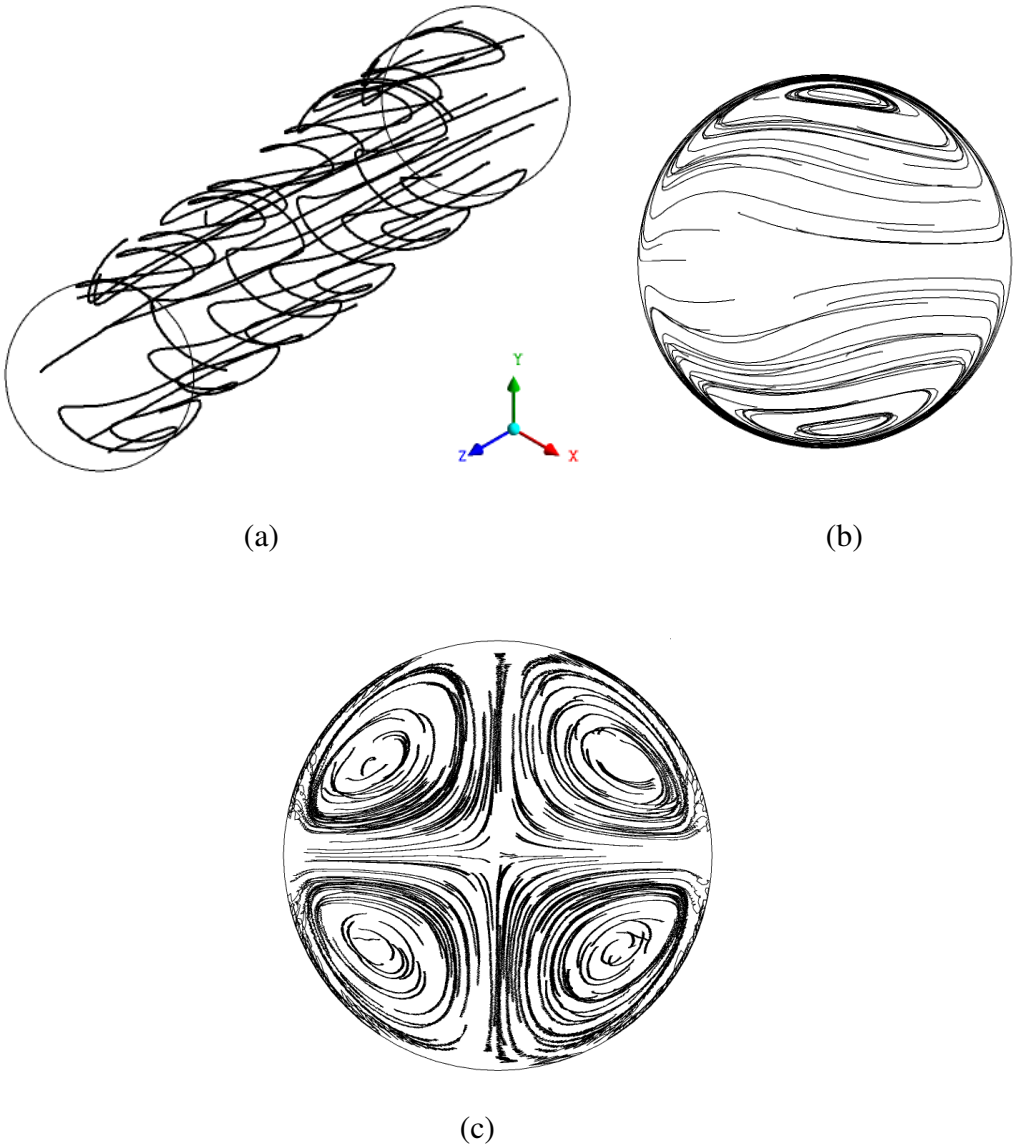

Figure 4.7: A sample of: (a) streamlines; (b) streamlines projected on pipe exit plane; (c) fluid trajectories projected on pipe exit plane;
$n = 1$; $k_0 = 5\times10^{-7}$ Pa s^n; $T_w = 180°$ C; $T_{in} = 85°$ C; $\bar{u} = 0.09$ m s^{-1}; $f = 25$ Hz;
$A = 2.0$ mm; $L = 400$ mm.

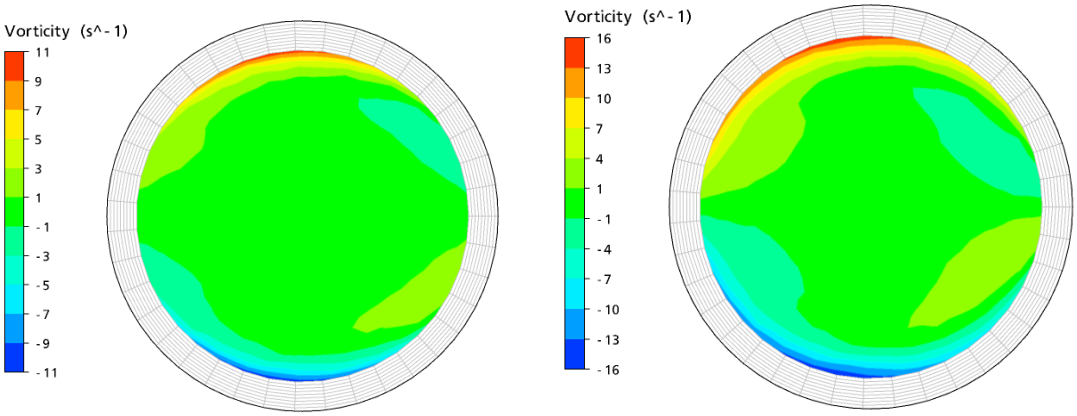

(a) A = 1.0 mm (b) A = 1.5 mm

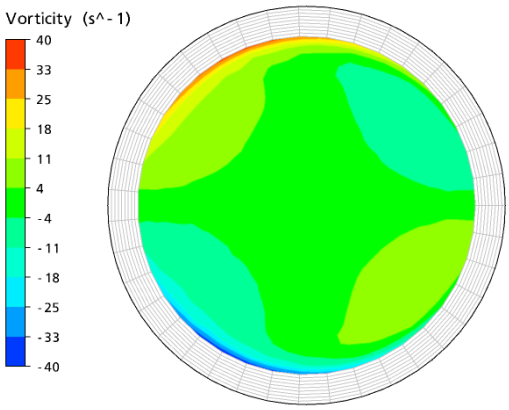

(c) A = 2.0 mm

Figure 4.8: Vorticity contour maps at different vibration amplitudes: n = 1; $k_0 = 5\times10^{-7}$ Pa s^n; T_w = 180° C; T_{in} = 85° C; $\bar{u}$ = 0.09 m s^{-1}; f = 50 Hz; L = 400 mm.

The increase in temperature uniformity due to vibration can also be demonstrated by plotting the mean radial temperature profiles, as shown in Figure 4.9. Due to the asymmetry in the temperature distribution around the axis (Figure 4.5), caused by the oscillations in the x direction, the pipe cross-section was divided into 10 annular sections of equal thickness and the area-average of the temperature in each section was calculated. Since the mean temperature profile thus obtained is symmetrical around the diameter, only half of the profile is shown in Figure 4.9. The results show that vibration has a flattening effect on the temperature profile which increases with

vibration amplitude. Moreover, as A increases, the fluid temperature in the vicinity of the pipe wall decreases, while that of the rest of the fluid increases. At A = 2.0 mm, the uniformity in the temperature profile is substantial, with the temperature at the pipe centre increasing by ~75% and that near the wall at r/R ~ 0.95 decreasing by ~20% compared to their steady-state values. Even at the lower amplitudes, significant improvements in the uniformity of the temperature distribution are observed. Figure 4.10 also shows that while in steady state the temperature along the pipe centreline (i.e. the lowest temperature in the pipe) remains virtually at its inlet value, a significant rise in this temperature along the pipe can be obtained under vibration. At the highest amplitude used, i.e. A = 2.0 mm, this rise is substantial.

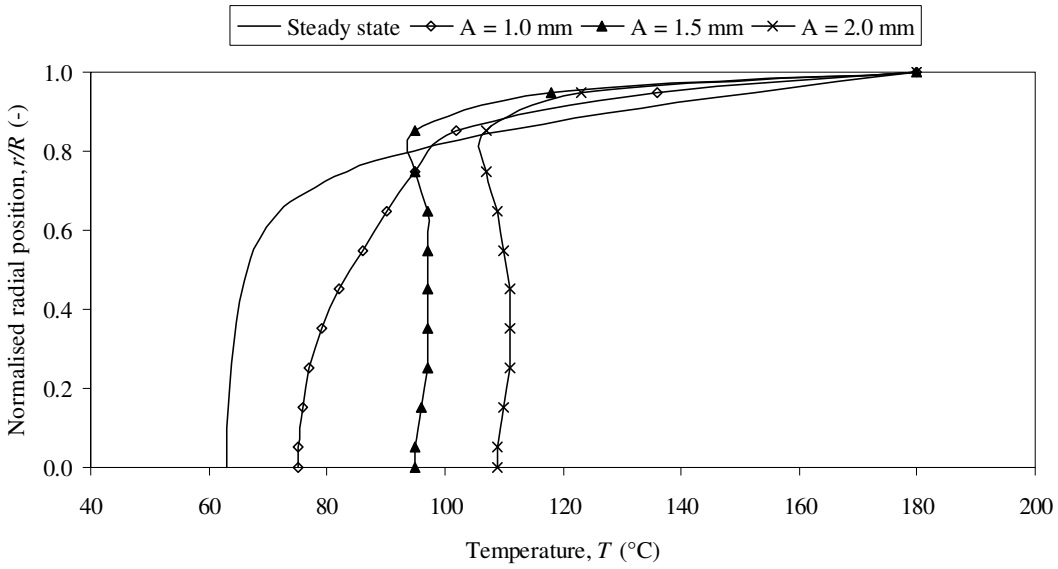

Figure 4.9: Effect of vibration amplitude on the mean temperature profile at the pipe exit:

$n = 1$; $k_0 = 5 \times 10^{-7}$ Pa s^n; $T_w = 180°$ C; $T_{in} = 85°$ C; $\bar{u}$ = 0.09 m s^{-1}; f = 50 Hz; L = 400 mm.

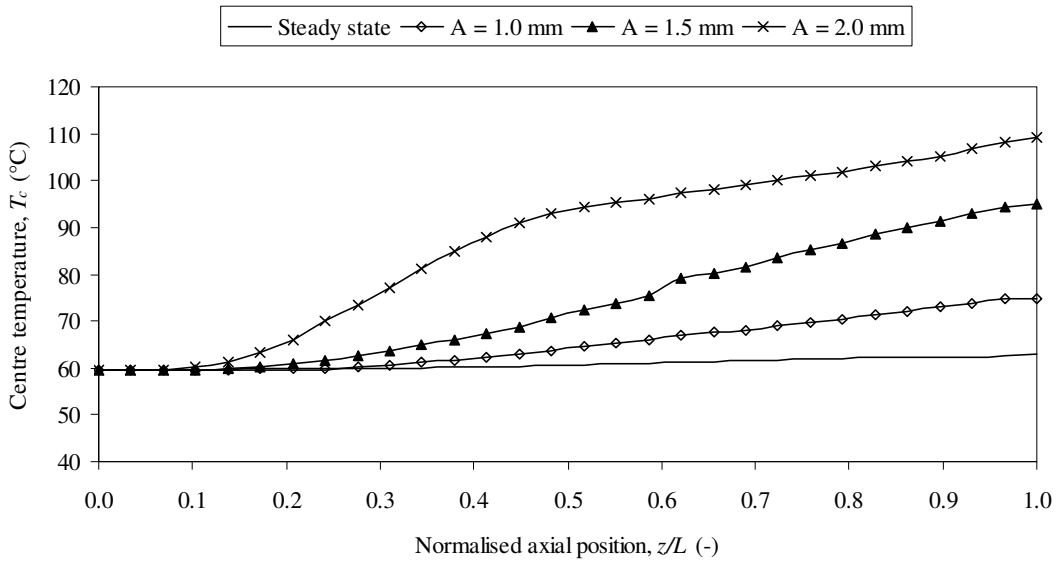

Figure 4.10: Effect of vibration amplitude on the axial variation of temperature at the pipe centre:
$n = 1$; $k_0 = 5 \times 10^{-7}$ Pa s^n; $T_w = 180°$ C; $T_{in} = 85°$ C; $\bar{u} = 0.09$ m s^{-1}; $f = 50$ Hz; $L = 400$ mm.

The effects of vibration on the development of the full temperature profile along the pipe are depicted in Figure 4.11 for a varying amplitude and a fixed frequency. Note that the temperature maps in the figure are shown in the x-z plane, which is the plane of vibration. The temperature maps show that without vibration the temperature profile develops extremely slowly, making very little progress along the relatively short pipe considered here (400 mm). In fact, using Equation (4.26), it can be shown that the steady-state temperature profile under the conditions shown in Figure 4.11 would require over 11 m to become fully developed. However, with vibration a much more rapid development of the temperature profile takes place. As shown in Figure 4.11, while the temperature under steady-state flow conditions remains virtually constant along the pipe axis, it rises rapidly by comparison in the vibrated flow, the rate of rise being a function of the vibration amplitude used. This can also be seen in Figure 4.12, where the area-averaged temperature is plotted along the pipe.

The implications of these results are significant for processes where a uniform temperature profile is desirable, such as food sterilisation. The fluid temperature near the wall can be reduced, thus avoiding overheating, while the temperature at the pipe centre can be increased rapidly to achieve sterility while significantly reducing the loss in quality that usually arises from over-processing.

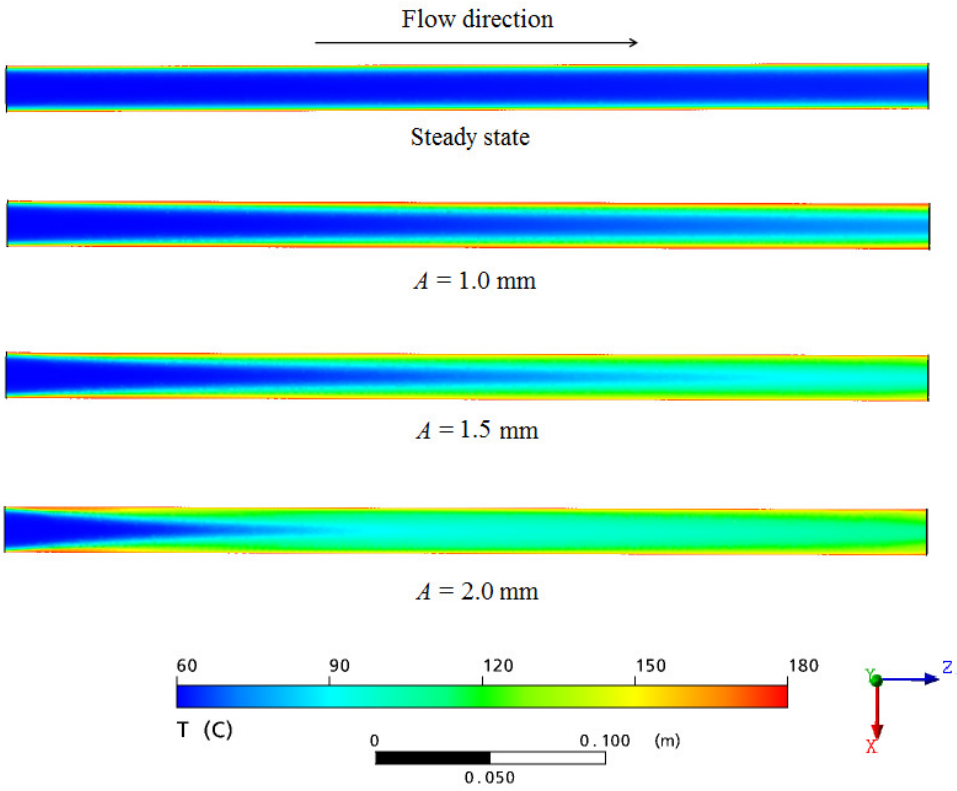

Figure 4.11: Effect of vibration amplitude on temperature distribution along the pipe: $n = 1$; $k_0 = 5 \times 10^{-7}$ Pa s^n; $T_w = 180°$ C; $T_{in} = 85°$ C; $\bar{u} = 0.09$ m s^{-1}; $f = 50$ Hz; $L = 400$ mm.

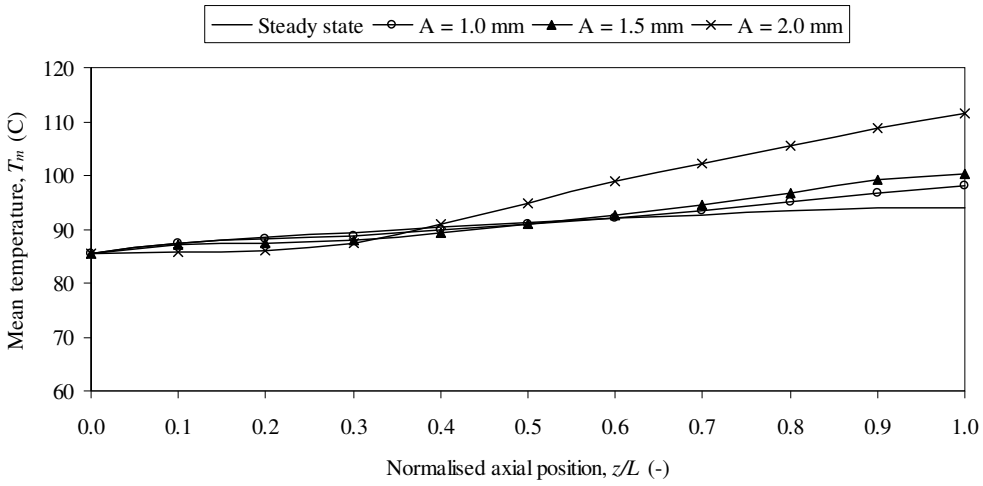

Figure 4.12: Effect of vibration amplitude on the area-averaged temperature along the pipe:
$n = 1$; $k_0 = 5\times10^{-7}$ Pa s^n; $T_w = 180°$ C; $T_{in} = 85°$ C; $\bar{u} = 0.09$ m s^{-1}; $f = 50$ Hz; $L = 400$ mm.

4.5.2. EFFECT OF VIBRATION FREQUENCY

Figure 4.13 compares the temperature contour maps at the pipe exit for vibration frequencies of 25, 50 and 75 Hz at a fixed amplitude A = 2.0 mm. As can be observed, the effect of vibration frequency is similar to that of vibration amplitude. The mean radial temperature profiles are also shown in Figure 4.14. A higher frequency leads to a more uniform temperature distribution with a large rise in the temperature at the centre. At f = 75 Hz the temperature distribution is almost completely uniform across ~ 90% of the pipe radius. It can also be seen that, while an increase in frequency from 0 to 75 Hz results in substantial improvements in the uniformity of the temperature distribution, the magnitude of the effect diminishes as f increases. These results then suggest that the influence of vibration on heat transfer is less sensitive to frequency than it is to amplitude. Figure 4.15 shows the axial variation of the centre temperature at different frequencies. It can also be seen in Figure 4.16 that vibration leads to an increase in the area-averaged temperature of the fluid. This suggests that vibration increases the flux of heat from the wall to the fluid. The effects of vibration frequency on the development of the x-z plane temperature

profile along the pipe are also depicted in Figure 4.17, where the effects are similar to those shown in Figure 4.11.

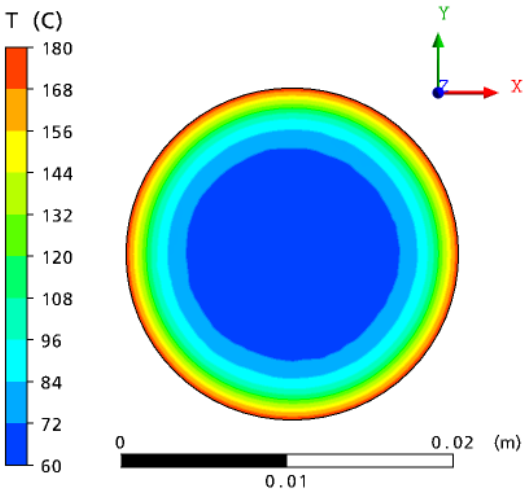

(a) Steady state ($f = 0$ Hz)

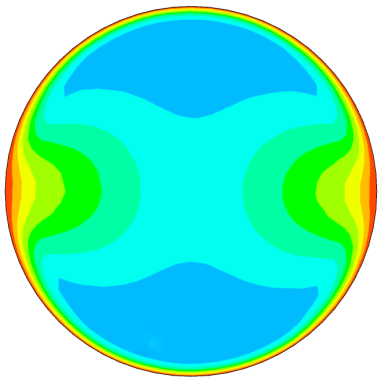

(b) $f = 25$ Hz

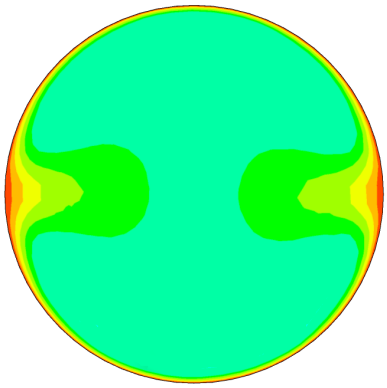

(c) $f = 50$ Hz

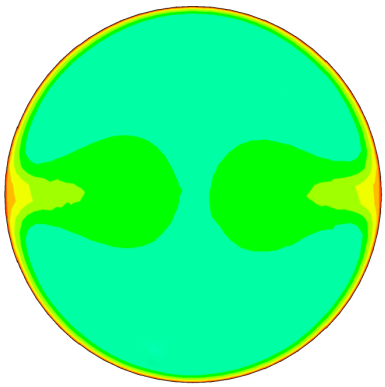

(d) $f = 75$ Hz

Figure 4.13: Effect of vibration frequency on temperature distribution at the pipe exit: $n = 1$; $k_0 = 5 \times 10^{-7}$ Pa s^n; $T_w = 180°$ C; $T_{in} = 85°$ C; $\bar{u} = 0.09$ m s^{-1}; $A = 2.0$ mm; $L = 400$ mm.

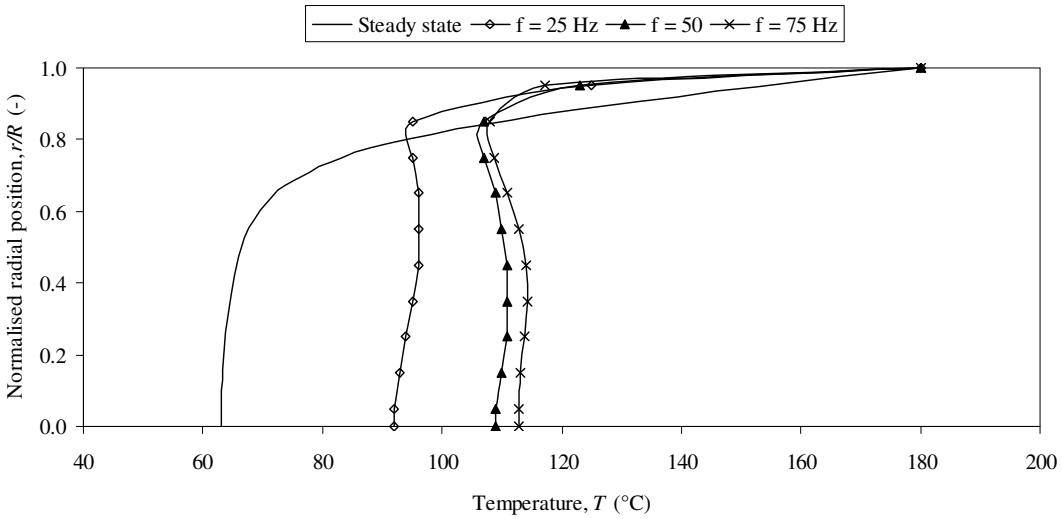

Figure 4.14: Effect of vibration frequency on the mean temperature profile at the pipe exit:

$n = 1$; $k_0 = 5 \times 10^{-7}$ Pa s^n; $T_w = 180°$ C; $T_{in} = 85°$ C; $\bar{u} = 0.09$ m s^{-1}; $A = 2.0$ mm; $L = 400$ mm.

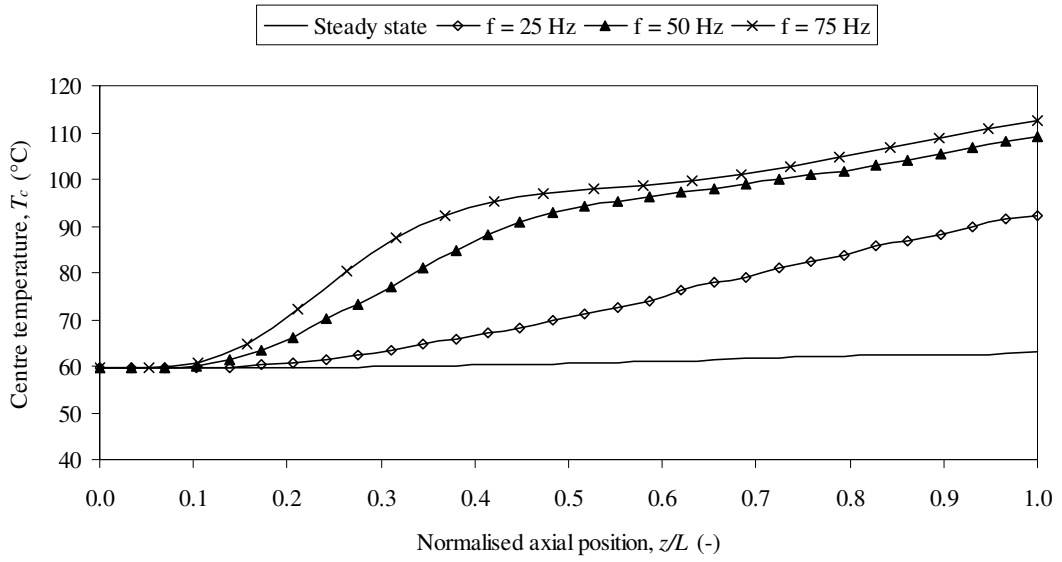

Figure 4.15: Effect of vibration frequency on the axial variation of temperature at the pipe centre:

$n = 1$; $k_0 = 5 \times 10^{-7}$ Pa s^n; $T_w = 180°$ C; $T_{in} = 85°$ C; $\bar{u} = 0.09$ m s^{-1}; $A = 2.0$ mm; $L = 400$ mm.

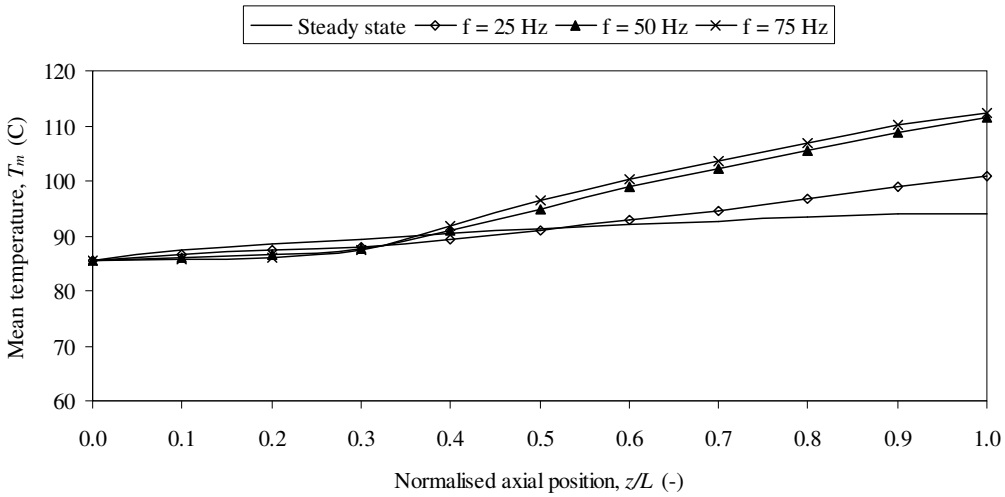

Figure 4.16: Effect of vibration frequency on the area-averaged temperature along the pipe:

$n = 1$; $k_0 = 5 \times 10^{-7}$ Pa s^n; $T_w = 180°$ C; $T_{in} = 85°$ C; $\bar{u} = 0.09$ m s^{-1}; $A = 2.0$ mm; $L = 400$ mm.

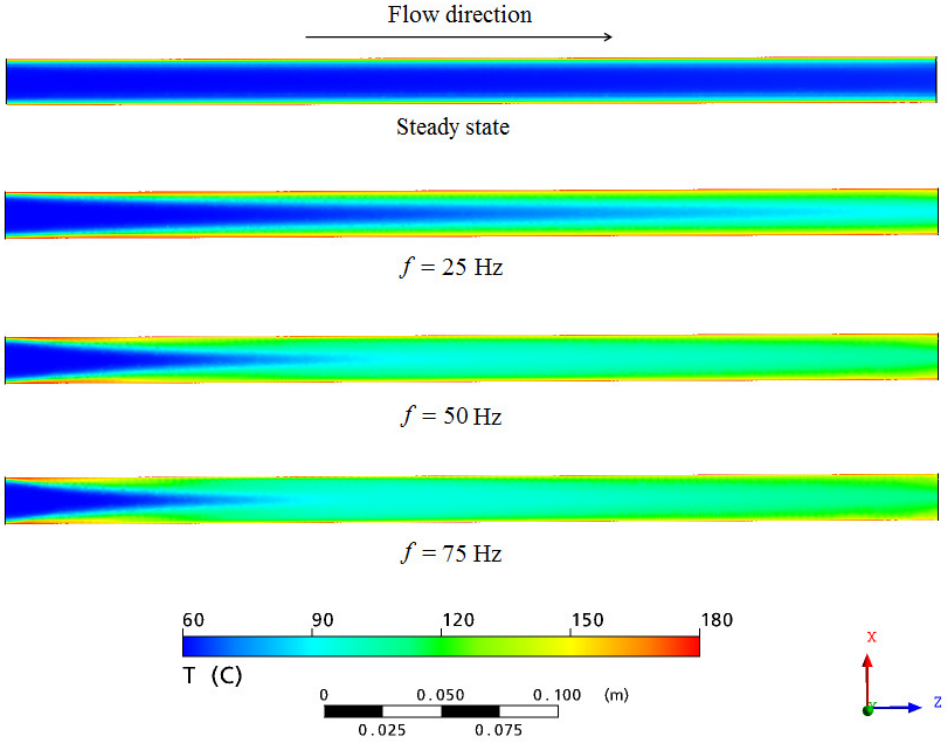

Figure 4.17: Effect of vibration frequency on temperature distribution along the pipe:

$n = 1$; $k_0 = 5 \times 10^{-7}$ Pa s^n; $T_w = 180°$ C; $T_{in} = 85°$ C; $\bar{u} = 0.09$ m s^{-1}; $A = 2.0$ mm; $L = 400$ mm.

Vibration enhances heat transfer by promoting convection. The values of the wall heat transfer coefficient estimated using the CFD results in conjunction with Equation (4.30) are presented in Table 4.3. Vibration causes a large enhancement in the heat transfer coefficient which is a function of the amplitude and frequency used, reaching several folds in some cases. The variations of the heat transfer coefficient in vibrational flow, h_v, as a function of A and f are plotted in Figure 4.18. Despite the small number of data points, these trends clearly corroborate the observations made so far that the vibrational effects reduce in significance as f increases, and that they are more sensitive to amplitude than frequency. The effects of amplitude would be expected to level off when A becomes comparable to the pipe radius.

Table 4.3: Comparison of heat transfer coefficient under steady-state flow and vibrated flow: $n = 1$; $k_0 = 5\times10^{-7}$ Pa s^n; $T_w = 180°$ C; $T_{in} = 85°$ C; $\bar{u} = 0.09$ m s^{-1}; $L = 400$ mm.

	f (Hz)	A (mm)	Re* (-)	Pr* (-)	h (W m^{-2} K^{-1})	h_v (W m^{-2} K^{-1})	E = h_v/h (-)
Effect of f	25	2.0	18	625	426	828	1.9
	50	2.0	18	625	426	1502	3.5
	75	2.0	18	625	426	1557	3.7
Effect of A	50	1.0	18	625	426	671	1.6
	50	1.5	18	625	426	799	1.9
	50	2.0	18	625	426	1502	3.5

*Calculated at the inlet temperature $T_{in} = 85°$ C

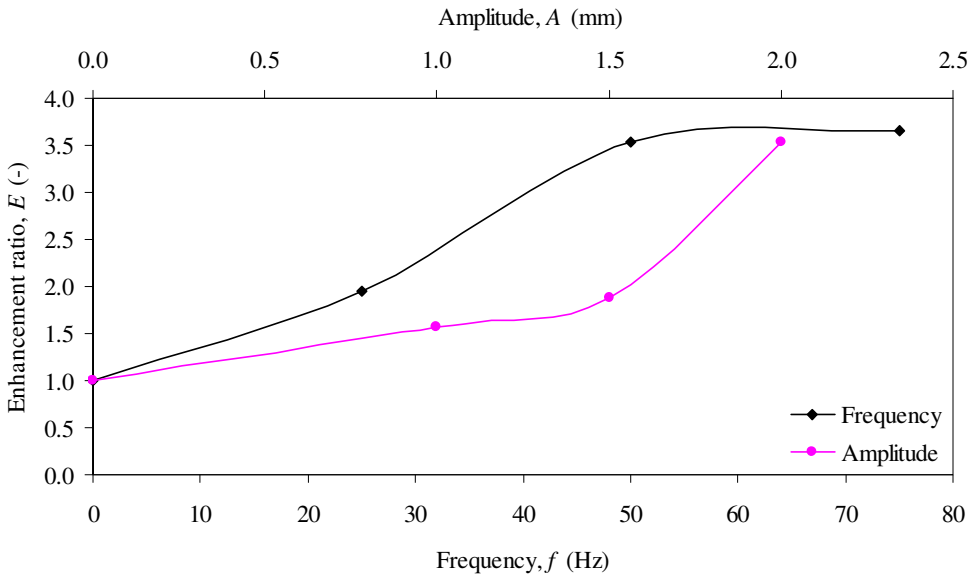

Figure 4.18: Effect of vibration amplitude and frequency on heat transfer coefficient: $n = 1$; $k_0 = 5\times10^{-7}$ Pa s^n; $T_w = 180°$ C; $T_{in} = 85°$ C; $\bar{u} = 0.09$ m s^{-1}; $L = 400$ mm.

In Chapter 3, and also in the work of Deshpande and Barigou (2001), it was shown that for a fixed pressure gradient along the pipe, vibration of isothermal flows caused an enhancement in the flow rate of shear thinning fluids while the flow rate of Newtonian fluids remained unaffected. It was also shown that the enhancement is a function of both vibration frequency and amplitude, but the same enhancement is generated with different amplitude-frequency combinations that correspond to the same peak acceleration $A\omega^2$. Results displayed in Figures 4.19 and 4.20 for different combinations of amplitude and frequency leading to the same peak acceleration show that this is not the case for non-isothermal flows. The temperature distributions are very different, the most uniform distribution being achieved at the largest amplitude and lowest frequency used.

Results also showed that, provided that a high vibration amplitude is used (e.g. $A = R = 10$ mm), a good degree of enhancement in the temperature distribution can be obtained at a very low frequency (e.g. $f = 5$ Hz), as shown in Figure 4.21.

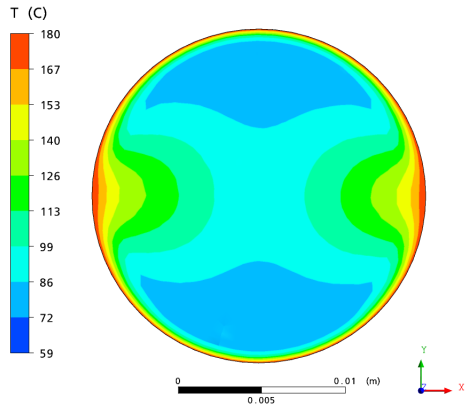

(a) f = 25 Hz, A = 2.0 mm

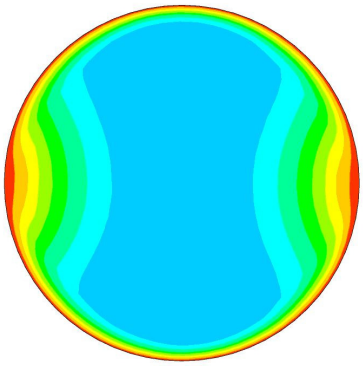

(b) f = 30 Hz, A = 1.39 mm

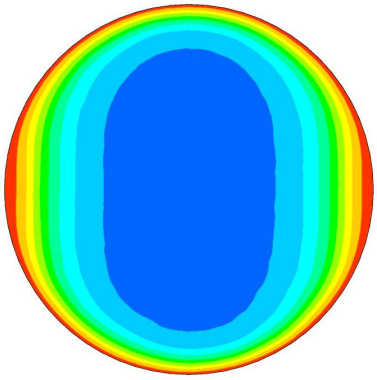

(c) f = 40 Hz, A = 0.78 mm

Figure 4.19: Temperature distribution at different combinations of vibration amplitude and frequency corresponding to the same peak acceleration $A\omega^2$ = 49.3 m s^{-2}:
n = 1; k_0 = 5 × 10^{-7} Pa s^n; T_w = 180° C; T_{in} = 85° C; $\bar{u}$ = 0.09 m s^{-1}; L = 400 mm.

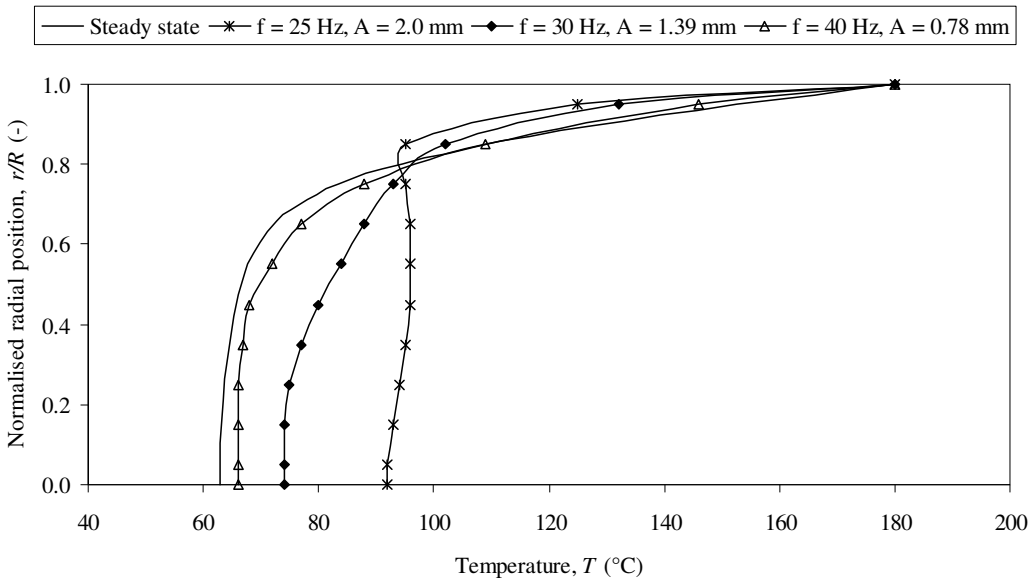

Figure 4.20: Mean temperature profile at different combinations of vibration amplitude and frequency corresponding to the same peak acceleration $A\omega^2 = 49.3$ m s^{-2}:

$n = 1$; $k_0 = 5 \times 10^{-7}$ Pa s^n; $T_w = 180°$ C; $T_{in} = 85°$ C; $\bar{u} = 0.09$ m s^{-1}; $L = 400$ mm.

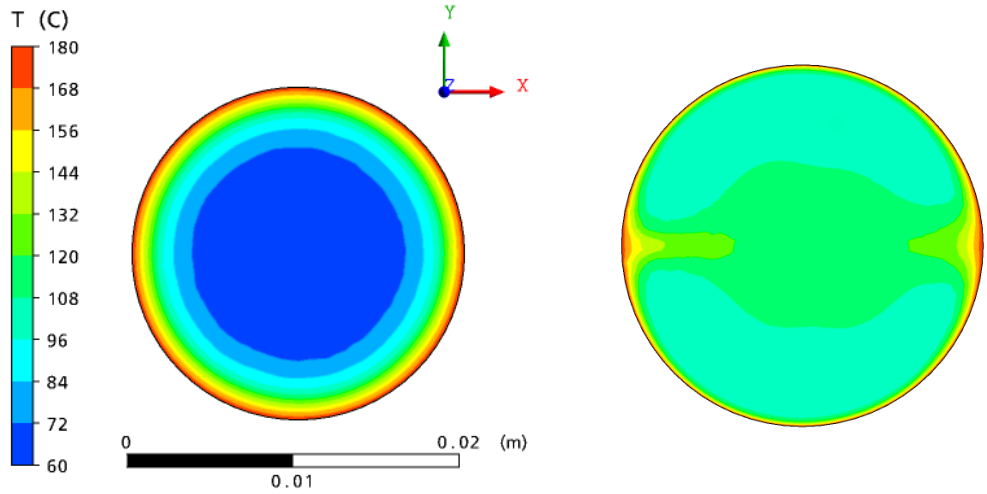

(a) Steady state (b) $f = 5$ Hz, $A = 10$ mm

Figure 4.21: Effect of a high vibration amplitude on temperature distribution:

$n = 1$; $k_0 = 5 \times 10^{-7}$ Pa s^n; $T_w = 180°$ C; $T_{in} = 85°$ C; $\bar{u} = 0.09$ m s^{-1}; $L = 400$ mm.

It can, therefore, be concluded that the mechanism governing the enhancement of heat transfer caused by forced vibration is different from that responsible for flow enhancement in non-Newtonian fluids, the latter being caused by the effects of the added shear on the viscosity of the fluid, while the enhancement in wall heat transfer and temperature uniformity across the pipe is caused by the radial mixing induced by transversal vibration. The extent of this mixing depends on the fluid radial displacement, which in turn is more dependent on vibration amplitude (i.e. pipe wall displacement) than frequency. The vibration Reynolds number defined as

$$\mathrm{Re}_{\mathrm{v}} = \frac{\rho A \omega D}{\mu_e} \tag{4.33}$$

again does not seem to be a criterion that governs the effects observed here since different combinations of A and f leading to the same value of Re_{v} yielded different temperature distributions and h_v values (see Table 4.3).

Thus, it has been established that the benefits of transversal vibration are threefold:

i. a much more uniform temperature profile compared to the steady state,
ii. a rapid development in the temperature profile along the pipe, and
iii. a substantial increase in wall heat transfer.

It is also plausible that the vigorous spiralling fluid motion generated would have further benefits; it should help reduce fouling of the pipe because of the energetic scrubbing action that the fluid motion would create at the wall which is the region of very high vorticity (reaching an order of magnitude of 10^3 s^{-1}), and would also in a two-phase solid-liquid flow help keep the solid particles in suspension, thus, enhancing homogeneity in heat transfer to both the continuous and dispersed phase.

4.5.3. EFFECT OF FLUID RHEOLOGY

4.5.3.1. Newtonian fluids

For a Newtonian fluid, the effect of viscosity was studied by varying k_0 in Equation (4.5) and the temperature maps are depicted in Figure 4.22. Profound effects are observed for both fluids under identical conditions of vibration (A = 2.0 mm, f = 50 Hz). However, as expected, the effects on the uniformity of the temperature profile and on the heat transfer coefficient are relatively more significant for the less viscous fluid. A lower viscosity promotes fluid mixing and therefore gives rise to a more uniform temperature distribution and better radial heat transfer. For a 10:1 reduction in μ, the enhancement in heat transfer was in the ratio 1:2.25. It should be noted that for both fluids, the Reynolds number at the pipe inlet was small (Re < 20).

While a near-uniform temperature distribution was achieved for the less viscous fluid (μ ~ 0.1 Pa s at the inlet) at f = 50 Hz (Figure 4.13), the more viscous fluid (μ ~ 1 Pa s at the inlet) required a higher frequency (f = 100 Hz) to achieve the same level of uniformity. Figure 4.23 shows the temperature distribution at different frequencies for the more viscous fluid (compare with Figure 4.13 for the less viscous fluid).

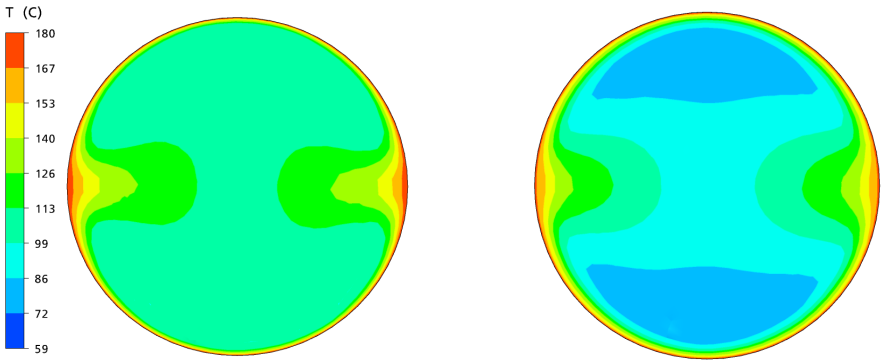

(a) $k_0 = 5 \times 10^{-7}$ Pa s^n (b) $k_0 = 5 \times 10^{-6}$ Pa s^n

Figure 4.22: Effect of viscosity on temperature distribution for Newtonian fluids: n = 1; T_w = 180° C; T_{in} = 85°C; $\bar{u}$ = 0.09 m s^{-1}; A = 2.0 mm; f = 50 Hz; L = 400 mm.

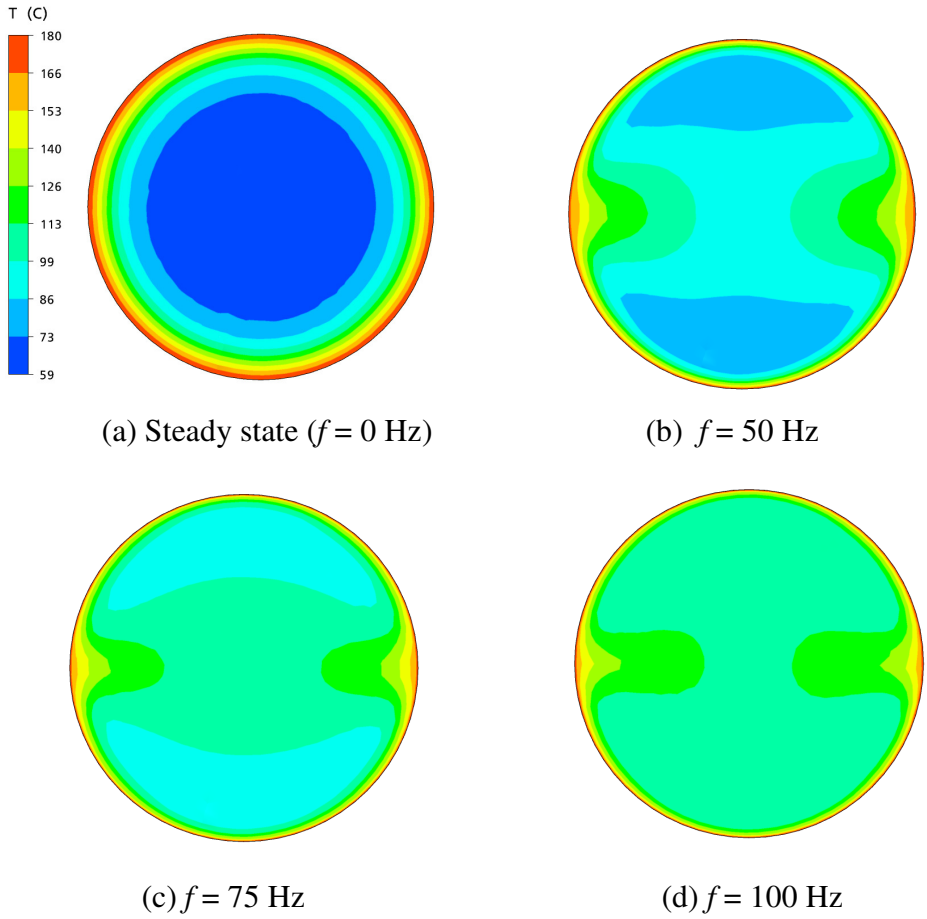

(a) Steady state (f = 0 Hz) (b) f = 50 Hz

(c) f = 75 Hz (d) f = 100 Hz

Figure 4.23: Temperature contours at different frequencies for a high viscosity fluid: n = 1; $k_0 = 5 \times 10^{-6}$ Pa s^n; T_w = 180° C; T_{in} = 85°C; $\bar{u}$ = 0.09 m s^{-1}; A = 2.0 mm; L = 400 mm.

Whilst the temperature distribution for an even more viscous fluid (μ ~ 6.5 Pa s) was only slightly affected by vibration at f = 25 and A = 2.0 mm, a significant enhancement was observed when the amplitude was increased to A = 5.0 mm, as shown in Figure 4.24. This suggests that the more viscous the fluid, the more energetic the vibration needs to be in order to achieve a considerable degree of mixing.

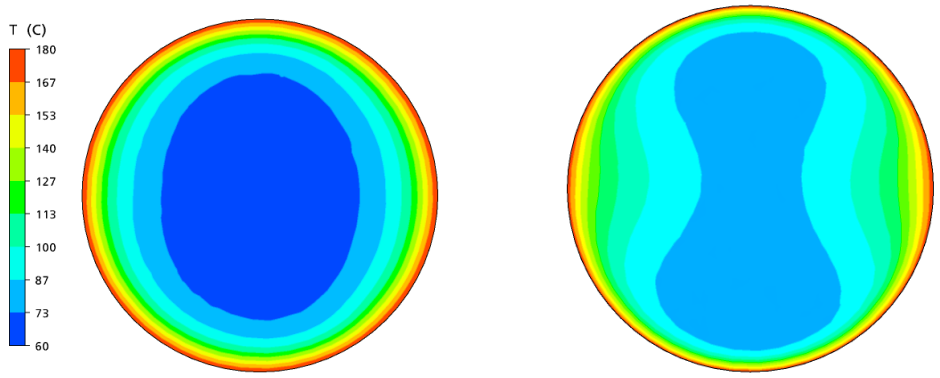

(a) A = 2.0 mm (b) A = 5.0 mm

Figure 4.24: Temperature contours for a highly viscous Newtonian fluid at two different amplitudes:
n = 1; $k_0 = 5 \times 10^{-5}$ Pa s^n; T_w = 180° C; T_{in} = 85°C; $\bar{u}$ = 0.09 m s^{-1};
f = 25 Hz; L = 400 mm.

4.5.3.2. Non-Newtonian fluids

Simulations were also run for power law fluids with n = 1, 0.8, and 0.65, but the same k_0 in Equation (4.6). The temperature contours for these rheologies which are presented in Figure 4.25 demonstrate the effect of the shear thinning index n for identical oscillations. As n reduces the viscosity of the fluid at a given shear rate is lower by virtue of the increased shear thinning. However, in a non-isothermal flow the effect of temperature as expressed by Equation (4.6) on the consistency index k and, hence, viscosity of the fluid is less for a smaller n. Thus, out of these two competing mechanisms, it appears that the degree of non-Newtonian behaviour in the range studied (n = 0.65-1.0) is predominant and leads to relatively more significant vibration effects. The fluid with n = 0.65 has the most uniform temperature distribution across the pipe; such an effect decreases to its minimum as the condition of zero pseudoplasticity is achieved, i.e. n = 1, as shown in Figure 4.25. It should be pointed out that the Newtonian fluid has the highest starting viscosity at the pipe inlet (~ 6.5 Pa s). Note that the steady state temperature distribution is almost identical for all n values in this short pipe.

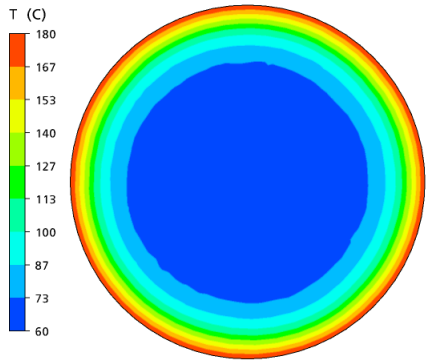

(a) Steady state (all n values)

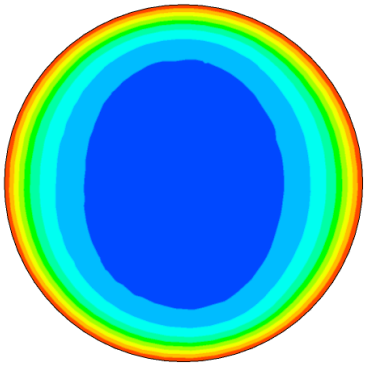

(b) n = 1.0 (f = 25 Hz, A = 2.0 mm)

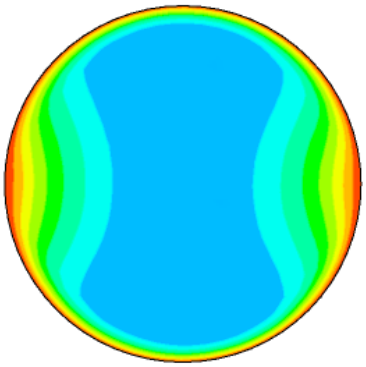

(c) n = 0.8 (f = 25 Hz, A = 2.0 mm)

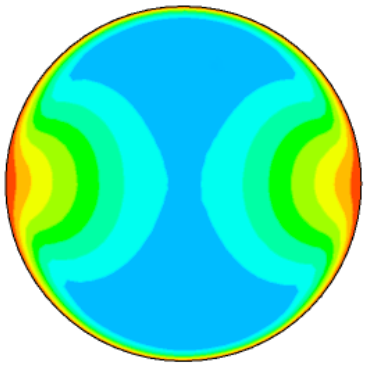

(d) n = 0.65 (f = 25 Hz, A = 2.0 mm)

Figure 4.25: Effect of flow behaviour index on temperature distribution: $k_0 = 5 \times 10^{-5}$ Pa s^n; T_w = 180° C; T_{in} = 85°C; $\bar{u}$ = 0.09 m s^{-1}; L = 400 mm.

4.5.4. EFFECT OF PIPE LENGTH

To achieve a given exit temperature under steady-state, a very long pipe is normally required since the temperature difference between the fluid and the wall decays exponentially along the pipe. With vibration, however, this can be achieved in much shorter pipes as the above results have shown. CFD results also showed that increasing the length of the vibrated pipe (f = 25 Hz, A = 2.0 mm) from 400 to 800 to 1200 mm, whilst keeping all the other parameters constant, results in an improved temperature profile being achieved at the outlet, as shown in Figures 4.26 and 4.27, since the fluid is, thus, subjected to vibration for a longer time. However, the degree of improvement reduces for larger L values as the driving force for heat transfer diminishes with increased uniformity in the temperature distribution.

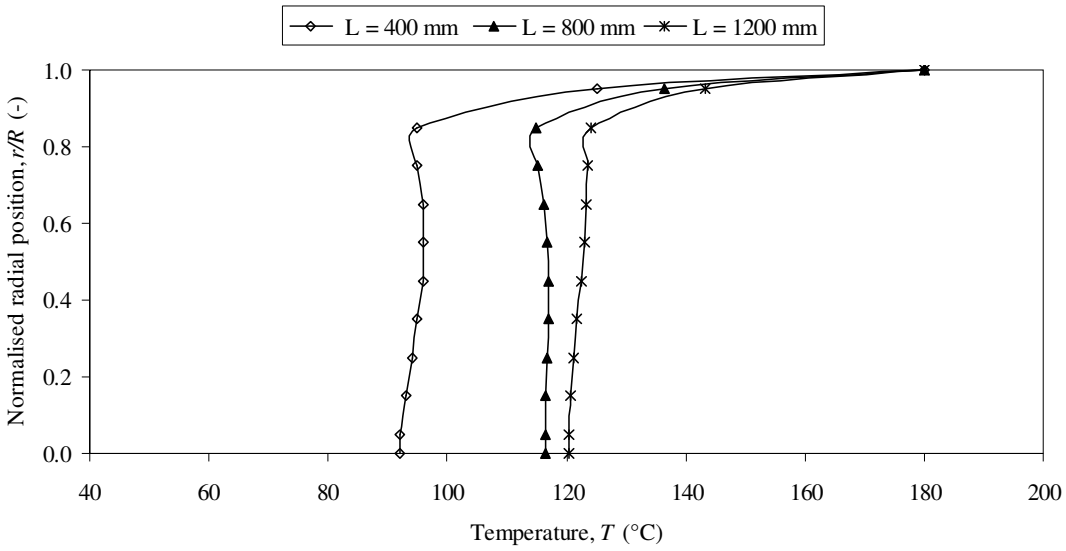

Figure 4.26: Effect of pipe length on temperature profile at the pipe exit: n = 1; $k_0 = 5 \times 10^{-7}$ Pa s^n; T_w = 180° C; T_{in} = 85° C; $\bar{u}$ = 0.09 m s^{-1}; A = 2.0 mm; f = 25 Hz.

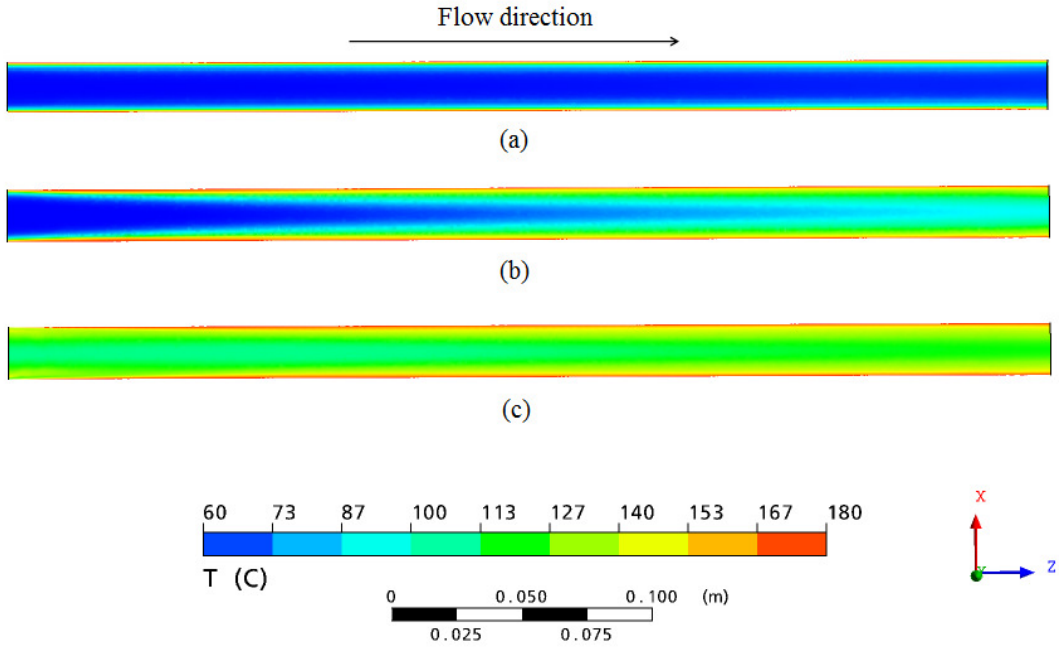

Figure 4.27: Effect of pipe length on temperature distribution along the pipe: (a) steady state; (b) vibration, L = 400 mm; (c) vibration, L = 1200 mm (only the last 400 mm section of the pipe is shown): $n = 1$; $k_0 = 5 \times 10^{-7}$ Pa s^n; $T_w = 180°$ C; $T_{in} = 85°$ C; $\bar{u} = 0.09$ m s^{-1}; $f = 25$ Hz; $A = 2$ mm.

As pointed out above in relation to Figure 4.11, vibration causes the temperature profile to develop rapidly over a relatively short pipe length, which means that the full effects are felt in the early stages of the flow and, hence, the remainder of the pipe is not as effective in improving the temperature distribution.

The results in Figure 2.28 depict typical plots of the variations of the dimensionless temperature profile Ψ (Equation (4.25)) along the pipe centreline which show that a thermal fully developed profile is achieved in the vibrated flow over a relatively short length of pipe. Thus, the thermal entrance length can be reduced substantially by at least an order of magnitude compared to its value in steady state flow (~11 m). Similarly, the value of h is rapidly enhanced in the early stages of the flow, and then drops off and remains unchanged thereafter beyond the thermal entrance region.

Initially, the enhancement in heat transfer increases rapidly due to vibration and the presence of large temperature differences over the cross-section. However, when a near-uniform temperature profile is achieved, the driving force for heat transfer declines and ultimately levels off.

In practice, and since long pipes on the metre scale are usually used, the use of vibration would mean a large enhancement in heat transfer characteristics can be achieved by using frequencies and amplitudes significantly lower than those used in this study. Alternatively, significantly shorter pipes could be used to achieve the same results (but at higher A and/or f). Therefore, the optimum vibration amplitude and frequency required depends, amongst other factors, on the pipe length.

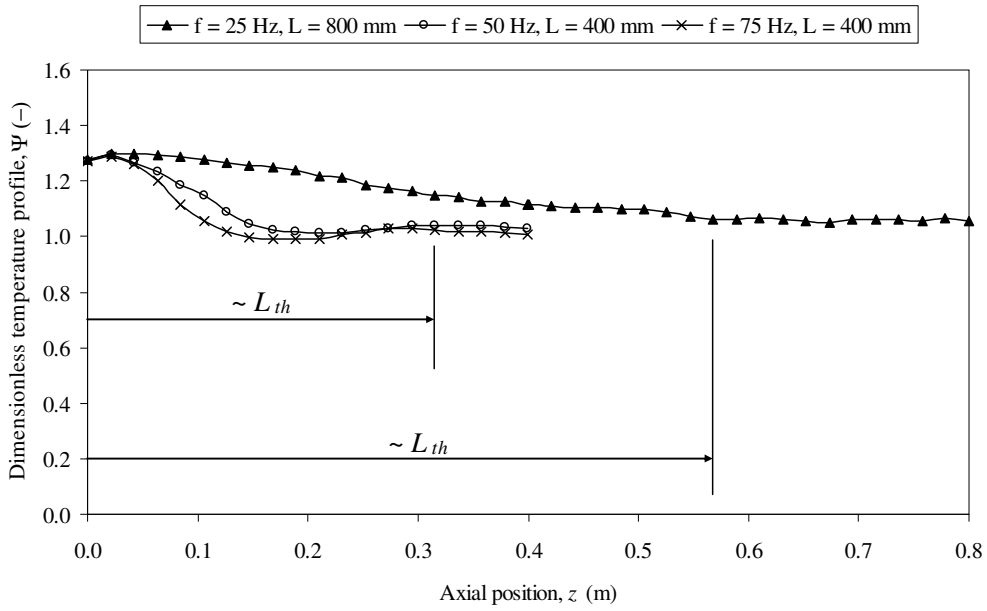

Figure 4.28: Variation of dimensionless temperature profile along the pipe centreline: $n = 1$; $k_0 = 5 \times 10^{-7}$ Pa s^n; $T_w = 180°$ C; $T_{in} = 85°$ C; $\bar{u} = 0.09$ m s^{-1}; $A = 2.0$ mm.

4.5.5. EFFECTS ON VELOCITY PROFILE

In steady flow, CFD results showed that the temperature dependence of the fluid viscosity has a significant flattening effect on the velocity profile, in agreement with the experimental and numerical results of Kwant *et al.* (1973(a) and (b)) (also see Section 4.4.1). However, CFD results for vibrational flow showed that vibration reduces this flattening in the velocity profile, i.e. vibration has a stretching effect on the velocity profile, as shown in Figure 4.29. As the temperature profile becomes more uniform due to vibration, the temperature near the wall decreases compared to the steady state, thus, increasing the viscosity and reducing velocity. On the other hand, the temperature near the pipe centre increases, thus, reducing the viscosity and increasing velocity. This effect increases with vibration frequency and amplitude, as shown in the figure.

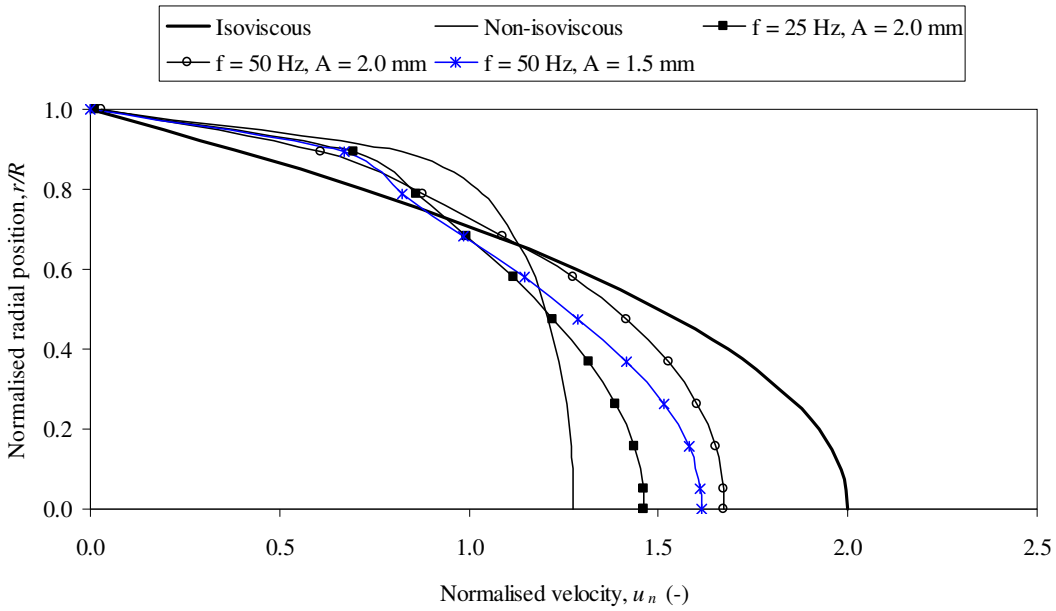

Figure 4.29: Effect of vibration on non-isoviscous velocity profile:
$n = 1$; $k_0 = 5 \times 10^{-7}$ Pa s^n; $T_w = 180°$ C; $T_{in} = 85°$ C; $\bar{u} = 0.09$ m s^{-1}; $L = 400$ mm.

4.6. CONCLUSIONS

A validated CFD model was used to show that a transversal mechanical vibration imposed at the wall of a pipe conveying a non-isothermal laminar flow generates a vigorous swirling fluid motion represented by a strong vorticity field and complex spiralling fluid streamlines and trajectories. This chaotic fluid motion results in convective currents at the wall and substantial radial fluid mixing leading to large enhancement ratios in wall heat transfer and a near-uniform radial temperature distribution. Temperature contours showed that without vibration the temperature profile develops extremely slowly along the pipe, as the temperature difference between the fluid and the wall decays exponentially along the pipe. With vibration, however, the temperature profile develops so rapidly that a given outlet temperature can be achieved along a much shorter pipe length. The thermal entrance length can be reduced by an order of magnitude or more compared to its value in steady state flow.

The observed effects are governed by the amplitude and frequency of vibration so that, for a given fluid viscosity, higher amplitudes and frequencies led to better improvements in heat transfer characteristics. Increasing vibration amplitude from 1.0 mm to 2.0 mm resulted in a substantial increase in the uniformity of the radial temperature distribution. Increasing vibration frequency from 25 Hz to 50 Hz also led to a significant effect. However, the effects appear to be more sensitive to the amplitude than the frequency of wall oscillations. Even low frequency oscillations (f = 5 Hz) were found to generate substantial enhancements in temperature uniformity but at large amplitudes (e.g. A = 10 mm).

More viscous fluids required a more energetic vibration to induce the required mixing. Shear thinning fluids, however, exhibited more pronounced vibrational effects which increased in significance as n was reduced in the range studied (n = 1.0-0.65).

Vibration was also found to have a significant stretching effect on the velocity profile at a constant flow rate. This effect is attributed to the influence of temperature on the viscosity. In steady non-isothermal flow, the velocity profile is flattened compared to

the isothermal profile. However, as the temperature profile becomes more uniform due to vibration, the temperature near the wall decreases compared to the steady state, thus, increasing the viscosity in this region and reducing velocity. On the other hand, the temperature near the pipe centre increases, thus, reducing the viscosity and increasing velocity there.

It can be argued that the strong spiralling fluid motion generated would have added benefits in reducing fouling of the pipe because of the cleaning action that the fluid motion would create at the wall, and in a two-phase solid-liquid flow it would help keep the solid particles in suspension and enhance liquid-particle heat transfer.

These results open up new opportunities for the potential application of mechanical vibration as an elegant non-intrusive technique in processes where reducing non-uniformity in heat transfer represents a challenge, such as in the thermal sterilisation of foods. This work can be extended in the future to the more complex flows of solid-liquid mixtures. In the following chapter, an investigation is carried out of the steady isothermal flow of solid-liquid suspensions as a first step in extending the vibration studies to such multiphase systems.

NOMENCLATURE

a	wall surface area, m^2
A	vibration amplitude, m
C_p	specific heat capacity, J kg^{-1} K^{-1}
D	pipe diameter, m
E	enhancement ratio, dimensionless
E_a	activation energy, kJ mol^{-1}
f	vibration frequency, Hz
Gr	Graetz number, dimensionless
h	heat transfer coefficient, W m^{-2} K^{-1}
h_v	vibrational heat transfer coefficient, W m^{-2} K^{-1}
k	fluid consistency index, Pa s^n
k_0	pre-exponential factor, Pa s^n
L	pipe length, m
L_h	hydrodynamic entrance length, m
L_{th}	thermal entrance length, m
$\dot{m}$	mass flow rate, kg s^{-1}
Nu	Nusselt number, dimensionless
n	flow behaviour index, dimensionless
p	fluid pressure, Pa
Pr	Prandtl number, dimensionless
r	radial coordinate, m
R	pipe radius, m
R_G	ideal gas constant, 8.314 J mol^{-1} K^{-1}
Re	Reynolds number, dimensionless
Re_v	vibration Reynolds number, dimensionless
t	time, s
T	local temperature, °C
T_c	centre temperature, °C
T_{in}	area-averaged inlet temperature, °C
T_m	area-averaged temperature at a given section, °C
T_{out}	area-averaged outlet temperature, °C
T_w	wall temperature, C
ΔT_m	log-mean temperature difference, °C
u	axial velocity, m s^{-1}
$\overline{u}$	mean axial velocity, m s^{-1}
u_n	normalised axial velocity, m s^{-1}
u_x	fluid velocity in the x direction, m s^{-1}
u_y	fluid velocity in the y direction, m s^{-1}
$\dot{x}$	wall velocity in the x direction, m s^{-1}
x	coordinate in horizontal direction, m
y	coordinate in vertical direction, m
z	coordinate in axial direction, m

Greek letters

$\dot{\gamma}$	shear rate, s^{-1}
ζ	vorticity, s^{-1}
η	apparent viscosity, Pa s
θ	dimensionless temperature, dimensionless
λ	thermal conductivity, W m^{-1} K^{-1}
μ	Newtonian viscosity, Pa s
μ_e	effective viscosity, Pa s
ρ	fluid density, kg m^{-3}
τ	shear stress, Pa
Ψ	dimensionless temperature profile, dimensionless
ω	angular frequency, s^{-1}

REFERENCES

Barigou, M., Mankad, S. & Fryer, P.J. 1998. Heat transfer in two-phase solid-liquid food flows: a review. *Trans IChemE*, 76, Part C, 3-29.

Bird, R.B., Armstrong, R.C., Hassager, O. & Curtiss, C.F. 1987. Dynamics of polymeric liquids, Vol. 1: Fluid Mechanics. 2nd Edition, John Wiley.

Çengel, Y.A. 2003. Heat Transfer: A Practical Approach. McGraw Hill Professional.

Chhabra, R.P. & Richardson, J.F. 1999. Non-Newtonian flow in the process industries: Fundamentals and engineering applications. Butterworth Heinemann.

Christiansen, E.B. & Craig, Jr., S.E. 1962. Heat transfer to pseudoplastic fluids in laminar flow. *AIChE J*., 8 (2), 154-160.

Deshpande, N. S. & Barigou, M. 2001. Vibrational Flow of non-Newtonian Fluids, *Chemical Engineering Science*, 56 (12), 3845-3853.

Holdsworth, S.D. 2004. Improving the Thermal Processing of Foods. Richardson, P. (Editor). Woodhead Publishing Limited, Cambridge, England.

Jung, A. & Fryer, P.J. 1999. Optimising the quality of safe food: Computational modelling of a continuous sterilisation process. *Chemical Engineering Science*, 54, 717-730.

Klaczak, A. 1997. Report from experiments on heat transfer by forced vibrations of exchangers. *Heat and Mass Transfer*, 32, 477-480.

Kreith, F. & Bohn, M.S. 1986. Principles of Heat Transfer. 4th Edition. Harper & Row, Publishers. New York.

Kwant, P.B, Zwaneveld, A. & Dijkstra, F.C. 1973(a). Non-isothermal laminar pipe flow – I. Theoretical. *Chemical Engineering Science*, 28, 1303-1316.

Kwant, P.B, Fierens, R.H.E. & Van Der Lee, A. 1973(b). Non-isothermal laminar pipe flow – II. Experimental. *Chemical Engineering Science*, 28, 1317-1330.

Lareo, C., Nedderman, R.M. & Fryer, P.J. 1997. Particle velocity profiles for solid-liquid food flows in vertical pipes. Part II. Multiple particles. *Powder Technology*, 93, 35-45.

Lee, Y. H. & Chang, S. H. 2003. The effect of vibration on critical heat flux in a vertical round tube. *Journal of Nuclear Science and Technology*, 40, (10), 734-743.

Liao, H-J., Rao, M.A. & Datta, A.K. 2000. Role of thermo-rheological behaviour in simulation of continuous sterilization of a starch dispersion. *Trans IChemE*, 78, Part C, 48-56.

Lin, S.H. 1976. Continuous high-temperature/short-time sterilization of liquid foods with steam-injection heating. *Chemical Engineering Science*, 31, 77-82.

Lyche, B.C. & Bird, R.B. 1956. The Graetz-Nusselt problem for a power-law non-Newtonian fluid. *Chemical Engineering Science*, 6, 35-41.

Rao, M.A., Rizvi, S.S.H., & Datta, A.K. (Editors). 2005. Engineering properties of foods. Third edition. CRC Press.

Rohsenow, W.M., Hartnett, J.P., & Cho, Y.I. 1998. Handbook of heat transfer. McGraw-Hill Professional.

Sastry, S.K., Shen, G.Q. & Blaisdell, J.L. 1989. Effect of Ultrasonic Vibration on Fluid-to-Particle Convective Heat Transfer Coefficients. *Journal of Food Science*, 54 (1), 229-230.

Simpson, S.G. & Williams, M.C. 1974. An analysis of high temperature short time sterilization during laminar flow. *Journal of Food Science*, 39, 1047-1054.

Steffe, J.F. 1996. Rheological methods in food process engineering. 2nd Edition. Freeman Press.

Tanner, R.I. 1985. Engineering Rheology. Clarendon Press, Oxford.

CHAPTER 5

SOLID-LIQUID FLOW OF COARSE NEARLY-NEUTRALLY BUOYANT PARTICLES IN NON-NEWTONIAN FLUIDS

Summary

While the measurement of solid and liquid phase velocity profiles in industrial solid-liquid mixtures is usually difficult, the results reported in this chapter show that CFD is capable of providing good predictions of these velocity profiles. The flow of coarse solid particles in non-Newtonian carrier fluids was numerically simulated using an Eulerian-Eulerian CFD model. The study is concerned with nearly-neutrally buoyant particles of 2-10 mm diameter conveyed by shear thinning fluids in laminar flow, in a 45 mm diameter pipe at concentrations up to 40% v/v. A small number of simulations were also run using shear-thickening carrier fluids. The flow fields predicted by the model are successfully validated by experimental measurements of particle velocity profiles obtained using Positron Emission Particle Tracking (PEPT) technique, while solid-liquid pressure drop is validated using relevant correlations gleaned from the literature. The effects of various parameters on the flow properties of the solid-liquid mixtures studied have been investigated over a wide range of conditions. Whilst the effects of varying the power law parameters and the mixture flow rate for shear thinning fluids are relatively small, particle diameter and concentration have a significant bearing on the flow regime, the uniformity of the normalised particle radial distribution, the normalised velocity profiles of both phases, and the magnitude of the solid-liquid pressure drop. The maximum particle velocity is always significantly less than twice the mean flow velocity for shear thinning fluids, but it can exceed this value in shear thickening fluids. In vertical down-flow, particles are uniformly distributed over the pipe cross section, and particle diameter and concentration have little effect on the normalised velocity and concentration profiles. Pressure drop, however, is greatly influenced by particle concentration.

5.1. LITERATURE REVIEW

5.1.1. MULTIPHASE SOLID-LIQUID FLOW

Multiphase flow of solid-liquid mixtures is encountered in a wide spectrum of industrial processes from the chemical, petrochemical, pharmaceutical, food, and biochemical industries, to mining, construction, pollution control, and power generation. Applications include the hygienic movement and processing of food and pharmaceutical products, the transport of coal and ores, and the secure transportation of effluent and waste products. In such systems, solid-liquid mixtures are conveyed in horizontal or/and vertical pipes.

Solid-liquid flows are usually complex and their behaviour is governed by a large number of factors, giving rise to a wide range of flow regimes. Among such factors are flow rate, pipe diameter and orientation, carrier fluid physical and rheological properties, and particle size, density and concentration. There is, therefore, an evident need to classify solid-liquid mixtures in order to provide a rational basis for describing their flow behaviour.

Classification of solid-liquid mixtures is a long standing theme in fluid mechanics. In one scheme of classification that recurs frequently in the literature, the behaviour of solid-liquid mixtures in horizontal pipes is classified into two categories: settling and non-settling slurries. The settling behaviour is usually associated with large solid particles, whereas the non-settling behaviour is frequently associated with fine particle suspensions (Brown and Heywood, 1991). However, this classification fails to describe the flow behaviour of large neutrally or nearly-neutrally buoyant particle suspensions encountered, for example, in the food industry.

Another scheme of classification describes two extremes of slurry behaviour based on the physical appearance of the slurry: homogeneous and heterogeneous slurries (Shah and Lord, 1991). This classification provides an indication of the distribution of solid particles over the pipe cross-section under flow conditions. Homogeneous mixtures

are those in which the distribution of solid particles is uniform over the pipe cross-section. Suspensions of fine solid particles, where the two phases do not separate to any significant extent during flow, tend to be reasonably homogeneous and are usually treated as such. Although a homogeneous solid-liquid suspension is essentially made up of two distinct phases, there are situations in which particular slurries can be described satisfactorily by single-phase models. Heterogeneous slurry flow, on the other hand, applies to slurries of usually coarse particles where the two phases behave distinctly with a pronounced particle concentration gradient which is a result of particle settling under the influence of gravity. The study of such slurries is therefore more complicated since the single-phase flow approximation is not applicable to such essentially heterogeneous flows.

Although the homogeneous and heterogeneous flow regimes seem distinct, the transition from one regime to the other is not clear cut, and there are flow situations which have some of the characteristics of each regime. For example, food particulates usually have densities close to that of the carrier fluid, resulting in little or no tendency for settling under gravity, a characteristic of homogeneous flows. On the other hand, in the presence of coarse solid particles common in food suspensions, the two phases behave distinctly and the mixture is considered heterogeneous. An intermediate flow has been reported to occur when conditions for homogeneous and heterogeneous flow exist simultaneously (Legrand *et al*., 2007).

The main distinction between homogeneous and heterogeneous flow lies in the distribution of solid particles in the pipe cross-section. Until recently, no quantitative criterion has been available in the literature to describe particle distribution. The criteria usually used to delineate different flow regimes are generally subjective. Legrand *et al*. (2007) used a method based on flow visualisation in order to characterise food suspensions with quantitative criteria by measuring the cumulative distribution of particles. The authors used large food particles with densities of 1048 and 1116 kg m^{-3} at concentrations up to 26% w/w.

A major factor which influences the flow behaviour of solid-liquid mixtures is the rheological properties of the carrier fluid. In many situations, viscous Newtonian or non-Newtonian fluids are used as the carrier media. These carrier fluids are used because: (a) they are in some cases dictated by the process, e.g. Newtonian heavy oil to transport solids out of wells, and continuous thermal processing of particulate food products in non-Newtonian fluids; and (b) when the flow is laminar, the transport of coarse particles in fluids of non-Newtonian rheology offers certain advantages:

(i) the apparent viscosity of a shear thinning fluid is a maximum at the centre of the pipe and this aids particle suspension (though some of this effect may be offset by the propensity of migration across streamlines and the enhanced settling velocities in sheared fluids);
(ii) the apparent viscosity is a minimum at the pipe wall, thus, the frictional pressure drop will be low and will increase only relatively slowly with increasing mixture velocity, hence leading to a lower power consumption; and
(iii) if the fluid exhibits a yield stress, it tends to assist the suspension of coarse particles in the central region of the pipe (Chhabra and Richardson, 1999).

In practical situations, the transport of particulate matter can occur with a wide size distribution (e.g. coal dust to large lumps); in this case the fine colloidal particles tend to form a pseudo-homogeneous shear thinning medium of enhanced apparent viscosity and density in which the coarse particles are conveyed. On the other hand, the heavy medium may consist of fine particles of a different solid, particularly one of higher density such as in the transport of overburden or cuttings in drilling muds. In such cases, the liquid vehicle usually behaves as a Bingham plastic whose yield stress and plastic viscosity increase as the solids concentration increases (Maciejewski *et al.*, 1997). The use (optional or otherwise) of non-Newtonian carrier fluids for processes which involve conveying of slurries through pipes, pipelines, or channels has been restricted by a lack of understanding of the behaviour of these flows.

The vast majority of the documented data on solid-liquid flow relate to water-based slurries of fine particles. The flow of particles in non-Newtonian fluids has only been

reported in a few studies. Charles and Charles (1971) transported fine sand particles in shear thinning clay suspensions. The head loss was six times smaller compared to that incurred using water as the carrier fluid. Similarly, Ghosh and Shook (1990) reported a reduction in pressure gradient for the flow of fine sand particles in a shear-thinning CMC solution, but not for larger pea gravel particles; this was attributed to the fact that these larger particles were conveyed in the form of a sliding bed and not as a suspension. Duckworth *et al*. (1983, and 1986) conveyed coal particles (up to 19 mm) in a slurry of fine coal which behaved as a Bingham plastic.

5.1.2. SOLID-LIQUID FOOD MIXTURES

Solid-liquid food mixtures are characterised by coarse solid particles with a small density difference with the carrier fluid, which in turn is usually highly viscous and often non-Newtonian. A fundamental understanding of the flow behaviour of solid-liquid food suspensions in horizontal and vertical pipes is essential for the design of food processing equipment, especially in food sterilisation. Continuous thermal sterilisation is the most significant sterilisation method, whereby the product is heated in a heating tube up to a temperature sufficient to kill all viable organisms, held at the same temperature in a holding tube for sufficient time to ensure temperature homogeneity and sterility, and then cooled (see Chapter 4, Section 4.1.1 for more details on continuous thermal sterilisation). Because solid-liquid food mixtures are usually heterogeneous (Lareo *et al*., 1997(a)), the process can involve a wide distribution of particle concentration, velocity, residence time, and, as a result, temperature; thus different parts of the mixture will be subject to different conditions leading to unpredictable variations in product quality. Usually, the holding tube length is designed based on the residence time of a Newtonian fluid in laminar flow where the maximum velocity is twice the mean flow velocity (Lareo and Fryer, 1998). This conservative assumption may result in an overcooked, although sterile, product (Zhang and Fryer, 1993; Mankad *et al*., 1995).

The fluid mechanics of such flows is still poorly understood. As noted by several researchers (e.g., Lareo *et al*., 1997(a); Fairhurst, 1998; Fairhurst *et al*., 2001;

Chakrabandhu and Singh, 2005; and Legrand *et al*., 2007), there is a lack of data on the flow behaviour of solid-liquid food mixtures. As a result, it is presently difficult to design equipment for the continuous aseptic processing of food mixtures that ensures both treatment homogeneity and conservation of product quality.

A number of studies have reported results relating to the horizontal pipe flow of solid-liquid food mixtures using real or model foods and a variety of experimental techniques. A detailed review of the literature up until 1997 can be found in Lareo *et al*. (1997(a)). However, information is still notably lacking at high solids concentrations, and some experimental results lack consistency. In particular, measurements and calculations of particle velocity and concentration profiles as well as solid-liquid pressure drop are scarce.

5.1.3. SOLID-LIQUID VELOCITY PROFILES

The velocity field of solid particles in a solid-liquid mixture determines the residence time distribution of particles, which is of particular relevance to the aseptic processing of solid-liquid food mixtures, where it is essential to ensure that the fastest moving particles receive adequate thermal treatment without causing overcooking and product quality degradation.

5.1.3.1. Horizontal flow

Velocity profiles have rarely been measured for coarse particle mixtures, particularly at high solids concentrations. Newitt *et al*. (1962) studied the horizontal flow of suspensions of Perspex, sand, gravel, and zircon particles in water. It was observed that the position of the maximum velocity was not at the pipe centreline but shifted upwards. The velocity profile of the mixture below this maximum-velocity point was found to be parabolic, whereas above this point it was found to fit a $1/7^{th}$ power law profile. The presence of solid particles reduced the liquid velocity in the pipe centre.

For the horizontal flow of coarse nearly-neutrally buoyant particles in suspensions, the literature is particularly limited. Roberts and Kennedy (1971) measured particle

and liquid velocities for suspensions of neutrally buoyant cubic and cylindrical solid particles of 1015 and 1052 kg m^{-3} density, respectively, and up to 30% solids concentration in a horizontal pipe of 50.8 mm diameter. Fluid and particle velocities were measured using pulsed injections of salt water and tagged radioactive particles, respectively. Solid particles were found to travel considerably faster than the mean liquid velocity, with the difference increasing with particle concentration.

Kowalewski (1980) used an Ultrasound Doppler technique to measure the velocity profiles of aqueous suspensions of spherical particles up to 50% concentration with a density lower than that of the carrier fluid and for particle-to-tube diameter ratios of 0.001 – 0.05. The velocity profiles were found to be blunted and were characterised by a simple empirical correlation. The degree of blunting was found to increase with particle concentration and size.

Altobelli *et al*. (1991) used Nuclear Magnetic Resonance (NMR) imaging techniques to measure the fluid velocity profile and particle distribution in solid-liquid suspensions flowing in a horizontal pipe in laminar flow for particle concentrations up to 39% v/v. The solid particles, which were made of plastic, had a diameter of 0.76 mm and density of 1030 kg m^{-3}, and the carrier fluid was a Newtonian viscous oil with a density of 875 kg m^{-3}. Experiments were conducted for mean fluid velocities in the range 1.7-22.3 cm s^{-1}. It was found that for particle concentrations up to 10% v/v the ratio of the centreline velocity to the mean mixture velocity exceeded 2.0, but decreased monotonically at higher concentrations.

Ding *et al*. (1993) performed a numerical analysis, using a computer programme (COMMIX-M), of the solid-liquid systems investigated by Altobelli *et al*. (1991). The numerical predictions of the fluid velocity were in close agreement with the experimental data. The authors concluded that further developments in the multiphase solid-liquid model used would lead to increased confidence in the capability of the model in simulating dense slurry flow systems, and that such developments would result from comparisons with a wide data base of experimental results.

Fregert (1995) studied the horizontal laminar flow of suspensions of nearly neutrally-buoyant particles in Newtonian carrier fluids in a 45 mm diameter pipe. The suspensions were fairly dilute with particle concentrations up to 10%, and the particle-to-pipe diameter ratio ranged from 0.10 to 0.16. The study determined both liquid and solid velocity profiles in addition to the particle concentration profile. It was found that (i) the maximum particle velocity occurred 4-6 mm above the pipe centreline, (ii) particle velocity was always smaller than the liquid velocity, and (iii) liquid velocity was generally slightly higher than that of the carrier fluid flowing alone.

McCarthy *et al*. (1997) used NMR to measure the velocity profile of solid-liquid suspensions as a function of flow rate, solids concentration and particle size. The pipe had a diameter of 26.2 mm, and the solid particles were alginate spheres of 2.5 mm and 5.0 mm diameters. The particles were suspended at concentrations of 10%, 20%, and 30% w/w in a 0.5% w/w carboxy-methyl-cellulose (CMC) carrier fluid whose rheology was best described by a power law model. The average flow velocity ranged between 2-35 cm s^{-1}. The authors described the solid-liquid suspension with a power law model by measuring the degree of bluntness in the solid-liquid velocity profile and then calculating the corresponding flow behaviour index which would result in the same degree of bluntness in single-phase flow. For the CMC solution flowing alone, the velocity profile, normalised using the mean flow velocity, showed increased bluntness as the flow rate was increased. For solid-liquid suspensions, the bluntness in the velocity profile was found to increase with particle concentration. The degree of bluntness was measured using the ratio of the flow behaviour index of the CMC carrier fluid flowing alone to that of the solid-liquid suspension. This ratio was found to reach 0.38 at 30% w/w solids.

Fairhurst *et al*. (2001) and Barigou *et al*. (2003) used the technique of Positron Emission Particle Tracking (PEPT) to determine the trajectories and velocity profile of coarse nearly-neutrally buoyant particles in non-Newtonian CMC carrier fluids. The solid particles used as model food particles were calcium alginate spheres of 5 and 10 mm diameters and 1020 kg m^{-3} density. Experiments were carried out at particle concentrations of 21 ± 2%, 30 ± 2% and 40 ± 2% v/v and mixture velocities

ranging from 24 to 125 mm s^{-1}. The non-Newtonian carrier fluids employed were 0.3%, 0.5%, and 0.8% w/w CMC solutions the rheology of which was characterised by an Ellis model. A gravity-driven flow loop was used wherein the solid-liquid mixture flowed through a down pipe followed by a horizontal pipe, each of 1400 mm length and 45 mm inner diameter.

The authors identified two flow situations: concentric flow and capsule flow. The concentric flow pattern, observed at moderately high particle concentrations (e.g. 30% v/v), was characterised by a slow moving annulus close to the pipe wall and a faster moving central region. In the annular region, the effect of particle settling due to gravity was observed. At the base of the pipe, particles travelled at lower velocities than those at the top of the pipe. Except at the base of the pipe, particles travelled at velocities greater than the mean mixture velocity. At a higher particle concentration (40% v/v), and as particles were confined in a space that was insufficient to accommodate the spatial configuration of concentric flow, particles formed agglomerates, thus leading to capsule flow.

Two types of solid phase velocity profile were measured: global velocity profile and top to bottom velocity profile. The global velocity profile was measured by dividing the pipe cross section into four concentric regions and calculating the mean axial velocity of particles in each region. The top to bottom profile was measured by dividing the pipe cross section into eight sections, four above and four below the pipe centreline, and then calculating the mean velocity in each section as a function of radial position. Global solid phase velocity profiles showed considerable flattening compared with the theoretical single-phase carrier fluid profile and were symmetrical about the pipe centreline. Such profiles showed significant deviations from the actual velocities of the solid particles, particularly near the pipe wall, since the global velocity profiles do not take account of the asymmetric flow of the particles due to particle settling. Top to bottom velocity profiles, on the other hand, were found to be generally asymmetrical around the pipe centreline since they do take into account the asymmetric nature of the flow. Such profiles were, therefore, more representative of

the actual particle velocities. Particles near the top of the pipe cross-section travelled at axial velocities significantly higher than those at the base of the pipe.

The degree of asymmetry in the top to bottom velocity profile, measured using a 'skewness parameter', was found to depend on the particle size and concentration, mean mixture velocity and carrier fluid viscosity. Asymmetry was strongly evident at the lowest particle concentration used (21% v/v) due to particle settling, with the position of the fastest flowing particles shifted ~2.5 mm above the centreline; while at higher particle concentrations velocity profiles were more symmetrical as particle settling was limited. The skewness of the solid phase velocity profile for 5 mm particles was found to be higher than that for 10 mm particles. It was also found that increasing the apparent viscosity of the carrier fluid reduced the skewness of the solid phase velocity profile.

In another study, Le Guer *et al*. (2003) used Ultrasound Doppler Velocimetry (UDV) to obtain the velocity profiles of suspensions of buoyant non-spherical particles (few millimetres in dimensions) in water, intended to mimic the flow behaviour of ice-water mixtures. Particle concentrations up to 20% w/w were investigated. The basic principle employed in UDV is the measurement of the time lapse between the transmission of ultrasonic bursts and reception of echoes from the flowing particles, thus allowing the measurement of the position of the particles. Flow patterns were determined by visualisation of the flow mixture. Two flow patterns were observed: flow with a stationary bed at low flow velocities, with particles rising to the top of the pipe and forming a stationary bed; and flow with a moving bed. Due to the formation of these beds of particles, the velocity profile of the mixture was found to be significantly deformed compared with the velocity profile of water flowing alone. The deformation of the velocity profile increased with particle concentration.

5.1.3.2. Vertical flow

The solid and liquid velocity profiles in vertical flow have been studied by several researchers. Durand (1953) measured velocity profiles for sand-water mixtures with particle diameters of 0.18, 1.0 and 4.6 mm, and found that the presence of solid particles up to 8% v/v had no effect on the velocity profile.

Newitt *et al*. (1961) measured liquid phase velocity profiles for the up-flow of suspensions of sand particles in water up to 15% v/v solids. Particle diameter was much smaller than the pipe diameter. It was observed that the velocity profile was flat over a large section of the pipe. As the particle concentration was increased, the liquid velocity at the pipe centre decreased and the velocity profile became flatter with a very steep gradient near the wall. At high flow velocities, coarse particles tended to move as a central core leaving an almost particle-free annulus at the wall, while at low velocities the distribution of particles was fairly uniform across the pipe cross-section. Similar results have been reported by several researchers amongst them Durand (1952), Toda *et al*. (1973) and Alajbegovic *et al*. (1994).

Sinton and Chow (1991) used NMR to study the Poiseuille Newtonian flow of suspensions of neutrally-buoyant plastic particles in a vertical tube. The particles had a median diameter of 0.131 mm and were suspended at concentrations of 21-52% v/v. It was found that the shape of the fluid velocity profile changed with particle concentration. The velocity profile was parabolic at low concentrations and flattened at higher concentrations. Ding *et al*. (1993) used the computer code COMMIX-M to compute fluid velocities for the same solid-liquid systems for which the experimental data of Sinton and Chow (1991) were obtained, and reasonable agreement was found.

Using a laser-Doppler anemometer, Alajbegovic *et al*. (1994) determined particle and fluid velocity profiles for dilute aqueous suspensions of non-neutrally buoyant particles of 2 mm diameter in vertical up-flow. Particles denser than the carrier fluid lagged the fluid close to the pipe centreline, but those flowing near the pipe wall were faster than the fluid. On the other hand, particles less dense than the carrier fluid travelled faster than the fluid at all radial positions. It was also observed that the

dense particles showed a uniform distribution across the pipe cross-section at low flow rates, while coring was observed at higher flow rates where a region near the pipe wall was observed to contain almost no particles. For the less dense particles, however, the distribution profile showed a maximum close to the pipe wall for low flow rates which flattened at higher flow rates.

Lareo *et al*. (1997(b) and 1997(c)) presented experimental results on particle velocity profiles for solid-liquid food mixtures flowing upwards in a 44 mm diameter pipe. A video recording technique was used to determine the position and axial velocity of tracer particles, thus allowing the calculation of velocity and distribution profiles of the particles. Particle concentrations up to only 10% w/v were used since at higher concentrations the tracer could not be reliably seen among the large number of particles in the pipe. The food particles used were cubed carrots with edge sizes within 6-10 mm and densities ranging mainly between 1016-1030 kg m^{-3}. The carrier fluids were 0.3% and 0.8% w/w CMC solutions (non-Newtonian). In most of the cases studied, no particles were observed to flow near the pipe wall. Results showed that as the particle concentration was increased, (i) the number of particles flowing in the central region of the pipe increased, (ii) the velocity profile of particles became flat near the pipe centreline, and (iii) some particles were seen to flow close to the wall. At the highest particle concentration used, the particle distribution was nearly uniform. Particle size was found to have little effect on the particle velocity profile near the pipe centreline, but increasing the particle size reduced the velocity of particles flowing near the pipe wall. Particle velocity near the centreline was similarly unaffected by the carrier fluid viscosity, but near the pipe wall velocity increased with viscosity.

An important conclusion of that work was that the assumption of Newtonian laminar flow for solid-liquid food mixtures is highly conservative since the maximum particle velocity measured experimentally never reached twice the mean mixture velocity as would be expected in a Newtonian fluid. The authors also stated that predicting particles velocities computationally was not then possible since particle behaviour could not be incorporated into Computational Fluid Dynamics (CFD) programmes.

Lareo and Fryer (1998) carried out an experimental study of the up- and down-flow of solid-liquid food mixtures in vertical pipes in order to determine the particles' time-of-flight. A metal detector technique was used, whereby a tracer is introduced into the system and is then detected as it passes between four metal coils. Cubed carrots were used as food particles at concentrations up to 26% w/v, with water, 0.3% and 0.8% w/v CMC, and 4% w/v starch solutions as the carrier fluids. Time-of-flight distributions were strongly dependent on the carrier fluid rheology and flow pattern (laminar or turbulent). For CMC carrier fluids, particles were found to travel rapidly in the central region of the pipe and more slowly near the pipe wall; this distribution was attributed to particle migration in the pipe. Slip velocity was also measured to show the difference between solid and liquid behaviour. For the starch solution, slip velocity was found to depend on particle concentration. At low particle concentrations the mean particle velocity was smaller than the mean liquid velocity, but increased and exceeded the mean liquid velocity at higher concentrations. For water and the CMC solutions, however, the mean particle velocity was always greater than the mean liquid velocity, resulting in a negative mean slip velocity which was nearly independent of particle concentration. It was thus shown that the rheology of the carrier fluid is a major factor in determining the behaviour of the solid particles.

Fairhurst *et al*. (2001) measured the velocity profile of solid particles in vertical down-flow using PEPT. The solid particles had a diameter of 10 mm and a density of 1020 kg m^{-3} and were suspended at 21%, 30% and 40% v/v concentrations in 0.5% and 0.8% w/w CMC solutions, at mean mixture velocities in the range 65-125 mm s^{-1}. As expected, the solid phase velocity profile was found to be symmetrical due to the absence of gravitational effects in vertical flow. The velocity profile was more flattened than that obtained under the same conditions in horizontal flow. This was considered an advantage on horizontal flow in thermal processing, since particle velocities are more uniform in vertical flow. In contrast with horizontal flow, particle trajectories showed little radial movement in vertical flow.

5.1.4. SOLID-LIQUID PRESSURE DROP

Pressure drop in multiphase solid-liquid flow remains one of the most difficult parameters to predict. Solid-liquid pressure drop depends on the flow regime, which in turn is dictated by the complex interaction of many variables (e.g. particle diameter, concentration and density, flow velocity and fluid viscosity).

It is well established that the presence of solid particles in a carrier fluid gives rise to an increase in the pressure drop incurred, but there are no theoretical models available for calculating such a pressure drop. However, many empirical and semi-empirical approaches do exist. Due to the strong dependence of pressure drop on the flow conditions, empirical correlations tend to be specific, not only to the flow regime for which they were developed, but also to the conditions under which the experimental data used in their derivation were obtained. Any attempt to use such correlations to predict pressure drop under other conditions is likely to lead to significant errors (Crowe *et al.*, 1998). Other restrictions to the use of such correlations are:

(i) the existing definitions of solid-liquid flow regimes are not clear cut, as explained above (Section 5.1.1), with the boundaries between the flow regimes being not well defined;
(ii) some solid-liquid systems may belong to more than one regime depending on the operating conditions; and
(iii) pressure drop data collected from the literature for the purpose of developing correlations are often not sufficiently detailed, as they are usually obtained without regard to their possible ultimate utility in developing such correlations (Turian and Yuan, 1977).

Owing to these difficulties, the estimation of solid-liquid pressure drop has been subject to considerable uncertainty.

The classical empirical correlation of Durand and Condolios (Durand and Condolios, 1952), which stands as a reference in the field of slurry flow, was developed using data for highly turbulent sand and gravel slurries with particle diameters in the range

0.2-25 mm, solid concentrations up to 60% v/v, and pipe diameters of 38-580 mm. Durand and Condolios found that their results were independent of particle diameter for particles larger than 20 mm in diameter. They therefore looked for a parameter which would be largely dependent on particle size for small particles but less so for larger ones and chose the drag coefficient on a particle at its terminal velocity. The correlation obtained contains two empirical constants. A wide range of different values of one of these constants can be found in the literature which serves to caution against the indiscriminate use of empirical methods outside the range of variables for which they were derived.

A number of authors reported that the Durand-Condolios correlation, while representing a milestone in the field, has limited applicability. For example, Rasteiro *et al.* (1993) commented that this correlation may produce deviations of up to 55% from measured values. Turian *et al.* (1971) also reported deviations exceeding 50%. Darby (1986), on the other hand, indicated that Durand-Condolios' correlation does not account for inter-particle interactions. Babcock (1971), who carried out a systematic series of experiments designed to asses the role of each of the groups in Durand-Condolios' correlation, argued that the dimensionless groups in the correlation are not sufficient to account for the influences of particle size and concentration and pipe diameter.

Zandi and Govatos (1967) proposed a modified version of Durand-Condolios' equation to correlate approximately 1000 data points collected from various sources. However, their correlation has been hampered by the exclusion of a large set of data points and the arbitrary transition criterion used to demarcate between flow regimes (Turian and Yuan, 1977).

Based on the theoretical approach advanced by Wilson (1942), and using their own experimental data, Newitt *et al.* (1955) proposed a set of regime-specific correlations and used transition velocities to delineate the flow regimes. The transition criteria used imply that the transition from one regime to the next is abrupt, which is not the case in reality (Turian and Yuan, 1977; Shook and Roco, 1991).

Turian and Yuan (1977) noted the importance of ordering experimental data relating to slurry pressure drop according to flow regimes, since it allows the classification of data into groupings of more manageable size compared to the vast number and range of variables influencing the flow. The authors proposed a set of four equations for the estimation of pressure drop for four different flow regimes: homogeneous flow, heterogeneous flow, saltation flow, and flow with a stationary bed. They used another set of equations to delineate the four flow regimes. The authors used a vast number of data points obtained from both the literature and their own work in arriving at these correlations. Apart from the complexity of the correlations, Shook and Roco (1991) showed that the prediction of pressure drop using these correlations may sometimes deviate considerably from actual values, even under conditions that are entirely within the range of data used in deriving the correlations, and that the problem is not one of regime definition.

Chhabra and Richardson (1985) presented a correlation for the prediction of the hydraulic pressure gradient based on experimental data relating to mixtures with a sliding bed. They concluded from a review of the literature that there were then insufficient reliable results for expressions to be given for the pressure gradients in other flow regimes.

Khan *et al*. (1987) discussed the works of principal investigators, including those of Durand and Condolios (1952) and Chhabra and Richardson (1985), and drew attention to some of the drawbacks of such correlations and the very wide discrepancies between the results of different researchers even when obtained under nominally similar conditions. They argued that, in these works, no account was taken of the substantial effect of particle concentration on drag, and that the particle concentration used was that measured in the discharged mixture which will, in general, be lower than that measured in situ which determines the nature of the flow. The authors, therefore, developed experimental techniques for measuring the in-pipe particle concentration and fluid velocity using γ-ray absorption and salt injection, respectively.

As can be seen, a purely experimental approach to the problem of pressure drop prediction in solid-liquid mixtures is faced by difficult constraints arising from (i) the abundance of the variables influencing the flow which makes the variety of solid-liquid systems almost unlimited, (ii) the wide range over which these variables may vary, and (iii) the limitations on accuracy and reproducibility of data (Turian *et al.*, 1971). Due to these difficulties, emphasis has more recently shifted to modelling of solid-liquid flows. As also noted by Shook and Roco (1991), as the data base for solid-liquid flow continues to grow, the importance of experimental correlations will gradually diminish compared to mechanistic models.

Rasteiro *et al.* (1993) derived a semi-theoretical correlation for the prediction of pressure drop in heterogeneous solid-liquid mixtures in turbulent flow. The authors first computed the concentration profile of solid particles in the pipe cross-section and then used it to calculate the pressure drop. The model adopted to describe the flow of suspensions states that the suspension of solid particles is a result of a dynamic equilibrium between the tendency of the particles to settle due to gravity and their tendency to disperse due to turbulence. By solving the model equations, the particle distribution was obtained. The pipe cross-section was divided into slices of nearly constant concentration and pressure drop was evaluated for each slice using the proposed correlation. The total pressure drop was then obtained by integrating these local pressure drops. The empirical constants in the correlation were determined using experimental data for solid particles of high density (up to 2650 kg m^{-3}) ranging in size from 0.16 to 1.28 mm in highly turbulent flow with velocities in the range 0.98-3.76 m s^{-1}. Particle concentration varied from 2% to 34% v/v.

The model was found to give improved pressure drop predictions compared to Durand-Condolios' correlation. Deviations from experimental data of less than 29% were obtained over the broad range of operating conditions considered, whereas Durand-Condolios' equation produced deviations up to 55% from the same experimental data.

Doron and Barnea (1993) developed a three layer model for the calculation of pressure drop which treats the flow of settling mixtures as being constituted of three layers: a stationary layer at the base of the pipe, a moving bed layer above it, and a heterogeneous suspension layer in the rest of the pipe. In a later study, Doron and Barnea (1995) compared new experimental data, obtained using particles of 3 mm diameter and 1240 kg m^{-3} density in water, to the predictions of the three layer model. The comparison showed satisfactory agreement. The pressure drop was found to increase with particle concentration. It should be noted that such models, usually applicable to heavy particles in turbulent flows, are not appropriate for estimating pressure drop in solid-liquid food suspensions where the densities of the two phases are similar and the objective of the flow is to avoid particle settling rather than to model the sedimentation layers.

For fine particles which give rise to homogeneous or near homogeneous suspensions, the suspension can be treated as a continuum and calculation of pressure drop can be based on the bulk properties of the suspension (Khan *et al*., 1987). This continuum approach may also be applied to dilute coarse particle suspensions where the solid-liquid suspension can be approximated as a single phase fluid with properties equivalent to the mean properties of the suspension. This approximation allows the calculation of pressure drop as a function of the suspension Reynolds number in the same way as in single-phase flows. This approach was used by Gradeck *et al.* (2005) to calculate the pressure drop of fairly dilute solid-liquid suspensions with coarse (d = 4.4 mm) nearly-neutrally buoyant alginate particles in water and glucose solutions (Newtonian) and CMC solutions (non-Newtonian) in a 30 mm diameter pipe. This method does not account for particle-particle interactions, which increase in significance with particle concentration, and is therefore inapplicable in concentrated suspensions.

A review of the relevant literature shows that the use of CFD models to predict solid-liquid pressure drop in suspensions of coarse nearly-neutrally buoyant particles has never been attempted. It is therefore necessary for the development of reliable solid-liquid flow models to test the capability of CFD in predicting pressure drop.

5.1.5. SUSPENSION VISCOSITY

Adequate understanding of the rheological behaviour of solid-liquid food suspensions is particularly essential in the aseptic processing of particulate foods. Despite its importance, only a few studies have been devoted to the rheological behaviour of solid-liquid food suspensions. This may be attributed to the fact that only a few types of viscometers can be used in characterising the flow behaviour of suspensions containing large particles, such as tube viscometers, wide-gap parallel plate viscometers, and wide-gap rotational viscometers. Even with these viscometers, difficulties still exist especially at high particle concentrations (Chakrabandhu and Singh, 2005).

For mixtures of fine suspended particles, the mixture can be regarded as a homogenous fluid with an effective viscosity that can be determined experimentally or theoretically. The literature contains a good deal of research in this area, and a number of correlations exist for estimating the viscosity of suspensions. Although, in principle, suspensions of coarse solid particles cannot be treated as homogenous fluids, many of these correlations have been used and validated for coarse nearly neutrally-buoyant food particles flowing in non-Newtonian carrier fluids by Chakrabandhu and Singh (2005). A homogenous suspension fulfils the condition that, when at rest, solid particles have a zero slip velocity. For a solid-liquid food suspension, solid particles are nearly-neutrally buoyant and the carrier fluid is usually viscous, thus resulting in a very small slip velocity.

The first calculation of the flow effective properties of a suspension in terms of the properties of its constituent phases dates back to Einstein's work on Brownian motion in 1905, where he developed the following equation for estimating the relative viscosity, μ_r, of infinitely dilute Newtonian suspensions as a function of particle volume fraction C_s (Jeffrey and Acrivos, 1976)

$$\mu_r = \frac{\mu_{susp}}{\mu_f} = 1 + 2.5C_s \tag{5.1}$$

where μ_{susp} is the suspension viscosity and μ_f is the fluid viscosity. This equation was derived with the assumption that particles are far enough apart not to influence each other and so to be treated independently of each other. For concentrated suspensions, however, this assumption is clearly not valid and particle-particle interactions must be taken into account. Therefore, several equations have been developed to extend Einstein's equation to suspensions of higher particle concentrations.

One of the earliest attempts was that of Mooney (1951) who used a theoretical approach to derive an equation for the viscosity of suspensions. This method accounted for hydrodynamic interactions and the mutual crowding effect of spherical particles on each other. The resulting equation is partly empirical as it contains an interaction parameter that is left for experimental determination. Mooney's equation takes the following form:

$$\mu_r = \exp\left(\frac{2.5C_s}{1-k_cC_s}\right) \tag{5.2}$$

The constant 2.5 was chosen to agree with Einstein's equation for infinitely dilute suspensions. Mooney described a method to estimate the crowding factor, k_c, which is related to the packing geometry, and concluded that $1.35 < k_c < 1.91$.

Power series expansions of Einstein's original equation have been suggested by many researchers to account for different factors that arise at high particle concentrations. These expansions take the form:

$$\mu_r = 1 + A_1C_s + A_2C_s^2 + A_3C_s^3 + \ldots \tag{5.3}$$

Thomas (1965) discussed a number of values for the coefficients A_i proposed by different researchers. Using experimental data relating to the viscosity of suspensions with particle diameters up to ~ 0.44 mm, he found that over 97.5% of the experimental data for $C_s < 0.25$ could be represented by the equation:

$$\mu_r = 1 + 2.5C_s + 10.05C_s^2 \tag{5.4}$$

For higher concentrations, a fourth term is required to account for particle-particle interactions and extend the validity of the equation up to C_s ~ 0.4. Following the suggestion of Eyring *et al*. (1964) that this fourth term should be of an exponential form, Thomas showed that the following equation gives a good fit to the experimental data:

$$\mu_r = 1 + 2.5C_s + 10.05C_s^2 + 0.00273\exp(16.6C_s) \tag{5.5}$$

From the data presented by Thomas (1965), there appears to be no effect of particle size on suspension viscosity for the range of particle size studied (up to ~0.44 mm).

Frankel and Acrivos (1967) used a theoretical approach to derive an equation for suspension viscosity as a function of particle concentration in the limit as the concentration approaches its maximum value C_{sm}. The resulting equation, which contains no empirical constants, was shown to give good agreement with available experimental data obtained from Rutgers (1962(a) and (b)) and Thomas (1965). The equation takes the following form:

$$\mu_r = C'\left[\frac{\left(C_s/C_{sm}\right)^{1/3}}{1-\left(C_s/C_{sm}\right)^{1/3}}\right] \quad C_s \to C_{sm} \tag{5.6}$$

For spherical particles C' = 9/8. Frankel and Acrivos used the C_{sm} value of 0.625 which was obtained by Thomas (1965) and which corresponds very closely to the mean solids volume fraction in a randomly packed bed of uniform spheres.

Some researchers described the rheology of suspensions in terms of power law parameters and derived mathematical representations for these parameters as a

function of the solids volume fraction C_s. One of such representations is a modified version of Mooney's equation (Equation (5.2)) proposed by Jarzebski (1981):

$$\ln \frac{k^*}{k} = \left(\frac{2.5 C_s}{1 - k_c C_s} \right)^n \tag{5.7}$$

where k^* and k are the consistency indices of the suspension and carrier fluid, respectively, and n is the flow behaviour index of the fluid.

Chakrabandhu and Singh (2005) investigated the applicability of the above expressions to suspensions of coarse nearly neutrally-buoyant food particles in a non-Newtonian carrier fluid. The predictions of these expressions were compared with experimental results obtained using a tube viscometer for a suspension of green peas (d = 8.4 mm) in a 1.5% w/v CMC solution. The expressions of Mooney (Equation (5.2)) and Frankel and Acrivos (Equation (5.6)) provided good agreement in the range of solids volume fraction 0.15-0.20 but failed to accurately predict the viscosity in the range 0.25-0.30. It was found that the following third order expansion of Einstein's equation provided the best fit to the experimental data:

$$\mu_r = 1 + 2.5 C_s + 10.05 C_s^2 + 20.84 C_s^3 \tag{5.8}$$

5.1.6. MULTIPHASE SOLID-LIQUID CFD

Computational fluid dynamics (CFD) has been a powerful tool in modelling multiphase flows. Despite the current capabilities of CFD in investigating complex multiphase flows, experimental data are still needed for the development of any numerical or computational model. As frequently noted in the literature, there is a lack of experimental data in many multiphase areas, particularly solid-liquid flows. Moreover, such data, when available, tend to be specific and apply only for the conditions under which they were obtained, as discussed above.

The use of CFD in modelling multiphase solid-liquid flow has been notably limited. As noted by van Wachem and Almstedt (2003), this is due to three factors: (i) the inherent complexity of the physical phenomenon of multiphase flow, reflected in the wide range of flow types and regimes encountered in such flows; (ii) the complex mathematical treatment of such flows remains still undeveloped; and (iii) the numerics required to solve multiphase governing equations are extremely complex.

Nevertheless, substantial effort has been directed at the development of CFD models for multiphase systems, and the application of these models in industry has been growing steadily. In fact, CFD models have reached such complex levels in their treatment of multiphase flows that they sometimes outstrip the ability to obtain experimental data with which to evaluate them (Kleinstreuer, 2003). Kleinstreuer (2003) discussed the capabilities of different CFD software packages in modelling a range of multiphase flows and presented several cases of the application of CFD in the study of complex biomedical engineering-related multiphase flows drawn from the results of the author's group of research. CFD models were constructed using the commercial code CFX 4.4 and validated using available experimental data.

Van Wachem and Almstedt (2003) presented an overview of the CFD models used for multiphase flows. The authors derived the governing equations and closure models for multiphase flow and presented and compared different methods and formulations used for modelling such flows. It was concluded that the application of CFD in studying multiphase flow is promising but nonetheless requires further development.

There are two numerical approaches used to model multiphase flows: the Eulerian-Eulerian and Eulerian-Lagrangian methods. The Eulerian-Eulerian method, also known as the two-fluid method, regards the dispersed phase as a continuous phase, i.e. as a fluid. This method accounts more easily for particle-particle interactions and is widely used for mixtures with high particle concentrations. Multiphase flow models within this method can be sub-divided into two categories: homogeneous and inhomogeneous. The homogeneous flow model views the mixture as one fluid with the bulk properties modified to account for the presence of the solid particles. The

inhomogeneous flow model, on the other hand, views the two phases as distinct, interacting continua.

Since the dispersed solid phase is treated as a continuum in the Eulerian-Eulerian approach, an effective viscosity has to be assigned to this phase. This imposes a conceptual difficulty since viscosity is a property of continuous fluids only. However, as discussed above, the literature contains a number of expressions for the calculation of suspension viscosity which can then be used to calculate a hypothetical solid phase viscosity. These expressions have been shown to represent the rheological behaviour of food suspensions satisfactorily (Chakrabandhu and Singh, 2005).

With the rapid increase of computational power, the particle tracking Eulerian-Lagrangian approach has become feasible. This approach calculates the trajectories of particles in the flow. This method is computationally expensive and valid only for very dilute mixtures, i.e. < ~ 2% v/v (van Wachem and Almstedt, 2003).

The success of any of these modelling methods depends on the accurate modelling and appropriate inclusion in the governing and closure equations of the various complex effects that occur in multiphase flows. This, however, requires a solid understanding of the fundamentals of multiphase flows. Numerical modelling and experimental approaches are complementary of each other, since experimental data are indispensable for the development and validation of numerical models while numerical models can provide more comprehensive data than experiment.

Norton and Sun (2006) conducted a state-of-the-art review of the applications of CFD in the food industry, including food sterilisation. A steady increase has been observed in the number of studies relating to CFD applications in the food industry. For example, CFD has helped overcome some of the difficulties in relating heat transfer in food products to sterility and quality levels. CFD can assist the understanding of the physical mechanisms that govern the various properties of food products, including solid-liquid mixtures.

Smith *et al*. (2000) conducted a CFD study of solid-liquid mixing in a tank using the commercial software CFX 4.2. The system consisted of a stationary liquid into which neutrally-buoyant solid particles 6.25 mm in diameter were dropped. The model was validated by comparing its predictions with experimental results obtained by the authors, and good agreement was found. The model was then extended to study the dispersion of solid particles in a horizontal channel flow. This study was intended as a first step towards simulating the dispersion of solid particles falling into a flowing melt.

Krampa-Morlu *et al.* (2004) used CFD to predict the flow features of aqueous solid-liquid slurries in turbulent upward pipe flow. Among the investigated features was the velocity profile. Particles had a density of 2650 kg m^{-3} and diameter of 0.47 or 1.7 mm at concentrations up to 30% v/v. The CFD model, formulated using the software CFX 4.4, was tested using the experimental results of Sumner *et al.* (1990). The agreement between CFD and experiment was generally good for the smaller particles but deteriorated for the 1.7 mm diameter particles. The authors concluded that the code failed to accurately predict important features of the flow using the default settings.

An example of the successful application of CFD in modelling solid-liquid food mixtures is the work of Abdul Ghani and Farid (2007) who used CFD to predict the temperature distribution and velocity and pressure profiles during high pressure compression of solid-liquid (beef-water) food mixtures within a 38 mm diameter cylinder. The CFD model, constructed using the commercial finite-volume code PHOENICS 3.5, was validated using experimental data reported in the literature, and a very close agreement was obtained. The CFD results showed for the first time the effect of forced convection heat transfer on the temperature distribution of the solid and liquid phases. The temperature distribution at different stages of the high pressure process was obtained.

Clearly, further work is needed to validate and utilise available CFD models in the study of solid-liquid food flows and highlight the developments needed for more

accurate predictions of the flow behaviour of such complex flow systems. This, in turn, will result in an increased confidence in the capability of CFD in modelling such multiphase flows.

In this chapter, an Eulerian-Eulerian CFD model is used to study the flow of coarse (2-10 mm) nearly-neutrally buoyant solid particles in non-Newtonian carrier fluids at high particle concentrations (up to 40% v/v). The CFD model is first validated extensively using experimental measurements of solid phase velocity profile obtained from the literature, in addition to empirical and semi-empirical pressure drop correlations. The model is then used to investigate the effects of particle diameter and concentration, mixture velocity and carrier fluid rheology on the solid and fluid velocity profiles, particle distribution, and pressure drop in horizontal flow, while a less extensive study is performed on vertical flow to outline the main differences between the two flow orientations.

5.2. THEORY

5.2.1. CARRIER FLUID RHEOLOGY

The non-Newtonian fluids used in this study are of the power law and Ellis rheological models. The apparent viscosity, η, of a power law fluid is given by

$$\eta = k\dot{\gamma}^{n-1} \tag{5.9}$$

where $\dot{\gamma}$ is shear rate, k is the consistency index and n is the flow behaviour index.

The velocity profile for a power law fluid flowing alone is given by the expression (Chhabra and Richardson, 1999)

$$u(r) = \overline{u}\left(\frac{3n+1}{n+1}\right)\left[1-\left(\frac{r}{R}\right)^{\frac{n+1}{n}}\right] \tag{5.10}$$

where $\overline{u}$ is the mean flow velocity, r is radial position and R is the pipe radius.

An Ellis model is described by the viscosity expression

$$\eta = \frac{\mu_0}{1+\left(\frac{\tau}{\tau_{1/2}}\right)^{\alpha-1}} \tag{5.11}$$

where μ_0 is the zero-shear viscosity, τ is the shear stress, $\tau_{1/2}$ is the shear stress at which the apparent viscosity has dropped to $\mu_0/2$, and α is a measure of the extent of shear thinning behaviour.

The velocity profile of an Ellis fluid is given by (Matsuhisa and Bird, 1965)

$$u(r) = \frac{\tau_w}{\mu_0}\left[\frac{R}{2}\left(1-\frac{r^2}{R^2}\right)+\left(\frac{\tau_w}{\tau_{1/2}}\right)^{\alpha-1}\left(\frac{R}{\alpha+1}\right)\left(1-\left(\frac{r}{R}\right)^{\alpha+1}\right)\right] \tag{5.12}$$

where τ_w is the wall shear stress.

5.2.2. INTER-PHASE DRAG FORCE

When a particle is in relative motion to a fluid, the drag force is defined as the component of the resultant force acting on the particle in the direction of the relative motion. The total drag force is made up of two components, the form drag and the skin friction. The form drag results from the non-uniform distribution of pressure on the particle, whereas the skin friction is due to the fluid shear stress at the particle surface.

Drag force can be calculated by applying dimensional analysis to experimental data. For a spherical particle in a Newtonian fluid, the drag force was found to depend on slip velocity, u_{slip}, particle diameter, d, fluid density, ρ_f, and viscosity μ_f. Two dimensionless groups are conventionally used to express the drag force: particle drag coefficient, C_D, and particle Reynolds number, Re_p (Seville *et al.*, 1997). The drag force for a spherical particle is given by

$$F_D = \frac{1}{2}C_D\rho_f u_{slip}^2\left(\frac{\pi d^2}{4}\right) \tag{5.13}$$

For creeping flow around a solid sphere in an unbounded expanse of fluid, the drag force, F_D, was obtained by Stokes in 1851, thus

$$F_D = 3\pi\mu_f d u_{slip} \tag{5.14}$$

The particle Reynolds number is defined by

$$\mathrm{Re}_p = \frac{\rho_f u_{slip} d}{\mu_f} \tag{5.15}$$

This Reynolds number indicates the nature of the flow around the solid particle. A low value of Re_p indicates creeping flow where the motion of the fluid is dominated by viscous effects. High Re_p values, on the other hand, indicate that fluid inertia is dominant. For a particle settling in an infinite expanse of a stationary carrier fluid, the slip velocity equals the particle terminal settling velocity, and so particle Reynolds number can be expressed in terms of the particle terminal settling velocity u_∞, (Brown and Heywood, 1991), thus

$$\mathrm{Re}_p = \frac{\rho_f u_\infty d}{\mu_f} \tag{5.16}$$

In general, C_D can be expressed as a function of particle Reynolds number:

$$C_D = f(\mathrm{Re}_p) \tag{5.17}$$

This form of relationship is used to correlate empirical drag measurements. By combining equations (5.13), (5.14), and (5.15), the drag coefficient in the creeping flow regime can be calculated from

$$C_D = \frac{24}{\mathrm{Re}_p} \qquad \text{for } \mathrm{Re}_p < 0.1 \tag{5.18}$$

This equation gives a good approximation for low particle Reynolds numbers (i.e. $Re_p < 0.1$) where inertial effects are negligible, with ~ 2% error in C_D at $Re_p = 0.1$, and nearly 20% error at $Re_p = 1$ (Seville *et al*., 1997). For higher Re_p values, i.e. outside Stokes regime, the drag coefficient is a function of many factors, particularly the flow regime and particle concentration. Calculating the drag coefficient for flow in a

confined geometry poses another problem since C_D is difficult to define in a shear field where there is a fluid velocity gradient across the solid particle.

As the particle concentration increases, particle-particle interactions play an increasingly significant role in determining the drag and settling velocity of individual particles. The effect of particle concentration is due to three contributions. Firstly, when a particle settles due to gravity, it displaces an equal volume of fluid, resulting in an upward fluid motion around the particle that increases the resistance to the motion of other solid particles. This effect becomes more pronounced as particle concentration increases due to the increased volume of displaced fluid. Secondly, the presence of solid particles modifies the fluid properties, which, in turn, affect the behaviour of the particles. Thirdly, the flow pattern of the fluid relative to the solid particles will be modified (Lareo *et al.*, 1997(a)). This phenomenon is known as hindered settling.

Many empirical expressions can be found in the literature for calculating C_D. These expressions have been reviewed and critically evaluated by Clift *et al.* (1978) and Khan and Richardson (1987). Such expressions are often highly complex and C_D is usually given in the form of a drag curve of C_D against Re_p.

5.2.3. PARTICLE SETTLING VELOCITY

When a solid particle is present in a stationary fluid that has a lower density than its own, the particle will settle under the influence of gravity. Initially, the particle will accelerate until it reaches a constant velocity known as the terminal settling velocity u_∞. Since drag is proportional to the slip velocity (Equations (5.13) and (5.14)), when the particle accelerates the drag force increases gradually until it becomes large enough to exactly balance the apparent weight of the particle, at which point the particle attains a constant velocity. This force balance is expressed as:

$$F_D = \frac{\pi d^3}{6}\left(\rho_s - \rho_f\right)g \tag{5.19}$$

where ρ_s is the solid particle density and g is gravitational acceleration.

For a sphere settling in the creeping flow regime in a Newtonian fluid, the terminal settling velocity can be obtained from Equations (5.14) and (5.16), with $u_{slip} = u_\infty$, thus

$$u_\infty = \frac{gd^2(\rho_s - \rho_f)}{18\mu_f} \tag{5.20}$$

Settling in a sheared fluid is a more complex problem on which literature is sparse and often contradictory. The structure and flow of the carrier fluid influences the drag and settling velocity of particles in a poorly understood way (Brown and Heywood, 1991).

5.2.4. LIFT FORCE

Particle rotation induced by velocity gradients in the flow field results in a pressure distribution on the particle that leads to a lift force known as the Saffman lift force. Particle rotation caused by other sources results in a pressure differential between both sides of the particle that leads to the Magnus lift force (Crowe *et al.*, 1998).

The lift force, F_l, caused by velocity gradients, is given by (van Wachem and Almstedt, 2003)

$$F_l = C_s \rho_f C_l (U_s - U_f) \times (\nabla \times U_f) \tag{5.21}$$

where C_l is the lift coefficient and U_s and U_f are the solid and liquid velocity vectors, respectively. A wide range of values can be found in the literature for C_l (van Wachem and Almstedt, 2003).

5.2.5. PARTICLE MIGRATION

Radial particle migration occurs when particles move across streamlines to some preferred region in the flow, usually due to lift forces. This phenomenon may result

in separation of the two phases which may in turn lead to the two phases having different residence times. Particle migration is particularly important in dilute suspensions where the radial movement of particles is not overshadowed by particle-particle interactions.

Segré and Silberberg (1961, 1962(a), and 1962(b)) studied dilute suspensions of neutrally buoyant spheres in laminar Newtonian flow through a vertical tube and observed that particles migrate to a thin annular region called the 'tubular pinch', an effect also reported by several other investigators (Lareo *et al*., 1997(a)).

In the vertical flow of viscoelastic fluids, particles have been observed to migrate towards the pipe axis where the velocity profile of the carrier fluid is flat (Karnis *et al*., 1963; Gauthier *et al*., 1971). The rate of migration depends on particle size and radial position. In pseudo-plastic fluids, particles migrate towards the pipe wall (Gauthier *et al*., 1971).

The migration of non-neutrally buoyant particles depends on the flow direction and the difference in density between the two phases. Particles denser than the carrier fluid migrate towards the pipe centreline in up-flow and towards the pipe wall in down-flow; whilst particles less dense than the fluid move towards the pipe wall in up-flow and towards the pipe centreline in down-flow (Lareo *et al*., 1997(a)).

5.2.6. SUSPENSION VISCOSITY

The presence of neutrally or nearly neutrally-buoyant solid particles in a carrier fluid influences the shear rate distribution and, hence, the suspension rheology. In general, fluids appear more viscous when solid particles are added and the viscosity varies spatially as a function of the local particle concentration in the pipe (McCarthy and Kerr, 1998). At low concentrations, the influence on the mixture viscosity is due to the excluded volume effect. Solid particles represent regions where the continuous deformation of shear cannot occur, and so the effective shear rate in the fluid is increased producing higher shear stresses at the boundaries, interpreted as an increase

in viscosity (Shook and Roco, 1991). At high concentrations, particle-particle contacts play a significant role in increasing the viscosity of the mixture.
Suspension viscosity is often expressed as a relative viscosity, μ_r, defined as the viscosity of the suspension, μ_{susp}, relative to that of the carrier fluid flowing alone, μ_f:

$$\mu_r = \frac{\mu_{susp}}{\mu_f} \tag{5.22}$$

In the Eulerian-Eulerian description of solid-liquid flows, both phases are regarded as continua. It is therefore necessary to define a viscosity term for the solid phase. For non-Newtonian suspensions, the fluid viscosity in Equation (5.22) can be taken as the local apparent viscosity, μ_a. The suspension apparent viscosity, μ_{susp}, can then be written in terms of μ_a and a solid viscosity, μ_s, thus

$$\mu_{susp} = (1 - C_s)\mu_a + C_s\mu_s \tag{5.23}$$

For very dilute suspensions where particle-particle interactions are negligible, Einstein's equation can be used to calculate the suspension relative viscosity as a function of particle concentration (Equation (5.1)). For more concentrated suspensions, attempts to take account of particle-particle interactions have resulted in modified versions of Einstein's equation. Thomas (1965) showed that series expansions of Einstein's equation can be used to account for various effects which arise at high particle concentrations. A second-order term can be used to account for particle-particle interactions, and another term accounts for the effect of particle rearrangement as the suspension is sheared.

Chakrabandhu and Singh (2005) compared the predictions of several expressions for suspension viscosity with experimental data obtained using green peas with an average diameter of ~8.4 mm and a density of ~1026 kg m^{-3}, suspended in a 1.5% w/v CMC solution (non-Newtonian) of ~1022 kg m^{-3} density. Particle concentration ranged from 15% to 30% v/v. They found that the following third order expansion,

originally developed for suspensions of fine particle (< ~0.44 mm), yielded the best agreement over the whole range of data considered:

$$\mu_r = 1 + 2.5C_s + 10.05C_s^2 + 20.84C_s^3 \tag{5.8}$$

As the particle concentration increases, particle-particle interactions become more probable, thus increasing the energy dissipation and leading to a more rapid increase of μ_r with C_s (Shook and Roco, 1991). The third order term was originally used to account for the rearrangement of particles as the suspension is sheared, and was therefore chosen to be proportional to the probability of a particle's transferring from one shear plane to another.

5.2.7. SOLID-LIQUID PRESSURE DROP

Durand and Condolios (1952) developed one of the earliest correlations for estimating solid-liquid head loss (Durand and Condolios, 1952; Turian *et al.*, 1971). The correlation was developed using data for highly turbulent sand and gravel slurries with particle diameters in the range 0.2-25 mm, solid concentrations up to 60% v/v, and pipe diameters of 38-580 mm, thus

$$\frac{i - i_w}{i_w C_s} = K\left[\frac{\overline{u}^2 C_D^{0.5}}{gd(s-1)}\right]^m \tag{5.24}$$

which can be written in a simplified form as

$$\phi = K\Psi^m \tag{5.25}$$

where

$$\Psi = \frac{\overline{u}^2 C_D^{0.5}}{gd(s-1)} \tag{5.26}$$

$\phi = \frac{i - i_w}{i_w C_s}$ is the dimensionless excess head loss, i and i_w are head losses for the solid-liquid mixture and for water flowing alone respectively, s is the ratio of particle to liquid density (i.e. $s = \rho_s/\rho_f$), and $\overline{u}$ is the mean flow velocity. The drag coefficient, C_D, is given for a spherical particle settling at its terminal velocity, u_∞ (Equation (5.20)), in a stagnant unbounded liquid by (Brown and Heywood, 1991)

$$C_D = \frac{4}{3}\frac{gd(s-1)}{u_\infty^2} \tag{5.27}$$

K and m are empirical constants. According to Dhodapkar *et al.* (2005), Durand-Condolios' correlation should only be used for $\Psi/C_s > 40$, corresponding to fully suspended heterogeneous flow.

While the value of m has generally been taken as -1.5, different values of K have been used depending on the solid-liquid system considered (Newitt *et al*., 1955; Zandi and Govatos, 1967; Turian *et al*., 1971; Turian and Yuan, 1977; Darby, 1986; Shook and Roco, 1991; Dhodapkar *et al.*, 2005). According to Darby (1986), many of the K values used in the literature are due to a misinterpretation of Durand-Condolios' work and the correct value should be 150, a value also reported by Turian *et al*. (1971) which accounts for the effect of particle density. Most notably, Zandi and Govatos (1967) proposed the following values which have been generally hailed as improvement on Durand-Condolios' original correlation: $K = 280$ and $m = -1.93$ for $\Psi < 10$, and $K = 6.3$ and $m = -0.354$ for $\Psi > 10$, all valid for $\Psi/C_s > 40$. Clearly, the wide variation in the values of such coefficients highlights the fact that such experimental correlations are specific to the range of variables for which they were derived.

Newitt *et al*. (1955) presented a set of regime-specific correlations for the prediction of pressure drop. The additional pressure drop incurred due to the suspended particles was related to the work needed to re-suspend them as they tended to settle under the influence of gravity. For the homogeneous flow regime, the correlation is:

$$\phi = 0.6(s-1) \tag{5.28}$$

and for the heterogeneous flow regime

$$\phi = 1100\frac{gdu_{\infty}(s-1)}{\overline{u}^3} \tag{5.29}$$

The semi-theoretical correlation developed by Rasteiro *et al.* (1993) for heterogeneous solid-liquid mixtures considers the total pressure drop per unit length, $\Delta P/L$, to be made up of the kinetic energy loss E_c, the viscous energy loss E_v, and the energy loss due to particle-particle interactions E_p, thus

$$\left[\frac{\Delta P}{L}\right]_{susp} = A_1E_c + A_2E_v + A_3E_p \tag{5.30}$$

where

$$E_c = \frac{\rho_f\overline{u}^2}{d(1-C_s)}; E_v = \frac{\mu_f\overline{u}}{(d(1-C_s))^2}; E_p = \frac{(\rho_s - \rho_f)gC_s^{\,2}}{(1-C_s)^3} \tag{5.31}$$

A_1, A_2, and A_3 are empirical constants which they determined by applying the method to experimental data obtained from the literature. The authors gave the values of these constants based on solid particles of high density (up to 2650 kg m^{-3}) and particle diameter in the range 0.16-1.28 mm in highly turbulent flow. Particle concentration varied from 2% to 34% v/v. The particles under these conditions were fully suspended as a result of the balance of forces which qualitatively resembles the flow of nearly-neutrally buoyant particles in laminar flow.

For dilute suspensions of coarse nearly-neutrally buoyant particles, Gradeck *et al.* (2005) used the continuum approach and considered the solid-liquid mixture to be equivalent to a single fluid with modified density and viscosity. The authors expressed the pressure drop per unit length in terms of the friction factor f, thus

$$f = \frac{1}{2}\frac{d}{\rho_{susp}\bar{u}^2}\frac{\Delta p}{L} \tag{5.32}$$

They found that for laminar flow

$$f = \frac{16}{\mathrm{Re}_s} \tag{5.33}$$

where the suspension Reynolds number, Re_s, is based on the mean suspension density, ρ_{susp}, pipe diameter, D, and the effective viscosity of the suspension, μ_{susp}, measured experimentally using the pressure drop-flow rate relationship for a homogeneous fluid for solid concentrations up to 15% v/v, i.e.

$$\mathrm{Re}_s = \frac{\rho_{susp}\bar{u}D}{\mu_{susp}} \tag{5.34}$$

Since the only variable used in this method to determine the pressure drop is the suspension viscosity, no account is taken of the influence of particle-particle interactions on pressure drop which increase in significance with particle concentration. This method was tested for fairly low concentrations up to 15% v/v (Gradeck *et al.*, 2005), with the largest deviations obtained at the highest concentration used, and therefore cannot be used for more concentrated suspensions.

5.2.8. FORMULATION OF CFD MODEL

5.2.8.1. Modelling of two-phase flow

The goal of modelling two-phase flow systems is to predict the averaged behaviour of the mixture or/and the flow field of the individual phases. Due to the presence of two interacting phases, a multiphase model requires solving a larger set of equations than is usually the case in single phase flow, and is therefore more computationally expensive.

Kleinstreuer (2003) discussed the different methods used to model two-phase flows and the different averaging procedures used to obtain the averaged equations from the instantaneous local (microscopic) equations.

The solid phase can be modelled either as an Eulerian phase (continuum) or a Lagrangian phase (trajectory method). The Lagrangian model adopted in commercial modelling codes is presently still limited to very dilute multiphase mixtures in steady flow (Van Wachem and Almstedt, 2003; Kleinstreuer, 2003; Crowe, *et al*., 1998), and therefore the Eulerian formulation is more appropriate for higher concentrations. Although regarding the solid phase as a continuum may appear as an inappropriate approximation, especially when it is constituted of coarse particles, the Eulerian approach has proved useful in predicting the averaged behaviour of solid particles in many solid-liquid flow situations.

The multiphase component of the CFD software CFX 10.0 used in this study contains a number of well established models which can be implemented as closures to the transport equations. The formulation of the model is described below.

5.2.8.2. Model formulation

A number of sources are available for the derivation of multiphase governing equations. The different assumptions made during the derivation of the governing equations constrain the type of two-phase flow to which they can be applied (Van Wachem and Almstedt, 2003).

The inhomogeneous Eulerian-Eulerian CFD model used to simulate the flow of solid-liquid food mixtures considered here is based on the following continuity and momentum equations.

Continuity equations

Assuming isothermal flow, a continuity equation can be written for the liquid phase as follows (van Wachem and Almstedt, 2003)

$$\frac{\partial}{\partial t}\left(\rho_f C_f\right)+\nabla\cdot\left(\rho_f C_f U_f\right)=0 \tag{5.35}$$

and similarly, for the solid phase

$$\frac{\partial}{\partial t}\left(\rho_s C_s\right)+\nabla\cdot\left(\rho_s C_s U_s\right)=0 \tag{5.36}$$

with the constraint that the sum of the solid and fluid phase volume fractions is equal to unity:

$$C_f + C_s = 1 \tag{5.37}$$

where the subscripts *f* and *s* denote the fluid and solid phase respectively, *U* is the velocity vector, and *t* is time.

Momentum equations

The momentum equation for each phase is derived to include, along with the forces acting on that phase, an inter-phase momentum transfer term that models the interaction between the two phases (van Wachem and Almstedt, 2003); thus for the liquid

$$\rho_f C_f\left[\frac{\partial U_f}{\partial t}+U_f\cdot\nabla U_f\right]=-C_f\nabla p+C_f\nabla\cdot\bar{\bar{\tau}}_f+C_f\rho_f g-M \tag{5.38}$$

and for the solid particles

$$\rho_s C_s\left[\frac{\partial U_s}{\partial t}+U_s\cdot\nabla U_s\right]=-C_s\nabla p+C_s\nabla\cdot\bar{\bar{\tau}}_s-\nabla P_s+C_s\rho_s g+M \tag{5.39}$$

where p is pressure, $\bar{\bar{\tau}}$ is the viscous stress tensor, P_s is solid pressure, and M is the interfacial momentum transfer per unit volume considered here to be made up of the

drag force, F_D, and the lift force, F_l. Note that interfacial forces between two phases are equal and opposite, so the net interfacial forces sum to zero. The other forces on the right hand side of the momentum equations are the pressure force, viscous force, gravitational force, as well as particle-particle interaction force for the solid phase represented by the solid pressure term. The inclusion of this term is particularly important for highly concentrated suspensions ($C_s > 0.2$) as the interactions increase with solids concentration. This solid pressure term is, therefore, a function of the solids volume fraction C_s (Gidaspow, 1994), thus

$$P_s = P_s\,(C_s) \tag{5.40}$$

The constitutive equation for solid pressure due to Gidaspow (1994) specifies the solid pressure gradient as

$$\nabla P_s = G(C_s)\nabla C_s \tag{5.41}$$

The function $G\,(C_s)$ is called the Elasticity Modulus, and is expressed as follows

$$G(C_s) = G_0 e^{E(C_{sm}-C_s)} \tag{5.42}$$

where G_0 is the reference elasticity modulus, E is the compaction modulus, and C_{sm} is the maximum packing parameter (maximum solids loading). There are no universally accepted values for these parameters; however, the values $G_0 = 1$ Pa, $E = 20 - 600$, have been suggested by Bouillard *et al.* (1989). The maximum packing parameter C_{sm} was determined by Thomas (1965) as 0.625 for spherical particles.

Inter-phase drag force

The inter-phase drag force per unit volume, F_D, is expressed by (Kleinstreuer, 2003; van Wachem and Almstedt, 2003)

$$F_D = \frac{3C_D}{4d} C_s \rho_f \left|U_s - U_f\right| \left(U_f - U_s\right) \tag{5.43}$$

For densely distributed particles at concentrations up to 20%, the expression by Wen and Yu (1966) can be used to calculate C_D, thus

$$C_D = (1-C_s)^{-1.65} \max\left[\frac{24}{\mathrm{Re}'}\left(1+0.15\,\mathrm{Re}'^{0.687}\right),\ 0.44\right] \tag{5.44}$$

where $\mathrm{Re}' = (1-C_s)\mathrm{Re}_p$. For higher concentrations (C_s > 0.2), the Gidaspow drag model is used where the inter-phase drag force per unit volume is given by (Ding and Gidaspow, 1990)

$$F_D = \left[150\frac{C_s{}^2\mu_f}{C_f d^2} + \frac{7C_s\rho_f\left|U_s-U_f\right|}{4d}\right]\left(U_f-U_s\right) \tag{5.45}$$

Lift force

The lift force acts perpendicular to the direction of the relative motion of the two phases. ANSYS CFX 10.0 contains a model for the shear-induced lift force acting on a dispersed phase in the presence of a rotational continuous phase. This lift force caused by velocity gradients is given by Equation (5.21).

Carrier fluid viscosity

In the simulations performed to validate the CFD model, the fluid rheology adopted was that used to model the pseudoplastic CMC solutions used in the experimental work of Fairhurst *et al.* (2001) and Barigou *et al.* (2003). These shear thinning fluids were described by the Ellis model (Equation (5.11)). On the other hand, the fluids used in the parametric study were described by the power law model (Equation (5.9)).

Solid phase viscosity

The solid phase viscosity is derived by rearranging Equation (5.23) to yield:

$$\mu_s = \frac{\mu_{susp} - (1-C_s)\mu_a}{C_s} \tag{5.46}$$

with the suspension viscosity, μ_{susp}, as calculated from Equations (5.8) and (5.22). Due to the non-Newtonian behaviour of the carrier fluid, the apparent viscosity of the fluid, μ_a, is used here, and so Equation (5.46) represents the local apparent viscosity of the solid phase.

5.3. CFD SIMULATION

The software package ANSYS Workbench 10.0 (ANSYS Inc.) was used to set up multiphase simulations. Due to the axial asymmetry of the flow, simulations were set up in three dimensions (X, Y, Z coordinates). The simulation process is divided into five stages: building the flow domain geometry, meshing the geometry, defining the flow, obtaining a solution and analysing the results. The geometry of the flow domain was created using the DesignModeler component of the package, while the remaining stages were performed using the software CFX 10.0. The inhomogeneous Eulerian-Eulerian multiphase model was adopted here since the Eulerian-Lagrangian model is valid only for very dilute mixtures.

5.3.1. GEOMETRY

The flow geometry consisted of a horizontal pipe 45 mm in diameter, as used in the experiments of Fairhurst (1998) and Fairhurst *et al*. (2001). The pipe length selected, L, needs to be greater than the maximum entrance length, L_e, i.e. the length required for flow to fully develop. In single phase Newtonian laminar flow, the entrance length can be estimated as a function of tube Reynolds number, Re_t, from (Shook and Roco, 1991)

$$\frac{L_e}{D} = 0.062\,\mathrm{Re}_t \tag{5.47}$$

$$\mathrm{Re}_t = \frac{\rho_f \overline{u} D}{\mu_f} \tag{5.48}$$

For two-phase solid-liquid flow, a similar correlation for predicting L_e does not exist. However, given the fact that the particles considered here were nearly-neutrally buoyant, one would expect the above correlation to give a reasonable estimate of L_e. Moreover, the use of shear thinning fluids as well as the presence of solid particles leads to flatter velocity profiles and, hence, the estimates yielded by the above

correlation are even likely to be conservative. In fact, the constant in Equation (5.47) reduces as the flow behaviour index n decreases, reaching a value of 0.034 when n = 0.5 (Rohsenow *et al.*, 1998). In addition to using this criterion, a number of numerical experiments were conducted with different pipe lengths. At lower Re_t values (< 200), a pipe length of 600 mm was sufficient to give fully developed flow of the suspensions considered whilst keeping computational cost low. Computational experimentation confirmed that using a longer pipe did not affect the velocity profiles of either phase or the pressure drop. At higher Re_t values, a length of 2000 mm was used.

5.3.2. MESH

The geometry was meshed into tetrahedral cells resulting in a grid of approximately 180×10^3 or 500×10^3 cells depending on the pipe length used. The 3D grid was optimised by conducting a mesh-independence study using different mesh sizes, starting from a coarse mesh and refining it until the results of the solid-liquid flow simulation were no more dependent on mesh size. Inflation layers covering about 20% of the pipe radius were created near the pipe wall in order to accurately account for the high gradients in variables in that region.

5.3.3. FLOW SPECIFICATION

5.3.3.1. Single-phase flow simulation

Simulations of the single-phase flow of non-Newtonian carrier fluids were conducted as an initial validation of the code and the numerical grid. The results were also used to reveal the effects of solid particles on the liquid velocity profile, by comparing the velocity profile of the liquid flowing alone to that which exists in a solid-liquid suspension. Furthermore, such simulations were useful in evaluating the capability of the code to predict the flow of fine particle suspensions that can be treated as homogeneous or pseudo-homogeneous and, hence, which can be represented by a non-Newtonian single phase fluid.

The rheology of the CMC carrier fluid, used in the validation of the model (see Section 5.4), was modelled using the apparent viscosity of an Ellis fluid (Equation (5.11)) (the Ellis parameter values are given later in Table 5.1). The apparent viscosity given by Equation (5.11) is a function of shear stress. It was not possible to model this equation directly in CFX 10.0 since shear stress is not available as a variable in its library of variable. Therefore, the viscosity equation was converted into an equation of apparent viscosity as a function of shear rate, and the following equation was obtained:

$$\mu_a = 1.0\times10^{-5}\dot{\gamma}^2 - 1.4\times10^{-3}\dot{\gamma} + 0.1178 \tag{5.49}$$

For the power law carrier fluids, Equation (5.9) was used to describe the fluid apparent viscosity.

Boundary conditions:

A mass flow rate boundary condition was used at the pipe inlet, while a zero gauge pressure was specified at the outlet. The usual no-slip boundary condition was assumed at the pipe wall.

Discretisation scheme:

The advection terms in the governing momentum equation (Equation (5.38) with C_f = 1 and M = 0 for single phase flow), were discretised using the Numerical Advection Correction Scheme (Chapter 2, Section 2.9.3) with β = 1 (Equation (2.18)), which is second-order accurate.

Convergence:

The solution was assumed to have converged when the RMS of the residual error of the mass and momentum equations reached 10^{-5} for all of the equations. This is a very good degree of accuracy and was attained within a reasonably short period of time requiring typically ~100 iterations.

5.3.3.2. Two-phase solid-liquid flow simulation

The solid particles were introduced into the continuous liquid phase as an Eulerian phase. The viscosity of the solid phase was modelled using Equation (5.46).

Due to the complexity of the solid-liquid flows considered here, simulations required a great deal of experimentation and optimisation. Of primary importance was the appropriate modelling of the forces and interactions acting between the two phases. The buoyancy force was taken into account due to the density difference between the liquid and solid phases (ρ_f = 1000 kg m^{-3}, ρ_s = 1020 kg m^{-3}). Forces due to particle collision required the introduction of an additional "Solid Pressure" term into the solid phase momentum equation (Equation (5.39)). A solid pressure model based on the Gidaspow model (Equations (5.41) and (5.42)) was used with default values of the model parameters: G_0 = 1 Pa, E = 600 and C_{sm} = 0.625. The drag force was modelled using the Wen Yu drag model (Equation (5.44)) for solid concentrations up to 20% v/v, and the Gidaspow drag model (Equation (5.45)) for higher concentrations. It should be noted here that the particle Reynolds number (Equation (5.15)) was computed based on the local apparent viscosity of the fluid used, thus taking account of the non-Newtonian behaviour of the fluid (He *et al.*, 2001). The lift force was modelled using Equation (5.21) with the default value C_l = 0.5; a range of C_l values were tested but they did not affect the results.

Boundary conditions:

The mixture mass flow rate was specified as the boundary condition at the pipe inlet, while at the outlet zero gauge pressure was specified. The homogeneous volume fraction of each phase was specified at the inlet. Using flow rate as a boundary condition is the common way of formulating pipe flow problems, i.e. one designs a system to deliver a given flow rate. Note, however, that using a pressure-specified inlet boundary condition is a stricter way of testing the CFD code as a flow rate boundary condition might be perceived as a way of helping to steer the simulation towards the right solution. This option was tested but it did not affect the results of the CFD computations. At the pipe wall, two different conditions were used for the liquid and solid phases. For the liquid phase the usual no-slip condition was used, while for

the solid phase free-slip was assumed in order to prevent the solid phase from adhering to the wall, which is consistent with the real flow behaviour of coarse particles near a solid boundary and is normal practice in the modelling of two-phase flows.

Discretisation scheme:

The High Resolution Scheme was implemented in discretising the advection terms in the governing equations. In this scheme, the value of the blend factor, β, in Equation (2.18), is not constant but is calculated locally to be as close to 1 as possible without resulting in non-physical variable values. Imposing a second-order accurate scheme (i.e. $\beta = 1$) in such complex simulations may result in difficult convergence.

Convergence:

Numerical convergence under steady state mode could not be attained for the solid-liquid flow considered here; consequently, simulations were run in the transient mode. It is recommended that simulations of steady state nature should be run under the transient mode when convergence difficulty is encountered, in order to enhance the stability of convergence (see Chapter 2, Section 2.10.2).

For a transient simulation, the time step size, number of iterations per time step and total number of time steps must be defined. The total timescale of the simulation is divided into small time steps. A small time step size results in smooth and stable convergence, thus requiring a small number of iterations to achieve convergence. On the other hand, a small time step generally prolongs the simulation time as a large total number of time steps is required. Although a relatively large time step size reduces the total number of time steps required, it generally results in difficult convergence and a large number of iterations per time step. Numerical experimentation was therefore conducted to optimise the time step size so as to give smooth and stable convergence and reduce the number of iterations required to reach the convergence target at each time step; accordingly, a small time step of 0.01 s was chosen.

Due to the steady state nature of the flow, the solution eventually reached steady state and met the convergence criterion which was set at a residual target RMS = 10^{-4}. This level of convergence was very good for such a complex flow problem. A higher level of convergence of RMS = 10^{-5} did not affect the results but prolonged the simulation time considerably. For the chosen time step size, 1-5 iterations were required to achieve convergence to RMS = 10^{-4} for all of the equations at each time step. On average, a total of ~ 200 time steps were required to achieve convergence.

5.4. VALIDATION OF CFD MODEL

5.4.1. VALIDATION PROCESS

Detailed measurements of the flow field in solid-liquid suspensions are very scarce due to the lack of suitable measurement techniques. Fairhurst (1998) carried out extensive experiments using the technique of Positron Emission Particle Tracking (PEPT) to determine the trajectories and velocity profile of coarse solid particles flowing in non-Newtonian CMC carrier fluids (Barigou *et al*., 2003; Fairhurst *et al.*, 2001). Hall effect sensors were also used to independently measure particle passage times and, thus, provide a further set of different results for validating the CFD computations. These unique sets of experimental results are used here for the purpose of evaluating the accuracy of the numerical CFD simulations. CFD predictions of pressure drop in solid-liquid flow, on the other hand, are assessed using correlations gleaned from the literature. The validation of velocity profiles and pressure drop in single-phase fluid flow simulations was based on exact analytical equations.

5.4.1.1. PEPT validation of solid phase velocity profile

PEPT uses a single positron-emitting particle as a flow tracer which is tracked in 3D space and time within operating equipment to reveal its full Lagrangian trajectory. PEPT is unique in flow visualisation terms, being able to examine flow phenomena in three dimensions that could not be observed as effectively by using other techniques. It is particularly useful for the study of multiphase flows, to map the flow of fluids and the flow of particles, where one component can be labelled and its behaviour observed. The method allows probing of opaque fluids and within opaque apparatus, a distinct advantage over optical visualisation methods such as Laser Doppler Velocimetry (LDV) or Particle Image Velocimetry (PIV).

The PEPT technique involves a labelled tracer particle, a positron camera and a location algorithm. The tracer particle is labelled with a radionuclide which undergoes β^+ decay emitting a positron in the process. The emitted positron immediately annihilates with an electron producing two γ-rays which travel in almost

opposite directions with an energy of 511 keV. The γ-rays are then detected simultaneously by the positron camera which consists of two position-sensitive detectors mounted on either side of the field of view and capable of locating a detected γ-ray to within ~ 5 mm (Fairhurst *et al*., 2001). The location algorithm uses the uncorrupted trajectories of the γ-ray pairs to calculate the location of the tracer particle to within the resolution of the camera. Many of the detected events are usually corrupt due to scattering of one or both of the γ-rays prior to detection (Parker and Fan, 2008). For any measurement made using PEPT, there are two sources of error: (i) the positron travels some distance before it encounters an electron, and (ii) an error associated with the camera. Further details of the technique and its applications can be found in Barigou (2004).

In the PEPT experiments of Fairhurst (1998) (also in Barigou *et al*., 2003; Fairhurst *et al.*, 2001), a gravity-driven flow loop was used where the solid-liquid mixture flowed through a down pipe followed by a horizontal pipe, each of 1400 mm length and 45 mm inner diameter, as shown in Figure 5.1. The purpose of using a gravity-driven loop was to avoid the problem of pumping high solid fraction flows. The solid particles used in the experiments were alginate spheres of 5 and 10 mm diameters. Experiments were performed at outlet solid volumetric concentrations of 21 ± 2%, 30 ± 2% and 40 ± 2% v/v and mixture velocities ranging from 24 to 125 mm s^{-1}.

A 600 μm resin bead, containing the positron emitting radionuclide ^{18}F (half life of 110 min), was imbedded inside an alginate particle and used as a radioactive tracer. The resin bead had no measurable effect on the density of the particle, its mass being ~ 0.0002% that of the particle. The tracer thus had the same physical properties (density, mechanical, surface roughness) as any other particle and thus flowed in the same manner through the system making the particle track obtained representative of the others. During an experimental run, single tracers were injected into the loop and collected at the exit; at least 50 particle trajectories were measured in order to obtain a representative sample (Barigou *et al.*, 2003; Fairhurst *et al.*, 2001).

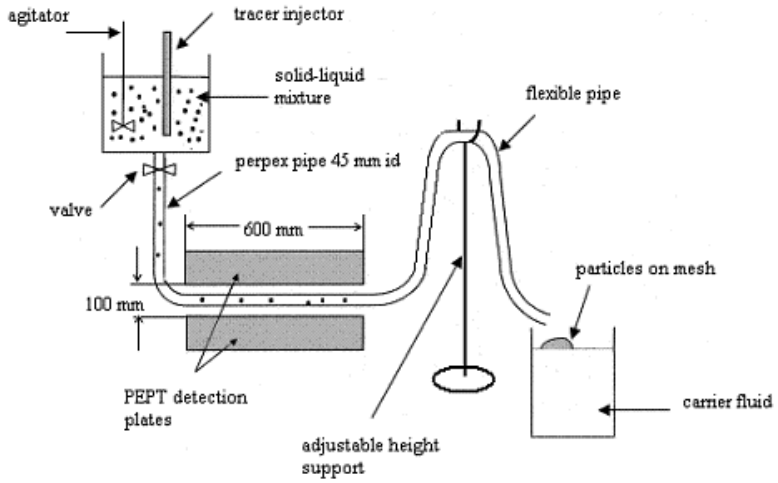

Figure 5.1: PEPT experimental rig (Fairhurst, 1998; Fairhurst *et al.*, 2001)

Particle velocity was obtained using an algorithm based on calculating the velocity of particles at different radial positions. This was achieved by following a particle at a particular radial position and measuring the distance between successive locations and the time required to travel this distance. Figure 5.2 shows a sample of the particle trajectories obtained by PEPT.

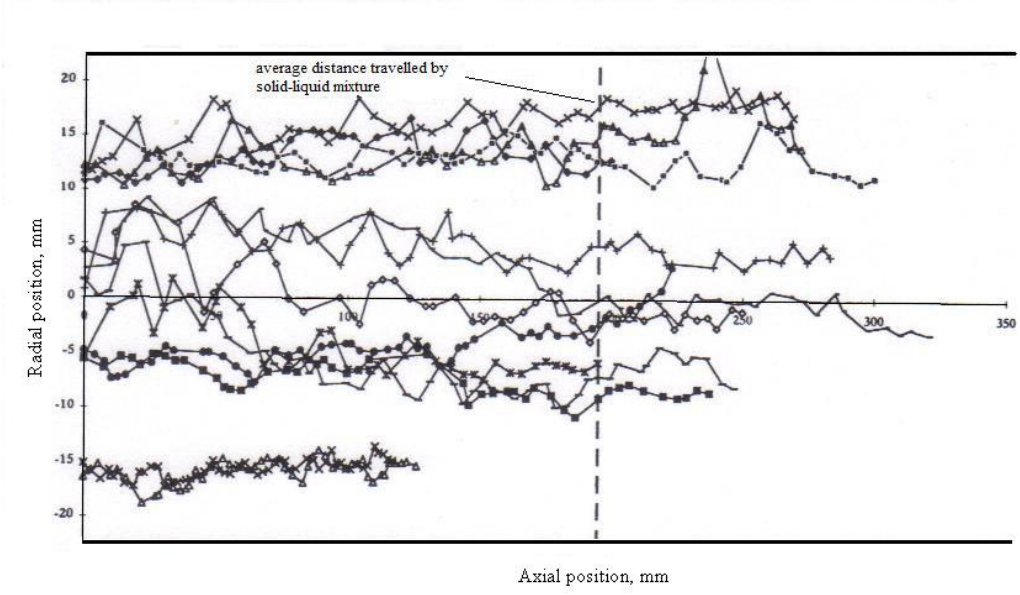

Figure 5.2: Sample particle trajectories obtained by PEPT (Fairhurst, 1998).

For horizontal flow, the velocity profile was obtained by dividing the pipe cross section into eight regions: four above and four below the pipe centreline as shown in Figure 5.3, thus taking into account the observed asymmetric nature of the particulate flow. In each region, the mean and standard deviation of the particle velocity were calculated. The mean velocity in each region was normalised using the mean flow velocity of the mixture, $\overline{u}$, and the resulting normalised velocity for each region was plotted against the radial position.

For vertical down-flow, the particulate flow was symmetrical due to the absence of particle settling, and the experimental velocity profile was obtained by dividing the pipe cross section into four concentric regions and measuring the average particle velocity in each region

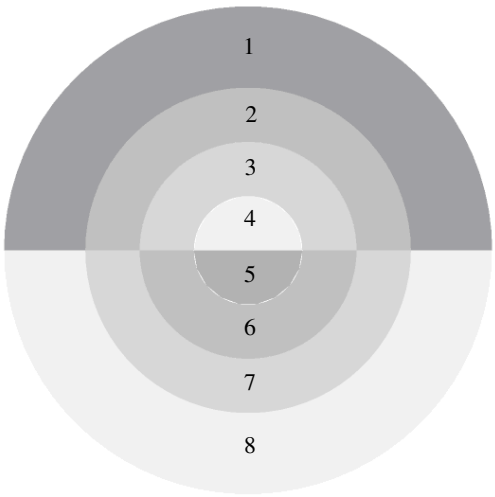

Figure 5.3: Division of pipe cross section into eight regions for solid phase velocity profile calculation.

5.4.1.2. Validation of pressure drop

Since no experimental data could be found in the literature for the type of suspension considered here, i.e. coarse particles in non-Newtonian or even Newtonian laminar flow, empirical and semi-empirical correlations were used to assess the CFD predictions of pressure drop. The CFD predictions were compared with those yielded

by Gradeck *et al.*'s correlation (Equations (5.32) and (5.34)); the correlation of Durand-Condolios (Equation (5.24)) in its original form (K = 150; m = -1.5), and in its modified form as proposed by Zandi and Govatos; the correlation advanced by Newitt *et al*. (Equation (5.29)); and the correlation proposed by Rasteiro *et al.* (Equations (5.30) and (5.31)). These correlations were considered particularly pertinent because of their apparent suitability to flows with a high particle concentration. However, it should be borne in mind that owing to the specific nature of empirical and semi-empirical correlations, these correlations are not expected to provide accurate predictions of the pressure drop of the suspensions used here, since empirical and even semi-empirical correlations can only be used with confidence for the range of experimental conditions under which they were developed.

5.4.2. VALIDATION RESULTS

5.4.2.1. Single-phase fluid flow

The first step in assessing the CFD model is to validate the flow field of the carrier fluid flowing alone. The rheological parameters of the two shear-thinning Ellis fluids used in the simulations are shown in Table 5.1. The velocity profiles calculated by CFD for the two fluids are compared with the exact analytical profiles (Equation (5.12)) in Figure 5.4. As can be seen in the figure, the agreement between theory and CFD is excellent for both fluids.

Homogeneous solid-liquid suspensions can often be represented by non-Newtonian single phase models, such as pseudoplastic fluids of the power law or Ellis types and viscoplastic (i.e. yield stress) fluids of the Herschel-Bulkley and Bingham plastic types. The flow of homogeneous suspensions can therefore be simulated accurately by CFD provided that the rheological parameters of the suspension are known.

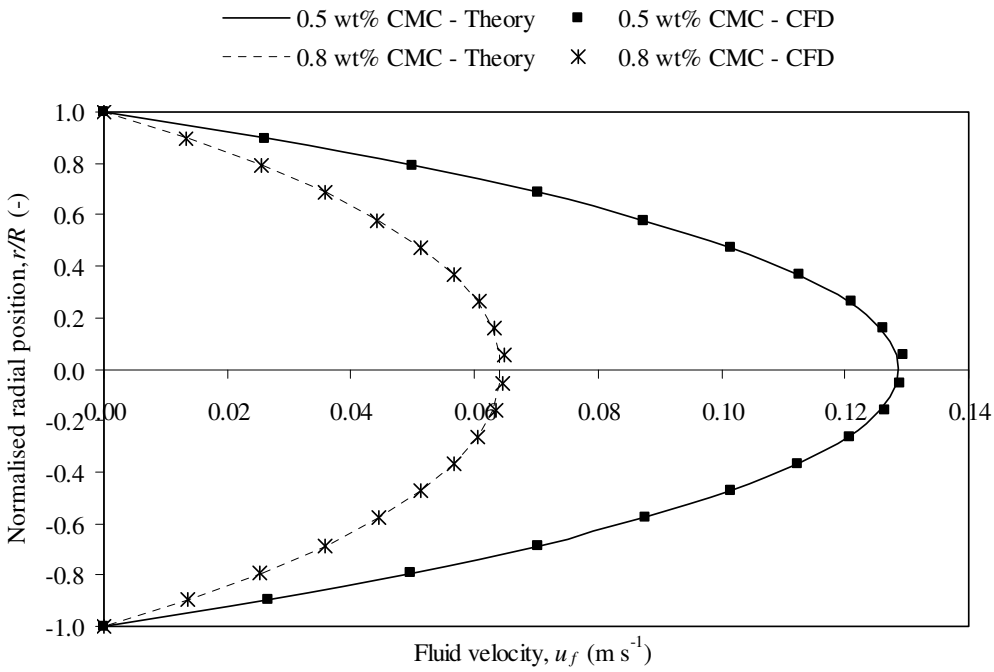

Figure 5.4: Comparison of theoretical and CFD velocity profiles of Ellis fluid flowing alone:
0.5% CMC, $\bar{u}$ = 66 mm s^{-1}; 0.8% CMC, $\bar{u}$ = 33 mm s^{-1}.

5.4.2.2. Two-phase flow: solid phase velocity profile

The CFD-predicted solid phase velocity profiles were validated using the experimental PEPT results obtained by Fairhurst (1998) (some of the results are also reported in Barigou *et al*. (2003) and Fairhurst *et al*. (2001)). The cases studied are summarised in Table 5.1.

The CFD velocity profiles for the cases considered here were obtained from the converged solution of the model at a section 100 mm upstream of the pipe exit, and are compared to the PEPT profiles in Figures 5.5-5.9 and 5.12-5.13 for horizontal and vertical flow, respectively.

Table 5.1: Range of PEPT experiments and corresponding CFD simulations.

	CMC (% w/w)	μ_0 (Pa s)	$\tau_{1/2}$ (Pa)	α (-)	d (mm)	ρ_s (kg m^{-3})	C_s (-)	$\bar{u}$ (mm s^{-1})	$\mathrm{Re}_p = \frac{\rho_f u_\infty d}{\mu_f}$	$\mathrm{Re}_t = \frac{\rho_f \bar{u} D}{\mu_f}$
Horizontal	0.5	0.12	6.6	2.03	5	1020	0.30	65	0.075	27.2
	0.5	0.12	6.6	2.03	10	1020	0.30	65	0.075	27.2
	0.8	0.62	7.4	2.03	10	1020	0.21	34	0.012	3.0
	0.8	0.62	7.4	2.03	10	1020	0.21	77	0.012	8.2
	0.8	0.62	7.4	2.03	10	1020	0.40	24	0.012	2.1
Vertical	0.5	0.12	6.6	2.03	10	1020	0.21	72	0.083	30.1
	0.5	0.12	6.6	2.03	10	1020	0.30	69	0.080	28.9

For horizontal flow, Figures 5.5-5.9 show a close agreement between CFD and experiment with the simulated profiles generally falling well within the experimental error bars. CFD simulation yields a smooth particle velocity profile, as can be seen in the figures, because the Eulerian-Eulerian numerical model used treats the solid phase as a continuum rather than individual particles. However, such a model has proved capable of providing a good prediction of the solid phase velocity profile under a wide range of flow conditions including considerably viscous non-Newtonian liquids and high solid concentrations up to 40% v/v.

A close examination of these velocity profiles shows that the position of the maximum particle velocity is not at the pipe centreline but slightly above it. This effect has also been observed by several researchers (Durand *et al*., 1953; Newitt *et al*., 1962; Fregert, 1995; and Fairhurst *et al*., 2001). The profiles also show that the particles flowing near the top of the pipe cross-section travel significantly faster than those at the bottom. This is a result of particle settling due to gravity, even though the solids density is only slightly higher than that of the carrier liquid. The degree of asymmetry was found to depend on the solids concentration and the particle Reynolds number (Barigou *et al.* 2003; Fairhurst *et al.*, 2001; Fairhurst, 1998). The velocity profile for the lowest solids concentration, C_s = 0.21 (Figures 5.7 and 5.8), is strongly asymmetrical with the point of maximum axial velocity shifted about 2.5 mm above the centreline. At C_s = 0.40 (Figure 5.9), however, the velocity profile is much more symmetrical indicating that gravitational effects are small; in this case, particle-particle interactions are clearly more significant. It is also noteworthy that, except near the bottom of the pipe, particles generally travel faster than the mean mixture velocity, as shown in Figures 5.5-5.9.

Another interesting feature is the velocity profile of the liquid phase and the effect of the dispersed solid phase on it. The CFD-calculated velocity profile of the carrier liquid in the suspension is compared in Figures 5.10-5.11 with the velocity profile of the same fluid flowing alone at the same total flow rate. The presence of solid particles clearly results in a fair degree of asymmetry and flattening in the carrier fluid velocity profile compared to that of the fluid flowing alone. Such a flattening of the

liquid velocity profile increases with particle concentration due to increased interactions between the carrier fluid and the solid particles (Figures 5.10 and 5.11). These effects will be explored in further detail in Section 5.5.

These results have significant implications for the flow of industrial solid-liquid mixtures, such as in the thermal sterilisation of food suspensions where both the solid and liquid velocity profiles are of paramount importance in estimating the hold-tube length to deliver safe but also good quality products. However, the measurement of velocity profile is difficult in thermal food processes owing to the invasive nature of most measurement techniques, opacity of the flows, the sometimes extreme processing conditions, and the inaccessibility of equipment. The results reported here show that CFD is indeed capable of providing good predictions of the flow behaviour of solid-liquid suspensions, particularly in such complex situations.

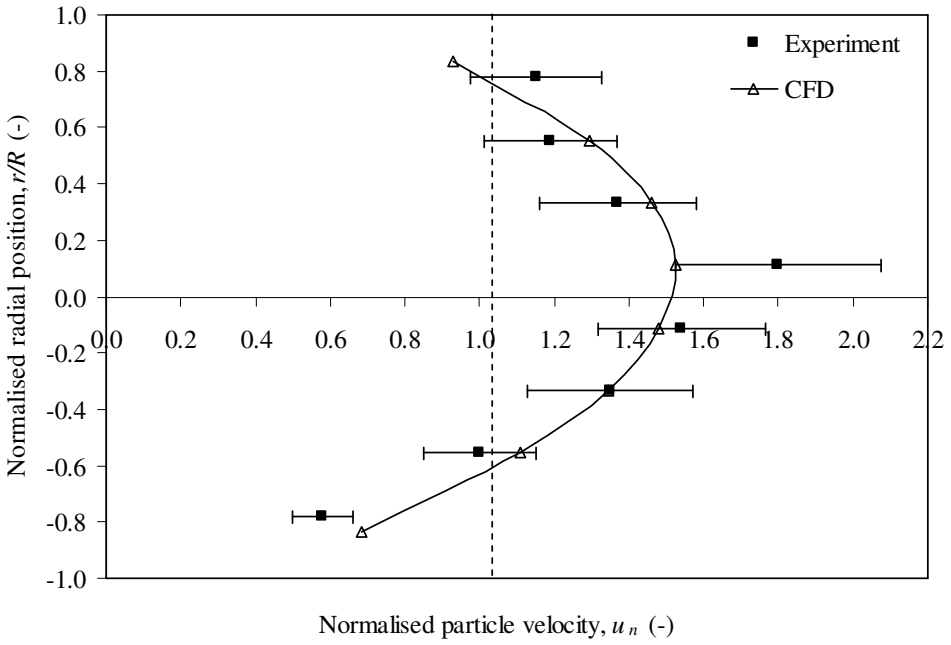

Figure 5.5: CFD-predicted and experimental solid phase velocity profiles compared: 0.5% CMC; ρ_s = 1020 kg m^{-3}; d = 5 mm; C_s = 0.30; $\overline{u}$ = 65 mm s^{-1}.

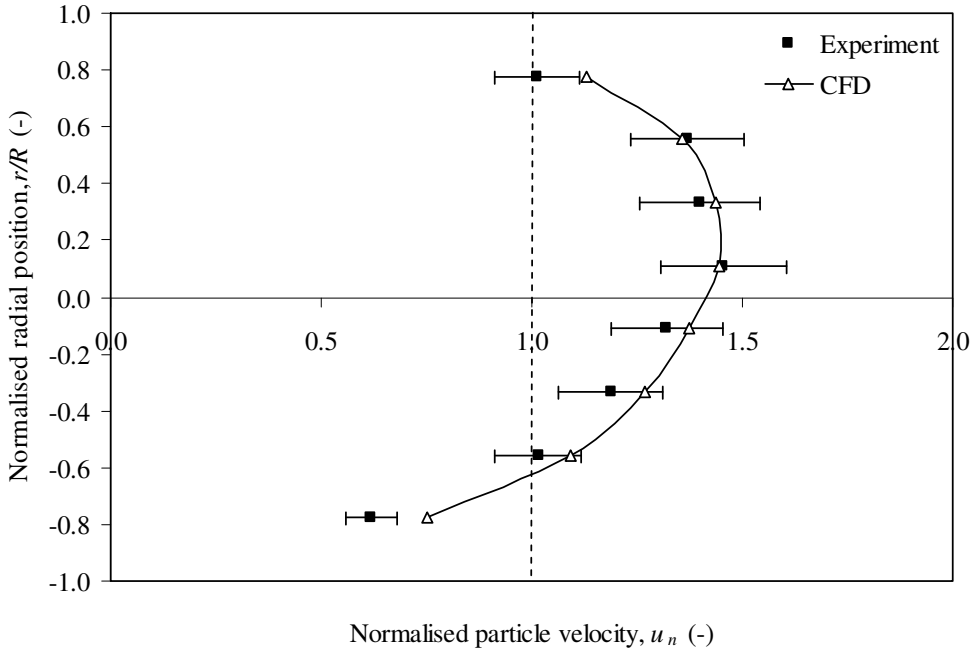

Figure 5.6: CFD-predicted and experimental solid phase velocity profiles compared: 0.5% CMC; ρ_s = 1020 kg m^{-3}; d = 10 mm; C_s = 0.30; $\overline{u}$ = 65 mm s^{-1}.

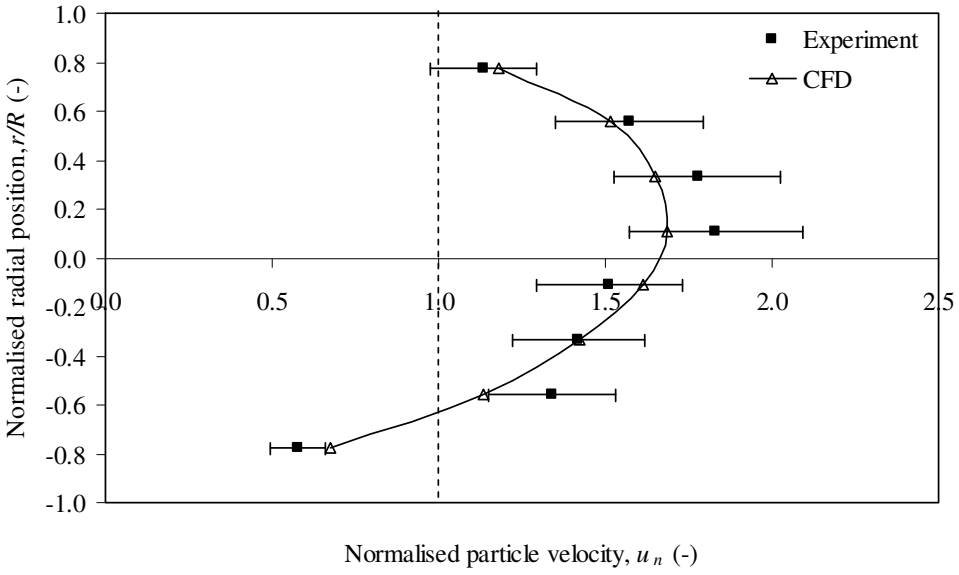

Figure 5.7: CFD-predicted and experimental solid phase velocity profiles compared: 0.8% CMC; ρ_s = 1020 kg m^{-3}; d = 10 mm; C_s = 0.21; $\overline{u}$ = 34 mm s^{-1}.

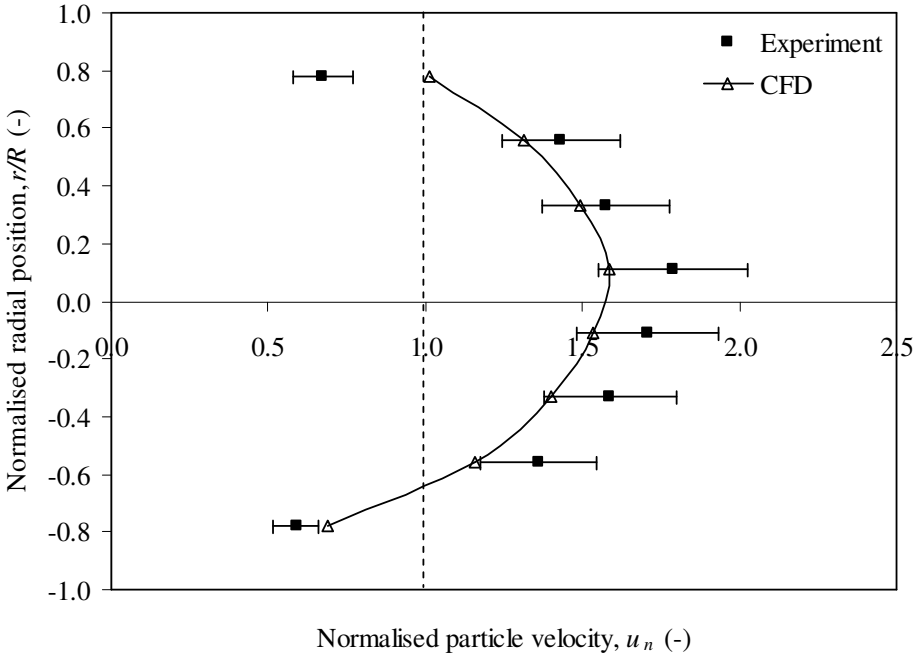

Figure 5.8: CFD-predicted and experimental solid phase velocity profiles compared: 0.8% CMC; ρ_s = 1020 kg m^{-3}; d = 10 mm; C_s = 0.21; $\overline{u}$ = 77 mm s^{-1}.

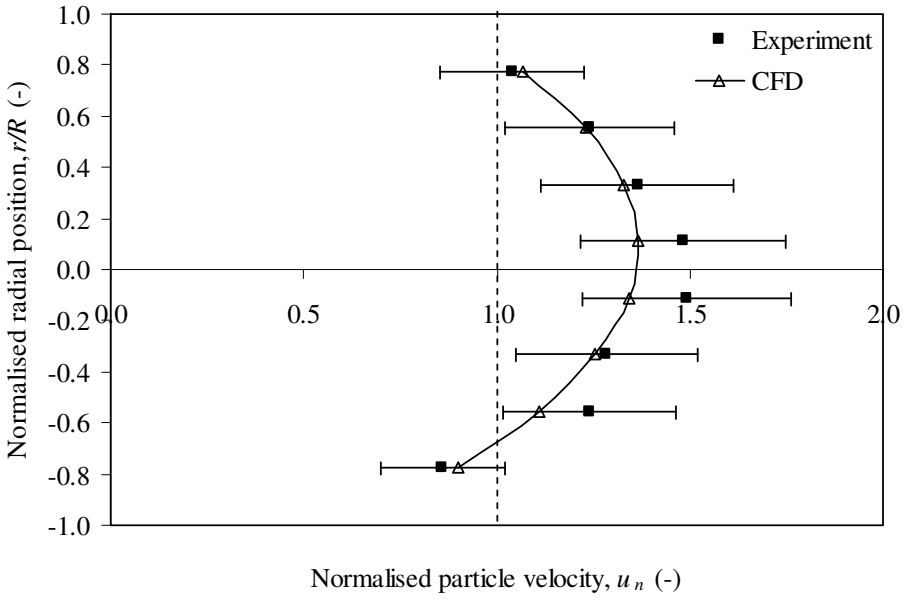

Figure 5.9: CFD-predicted and experimental solid phase velocity profiles compared: 0.8% CMC; ρ_s = 1020 kg m^{-3}; d = 10 mm; C_s = 0.40; $\overline{u}$ = 24 mm s^{-1}.

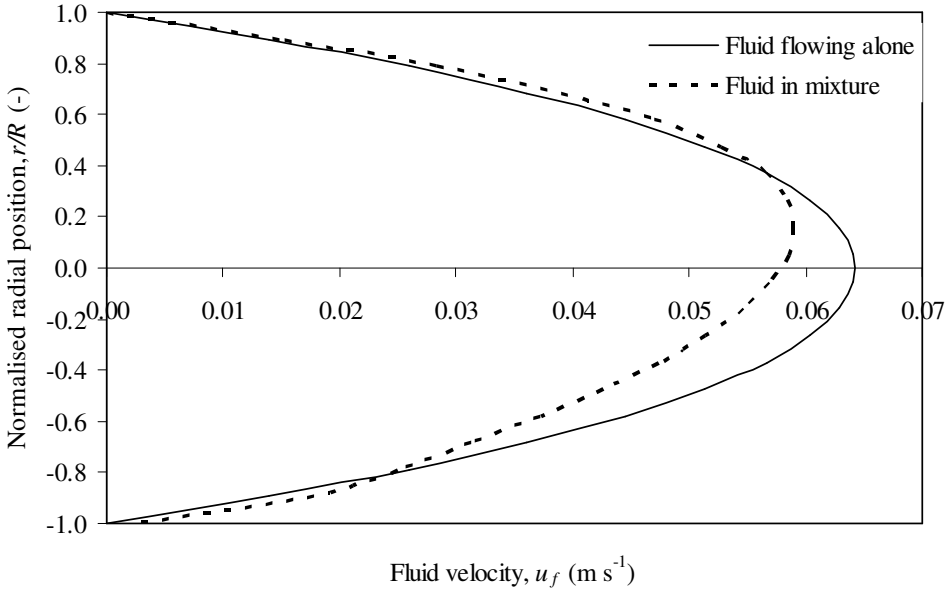

Figure 5.10: Effect of solid particles on the fluid velocity profile as predicted by CFD: 0.8% CMC; ρ_s = 1020 kg m^{-3}; d = 10 mm; C_s = 0.21; $\overline{u}$ = 34 mm s^{-1}.

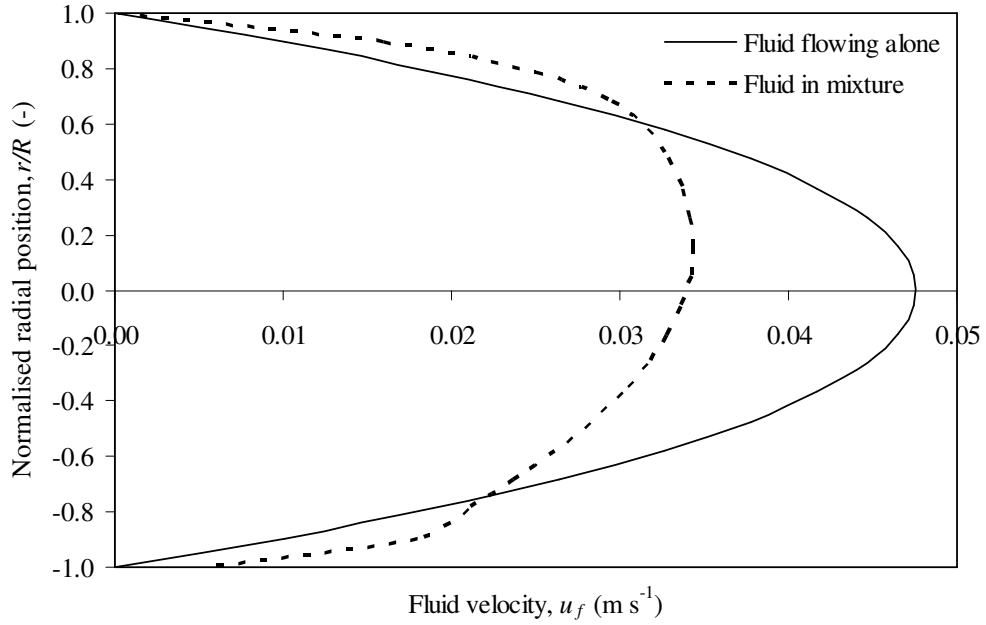

Figure 5.11: Effect of solid particles on the fluid velocity profile as predicted by CFD: 0.8% CMC; ρ_s = 1020 kg m^{-3}; d = 10 mm; C_s = 0.40; $\overline{u}$ = 24 mm s^{-1}.

For vertical down-flow, the agreement between CFD and experiment was very good for C_s = 0.21 (Figure 5.11) but less so for the higher concentration C_s = 0.30 (Figure 5.12). The negative sign in the values of the normalised particle velocity is due to the direction of flow (down-flow).

It can be seen that the solid phase velocity profile in vertical flow, whether determined by experiment or CFD, is symmetrical around the pipe centreline, in contrast with horizontal flow where particle settling gives rise to asymmetrical velocity profiles.

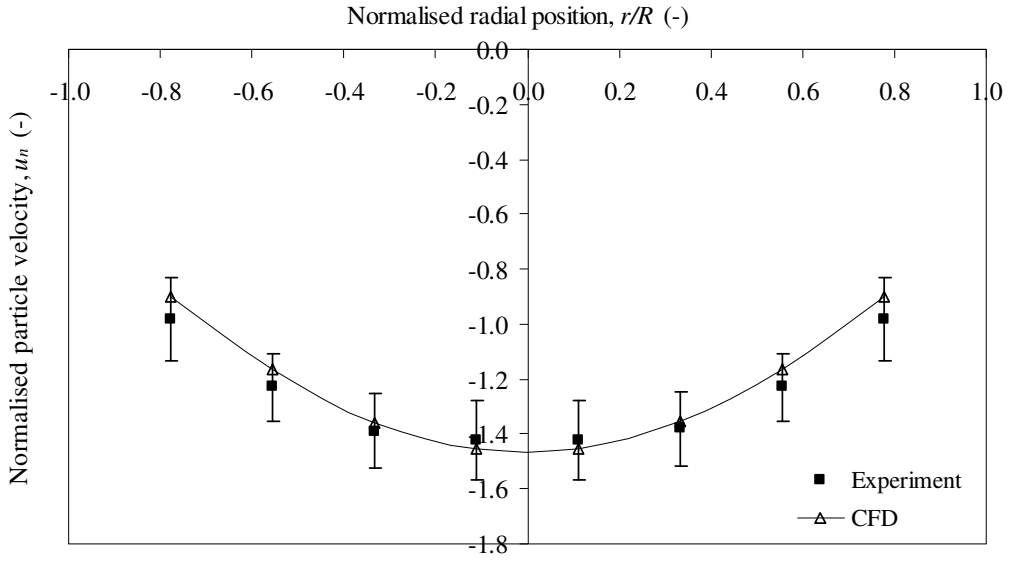

Figure 5.12: Comparison of experiment and CFD prediction of solid phase velocity profile in vertical down-flow:
0.5% CMC; ρ_s = 1020 kg m^{-3}; d = 10 mm; C_s = 0.21; $\bar{u}$ = 72 mm s^{-1}.

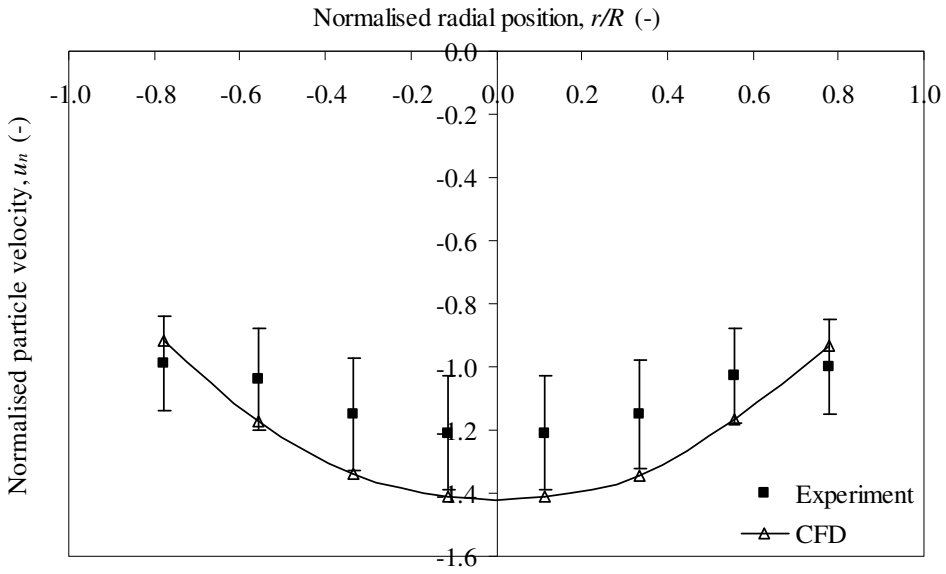

Figure 5.13: Comparison of experiment and CFD prediction of solid phase velocity profile in vertical down-flow:
0.5% CMC; ρ_s = 1020 kg m^{-3}; d = 10 mm; C_s = 0.30; $\bar{u}$ = 69 mm s^{-1}.

5.4.2.3. Two-phase flow: particle passage times

Prediction of particle passage times is sometimes required, for example in particulate food processing where control of the time period for which the mixture constituents are subjected to treatment conditions is critical. It is important to be able to predict both the minimum and maximum passage times of particles in the heating and holding sections of the system, and ideally the whole distribution of passage times should be known. The particle passage times calculated using CFD for horizontal solid-liquid flow are compared with the experimental results of Fairhurst and Pain (1999) who determined the particle passage time experimentally using either Hall effect sensors (Tucker and Heydon, 1998) or visual tracers made of sodium alginate dyed with methyl blue. In all experiments at least 50 passage times were measured. The two methods gave practically the same results. By tracing a large number of representative particles, the minimum, maximum, and mean passage times were determined and were then normalised by the average passage time of the suspension. The normalised minimum, nPT_{min}, maximum, nPT_{max}, and mean passage time, nPT_{mean} were computed from the numerically simulated solid phase velocity profile.

The CFD calculation of passage time matched to a very good degree of accuracy the experimentally determined passage time values, with a maximum deviation of 10%, as shown in Table 5.2. This agreement with experiment provides a further validation of the CFD results since the passage time experimental data were obtained using a different experimental technique to that used in measuring the solid phase velocity profile.

By comparing the passage time data for the three cases simulated, it appears that increasing the particle diameter at the same solids concentration generally increases nPT_{min}, which corresponds to the fastest flowing particles in the flow, while reducing nPT_{max}, which in turn corresponds to the slowest moving particles. A similar effect was observed when the particle concentration was increased.

5.4.2.4. Two-phase flow: solid-liquid pressure drop

To test the accuracy of CFD computations of pressure drop in solid-liquid food suspensions, CFD simulations were performed using a range of coarse particle diameters, particle concentrations and Reynolds numbers based on fluid effective viscosity, as shown in Table 5.3.

The pressure drop per unit length was computed in the downstream half of the pipe, i.e. away from the entrance region. The CFD predictions of pressure drop per unit length are compared in Table 5.3 with the predictions of empirical and semi-empirical correlations. Overall, Rasteiro *et al.*'s semi-empirical correlation provided the best agreement with CFD, as can be seen in the table. In most of the cases studied, the agreement was within ~15% even at high particle concentrations, which can be considered very good considering the complexity of the flow. Agreement between CFD and Gradeck *et al.*'s correlation was also very good (~10%) at low particle concentrations, but deteriorated at higher concentrations which were outside the range of their experimental data and therefore fell outside the correlation's range of validity (i.e. $C_s > 15\%$ v/v).

Table 5.2: Particle passage time: CFD and experimental measurements compared.

CMC (% w/w)	*D* (mm)	$\bar{u}$ (m s^{-1})	C_s (-)	$\mathrm{Re}_t = \frac{\rho_f \bar{u} D}{\mu_f}$	nPT_{min}		nPT_{max}		nPT_{mean}	
					Experiment	CFD	Experiment	CFD	Experiment	CFD
0.5	10	0.23	0.31	106	0.74	0.71 (-4%)[a]	1.11	1.19 (+7%)	0.92	0.99 (+8%)
0.5	5	0.23	0.32	106	0.67	0.67 (0%)	1.60	1.51 (-6%)	0.98	1.00 (+2%)
0.5	5	0.23	0.41	106	0.84	0.76 (-10%)	1.16	1.15 (-1%)	0.93	0.99 (+7%)

[a] Deviation of CFD prediction from experimental data

The agreement with the correlations of Durand-Condolios, Newitt *et al*. and Zandi and Govatos was much less satisfactory, with deviations exceeding 100% in some cases. Disagreement seems generally to worsen as particle concentration increases, particle diameter decreases and Reynolds number increases. Several researchers have reported large deviations of the Durand-Condolios correlation from experimental measurements. Rasteiro *et al.* (1993) reported considerable deviations of about 55% when comparing Durand-Condolios' correlation with a large set of experimental data from the literature including their own. Turian *et al*. (1971) also reported deviations exceeding 50%. Shook and Roco (1991) and more recently Dhodapkar *et al.* (2005) stated that Durand-Condolios' correlation and its modified versions are not recommended for suspensions with coarse particles, but they did not justify their statement.

A closer look at the results reported in Table 5.3 reveals that the prediction of pressure drop according to Durand-Condolios' correlation showed little influence of particle concentration on pressure drop, in agreement with the reported observations of Babcock (1971), who found that the groups included in the Durand-Condolios correlation were not sufficient to account for the effects of particle concentration and size. At all concentrations, the predicted pressure drop in solid-liquid flow was only slightly higher than for the fluid flowing alone, whereas CFD and other correlations (Gradeck *et al.*, Rasteiro *et al*.) predicted much higher pressure drops due the presence of the solid particles, sometimes as much as a three-fold increase at high concentrations.

Newitt *et al.*'s correlation was slightly more sensitive to particle concentration, but for a given concentration it showed a significant reduction in pressure drop with decreasing particle diameter contrary to an expected moderate increase because of the corresponding higher number of particles. Durand-Condolios' and Zandi and Govatos' correlations seem to suffer from the same deficiency but to a lesser degree. Gradeck *et al.*'s and Rasteiro *et al.*'s correlations do not incorporate the effect of particle diameter, as shown in Table 5.3. All these effects, however, were predicted by the CFD model used.

An exhaustive validation of CFD would require more extensive experimental data on pressure drop, which are presently unavailable in the literature. Nonetheless, the validation study has shown that overall CFD is capable of giving reasonable predictions of this important design parameter for the type of suspension investigated.

It emerges then that CFD offers a real potential in the study of solid-liquid flow systems, particularly where experimental data is lacking. It can provide useful information on the flow of solid-liquid suspensions, especially solid and liquid phase velocity profiles, which experiment may sometimes be unable to provide. However, validation of CFD models using experimental data will always be required and so experimental studies will always be needed for the development of CFD models.

Table 5.3: Comparison of CFD predictions of solid-liquid pressure drop with literature correlations.

					$\Delta P/L$ (Pa m^{-1})					
d (mm)	C_s (-)	ρ_s (kg m^{-3})	$\bar{u}$ (m s^{-1})	$\mathrm{Re}_t = \frac{\rho_f \bar{u} D}{\mu_f}$	CFD	Rasteiro *et al.* (1993) (Equation (5.30))	Gradeck *et al.* (2005) (Equation (5.32))	Newitt *et al.* (1955) (Equation (5.29))	Zandi and Govatos (1967) (Equation (5.24))	Durand and Condolios (1952) (Equation (5.24))[b]
2	0.20	1020	0.221	100	624	629 (-1%)[a]	719 (-13%)	379 (+65)	411 (+52%)	353 (+77%)
	0.30	1020	0.221	100	848	815 (+4%)	1116 (-24%)	394 (+115%)	442 (+92)	354 (+140%)
	0.40	1020	0.221	100	1070	1104 (-3%)	1712 (-38%)	408 (+162%)	473 (+126%)	357 (+200%)
5	0.20	1020	0.221	100	555	629 (-12%)	719 (-23%)	524 (+6%)	448 (+24%)	369 (+50%)
	0.30	1020	0.221	100	731	815 (-10%)	1116 (-34%)	612 (+19%)	498 (+47%)	378 (+93%)
	0.40	1020	0.221	100	928	1104 (-16%)	1712 (-46%)	699 (+33%)	547 (+70%)	387 (+140%)
5	0.10	1020	0.022	10	46	49 (-6%)	48 (-4%)	NA	NA	NA
	0.10	1020	0.221	100	452	498 (-9%)	478 (-5%)	437 (+3%)	499 (-9%)	359 (+26%)
	0.10	1020	1.107	500	2448	2479 (-1%)	2394 (+2%)	1757 (+36%)	1831 (+34%)	1754 (+40%)
10	0.10	1020	0.022	10	42	49 (-15%)	48 (-12%)	NA	NA	NA
	0.20	1020	0.221	100	488	629 (-22%)	719 (-32%)	1040 (-53%)	491 (-1%)	431 (+13%)

[a] Deviation of CFD prediction from correlation; [b] K = 150, m = -1.5

5.5. RESULTS AND DISCUSSION

A parametric study was conducted to determine the influence of various parameters on the flow properties of coarse solid particles in non-Newtonian carrier fluids of the power law type. Most of the simulations were performed for shear thinning fluids (i.e. $n < 1$) in horizontal flow, with a smaller set of vertical flow cases being carried out to investigate the influence of flow direction and these are discussed in a separate section. A few simulations were also conducted for shear thickening fluids (i.e. $n > 1$). The variables investigated were: particle size, mean particle concentration, mean mixture velocity, and power law parameters. The range of the numerical experiments conducted for each parameter studied is summarised in Table 5.4. The effects of the above mentioned variables on solid and fluid phase velocity profiles, radial particle distribution, and pressure drop are investigated.

5.5.1. PARTICLE DIAMETER

Food particles are usually coarse and have diameters on the millimetre scale. In this study, particle diameter was varied in the range 2-9 mm, corresponding to particle-pipe diameter ratios of d/D = 0.044-0.20. All the other flow parameters were held constant, as shown in Table 5.4.

5.5.1.1. Effect on solid phase velocity profile

The velocity profile of the solid phase was obtained at a section 100 mm upstream of the pipe exit and was normalised using the mean mixture velocity, $\overline{u}$. Sample results are shown in Figure 5.14 for d = 2, 4, 6 and 9 mm. The solid phase velocity profile is generally asymmetrical about the central axis, with particles flowing at higher velocities near the top wall of the pipe than near the base, but the degree of asymmetry depends on particle diameter. At d = 2 mm, the velocity profile is nearly symmetrical, with the particles close to the pipe wall constituting a slow moving annular region, while at larger diameters the asymmetry in the velocity profile becomes increasingly more pronounced. These results are in agreement with the experimental observations and PEPT measurements of Fairhurst (1998) for 5 and 10

mm diameter particles. Such asymmetrical profiles have also been reported for sand and water slurries (Newitt *et al.*, 1962) and for dilute food mixtures of up to 10% v/v solids (Fregert, 1995).

This asymmetry in the solid phase velocity profile is a result of particle settling due to the density difference between the two phases, even though this difference here is relatively small. To confirm this, a simulation was conducted with neutrally buoyant particles (i.e. $\rho_s = \rho_f$). The CFD-predicted velocity profiles of nearly-neutrally buoyant particles ($s = \rho_s/\rho_f = 1.02$) and of neutrally buoyant particles ($s = 1.00$) flowing under the same flow conditions are compared in Figure 5.15. The velocity profile of neutrally buoyant particles is exactly symmetrical due to the absence of particle settling. This result highlights the significance of any density difference between the two phases even when this difference is small.

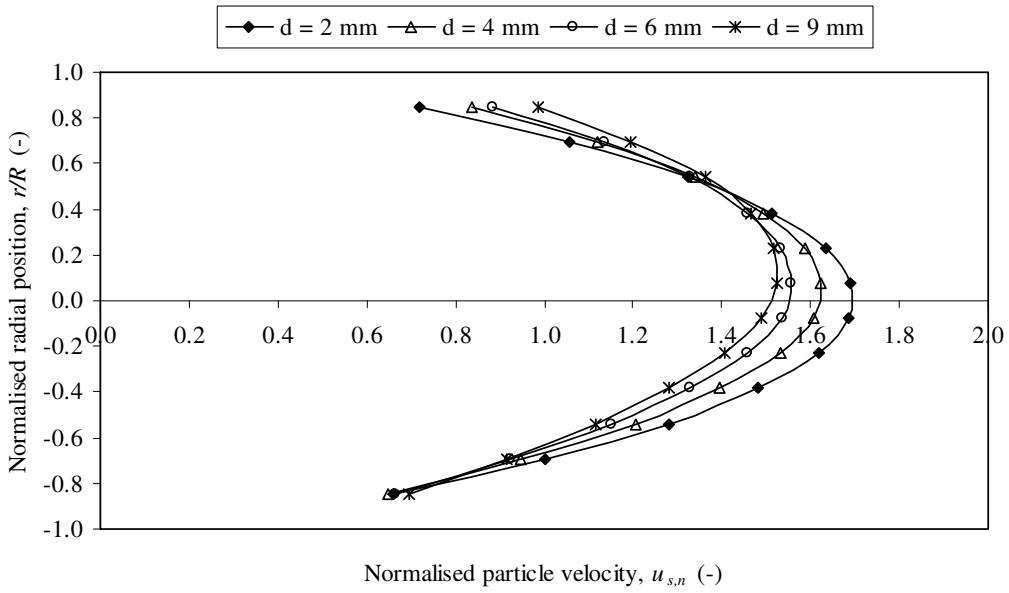

Figure 5.14: Effect of particle diameter on normalised solid-phase velocity profile: k = 0.16 Pa s^n; n = 0.81; ρ_s = 1020 kg m^{-3}; C_s = 0.25; $\bar{u}$ = 125 mm s^{-1}.

Table 5.4: Range of parametric CFD study for shear thinning fluids.

Direction of flow	Parameter investigated	k (Pa s^n)	n (-)	ρ_f (kg m^{-3})	ρ_s (kg m^{-3})	d (mm)	C_s (-)	u_m (mm s^{-1})	$\mathrm{Re}_t = \frac{\rho_f u_m D}{\mu_f}$	$\mathrm{Re}_p = \frac{\rho_f u_\infty d}{\mu_f}$
Horizontal	d	0.16	0.81	1000	1020	2-9	0.25	125	60	0.003-0.37
	C_s	0.16	0.81	1000	1020	4	0.05-0.40	125	60	0.026
	u_m	0.16	0.81	1000	1020	4	0.25	25-125	9-60	0.020-0.026
	n	0.15	0.6-0.9	1000	1020	4	0.30	125	50-116	0.025-0.031
	k	0.15-20	0.65	1000	1020	4	0.30	125	1-102	0-0.026
Vertical	d	0.16	0.81	1000	1020	2-8	0.25	66	28	0.003-0.22
	C_s	0.16	0.81	1000	1020	4	0.05-0.30	66	28	0.023

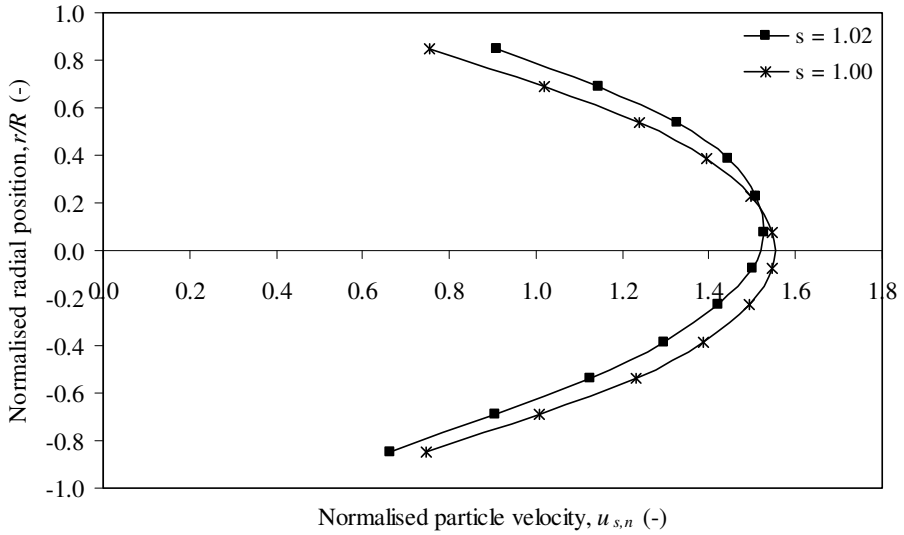

Figure 5.15: Normalised solid-phase velocity profile for neutrally buoyant and nearly-neutrally buoyant particles:
$k = 0.16$ Pa s^n; $n = 0.81$; $d = 7$ mm; $C_s = 0.25$; $\bar{u} = 125$ mm s^{-1}.

Two other features of the solid phase velocity profile which are affected by particle diameter are the position and value of the maximum particle velocity. While the maximum velocity occurs at the pipe centre for a fluid flowing alone, the maximum solid velocity in the solid-liquid mixtures studied lies generally above the centreline. The exact location of the fastest particle varies with particle diameter. For the smallest particles, the maximum of the velocity profile is located almost at the centre, but as d increases it shifts above the centreline. Moreover, the value of the maximum particle velocity decreases for coarser particles, which is in agreement with experimental observations for coarse particles of 5 and 10 mm diameter (Fairhurst, 1998; McCarthy *et al.*, 1997).

The particle velocity profile can have important implications in applications such as food processing where the aim is to safely sterilise the fastest particles without overcooking the slowest ones. The results in Figure 5.14 show that particles generally travel faster than the mean mixture velocity, $\bar{u}$, and the fastest amongst them travel at a velocity considerably less than twice the mean value. It is common practice in food

sterilisation, for example, to design holding tube lengths assuming that the maximum velocity is twice the average velocity, i.e. assuming laminar Newtonian flow (Lareo *et al.*, 1997(a)). Such an assumption is clearly conservative for shear thinning fluids and can, therefore, result in losses of nutrients and quality. On the other hand, particles flowing in shear-thickening carrier fluids can reach a maximum velocity greater than twice the mean flow velocity, $2\bar{u}$, as shown in Figure 5.16. It should be noted that a shear thickening fluid flowing alone has a maximum velocity greater than $2\bar{u}$. At moderate values of the flow behaviour index, *n*, above unity, the maximum fluid velocity is reduced to below $2\bar{u}$ since the velocity profile is flattened owing to the presence of the solid particles, similar to what happens in shear thinning fluids (see Section 5.5.4.1 below). At values of *n* substantially above unity, both the fluid and particle maximum velocities can exceed $2\bar{u}$. In such cases, estimation of a holding tube length based on a maximum velocity of twice the mean velocity will not be sufficient to ensure a safe process.

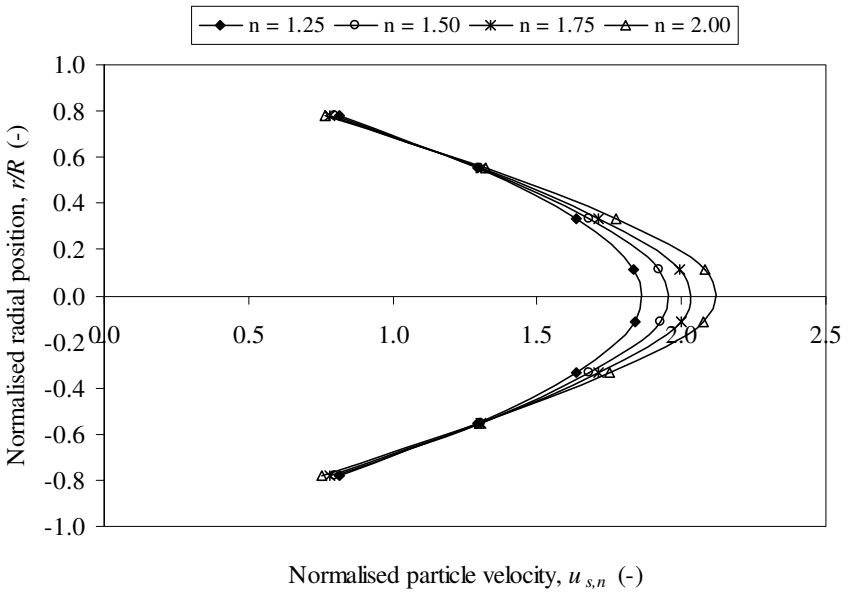

Figure 5.16: Solid-phase velocity profile in shear-thickening carrier fluids: k = 0.16 Pa s^n; d = 2 mm; C_s = 0.30; $\bar{u}$ = 125 mm s^{-1}.

5.5.1.2. Effect on carrier fluid velocity profile

Figure 5.17 shows how larger solid particles have a much more significant blunting effect on the velocity profile of the fluid than smaller particles. In addition, particles induce a degree of asymmetry in the fluid velocity profile which increases with particle size. Fluid near the base of the pipe does not adhere to the wall despite the no-slip boundary condition imposed there. Solid particles near the base of the pipe have a non-zero velocity due to the solid free-slip condition at the wall. The flowing particles disrupt the boundary layer at the pipe wall and sweep the fluid away, thus resulting in a small, but non-zero, fluid velocity in this region.

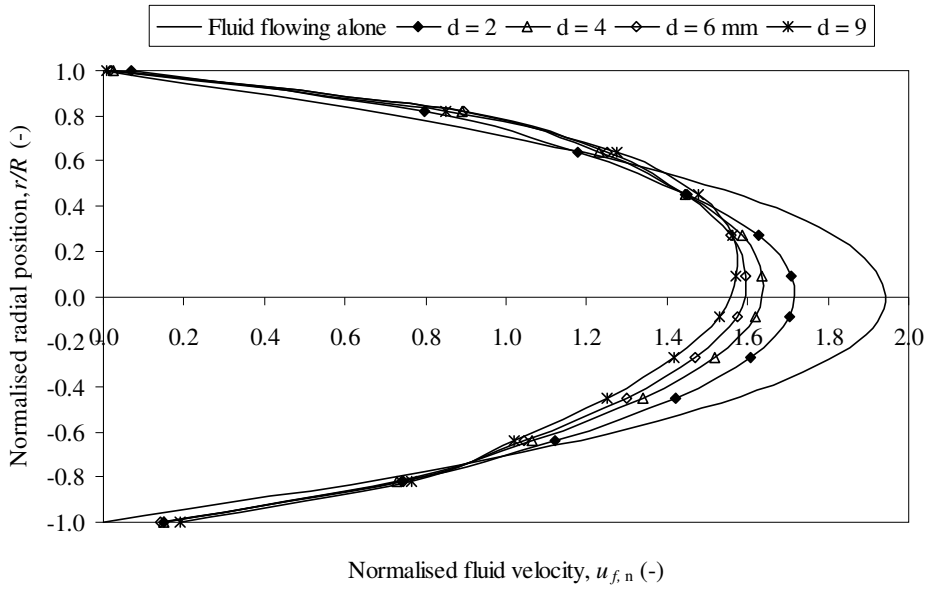

Figure 5.17: Effect of particle diameter on normalised carrier fluid velocity profile: k = 0.16 Pa s^n; n = 0.81; ρ_s = 1020 kg m^{-3}; C_s = 0.25; $\bar{u}$ = 125 mm s^{-1}.

5.5.1.3. Effect on particle concentration profile

The effect of particle size on the normalised radial distribution of the solid phase in the pipe is depicted in Figure 5.18. The normalised local particle concentration is calculated as the ratio of the local volume fraction at a given radial position to the mean volume fraction over the pipe cross-section. In general, three regions can be identified:

(i) a low-concentration region near the top of the pipe section;

(ii) a central region with a nearly uniform solids concentration; and

(iii) a high concentration region near the bottom of the pipe where the local solid fraction significantly exceeds the mean value.

As discussed above, the effect of particle settling becomes more pronounced at larger particle diameters, leading to higher particle concentrations near the bottom of the pipe. Indeed, the CFD-predicted concentration profiles demonstrate this effect clearly in Figure 5.18 for a range of particle sizes. Regions (i) and (iii) of the concentration profile at the top and bottom of the pipe, respectively, constitute a slow moving annular region encompassing a fast moving central core (region (ii)). The CFD results show that the diameter of the central core increases as particle size is reduced. Smaller particles, like neutrally buoyant particles, exhibit an entirely uniform radial distribution which is indicative of a pseudo-homogeneous flow.

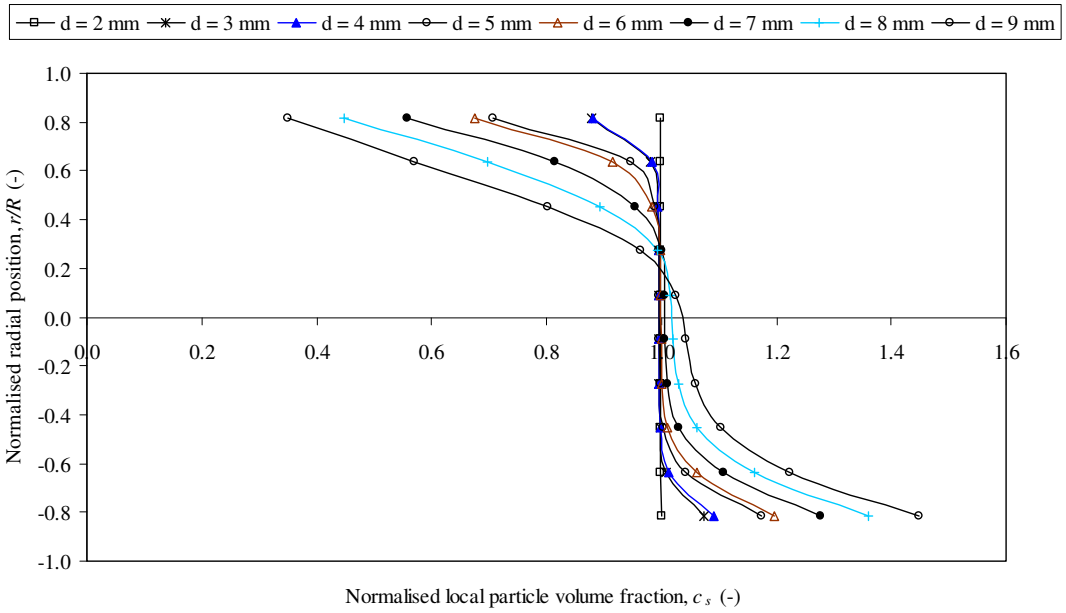

Figure 5.18: Effect of particle diameter on radial particle concentration profile: $k = 0.16$ Pa s^n; $n = 0.81$; $\rho_s = 1020$ kg m^{-3}; $C_s = 0.25$; $\bar{u} = 125$ mm s^{-1}.

5.5.1.4. Effect on pressure drop

In addition to friction arising from the flow of the carrier fluid, the presence of the particles introduces three additional sources of friction: particle-particle, particle-fluid and particle-wall friction, all of which are influenced by the surface area and, therefore, the diameter of the particles. The CFD model predicts a decrease in pressure drop as particle diameter increases, as shown in Figure 5.19 representing the percentage increase in pressure drop per unit length relative to that incurred by the carrier fluid flowing alone at the same flow rate. As d increases, at a constant particle concentration, the total surface area of the solid phase decreases, thus reducing particle-particle, particle-fluid, and particle-wall friction, hence the observed decrease in pressure drop. Such a reduction in pressure drop, however, diminishes in significance at larger values of d, probably due to the increased propensity of particle settling which tends to increase particle-wall friction.

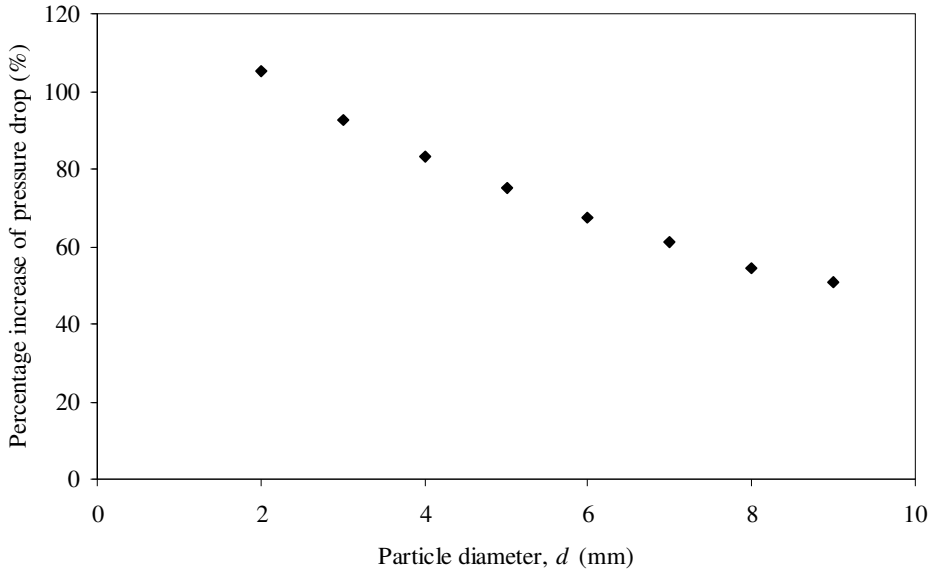

Figure 5.19: Effect of particle diameter on percentage increase in pressure drop relative to fluid flowing alone:
$k = 0.16$ Pa s^n; $n = 0.81$; $\rho_s = 1020$ kg m^{-3}; $C_s = 0.25$; $\overline{u} = 125$ mm s^{-1}.

5.5.2. PARTICLE CONCENTRATION

The concentration of the solid phase was varied from 5% to 40% v/v while holding the other parameters constant, as shown in Table 5.4. Significant effects were observed, as discussed below.

5.5.2.1. Effect on solid phase velocity profile

The solid phase velocity profiles predicted by CFD at different particle concentrations are presented in Figure 5.20. The results show that increasing the particle concentration gives rise to increased blunting of the solid phase velocity profile, thus lowering the maximum velocity of particles near the pipe centre and raising the velocity of particles flowing near the wall, in agreement with experimental findings (Fairhurst *et al*., 2001; Fairhurst, 1998).

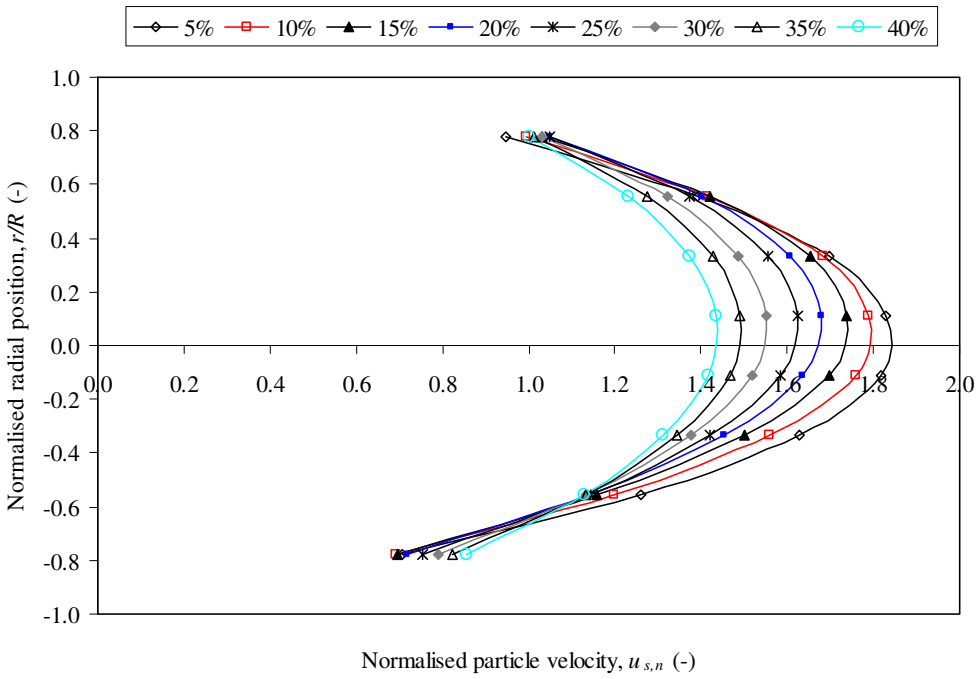

Figure 5.20: Effect of particle concentration on normalised solid-phase velocity profile:

k = 0.16 Pa s^n; n = 0.81; ρ_s = 1020 kg m^{-3}; d = 4 mm; $\bar{u}$ = 125 mm s^{-1}.

5.5.2.2. Effect on carrier fluid velocity profile

Figure 5.21 shows the effect of particle concentration on the carrier fluid velocity profile. The results indicate that increasing the particle concentration has a similar flattening effect on the velocity profile of the carrier fluid as it has on the solid phase velocity profile. As pointed out above, the fluid layer near the bottom wall of the pipe has a non-zero velocity that increases with solids concentration. This is due to the increasing velocity of the solid particles at higher C_s values (Figure 5.20), which disrupt the fluid boundary layer at the wall and generate a significant fluid slip. It is interesting to note that at C_s = 0.4, for example, the fluid velocity at the bottom wall reaches a value about 20% the maximum fluid velocity.

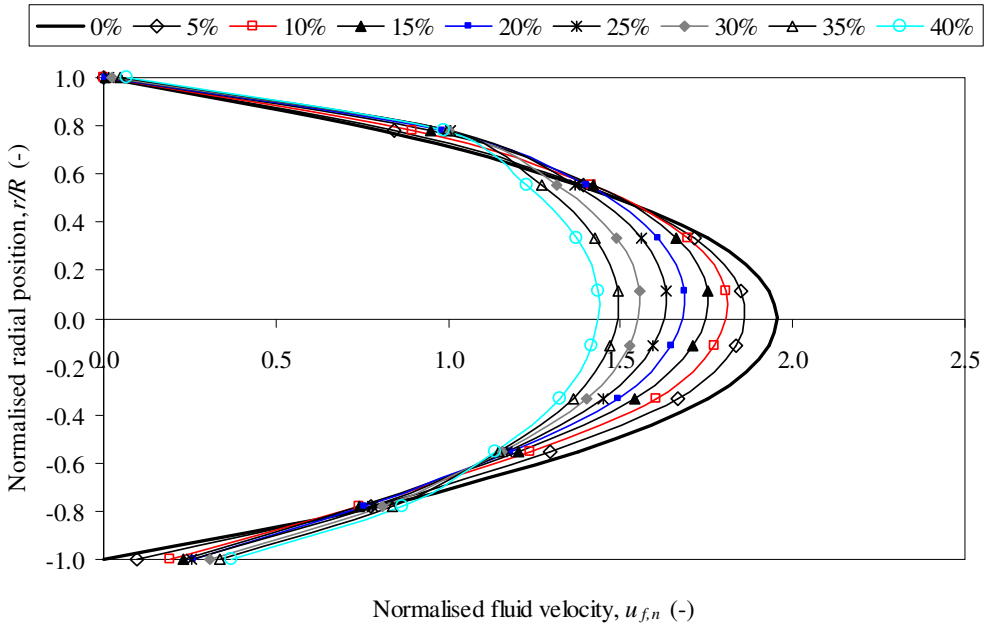

Figure 5.21: Effect of particle concentration on normalised carrier-fluid velocity profile:

k = 0.16 Pa s^n; n = 0.81; ρ_s = 1020 kg m^{-3}; d = 4 mm; $\bar{u}$ = 125 mm s^{-1}.

5.5.2.3. Effect on particle concentration profile

The normalised concentration profile of the solid particles is plotted at different particle concentrations in Figure 5.22. The radial particle distribution becomes

increasingly more uniform at higher solid concentrations. At 40% v/v the concentration profile is almost flat across the entire pipe cross section. As the maximum packing concentration is approached, no space is available for particles to settle out, thus leading to a uniform concentration profile. Experimental particle tracks determined by PEPT have led to the same observations and the identification of a 'capsule flow' regime at such high particle concentrations (Barigou *et al.*, 2003; Fairhurst *et al.*, 2001). At lower C_s values, the central core region becomes more and more asymmetrical around the centreline as the local particle concentration in the top half of the pipe declines due to particle settling.

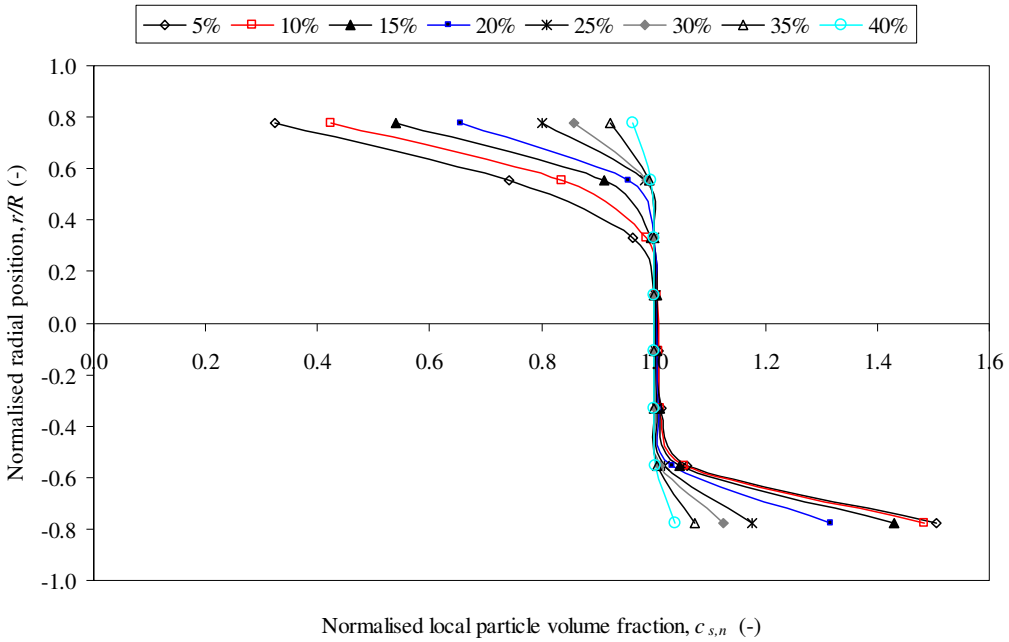

Figure 5.22: Effect of particle concentration on normalised particle concentration profile:

$k = 0.16$ Pa s^n; $n = 0.81$; $\rho_s = 1020$ kg m^{-3}; $d = 4$ mm; $\bar{u} = 125$ mm s^{-1}.

5.5.2.4. Effect on pressure drop

As discussed above, the presence of solid particles in the carrying medium increases the pressure drop incurred due to particle-particle, particle-fluid and particle-wall interactions. Friction losses due to these interactions increase as the solid

concentration increases, the number of particles increases and, hence, the total surface area of the solid phase increases. The percentage increase in pressure drop per unit length relative to that incurred by the carrier fluid flowing alone at the same flow rate was obtained from the CFD simulations at different particle concentrations, and the results are plotted in Figure 5.23. As can be seen in the figure, there is a steep rise in the mixture pressure drop as a function of C_s; an increase in particle concentration from 5% to 40% v/v results in more than a 100% increase in pressure drop. This represents a substantial rise in pressure drop compared to the carrier fluid flowing alone.

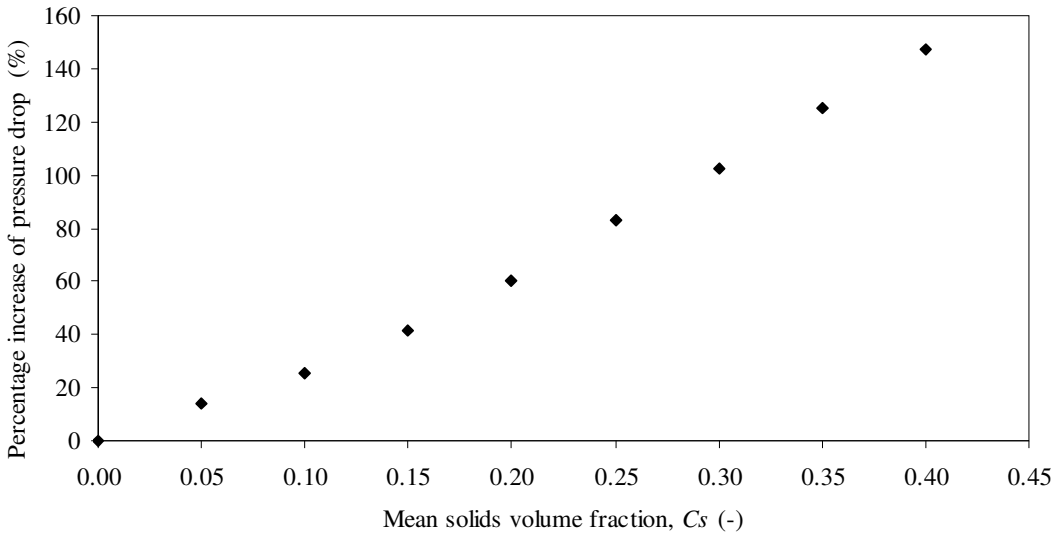

Figure 5.23: Effect of particle concentration on percentage increase in pressure drop relative to fluid flowing alone:
$k = 0.16$ Pa s^n; $n = 0.81$; $\rho_s = 1020$ kg m^{-3}; $d = 4$ mm; $\bar{u} = 125$ mm s^{-1}.

5.5.3. MIXTURE VELOCITY

Varying the mean mixture velocity in the range 25-125 mm s^{-1}, which covers the typical velocities normally used in food processing, whilst holding the other flow conditions constant as shown in Table 5.4, had little effect on the normalised solid phase and liquid phase velocity profiles, normalised particle concentration profile, and

increase of pressure drop per unit length relative to the carrier fluid flowing alone. The solid phase velocity profile results are consistent with the experimental PEPT measurements obtained by Fairhurst (1998).

5.5.4. RHEOLOGICAL PROPERTIES

The effects of varying the rheological parameters of the shear-thinning carrier fluid, namely, the flow behaviour index and the flow consistency index, were investigated.

5.5.4.1. Flow behaviour index, n

The flow behaviour index, n, indicates the extent of departure from Newtonian behaviour and is a measure of the degree of shear thinning of the fluid. This parameter was varied in the range 0.6-0.9 whilst all the other parameters were kept constant at the values shown in Table 5.4. Note that the case of shear-thickening carrier fluids, i.e. $n > 1$, has already been addressed above (see Section 5.5.1.1) in the context of the influence of shear thickening on the fluid and solid phase velocity profiles.

5.5.4.1.1. Effect on carrier fluid velocity profile

The effects of the flow behaviour index on the velocity profile of the carrier fluid in the suspension are depicted in Figure 5.24. There is a gradual flattening of the fluid velocity distribution as n is decreased, i.e. as shear thinning increases. There is a certain degree of asymmetry caused by the slip layer at the bottom of the pipe, as discussed above.

The velocity profile of the carrier fluid in the suspension is compared to that of the same fluid flowing alone in Figures 5.25 and 5.26 for the lowest and highest n values used, respectively. The presence of the particles has a significant flattening effect on the fluid velocity profile, where the maximum fluid velocity is reduced by some 20%. This effect was observed for all n values used.

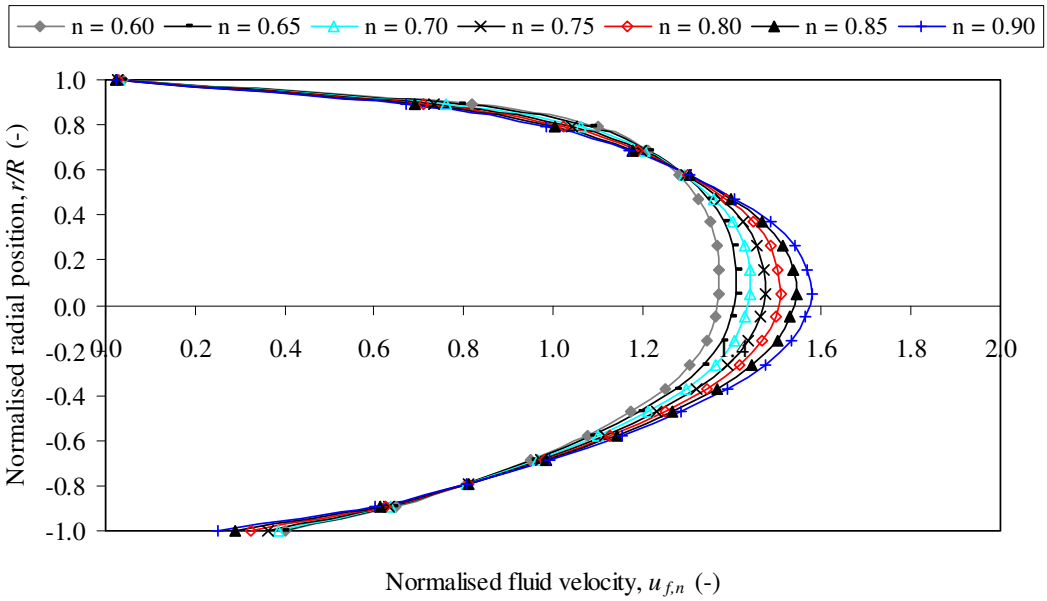

Figure 5.24: Effect of flow behaviour index on normalised carrier-fluid velocity profile:
k = 0.15 Pa s^n; ρ_s = 1020 kg m^{-3}; C_s = 0.30; d = 4 mm; $\overline{u}$ = 125 mm s^{-1}.

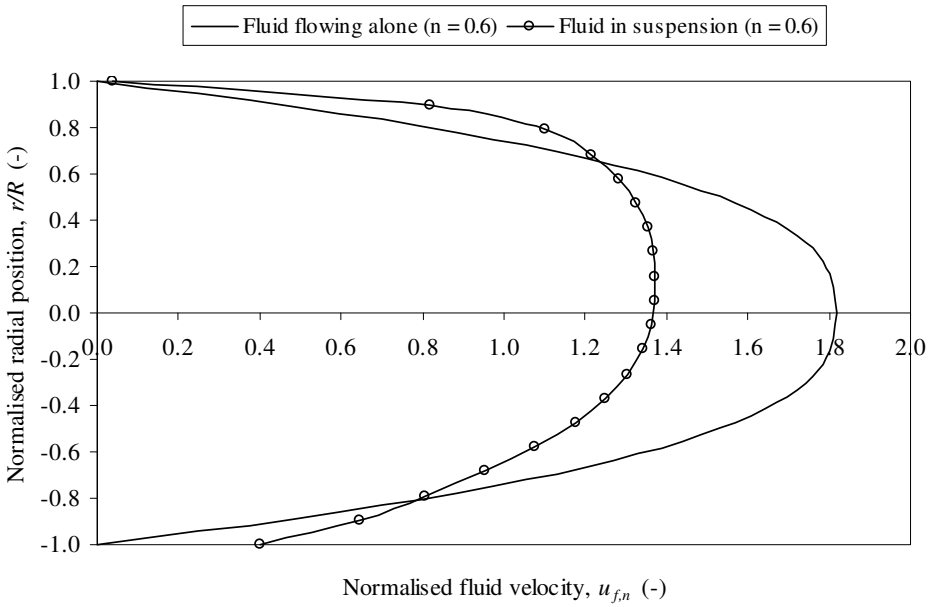

Figure 5.25: Effect of solid phase on normalised carrier-fluid velocity profile:
k = 0.15 Pa s^n; n = 0.60; ρ_s = 1020 kg m^{-3}; C_s = 0.30; d = 4 mm; $\overline{u}$ = 125 mm s^{-1}.

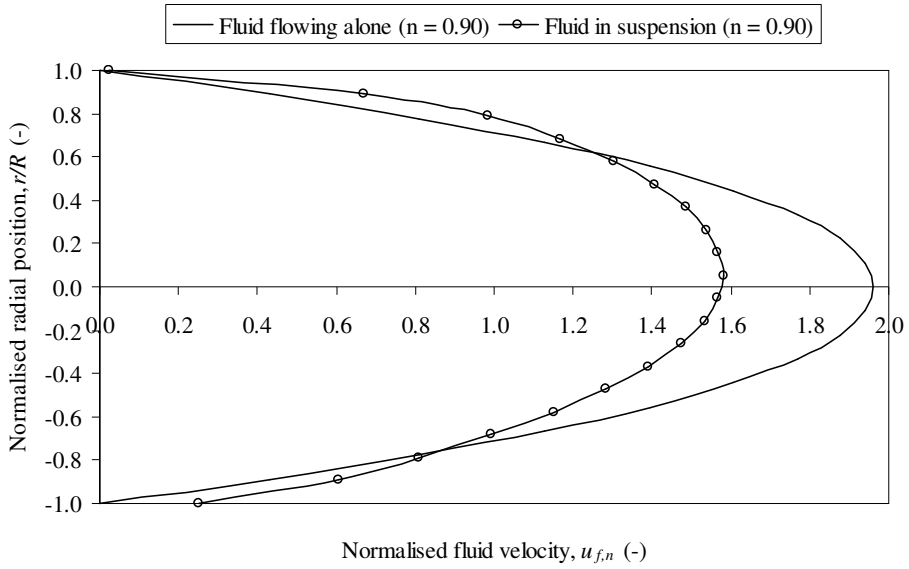

Figure 5.26: Effect of solid phase on normalised carrier-fluid velocity profile: k = 0.15 Pa s^n; n = 0.90; ρ_s = 1020 kg m^{-3}; C_s = 0.30; d = 4 mm; $\overline{u}$ = 125 mm s^{-1}.

5.5.4.1.2. Effect on solid phase velocity profile

The CFD-predicted velocity profiles presented in Figure 5.27 show that particles in the top half of the pipe travel faster than those in the bottom half of the pipe, with the maximum occurring slightly above the centreline. This asymmetry in the velocity profile is greater for more shear thinning fluids, i.e. for lower values of n. Enhanced shear thinning also leads to a blunter solid phase velocity profile as the fluid velocity profile becomes flatter (Figure 5.24). However, similar to the velocity profile of the carrier fluid, the effects are not large for the practical range of n values investigated here: reducing n from 0.9 to 0.6 leads to ~12% reduction in the maximum particle velocity.

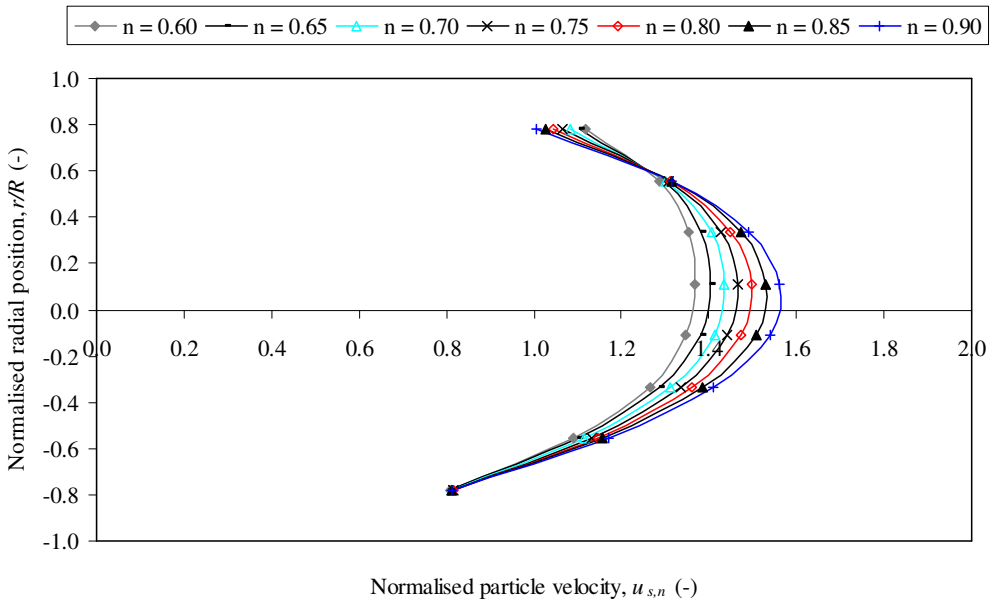

Figure 5.27: Effect of flow behaviour index on normalised solid-phase velocity profile:

k = 0.15 Pa s^n; ρ_s = 1020 kg m^{-3}; C_s = 0.30; d = 4 mm; $\bar{u}$ = 125 mm s^{-1}.

5.5.4.1.3. Effect on concentration profile

Simulations showed that n had little effect on the particle concentration profile within the range of values studied, i.e. n = 0.6-0.9.

5.5.4.1.4. Effect on pressure drop

The increase in pressure drop in solid-liquid flow relative to the single-phase pressure drop was found to be independent of the flow behaviour index. It may therefore be inferred that the increase in pressure drop due to the presence of the solid phase is independent of the non-Newtonian behaviour of the carrier fluid so long as an effective viscosity can be defined for the fluid. This explains the good agreement obtained between the CFD predictions of pressure drop for mixtures with a non-Newtonian carrier fluid and the predictions of the semi-empirical correlation of Rasteiro *et al.* (1993), originally derived for a Newtonian fluid (see Table 5.3).

5.5.4.2. Consistency index, k

The consistency index, k, was varied in the range 0.15 - 20 Pa s^n while the other variables were kept constant (Table 5.4). No significant effects were observed on the normalised solid phase and liquid phase velocity profiles, normalised particle concentration profile, and percentage increase of pressure drop relative to single-phase pressure drop.

5.5.5. VERTICAL DOWN-FLOW

The effect of flow orientation was studied by considering vertical down-flow in the same 45 mm diameter pipe. The range of parameters investigated is shown in Table 5.4.

CFD results showed that varying the particle diameter in the range 2-8 mm at C_s = 0.25 had little effect on the normalised solid phase and liquid phase velocity profiles and normalised concentration profile in vertical flow. Figure 5.28 shows the solid phase velocity profiles at different d values. The carrier fluid velocity profiles were found to be nearly identical to the solid phase profiles. The distribution of particles was remarkably uniform over the pipe cross section, due to the absence of particle settling in the pipe. Increasing the particle diameter from 2 mm to 8 mm resulted in only ~10% reduction in pressure drop compared to single phase fluid flow, as shown in Figure 5.29. This can also be explained by the absence of particle settling which, in turn, reduces particle-wall and particle-particle friction losses.

Solid concentration, varied within the range 5-30% v/v at d = 4 mm, also had no effect on the normalised solid phase velocity profile (Figure 5.30), liquid phase velocity profile and normalised concentration profile. The solid-liquid pressure drop, however, was substantially affected, as shown in Figure 5.31. Increasing solids concentration led to an increased pressure loss due to increased particle-particle, particle-fluid and particle-wall interactions.

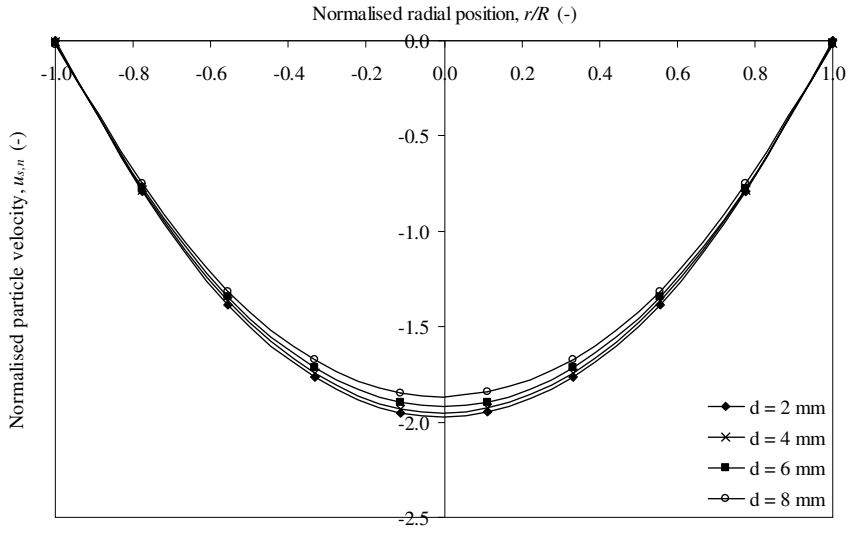

Figure 5.28: Effect of particle diameter on normalised solid phase velocity profile in vertical down-flow:
k = 0.16 Pa s^n; n = 0.81; ρ_s = 1020 kg m^{-3}; C_s = 0.25; $\overline{u}$ = 66 mm s^{-1}.

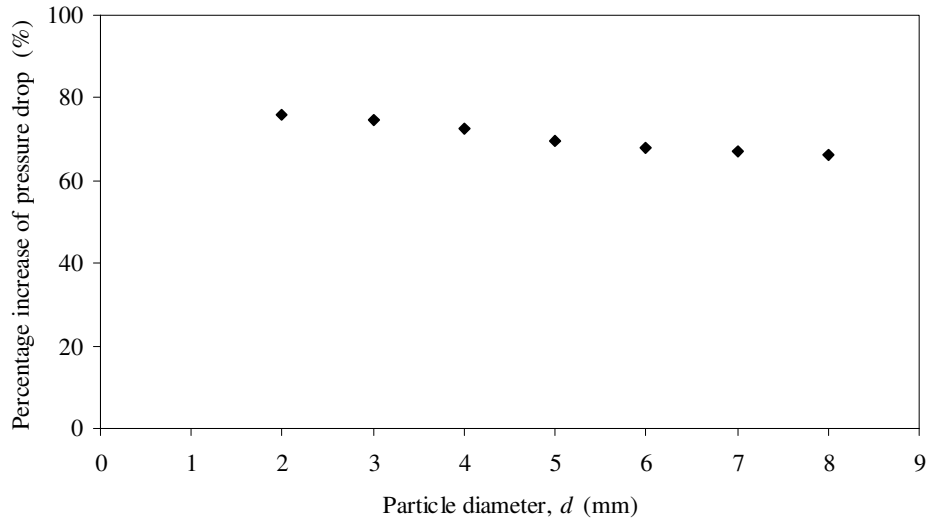

Figure 5.29: Effect of particle diameter on percentage increase in pressure drop relative to fluid flowing alone in vertical down-flow:
k = 0.16 Pa s^n; n = 0.81; ρ_s = 1020 kg m^{-3}; C_s = 0.25; $\overline{u}$ = 66 mm s^{-1}.

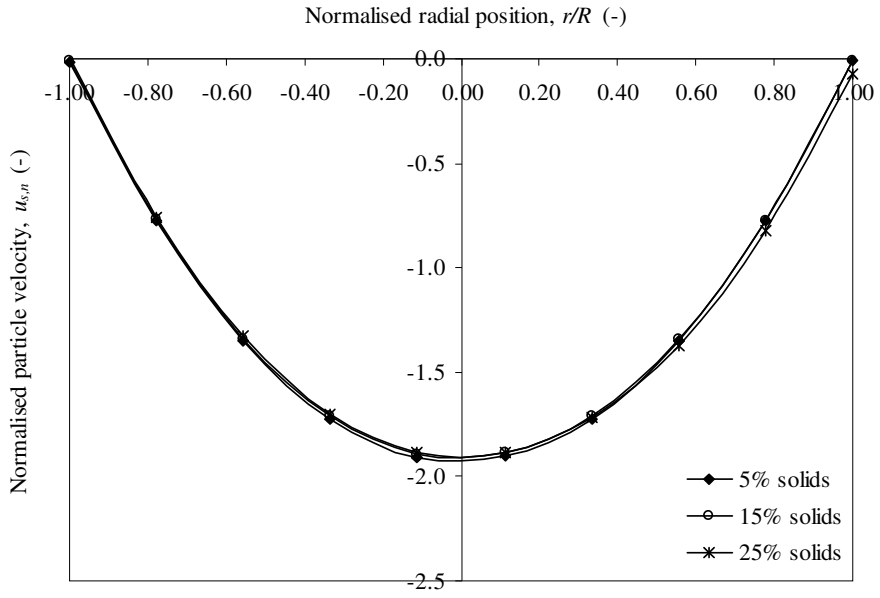

Figure 5.30: Effect of particle concentration on normalised solid phase velocity profile in vertical down-flow:
k = 0.16 Pa s^n; n = 0.81; ρ_s = 1020 kg m^{-3}; d = 4 mm; $\bar{u}$ = 66 mm s^{-1}.

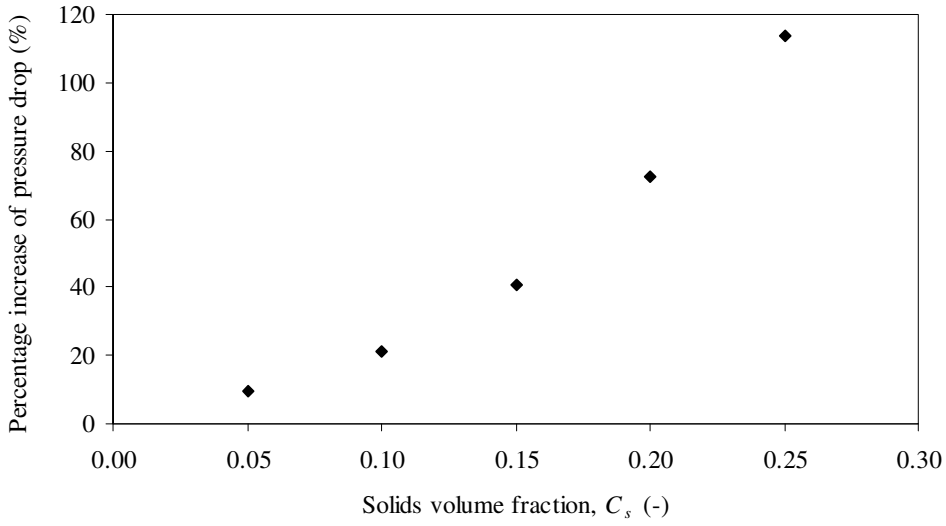

Figure 5.31: Effect of particle concentration in vertical down-flow on percentage increase in pressure drop relative to fluid flowing alone:
k = 0.16 Pa s^n; n = 0.81; ρ_s = 1020 kg m^{-3}; d = 4 mm; $\bar{u}$ = 66 mm s^{-1}.

5.6. CONCLUSIONS

CFD simulations of solid-liquid suspension flow of coarse nearly-neutrally buoyant particles in non-Newtonian fluids were performed using an Eulerian-Eulerian numerical model in order to assess the capability of CFD to predict the main features of such flows, namely, carrier fluid and solid phase velocity profiles, particle passage times, and mixture pressure drop. The Eulerian-Eulerian CFD model adopted within CFX 10.0 was capable of predicting the velocity profile of the carrier liquid flowing alone to an excellent degree of accuracy, in comparison with the exact theoretical velocity profile. Results showed that CFD is, thus, also capable of predicting the flow of homogeneous suspensions which can be approximated by single phase rheology such as pseudoplastic and viscoplastic types which are representative of many industrial suspensions.

The solid phase velocity profiles predicted by CFD generally matched the experimentally determined velocity profiles obtained by PEPT to a very good degree of accuracy. Minimum, maximum, and mean particle passage times measured by Hall effect sensors also agreed very well with CFD computations. The prediction of particle passage time has significant implications for the flow of industrial solid-liquid suspensions, as for example in the thermal sterilisation of food suspensions where sterility must be ensured without overcooking the solid particles. CFD predictions of solid-liquid pressure drop also showed a good agreement over a wide range of conditions with the semi-empirical correlation of Rasteiro *et al.* (1993), as well as with the more recent correlation of Gradeck *et al.* (2005) at low solid concentrations. Other older correlations (Durand and Condolios, 1952; Zandi and Govatos, 1967; Newitt *et al.*, 1955) showed much larger deviations from CFD, exceeding 100% in some cases. Their limitations in predicting the effects of solids concentration and particle size have been demonstrated.

Whilst a thorough validation of CFD would require more extensive experimental data on pressure drop, which are presently unavailable in the literature, the study conducted here has shown that, overall, CFD is capable of giving predictions which

are no worse but probably more reliable than the correlations available in the literature as it is based on the solution of the governing equations of motion.

The CFD model was then used to conduct a parametric study of the horizontal and vertical flow of coarse nearly-neutrally solid particles in power-law carrier fluids. The model was used to investigate the effects of particle diameter and concentration, mean flow velocity, and rheological properties of the carrier fluid on the solid phase and liquid phase velocity profiles, particle concentration profile, and pressure drop.

For particles larger than ~4 mm, the velocity profile of the solid phase exhibited a significant degree of asymmetry which increased with particle size due to the increased propensity of particle settling. Also, with increasing particle size, the maximum solids velocity decreased and the position at which this velocity occurred shifted upwards above the centreline. Particles generally travelled faster than the mean mixture velocity, and while the maximum particle velocity was considerably less than twice the mean mixture velocity in shear-thinning carrier fluids, it exceeded this value in strongly shear thickening fluids (~$n > 1.75$). Larger particles also caused significant blunting and asymmetry in the liquid phase velocity profile. Whereas the particle concentration profile was nearly uniform for smaller particles (2 mm), indicating a pseudo-homogeneous flow, increasing the particle diameter distorted the concentration profile due to enhanced settling. The solid-liquid pressure drop declined as particle diameter increased.

As the solids concentration was increased, the solid phase and liquid phase velocity profiles became flatter and the particles were radially more uniformly distributed. Increasing the concentration also increased the pressure drop incurred considerably as the friction losses due to particle interactions increased. Increasing the mean flow velocity had no noticeable influence on the normalised velocity profile of either phase, the normalised particle concentration profile, or the pressure drop increase relative to the carrier fluid flowing alone.

Similarly, the fluid consistency index of the carrier fluid did not have any influence on the normalised velocity profiles, normalised particle distribution, or pressure drop increase relative to single-phase flow. However, more shear thinning, i.e. lower n, induced a gradual flattening of the velocity profile of the solid phase and of the liquid phase relative to the fluid flowing alone. No significant effects were observed on the normalised particle concentration profile or the increase in pressure drop compared to single phase flow.

In vertical down-flow, particle radial distribution was remarkably uniform under all conditions investigated. The normalised solid-phase and liquid-phase velocity profiles and normalised particle concentration profile were independent of particle size and concentration under the conditions studied. However, increasing particle concentration resulted in a significant rise in pressure drop relative to single phase flow.

This study serves as a first step in extending the vibration work reported in previous chapters to solid-liquid suspensions. For this purpose, it may be necessary to combine Discrete Element Modelling (DEM) with CFD to study such complex flows.

NOMENCLATURE

C_D	drag coefficient (-)
C_l	lift coefficient (-)
C_s	solids volume fraction (-)
C_{sm}	maximum solids volume fraction (-)
d	particle diameter (mm)
D	pipe diameter (m)
E	compaction modulus (-)
f	friction factor (-)
F_D	drag force per unit volume (N m^{-3})
F_l	lift force per unit volume (N m^{-3})
g	gravitational acceleration (m s^{-2})
G_0	reference elasticity modulus (Pa)
k	consistency index (Pa s^n)
L	pipe length (m)
L_h	entrance length (m)
n	flow behaviour index (-)
p	pressure (Pa)
P_s	solids pressure (Pa)
Q	Volumetric flow rate, m^3 s^{-1}
r	radial position (m)
R	pipe radius (m)
Re_p	particle Reynolds number (-)
Re_{susp}	suspension Reynolds number (-)
Re_t	tube Reynolds number (-)
s	particle-fluid density ratio (-)
t	time (s)
u	local velocity (m s^{-1})
$\bar{u}$	mean mixture velocity (m s^{-1})
U_f	fluid velocity vector
U_s	solids velocity vector
u_f	local fluid velocity (m s^{-1})
$u_{f,n}$	normalised local fluid velocity (-)
u_m	mean mixture velocity (m s^{-1})
u_s	local solids velocity (m s^{-1})
u_{slip}	slip velocity (m s^{-1})
$u_{s,n}$	normalised local solids velocity (-)
u_∞	sedimentation velocity (m.s^{-1})

Greek letters

$\dot{\gamma}$	shear rate (s^{-1})
η	fluid apparent viscosity (Pa s)
μ_f	fluid effective viscosity (Pa s)
μ_r	relative suspension viscosity (-)

μ_s	solids viscosity (Pa s)
ρ_f	fluid density (kg m^{-3})
ρ_s	solid density (kg m^{-3})
τ	shear stress (Pa)

Subscripts

f	fluid
s	solid
m	mean
susp	suspension

REFERENCES

Abdul Ghani, A.G. & Farid, M.M. 2007. Numerical simulation of solid-liquid food mixture in a high pressure processing unit using computational fluid dynamics. *J. Food Eng.,* 80 (4), 1031-1042.

Alajbegovic, A., Asad, A., Bonetto, F. & Lahey Jr., R.T. 1994. Phase distribution and turbulence structure for solid/liquid up-flow in a pipe. *Int. J. Multiphase Flow,* 20 (3), 453-479.

Altobelli, S.A., Givler, R.C. & Fukushima, E. 1991. Velocity and concentration measurements of suspensions by nuclear magnetic resonance imaging. *J. Rheol,* 35 (5), 721-734.

Babcock, H.A. 1971. Heterogeneous flow of heterogeneous solids. In: Advances in solid-liquid flow in pipes and its application. Zandi, I. (Editor), Pergamon Press, N.Y.

Barigou, M. 2004. Particle tracking in opaque mixing systems: an overview of the capabilities of positron emission tomography, *Chem. Eng. Res. Des.*, 82 (A9), 1258-1267.

Barigou, M., Fairhurst, P. G., Fryer, P.J. & Pain, J.-P. 2003. Concentric flow regime of solid-liquid food suspensions: theory and experiment. *Chemical Engineering Science,* 58, 1671-1686.

Bouillard, J.X, Lyczkowski, R.W. & Gidaspow, D. 1989. Porosity distribution in a fluidised bed with an immersed obstacle. *AIChE J*., 35, 908-922.

Brown, N.P. & Heywood, N.I. 1991. Slurry handling: design of solid-liquid systems. Elsevier Science Publishing LTD.

Chakrabandhu, K. & Singh, R.K. 2005. Rheological properties of coarse food suspensions in tube flow at high temperatures. *Journal of Food Engineering*, 66, 117-128.

Charles, M.E. & Charles, R.A. 1971. In: Advances in solid-liquid flow and its applications. Zandi, I. (Editor), Pergamon.

Chhabra, R.P. & Richardson, J.F. 1999. Non-Newtonian flow in the process industries: Fundamentals and engineering applications. Butterworth Heinemann.

Chhabra, R.P. & Richardson, J.F. 1985. Hydraulic transport of coarse particles in viscous Newtonian and non-Newtonian media in a horizontal pipe. *Chem Eng Res Des*, 63, 390-397.

Clift, R., Grace, J.R. & Weber, M.E. 1978. Bubbles, drops and particles. Academic Press, Inc, NY.

Crowe, C.T., Sommerfeld, M. & Tsuji, Y. 1998. Multiphase flows with droplets and particles. CRC Press LLC.

Darby, R., 1986. Encyclopedia of Fluid Mechanics. Vol 5, Slurry flow technology. Cheremisinoff, N.P. (Editor). Gulf Publishing Company, Houston, Texas.

Dhodapakar, S., Jacobs, K. & Hu, S. 2005. In: Crowe, C.T. (Editor), Multiphase Flow Handbook. Fluid-Solid Transport in Ducts. CRC Press, Boca Raton, FL.

Ding, J. & Gidaspow, D. 1990. A Bubbling fluidization model using kinetic theory of granular flow. *AIChE J.*, 36 (4), 523-538.

Ding, J., Lyczkiwski, R.W., Sha, W.T., Altobelli, S.A. & Fukushima, E. 1993. Numerical analysis of liquid-solids suspension velocities and concentrations obtained by NMR imaging. *Powder Technology*, 77, 301-312.

Doron, P. & Barnea, D. 1995. Pressure drop and limit deposit velocity for solid-liquid flow in pipes. *Chemical Engineering Science,* 50 (10), 1595-1604.

Doron, P. & Barnea, D. 1993. A three-layer model for solid-liquid flow in horizontal pipes. *Int. J. Multiphase Flow*, 19, 1029-1043.

Duckworth, R.A., Pullum, L. & Lockyear, C.F. 1983. The hydraulic transport of coarse coal at high concentration. *J. Pipelines*, 3, 251-65.

Duckworth, R.A., Pullum, L., Addie, G.R. & Lockyear, C.F. 1986. Pipeline transport of coarse materials in a non-Newtonian carrier fluid. Hydrotransport 10, Paper C2, 69-88.

Durand R. 1953. Basic relationship of the transportation of solids in pipes-experimental research. *Proc. of Minnesota Int. Hydraulic Convention*. Minneapolis, MN, 89-103.

Durand, R. 1952. “The hydraulic transportation of coal and other materials in pipes,” Colloq. of National Coal Board, London. Cited in Wasp, E.J., Kenny, J.P. & Ghandi, R.L. 1979. Solid-liquid flow: slurry pipeline transportation. Trans Tech Publications, Clausthal, Germany.

Durand, R. & Condolios, E. 1952. Experimental study of the hydraulic transport of coal and solid materials in pipes. *Proc. Colloq. on the hydraulic transport of coal*. National Coal Board, London, UK, Paper IV, 39-55. [Cited in: Shook and Roco, 1991]

Eyring, H., Henderson, D., Stover, B.J. & Eyring, E.M. 1964. Statistical mechanics and dynamics. Wiley, New York.

Fairhurst, P.G., Barigou, M., Fryer, P.J., Pain, J-P. & Parker, D.J. 2001. Using positron emission particle tracking (PEPT) to study nearly neutrally buoyant particles in high solid fraction pipe flow. *Int. Journal of Multiphase Flow*, 27, 1881-1901.

Fairhurst, P.G. & Pain, J.P. (1999). Passage time distribution for high solid fraction solid-liquid food mixtures in horizontal flow: unimodal size particle distributions. *Journal of Food Engineering*, 39, 345-357.

Fairhurst, P.G. 1998. Contribution to the study of the flow behaviour of large nearly neutrally buoyant spheres in non-Newtonian media: application to HTST processing. Ph.D. Thesis, Université de Technologie de Compiègne, France.

Frankel, N.A. & Acrivos, A. 1967. On the viscosity of a concentrated suspension of solid spheres. *Chemical Engineering Science*, 22, 847-853.

Fregert, J. 1995. Velocity and concentration profiles for a laminar flow for a fluid containing large spheres in a horizontal pipe. Ph.D thesis, Lund University, Sweden.

Gauthier, F., Goldsmith, H.L. & Mason, S.G. 1971. Particle motions in non-Newtonian media. II. Poiseuille flow. *Trans. Soc. Rheol.*, 15 (2), 297-330.

Ghosh, T. & Shook, C.A. 1990. In: Freight pipelines, H. Liu and G.F. Round (Editors), Hemisphere.

Gidaspow, D. 1994. Multiphase flow and fluidisation: continuum and kinetic theory descriptions. Academic Press.

Gradeck, M., Fagla, B.F.Z., Baravian, C. & Lebouché, M. 2005. Technical Note: Experimental thermomechanic study of Newtonian and non-Newtonian suspension flows. *Int. Journal of Heat and Mass Transfer*, 48, 3769-3477.

He, Y.B., Laskowski, J.S. & Klein, B. 2001. Particle movement in non-Newtonian slurries: the effect of yield stress on dense medium separation. *Chemical Engineering Science*, 56, 2991-2998.

Hu, H.H., Patankar, N.A. & Zhu, M.Y. 2001. Direct numerical simulations of fluid-solid systems using the arbitrary Lagrangian-Eulerian technique. *Journal of Computational Physics*, 169, 427-462.

Jarzebski, G.J. 1981. On the effective viscosity of pseudoplastic suspensions. *Rheol. Acta,* 20, 281-287.

Jeffrey, D.J. & Acrivos, A. 1976. The rheological properties of suspensions of rigid particles. *AIChE J.,* 22 (3), 417-432.

Jung, A. & Fryer, P.J. 1999. Optimising the quality of safe food: Computational modelling of a continuous sterilisation process. *Chemical Engineering Science*, 54, 717-730.

Karnis, A., Goldsmith, H.L. & Mason, S.G. 1963. Axial migration of particles in Poiseuille flow. *Nature*, 200, 159-160.

Khan, A.R. & Richardson, J.F. 1987. The resistance to motion of a solid sphere in a fluid. *Chem. Eng. Commun.,* 62, 135-150.

Khan, A.R., Pirie, R.L. & Richardson, J.F. 1987. Hydraulic transport of solids in horizontal pipelines – predictive methods for pressure gradients. *Chemical Engineering Science,* 42 (4), 767-778.

Kleinstreuer, C. 2003. Two-phase flow: theory and applications. Taylor & Francis Books, Inc.

Kowalewski, T.A. 1980. Velocity profiles of suspension flowing through a tube. *Arch Mech,* 32 (6), 857-865.

Krampa-Morlu, F.N., Bergstrom, D.J., Bugg, J.D., Sanders, R.S. & Schaan, J. 2004. Numerical Simulation of dense coarse particle slurry flows in a vertical pipe. 5th International Conference on Multiphase Flow, ICMF'04, paper No.460.

Lareo, C.A. & Fryer, P.J. 1998. Vertical flows of solid-liquid food mixtures. *J. Food Eng.,* 36, 417-443.

Lareo, C., Fryer, P.J. & Barigou, M. 1997(a). The fluid mechanics of two-phase solid-liquid food flows: a review. *Trans. IChemE*, *Part C, Food Bioproducts Processing* 75, 73-105.

Lareo, C., Branch, C.A. & Fryer, P.J. 1997(b). Particle velocity profiles for solid-liquid food flows in vertical pipes, Part I: single particles. *Powder Technology,* 93, 23-34.

Lareo, C., Nedderman, R.M. & Fryer, P.J. 1997(c). Particle velocity profiles for solid-liquid food flows in vertical pipes, Part II: multiple particles. *Powder Technology*, 93, 35-45.

Legrand, A., Berthou, M. & Fillaudeau, L. 2007. Characterization of solid-liquid suspensions (real, large non-spherical particles in non-Newtonian carrier fluid) flowing in horizontal and vertical pipes. *Journal of Food Engineering*, 78, 345-355.

Le Guer, Y., Reghem, P., Petit, I. & Stutz, B. 2003. Experimental study of a buoyant particle dispersion in pipe flow. *Trans IChemE*, 81, Part A, 1136-1143.

Maciejewski, W., Lord, E., Gillies, R. & Shook, C. 1997. Pipeline transport of large ablating particles in a non-Newtonian carrier. *Powder Technology*, 94, 223-228.

Mankad, S., Branch, C. A. & Fryer, P. J. 1995. The e¤ect of particle slip on the sterilisation of solid-liquid food mixtures. *Chemical Engineering Science*, 50 (8) 1323-1336.

Matsuhisa, S. & Bird, R.B. 1965. Analytical and numerical solutions for laminar flow of the non-Newtonian Ellis fluid. *AIChE J.*, 11 (4), 588-595.

McCarthy, K.L. & Kerr, W.L. 1998. Rheological characterization of a model suspension during pipe flow using MRI. *J. Food Eng.*, 37, 11-23.

McCarthy, K.L, Kerr, W.L. & Kauten, R.J. 1997. Velocity profiles of fluid/particulate mixtures in pipe flow using MRI. *J. Food Process. Eng*, 20, 165-177.

McCarthy, K.L., Kauten R.J. & Walton, J.H. 1996. Dynamics of fluid/particulate mixtures in tube flow. Short Communication. *Magnetic Resonance Imaging*, 14, 995-997.

Mooney, M. 1951. The viscosity of a concentrated suspension of spherical particles. *Journal of Colloid Science,* 6, 162-170.

Newitt, D.M., Richardson, J.F., Abbott, M. & Turtle, R.B. 1955. Hydraulic conveying of solids in horizontal pipes. *Trans. Inst. Chem. Engrs.*, 33, 93-110.

Newitt, D.M., Richardson, J.F. & Gliddon, J.F. 1961. Hydraulic conveying of solids in vertical pipes. *Trans. Instn. Chem. Eng.*, 39, 93-100.

Newitt, D.M., Richardson, J.F. & Shook, C.A. 1962. Hydraulic conveying of solids in horizontal pipes. Part II: Distribution of particles and slip velocities. In: *Proceedings: Interaction between fluids and particles*, *IChemE*, London, 87-100.

Norton, T. & Sun, D.W. 2006. Computational fluid dynamics (CFD) an effective and efficient design and analysis tool for the food industry: A review. *Trends in Food Science & Technology,* 17, 600-620.

Rasteiro M.G., Figueiredo M.M. & Franco H. 1993. Pressure drop for solid/liquid flow in pipes. *Particulate Science and Technology*, 11, No. 3-4: 147-155.

Roberts, C.P.R. & Kennedy, J.F. 1971. Particle and fluid velocities of turbulent flows of suspensions of neutrally buoyant particles. In Advances in Solid-Liquid Flow in Pipes and Its Applications. Zandi, I. (Editor), 59-72. Pergamon Press, Oxford, UK.

Rohsenow, W.M., Hartnett, J.P. & Cho, Y.I. 1998. Handbook of heat transfer. McGraw-Hill Professional.

Rutgers, R. 1962(a). Relative viscosity of suspensions of rigid spheres in Newtonian liquids. *Rheol. Acta*, 2, 202-210.

Rutgers, R. 1962(b). Relative viscosity and concentration. *Rheol. Acta*, 2, 305-348.

Segré, G. & Silberberg, A. 1962(a). Behaviour of macroscopic rigid spheres in Poiseuille flow. Part 1. Determination of local concentration by statistical analysis of particle passages through crossed light beams. *J. Fluid Mech*, 14, 115-135.

Segré, G. & Silberberg, A. 1962(b). Behaviour of macroscopic rigid spheres in Poiseuille flow. Part 2. Experimental results and interpretation. *J. Fluid Mech*, 14, 136-157.

Segré, G. & Silberberg, A. 1961. Radial particle displacements in Poiseuille flow of suspensions. *Nature,* 189, 209-210.

Seville, J.P.K., Tüzün, U. & Clift, R. 1997. Processing of particulate solids. Chapman & Hall, UK.

Shah, S.N. & Lord, D.L. 1991. Critical velocity correlations for slurry transport with non-Newtonian fluids. *AIChE J.,* 37 (6), 863-870.

Shaw, C.T. 1992. Using computational fluid dynamics. Prentice Hall International (UK) Ltd.

Shook, C.A. & Roco, M.C. 1991. Slurry flow: principles and practice. Butterworth-Heimemann.

Sinton, S.W. & Chow, A.W. 1991. NMR flow imaging of fluids and solid suspensions in Poiseuille flow. *J. Rheol*, 35 (5), 735-771.

Smith, K.M., Davidson, M.R & Lawson, N.J. 2000. Dispersion of neutrally buoyant solids falling vertically into stationary liquid and horizontal channel flow. *Computers & Fluids*, 29, 369-384.

Sumner, R.J., McKibben, M.J. & Shook, C.A. 1990. Concentration and velocity distributions in turbulent vertical slurry flows. *Ecoulements Solide-Liquide*, 2 (2): 33-42.

Thomas, D.G. 1965. Transport characteristics of suspensions. Part VIII. A note on the viscosity of Newtonian suspensions of uniform spherical particles. *Journal of Colloid Science*, 20, 267-277.

Toda, M., Shikawa, T., Saito, S. & Maeda, S. 1973. On the particle velocities in solid-liquid two-phase flow through straight pipes and bends. *J. Chem. Eng. Japan,* 6 (2), 140-146.

Tucker, G.S. & Heydon, C. 1998. Food particle residence time measurement for the design of commercial tubular exchangers suitable for processing suspensions of solids in liquids. *Trans. IChemE, Part C, Food and Bioproducts Processing*, 76, 208-216.

Turian, R.M. & Yuan, T.F. 1977. Flow of Slurries in Pipelines. *AIChE J.*, 23 (3), 232-243.

Turian, R.M., Yuan, T.F. & Giacomo, M. 1971. Pressure drop correlation for pipeline flow of solid-liquid suspensions. *AIChE J.*, 17, No. 4, 809-817.

Van Wachem, B.G.M. & Almstedt, A.E. 2003. Methods for multiphase computational fluid dynamics. *Chemical Engineering Journal*, 96, 81-98.

Wen, C.Y. & Yu, Y.H. 1966. Mechanics of Fluidization, *Chem. Eng. Prog. Symp.* Ser., 62, 100-108.

Wilson, W.E. 1942. Mechanics of flow, with non-colloidal, inert solids. *Trans ASCE*, 107, 1576-1594.

Zandi, I. & Govatos, G. 1967. Heterogeneous flow of solids in pipelines. J*ournal of Hydraulics Division*, Proceedings of the American Society of Civil Engineers, May, 93 (HY3): 145-159.

Zhang, L. & Fryer P.J. 1993. Models for the electrical heating of solid liquid food mixtures. *Chem. Eng Sci*., 48 (4) 633-642.

6. CONCLUSIONS AND FURTHER WORK

6.1. CONCLUSIONS

Validated CFD models have been used to study three complex flows: (i) isothermal flow of non-Newtonian fluids in a mechanically vibrated pipe, (ii) heat transfer to Newtonian and non-Newtonian fluids in vibrational flow, and (iii) solid-liquid flow of coarse nearly-neutrally buoyant particles in non-Newtonian carrier fluids.

The results of the first investigation have shown that, while Newtonian fluids are not affected by the superimposition of a sinusoidal mechanical vibration, non-Newtonian fluids undergo substantial changes. The superimposition of rotational oscillation was shown to have a large influence on the velocity profile, and hence flow rate, of shear thinning, shear thickening, and viscoplastic fluids. The changes in velocity profile and flow rate were attributed to changes in the apparent viscosity imparted by the additional applied shear. Vibration caused the velocity profile of shear thinning and viscoplastic fluids to stretch in the flow direction, thus, increasing the total flow rate. The enhancement in flow was calculated as the ratio of vibrational flow rate to steady state flow rate. The velocity profile of shear thickening fluids, on the other hand, was flattened under vibration due to the increase in viscosity caused by the added shear, thus, leading to flow retardation.

The extent of such effects was found to depend on vibration parameters, fluid rheological properties and pressure gradient. The enhancement ratio for a shear thinning fluid increased with vibration frequency and amplitude, but different combinations of frequency and amplitude corresponding to the same maximum acceleration gave the same enhancement. While increasing vibration frequency or amplitude resulted in elongated velocity profiles, the normalised velocity profile was only slightly affected, thus, indicating that vibration did not alter the flow characteristics significantly under the vibration and flow conditions used. Although flow enhancement ratios as high as 5 for power law fluids and 12 for Herschel-Bulkley fluids were achieved using sonic frequencies, it was found that the increase in

enhancement ratio with vibration frequency reaches a limit beyond which no further enhancement is achieved. The effect of increasing vibration frequency, therefore, decreases at high frequencies.

The enhancement ratio was also sensitive to the flow behaviour index, consistency index, and yield stress. The more pronounced the non-Newtonian behaviour of the fluid, the stronger the effect of vibration on its flow. For shear thinning fluids, the flow enhancement ratio increased as the flow behaviour index was reduced, i.e. as shear thinning increased, due to the increased dependence of the fluid viscosity on shear. The velocity profile underwent considerable elongation under vibration compared with the steady-state velocity profile for all flow behaviour index values considered. For shear thickening fluids, the flow enhancement ratio decreased below unity as the flow behaviour index was increased, due to the increased shear thickening. Increases in the flow consistency index for a shear thinning fluid gave rise to higher flow enhancement ratios. For viscoplastic fluids, the flow enhancement ratio increased exponentially with the yield stress. This enhancement was most pronounced when shear thinning and yield stress effects were coupled (i.e. for Herschel-Bulkley fluids).

Increases in pressure gradient, and hence steady-state flow rate, led to reduced flow enhancements. The potential for flow enhancement, it can be concluded, diminishes with increasing steady-state flow rate.

While mechanical vibration with frequencies on the sonic scale produced substantial enhancements in the flow of low to moderately viscous fluids, it had limited scope for enhancing the flow of highly viscous fluids. Ultrasonic rotational vibration, however, was very effective at enhancing the flow of extremely viscous materials (k ~10 kPa s^n, n ~0.3, τ_0 ~200 kPa) leading sometimes to two orders of magnitude increases in flow rate for extremely viscous Herschel-Bulkley fluids, thus, offering a great potential for the processing of such complex materials.

Different vibration modes resulted in different degrees of flow enhancement. Under identical conditions, sinusoidal pipe oscillations in the direction of flow produced flow enhancements which were greater than those generated by rotational oscillations, which, in turn, were greater than those produced by transversal oscillations in a direction normal to the flow. Nonetheless, the three modes of oscillation yielded substantial enhancements in flow, and the choice of vibration mode for a given process is largely a matter of convenience.

Flow visualisation using particle trajectories revealed a degree of angular secondary motion in the fluid induced by rotational oscillation. The trajectories showed that fluid particles experience angular oscillations, the amplitude of which increases as the distance from the wall decreases.

The benefits of mechanical vibration are not limited to flow enhancement. The results of the second investigation showed that a transversal mechanical vibration imposed at the wall of a pipe conveying a Newtonian or non-Newtonian fluid in non-isothermal laminar flow generates a vigorous swirling fluid motion represented by a strong vorticity field and complex spiralling fluid streamlines and trajectories. This chaotic fluid motion results in strong convective currents at the wall and substantial radial fluid mixing leading to large enhancement ratios in wall heat transfer and a near-uniform radial temperature distribution. Temperature contours showed that without vibration the temperature profile develops extremely slowly along the pipe, as the temperature difference between the fluid and the wall decays exponentially along the pipe. With vibration, however, the temperature profile develops so rapidly that a given outlet temperature can be achieved along a much shorter pipe length. The thermal entrance length can be reduced by an order of magnitude or more compared to its value in steady state flow.

The observed effects were governed by the amplitude and frequency of vibration so that, for a given fluid viscosity, higher amplitudes and frequencies led to better improvements in heat transfer characteristics. More viscous fluids required a more energetic vibration but the effects appear to be more sensitive to the amplitude than

the frequency of wall oscillations. Compared to Newtonian fluids, shear thinning fluids exhibited more pronounced vibrational effects which increased in significance as the flow behaviour index was reduced, i.e. as shear thinning increased.

Transverse vibration in non-isothermal conditions also had a significant stretching effect on the velocity profile at a constant flow rate, even for a Newtonian fluid. In a Newtonian fluid, this effect is attributed to the influence of temperature on the viscosity. In steady non-isothermal flow, the velocity profile is flattened compared to the isothermal profile. However, as the temperature profile becomes more uniform due to vibration, the temperature near the wall decreases compared to the steady state, thus, increasing the viscosity in this region and reducing velocity. On the other hand, the temperature near the pipe centre increases, thus, reducing the viscosity and increasing velocity there.

It can also be argued that the strong spiralling fluid motion generated would have added benefits in reducing fouling of the pipe because of the cleaning action that the fluid motion would create at the wall, and in a two-phase solid-liquid flow it would help keep the solid particles in suspension and enhance liquid-particle heat transfer. These results open up new opportunities for the potential application of mechanical vibration as an elegant non-intrusive technique in processes where reducing non-uniformity in heat transfer represents a challenge.

In the third investigation, CFD simulations of the solid-liquid suspension flow of coarse nearly-neutrally buoyant particles in non-Newtonian fluids were performed using an Eulerian-Eulerian numerical model. The CFD computations of solid phase velocity profile and particle passage times matched the experimental PEPT and Hall effect sensors measurements to a very good degree of accuracy.

Results showed that, except for the smaller particles (< 4 mm), the velocity profile of the solid phase exhibited a significant degree of asymmetry which increased with particle size due to the increased propensity of particle settling. Also, with increasing particle size (d > 4 mm), the maximum solids velocity decreased and the position at which this velocity occurred shifted upwards above the centreline. Particles generally

travelled faster than the mean mixture velocity, and while the maximum particle velocity was considerably less than twice the mean mixture velocity in shear-thinning carrier fluids, it exceeded this value in strongly shear thickening fluids (~ $n > 1.75$). Larger particles also caused significant blunting and asymmetry in the liquid phase velocity profile. Whereas the particle concentration profile was nearly uniform for smaller particles ($d < 3$ mm), indicating a pseudo-homogeneous flow, increasing the particle diameter distorted the concentration profile due to enhanced settling. The solid-liquid pressure drop declined as particle diameter increased.

At higher solid concentrations, the solid phase and liquid phase velocity profiles became flatter and the particles were radially more uniformly distributed. Increasing the concentration also increased the pressure drop incurred considerably as the friction losses due to particle interactions increased. Increasing the mean flow velocity had no influence on the normalised velocity profile of either phase, the normalised particle concentration profile, or the pressure drop increase relative to the carrier fluid flowing alone.

The fluid consistency index did not have any influence on the normalised velocity profiles, normalised particle distribution, or pressure drop increase relative to single-phase flow. However, more shear thinning, i.e. lower n, induced a gradual flattening of the velocity profile of the solid phase and of the liquid phase relative to the fluid flowing alone. No significant effects were observed on the normalised particle concentration profile or the increase in pressure drop compared to single phase flow.

In vertical down-flow, particle radial distribution was remarkably uniform under all conditions investigated. The normalised solid-phase and liquid-phase velocity profiles and normalised particle concentration profile were independent of particle size and concentration under the conditions studied. However, increasing particle concentration resulted in a significant rise in pressure drop relative to single phase flow.

These results have important practical implications for the processing of solid-liquid food mixtures where knowledge of the solid phase and liquid phase velocity profiles

is crucial for the design of the process. The Eulerian approximation of the solid phase has thus been shown to be useful in predicting the behaviour of such systems.

6.2. FURTHER WORK

This work has shown that mechanical vibration can improve the processing of viscous fluids in single-phase flow. It also highlights the need for further research in this area which can build on the results reported here. The following are recommendation for future work:

1. The heat transfer enhancement reported here is obtained at a uniform wall temperature and is therefore accompanied by an increase in the heat flux required. It is therefore necessary to investigate the feasibility of providing the much enhanced heat flux under vibration conditions. This can help to assess the viability of mechanical vibration, over a range of vibration conditions, as a means of enhancing heat transfer and temperature uniformity in industry.

2. The heat transfer enhancement study was conducted at low Reynolds numbers (Re up to ~20). More work is needed to cover a wider range of Re.

3. The effects of vibration under a uniform and constant wall heat flux need also to be investigated and compared with the results obtained here.

4. The study of heat transfer enhancement by means of vibration can be extended to two-phase solid-liquid systems. This can be performed initially at a low solids concentration and using the Lagrangian particle tracking CFD model, in order to gain a fundamental understanding of the effects present in this complex flow. It may also be necessary to conduct some experimental work to provide measurements to validate the CFD model. It may also be useful to combine Discrete Element Modelling (DEM) with CFD to tackle this problem.

5. Work is needed to determine the economic and technological viability of using vibration as a means of enhancing flow and heat transfer.